Instructive Graphene Oxide Biomaterials for Neural Tissue Engineering

John Brewster

Submitted in accordance with the requirements for the degree of

Doctor of Philosophy

The University of Leeds

Institute of Medical and Biological Engineering

2021

Intellectual Property

The candidate confirms that the work submitted is his own and that appropriate credit has been given where reference has been made to the work of others.

This copy has been supplied on the understanding that it is copyright material and that no quotation from the thesis may be published without proper acknowledgement.

Acknowledgements

First I must express my gratitude, appreciation and respect for the efforts of my supervisors, Dr Lin-Hua Jiang, Dr Xuebin Yang and Dr Xiaodong Jia, without whom this work would not have been possible. Thank you for all of your invaluable guidance and careful supervision during my PhD research. Our discussions throughout all the challenges of this work have kept me grounded and focused despite trying times. It has been a privilege to contribute and be part of your lab.

I would like to thank my internal examiner Dr Jessica Kwok for her advice and encouragement during my annual reviews and beyond. I must also recognise and thank the Institute for Medical and Biological Engineering and their Tissue Engineering and Regenerative Medicine Centre for Doctoral Training. This programme provided an opportunity I had never expected to have.

Thanks are owed to all of my colleagues from the CDT, in particular Daniel Secker and Trang Nguyen, for their support and assistance. They have been sources of strength and solidarity during the pursuit of this research and became irreplaceable friends.

Personally I would like to express my love and thanks to my wife, Collette who always had confidence in my ability, even when I didn't. Finally my children whom paradoxically served as my greatest motivation and most severe impediment to the completion of my research. I don't know how they have tolerated me as a husband and father for the last 5 years.

Abstract

Graphene oxide (GO) is a nanomaterial that has gained increasing interest for its use in neural tissue engineering (NTE) for its structural and conductive properties. There is also evidence that GO has the instructive potential of enhancing neurogenesis and regulating inflammation. The aim of the study presented in this thesis is to establish 2-dimensional (2D) and 3D models and to examine the effects of GO on neural cells in the central nervous system to further the understanding of GO as an instructive biomaterial for NTE.

In the first part of the study, thin 2D GO films were generated, and characterised. Thin GO films of 50 nm cross sectional thickness were consistently produced using spin coating technique, from aqueous suspension of commercial GO, on glass coverslips without or with prior coating by polyethylenimine. The GO films were uniform in thickness and structure. Raman spectra show that the GO films were amorphous and had two peaks characteristic of GO. Quantification of atomic percentage using X-ray photoelectron spectroscopy (XPS) indicates that the GO films contained twice as much carbon than oxygen and the molecular structure with oxygen bound in polar epoxide and carboxylic acid groups. XPS also indicates the GO surface can adsorb biomolecules during cell culture, which was resistant to washing.

The next part of the study tested the biocompatibility of the 2D GO films as a substrate supporting neural cells, using neural cell lines (human SH-SY5Y neuroblastoma cell, and mouse BV2 microglial cell) and primary mouse or rat neural cell cultures (hippocampal neurons, microglia and astrocytes). For all these types of neural cells, GO supported cell attachment, proliferation, and maturation, without inducing cell death. In addition,

there was a significant increase in neurite extension in SH-SY5Y cells on the GO films, under differentiation conditions, suggesting enhanced differentiation. GO did not induce inflammatory phenotypes of microglia cells. The GO films were also leveraged as a drug-delivering vector to further enhance the instructive capacity of GO. The GO films, with prior treatment with ibuprofen, a COX-2 inhibitor involved in microglial activation and inflammation, significantly reduced LPS-induced activation of primary microglia. These results suggest that GO exhibits an excellent biocompatibility as a substrate for neural cells and an ability of enhancing neuronal differentiation, as well as act as a drug-delivery vector.

The last part of the study explored combination of GO with Gel-Ma hydrogels to construct 3D scaffolds for NTE, using two approaches, namely, suspension and layered. Under conditions with suspension of neural cells and GO in hydrogels, neuronal cells survived well, but failed to mature. GO and hydrogels, when assembled in layers, supported maturation of neurons, as well as viability, and formation of networks with astrocytes in co-culture. Furthermore, neuronal cells extended into the hydrogel layer, albeit that the hydrogel remained mechanically slightly stiffer than native brain tissues.

In summary, the results from generation and characterisation of GO as 2D films, construction of 3D scaffolds by combining GO and Gel-Ma hydrogels, and examination of their interactions with major types of neural cells, demonstrate desirable functionalities of GO as a substrate in supporting and regulating neural cell function. The findings provide clear evidence to support the instructive potential of GO as a biomaterial for applications in NTE. The GO 2D film model is a robust platform for further study of GO properties and the mechanism by which GO regulates neural cell function.

Contents

Acronyms

BBB blood-brain barrier

CE chemical exfoliation

CNS central nervous system

CVD chemical vapour deposition

Gel-Ma Gelatin-Methacryloyl

Gel-Nor Gelatin-Norbornene

GO Graphene Oxide

LPE liquid phase exfoliation

ME mechanical exfoliation

MSC mesenchymal stem cell

PLL poly-L-lysine

rGO reduced Graphene Oxide

List of Figures

List of Tables

Chapter 1

Introduction

1.1 A Brief Perspective on Biomaterials

Biomaterials are defined as substances engineered to interact with a biological system which alone or as part of a complex can direct the progress of a therapeutic or diagnostic process. These materials are highly varied, include polymers, self assembling materials as well as vectors, and consider the immunological and toxicological consequences of a material *in vitro* and *in vivo* [1].

Biomaterials historically have been used to restore function lost by degraded natural components. An excellent example for the restoration of lost function is dental implants to replace lost teeth which can be evidenced back over a thousand years. Initial evidence of artificial teeth roots carved from wood with stone caps indicates teeth were being replaced with rudimentary biomaterials [2].

However the use of septic and frangible materials like wood and stone could be expected to have caused significant discomfort and have a limited functional lifetime. As technology progressed over time inert, more durable and biotolerant materials such as gold or porcelain began to be used instead. In the last century the emergence of bioneutral and bioactive materials that can stimulate peripheral healing and secure integration such

as polymers, ceramic and advanced alloys have led to the implants seen in the modern day [3].

This example of teeth being replicated in biomaterials which provided an artificial replacement to tissue lost through ageing or injury has a mirror in tissue and organ transplantation. Up to five hundred years ago, autografted and allografted skin tissue to regenerate injuries had been attempted, however such grafts were often met with limited success until greater understanding of transplant immunology at the turn of the 20th century [4]. Developments in immunology began to allow functional grafts for many lost tissues.

Skin grafting is now a widely available standard treatment thanks to understanding of rejection, preservation of donor material, and robust tissue banking. More complex organs such as kidney transplants from deceased donors had been attempted at the same time. The first successful functional kidney transplant between living twins in the early 1950's led to the first preserved kidney transplant in the 1960's. A major limitation to these transplants was the requirement for anti-rejection medication for life of the recipient to protect the transplanted organ from the host immune system. However transplant donation has often been orders of magnitude lower than patients in need, creating an issue in supply [5].

To overcome the limitations of inert biomaterials and compensate the supply of donor tissues, a new field of research, tissue engineering was broadly defined in 1988. This new field encompasses the principles and methods of engineering and life sciences toward the fundamental understanding of structure-function relationships; examining normal and pathological mammalian tissues and therefore develop biological substitutes to restore, maintain or improve tissue function. Tissue Engineering research began to investigate and develop novel biomaterials that could artificially replicate the function of a tissue in the same manner as a transplant graft whilst remaining biotolerant and more available than donor sources [6, 2].

In the following sections, biomaterial approaches to tissue engineering scaffolds are discussed with a specific focus on how these technologies have progressed. In particular

the combinations of materials, cells and inductive factors which have so far resulted in successful tissue substitution or generation of *in vitro* tissues which exhibit functional structures. These reports have been examined to see how their technologies can continue to be translated into more complex and delicate tissues, such as the brain or spinal cord.

1.2 Tissue Engineering Biomaterials

Tissue engineering is considered to comprise the design and construction of man-refined implants to mimic the native extracellular environment. Commonly materials such as de-cellularised and/or xenogenic tissues, electrospun polymers, nanomaterials and hydrogels are combined with instructive chemical, electrical, pharmacological and topographical cues, to influence cell behaviour. Therefore Biomaterials are an integral part of tissue engineering.

A material may be chosen for favourable characteristics as culture surfaces for cell populations that simulate or substitute extracellular matrix to direct and support cell growth. However a material may also be chosen for desirable bioabsorbable performance and/or mechanical strength to support a regenerating defect. A single material may provide all the requirements during regeneration, however scaffolds can be complex and multi-material, with each component meeting a biological need. The functionality of a tissue engineering implant can be described by the interactions between native tissue and the implant. An inert scaffold provides only a physical structure permissible to healing. A therapeutic scaffold may include instructive factors to direct and control the healing behaviour within itself, whilst a living scaffold may include cells to facilitate eventual development into an allograft alternative.

1.2.1 Nanomaterials in Tissue Engineering

Nanoscale engineering of scaffold structures has led to scaffold design becoming more complex and allowed for biologic signalling to be introduced by otherwise inert scaffolds.

This can range from introducing complex topographies to aid in tissue integration, to materials which control cell fate at the material-tissue interface. Such advanced engineering has trended towards artificial recreation of natural tissue architecture, providing biosimilar arrangements and structures for cells during regeneration [7]. Examples of this can be seen in the surface coating of joint and vascular implants to allow for ingrowth of native tissues faster and more robust tissue-implant interface with less scar tissue formation [8]. This leads to a longer implant lifetime, reduced patient morbidity from revision and improved patient outcomes.

Scaffold research has also explored inclusion of nanomaterial isoforms of otherwise common biotolerant materials including transition metals such as iron (as steel), gold, molybdenum and titanium. Non-metal elements silicon and carbon including graphene are also more commonplace as structural and surface components in nano-engineered biomaterials. Such additives are selected to enhance the properties of other biomaterials. Such enhancements include imparting conductivity to polymers, additional binding sites for pharmaceutically functional molecules and reinforced mechanical strength [9].

Inclusion of nanomaterials in 2D and 3D culture systems *in vitro* are reported to enhance cell growth and tissue generation, attributed to the increased resolution to provide topography, physiochemical cues and vectors to the scaffold system [10]. Modification of biomaterials with nanomaterials to improve or supplement material properties is a growing field with new research conducted constantly. Nanomaterial inclusion remains controversial with concerns over nano-toxicity and contamination of surrounding tissues with nano-particulate matter. This is particularly true of metallic nanomaterials following the metal on metal hip scandal and accumulation of chromium nanoparticles within the pelvic tissue of hip transplant recipients in the late 20^{th} century [11].

1.2.2 Engineered Tissue Substitutes

Tissue engineering research also includes the *in vitro* generation of functional artificial tissue as tissue substitutes. Such applications of artificially generated tissue include research

models to reduce animal use in research as well as research to validate pharmaceuticals for safety and mode of efficacy [12].

One aim of tissue engineering is to replace or regenerate otherwise terminally damaged or lost tissues of the body with functional biocompatible artificially engineered constructs [13]. Though autograft and allograft materials remain the gold standard for tissue replacement, several tissue engineering solutions have matured and have a history of use clinically. Biomaterial implants have a number of advantages over graft tissue including reducing the risks associated with allograft, reduced donor site morbidity associated with autogenic grafts. Tissue substitutes have historically included autogenic, allogenic and xenogenic transplants. Biomaterials and tissue engineered products are supplementing the use of transplanted tissues in like for like applications. Increasingly advanced materials are seeing more use over the last decade, coming closer to replicating the gold standard transplant tissue as seen in Table 1.1.

Common to all tissue engineering scaffolds is the target tissue having insufficient regenerative potential, either due to a lack of tissue regeneration, rapid scar formation or essential function. The history of research has led to widespread understanding of the three component understanding of tissue engineering: *Cells, Scaffolds* and *Growth factors.* A good example of this understanding in tissue engineering is seen in bone defect grafting.

An inert but bioabsorbable biomaterial natural coral converted to coralline-hydroxyapatite has been used as a scaffold to repair bone defects. Coral implants began to resorb as natural bone regrew and showed improvement in the outcome of bone grafts. However the coral material was not perfect [26]. The mechanical strength of the coral implants was lower than native bone and could become easily damaged, an effect further compounded by the sterilisation processing required to create the implant. Generation of bone through the graft was also progressive from the edges. This resulted in protracted, though positive, healing durations. These inert permissive scaffolds fill the defect and allow native tissue to grow into the graft. Within these scaffolds the complex structure provides topography, whilst physical therapy introduces strain and mechanical direction to native osteocytes

Table 1.1: Examples of progression in tissue engineered solutions

Tissue	Transplant / Graft source	TE Material 2008	Reference	TE Material 2018	Reference
Bone	Autogenic, Allogenic	Natural coral	Petite *et al.*. [14]	Bioceramic composites	Ginebra *et al.*.[15]
Cartilage	Autogenic	Acellular hydrogel	Temenoff *et al.*. [16]	Regenerative instructive therapy	Rosa *et al.*. [17]
Ligament	Autogenic	Polymers	Funakoshi *et al.*. [18]	Decellularised tendons	Jones *et al.*. [19]
Cardiac Valves	Allogenic, Xenogenic	Mechanical	Nair *et al.*. [20]	Decellularised or In-vitro synthetic valve	Glaser *et al.*. [21]
Vascular	Autogenic	Synthetic Polymer	Innocente *et al.*. [22]	Decellularised tissue	Lin *et al.*. [23]
Dermis	Autogenic, Allogenic	Collagen patch	MacNeil. [24]	Decellularised Dermis, In-vitro tissue	Savoji *et al.*. [25]

stimulating bone maturation [27].

Material substitutes can provide mimicry of mechanical functions and physical support, for example as mechanical cardiac valves responding to hydraulic pressure from blood flow [28]. Likewise nerve conduits can guide nerve growth both chemically and topographically [29]. However such functional constructs do not yet fully replicate and replace original tissue, requiring a period of integration before normal function is restored.

1.2.3 Inductive and Living Scaffolds

More complex later generations of these scaffolds provide a more active regenerative medicine solution. Osteoinductive hydroxyapatite grafts use a similar synthetically generated or farmed scaffold material. However the scaffold is enhanced with osteoinductive growth factors as a surface chemistry modification to introduce instructive components to an otherwise inert mechanical implant.

Bespoke versions of these grafts may also include therapeutic cell populations generated from a patients own cells to provide innate regenerative capacity [30]. Inclusion of cells resulted in a greater rate of healing than inert scaffolds alone. Additionally implants could regenerate larger bone defects than natural healing or inert material alone [31].

However inductive and cell therapy grafts have more stringent regulatory controls than a single material inert implant. The limiting factor in cell therapy active implants is the increased cost, complexity and decreased shelf life compared to inert implants and allograft material [32]. As such cell therapy products are highly bespoke and specialised, used thus far in trial circumstances without widespread adoption [27].

Innovated tissues, endocrine tissues and organs such as the heart and brain are reliant on metabolic cell function cannot be substituted by current materials alone, cellular functions can only be replicated by equivalent cells. Similarly inert scaffolds which provide mechanical support require integration and population with native cells are not suitable for tissues which have very low regenerative potential. Particularly in the brain and spinal cord no material substitute exists which is able to replicate the function of

neurons, or glial cells. In these areas, scaffolds combined with suitable replacement cells may be the only option for tissue substitution.

Stem cell therapies with pluripotent stem cells have been investigated for such tissues including cardiac injury and neurodegeneration due to the potential of a cell therapy to differentiate and generate required tissues *in situ* [33]. There are however several drawbacks to cell therapies such as inconsistent results and a risk of non-specific tissue generation. Of particular concern is teratoma formation as transplanted cells can disperse away from the target site [34, 35, 36]. Provision of cells *via* a tissue engineering living scaffold may mitigate this risk.

Autologous transplant of *in vitro* purified and cultured olfactory ensheathing cells from the nasal passage to damaged spinal cords has reported some success in restoring spinal cord function [37, 38]. Although to date only limited neurological improvement has been reported in clinical trials, this approach is one of few to approach lesions that are already scarred with neurological voids within the target site. The reported success in this trial suggests that tissue engineering with neural stem cells has potential as a future treatment for chronic neural lesions [39].

These grafts utilising autologous multi-potent cells present interesting opportunities for engineered tissue substitutes to become more like true transplant materials, capable of quickly supplanting the function of damaged tissues. For cellular therapies to become more widespread, challenges remain to be overcome. The tissues that would most benefit from such tissue substitutes; post mitotic tissues with no currently suitable transplant or graft, include neural tissue, however these cells are fastidious to the cellular micro-environment and have poor long term survival outside of their native growth environment. Therefore, biomaterials with instructive and permissive properties to cell populations will be a foundation of future tissue engineering scaffolds. To date research has investigated ways to further enhance biomaterials and scaffolds with additional factors such as nanomaterials, cells and growth factors. The following sections specifically discuss hydrogels as a promising material for soft tissue engineering, and the research surrounding graphenes,

a carbon nanomaterial of interest for imparting further functionality to scaffolds.

1.3 Hydrogels in Tissue engineering

In tissue engineering scaffolds, biomaterials are used to create the construct for implantation or culture of biological material. In some cases, such as the natural corals cited above and historical uses of inert biomaterials, these are hard or rigid structures upon which tissue is grown. However for soft tissues, a more mechanically soft material is required. In native tissues, extracellular matrix is comprised primarily of collagen fibre connective tissue enhanced with glycosaminoglycans secreted by cells during maturation to provide an instructive 3D extracellular micro-environment and substrate for cells forming complex tissue. Hydrogel matrices are commonly used as substitutes for extracellular matrix in tissue engineering to produce scaffolds for cell culture. Several hydrogels have been proposed for nerve guidance conduits, and more central nervous system (CNS) scaffolds including polyacrylamide, alginate, hyaluronic acid and cross-linked DNA [40].

Hydrogels are three-dimensional, highly absorbent to water, macromolecular polymer gel constructs derived from a cross linked network of polymer chains. Hydrogels are similar in appearance to common gel, such as edible gelatine confectionery, which comprises denatured collagen polymer chains entangled into a thermally sensitive matrix. These gels are thermosensitive, hydrogels differ in that their physical structure is thermally resistant once cross linked. In hydrogels the polymer chains, which may also be referred to as macromer chains, are cross linked with covalent bonds to form a more stable gel which is resistant to dissolution, temperature and changes in osmolarity or pH [41].

Hydrogels have been used as biomaterials in a range of applications since their first report, initially contact lens material during the 1960's [42]. Hydrogels are well suited for applications in biological systems due to their high capacity to absorb and retain water as a liquid phase within the polymer matrix. This allows for delivery of soluble molecules via hydrogel interfaces as well as for hydrogels to exist in equilibrium with hydrated environ-

ments such as within the body, such as the eye as in the previous example. Mechanically this high water content leads to a highly compliant material which in general does not dehydrate or irritate peripheral tissues. The capacity for a hydrogel to provide a compliant and biosimilar material-tissue interface is one of its most desirable attributes. Hydrogel materials such as fibrinogen sealant are commonly used and marketed as a biocompatible glue for use during surgery and the treatment of wounds with a bioabsorbable filler.

Many common hydrogel polymers are derived from biodegradable sources and have high biocompatibility, hydrogels are often used to provide a compatible material-tissue interface *in vivo* [43]. Hydrogels in tissue engineering serve as scaffolds, and may include cells within the gel formulation as in biofabrication of so called 'living scaffolds' [44]. Bio-fabrication with hydrogels often includes gels formulated to replicate extracellular matrix. Extracellular matrix components are commonly used as the basis of such gels and thus create tissue substitutes with analogous chemistry to native tissue [45, 46, 47, 48, 49]. Encapsulated stem cell populations in living scaffolds have been shown retain differentiation potential within a hydrogel matrix [50, 51]. In a model of neural tissue generation, encapsulated neurons are reported to form complex axonal networks [52] whilst permissible materials show that native tissue can enter a scaffold indicating hydrogels can function as nerve conduit [53, 54].

1.3.1 Composition and Preparation of Hydrogels

When hydrated, Hydrogels can be up to 99% water by mass, depending on formulation [55]. Hydrogels absorb water via osmotic, hydration and capillary interactions within the hydrophilic polymer matrix. Once swollen hydrogels can retain water in equilibrium and resist further expansion, retaining a maximum physical dimension. Hydrogels are also commonly used to support and deliver other materials, such as nanomaterials, as composite material whilst still retaining the physical and mechanical properties of the hydrogel [56]. Furthermore hydrogels are commonly bioabsorbable and can be gradually replaced with native tissue. Hydrogels therefore are distinct from other biomaterials

used for composites such as electro-spun polymers which are frequently dried and more permanent than hydrogels when used as a supporting substrate.

Widely used biomaterial hydrogels are comprised of macromer chains including dextran [57], gelatin [58], hyaluronic acid and chondroitin sulfate [59], poly-vinyl-alcohol [60], chitosan [61] and cellulose [52]. Macromer chains are functionalised to allow controllable cross linking between readily reactive pendant groups such as methacrylate, tyramine or norbornene. Hydrogel formulations may include a secondary cross linking molecule such as branched polyethylene-glycol which bridges between reactive groups on the macromer.

Further to the choice of macromer and functionalisation for a hydrogel, the cross linking system is also important. Cross linking is the primary way in which material properties of hydrogels are tuned, controlled and specialised for their application. External stimulation which causes propagation of a stoichiometric reaction with no bi-products is described as a 'Click Chemistry' [62]. Click Chemistry provides switchable, temporal control over the cross linking process, otherwise referred to as 'Clickable' [63].

Two types of cross linking reaction have been described, a theoretical presentation is seen in Figure 1.1. The first type is step growth describes a system where all molecules present in the initial pre-gel mixture can react. Examples of step growth hydrogels include thiolated gels, where thiol groups on the macromer can polymerise with target groups on a linker molecule. Step growth is characterised by high initial rates of reaction where linker molecule begins to bond to macromer. Only the later stages of the reaction produce high molecular weight macromolecules where bonded macromer links to other macromer [65]. This system is rate limited by the ability of large the intermediate molecules being able to cross link together [66]. Thus step growth systems are delicate and require careful optimisation to ensure cross linking has completed.

The second mechanism is chain growth, where the reaction propagates throughout the system reacting only at an active site thus reaction rate is limited by the presence or absence of a tertiary initiator [67]. Chain growth systems are said to generate more

consistent hydrogels, as cross linking can only occur on growing chains not in side reactions, providing a greater degree of control over the rate of reaction. However in a chain growth system, as all macromer cross linking groups are reactive together, there is a risk of 'Cyclisation'. Therefore chain growth systems can produce numerous molecular weight agglomerations throughout the reaction [68, 65]. Additionally, a chain growth system, once initiated will continue until all available macromer linking groups are consumed, providing less scope for control of the resulting gel properties. Methacylate-based hydrogels are an example of chain growth systems, where methacrylate groups will polymerise until completion.

Over the years, several hydrogel cross-linking initiator systems have been pioneered. Free radical propagation is commonly used to catalyse the cross linking reaction, with free radical generation derived from a number of sources including; redox reactions [69], irradiation with gamma radiation [70], heat [16], changes in pH [71] and ultraviolet or visible light in so called 'Photo-Click' [72].

Photo-Click reactions are the most common and convenient form of hydrogel initiator presented, particularly in biofabrication and tissue engineering. Several photo-Click systems are commercially marketed. Photo-Click initiated hydrogels rely on the generation of free radicals from a molecule, typically a persulfate, following absorption and excitation of a photo initiator sensetive to a specific wavelength of light. Commercially available traditional UV photoinitators such as Irgacureő (1-[4-(2-hydroxyethoxy)-phenyl]-2-hydroxy-2-methyl-1-propan-1-one) and LAP (lithium phenyl(2,4,6-trimethylbenzoyl) phosphinate) are available with sensitivities to a range of UV wavelengths.

However the above photo-click initiator systems have limitations for tissue engineering. UV wavelengths are typically cytotoxic through DNA damage, thus if a hydrogel is used with encapsulated cells UV photo click systems result in a loss of cell viability. Similarly, photo-click initiators are often limited by light penetration distance as the initiator reduces the intensity of the incident light during cross linking [73]. Consequently, new research into visible wavelength initiator systems using excitable transition metal complexes such as

Ruthenium are reported to have enhanced penetration, improved survival of cells exposed to the cross linking process, and comparatively more biocompatible micro-environments compared to UV initiated commercial initiator systems [74, 60, 75, 76, 73].

Particularly where hydrogels are used to encapsulate other biomaterials, the use of initiator systems can alter the encapsulated material surface chemistry. However this can be used as a positive by providing an avenue to include an encapsulated material into a hydrogel matrix covalently. In recent work hydrogels are more commonly modified with nanomaterials to provide enhanced physiochemical properties compared to the hydrogel alone. Nanomaterials have been used to provide topographical, conductive and pharmacological properties to hydrogels [40].

1.3.2 Gelatin Hydrogels

Gelatin is commonly used in bio-fabrication applications as a high print fidelity material [49]. Gelatin is also of interest for use with nanomaterial applications as the polar groups found throughout the gelatin chain provide excellent hydrophilicity and the long chain structure can effectively encapsulate nanomaterial loads [77]. Additionally these properties allow gelatin to form thin films, permeable to oxygen making it suitable for generation of thin tissue culture models.

Gelatin hydrogels remain of interest in tissue engineering as a highly adaptable platform for modification. Gelatin is biodegradable, in contrast to synthetic hydrogel formulations, which is desirable for a tissue scaffold destined to be replaced with host tissue, but may pose a challenge if gels degrade too quickly. As a biopolymer derivative of collagen, Gelatin macromers have advantages in biocompatibility and cell adhesion compared to synthetic polymer macromers [60]. Gelatin remains highly hydrophilic and the gelatin chain retains biosimilar chemical composition found in collagen, resulting in excellent cell adhesion characteristics [77]. However this also poses challenges; gelatin macromers are much larger in molecular weight and lower in thermal stability than synthetic polymers, resulting in mechanically softer gels for at similar w/v formulations. Additionally gelatin

macromers are more prone to cyclisation than lower weight macromers [78].

In this thesis, two similar gelatine based hydrogels have been used; Gelatin-Methacryloyl (Gel-Ma), and Gelatin-Norbornene (Gel-Nor). These hydrogels allow a comparison between chain-growth and step-growth cross linking. This distinction in cross linking chemistries is of interest as the long term endurance of these gels as scaffolds has been rarely examined and compared in literature.

1.4 A Brief Perspective on Graphene

Graphene is a two dimensional atomic carbon allotrope where the atoms are arranged as sheets, first described in Novoselov and Geim in 2004, involving separation of the z-stacked sheets from the graphite block into several graphene sheets [79]. Previously the molecular structure of graphite as stacked sheets of carbon lattice was common knowledge. Novoselov and Geim's presentation of the separated carbon sheets accompanied by a description of the surprising physical and electrical properties kick started a wave of novel research and development utilising graphene in all fields of materials science and engineering, from electronics to construction, pharmaceuticals to biology. The initial discovery of graphene in Manchester, UK, involved simple mechanical exfoliation (ME) using adhesive tape to adhere separate the weakly bound sheet of graphene from a block of graphite. Subsequent interest and development has led to more complex techniques being developed, characterised, published and industrialised. In 2020 the global graphene market is predicted to exceed 140 million USD [80].

1.4.1 Pristine Graphene

Individual sheets liberated from graphite are pure carbon, and described as *Pristine* graphene. This is defined as the essential monolayer sp^2 hybridised carbon lattice, comprised of a single sheet of purely carbon atoms bonded in a hexagonal structure. Within this lattice, each carbon atom has four bonds: three (Carbon Carbon) bonds forming the

planar lattice leaving one dissociated bond.

Other carbon nano-shapes such as Buckminsterfullerene spheres and carbon nanotubes can be described in terms of 3D shapes formed from pristine graphene sheets [81]. Such carbon structures have previously been investigated for a variety of applications including mechanical reinforcement in materials research and pharmaceutical vectors in medical research [82]. In comparison to other carbon nano-shapes, graphene sheets only present surface area in a 2D plane, with no defined edge or finite geometry. This presents opportunities for graphene to be prepared with heterogeneous patterning of functionality within a single sheet [83].

Pristine graphene is available from commercial sources, however graphene production and application remains an area of constant innovation with groups often producing graphene for research locally. One of the earliest innovation in nanomaterials research for graphene production is chemical vapour deposition (CVD). By utilising high temperature to generate graphene sheets directly from gaseous carbon sources such as methane of potentially unlimited size [84]. CVD remains the only widespread growth based methods for generation of pristine graphene independent of graphite stock material.

One of the main drawbacks to CVD is the technique remaining highly specialised and costly. As a consequence of these economic and technical challenges, further refinements to ME techniques to liberate graphene from graphite stock have been developed since 2004. One such common method is liquid phase exfoliation (LPE) where organic solvents and surfactants are used to suspend graphite powders. In suspension, the graphite layers are intercalated by the surfactants increasing the distance between the graphene sheets of the graphite stock, and thus weakening the interlayer bonds. Subsequently the graphite stock can be dissociated via mechanical exfoliation into graphene layers. Therefore LPE provides pristine graphene in relative bulk, following extraction from the solvent [85]. The pristine graphene platelets produced by LPE differ from the sheets generated by CVD techniques, due to finite sheet size and variable geometry in the number of graphene layers generated from the original stock.

Dissociated π-bonds, which in graphite result in the z-stacking of graphene sheets, allow for the free movement of electrons in graphene which results in excellent electrical conductivity. The electrical properties of pristine graphene showed potential initially for electronics and computing applications as a novel semiconductor, similar to silicon. Single and multi layer graphenes show similar yet distinct physiochemical properties [86]. Recent research has revealed a broader potential including biotechnology [87]. Highly conductive pristine graphene has been examined for bio-interfacing applications including biosensors and neural probes [88]. However use of pristine graphene remains uncommon outside of electronics research.

1.4.2 Graphene Oxide

Another graphene material more commonly found in biotechnology research is Graphene Oxide (GO). In general, GO is a graphene lattice with extensive covalently bonded oxygen, making GO more hydrophilic than pristine graphene. Though graphene itself was first isolated from graphite in 2004, previous chemists had described oxidative processing of graphite into graphite oxides. The first efficient preparation described by Hummers and Offeman in 1958 provided a method of producing graphite oxide in bulk with reduced risk of energetic side reactions [89]. The processing of graphite to graphite oxide described in Hummers method involves using strong acids and oxidant compounds to introduce oxygen containing groups to the carbon lattice of each graphene sheet. Therefore the oxygen groups consume π-bonds, as well as disrupting the carbon lattice. In this way the oxygen containing groups increase the z-stack distance and reduce the interlayer forces in a similar manner to the intercalation effects utilised during LPE. The reduced interlayer forces allows for subsequent exfoliation via sonication to separate the graphite oxide into individual, GO sheets [90]. The structure of GO produced by these chemical exfoliation (CE) methods is highly variable and an area of continued discussion in literature [91]. An accepted model is presented as seen in Figure 1.2; GO has polar species including epoxide, carbonyl and carboxyl groups across the lattice.

CE techniques are capable of producing similar single and multi layer sheets in a manner similar to LPE, with sizes and geometries dictated by the starting graphite stock and degree of oxidation. CE methods most commonly reported in literature produce a carbon : oxygen ratio of approximately 1 : 2 [92]. This represents an upper end high degree of oxidation, and many groups report conflicting physical properties of GO in suspension, importantly descriptions of the colour in aqueous suspension range from orange similar to graphite oxide, to brown and black. It is widely accepted that the colour of the GO suspension corresponds to the degree of oxidation [93].

GO can be described as a hydrophilic derivative of graphene with more direct potential for further chemical functionalisation than pristine graphene by targeting the extensive oxygen containing epoxide and carboxylic acid groups [91, 92]. In contrast to pristine graphene, GO is more immediately useable in tissue engineering, where the cell material interface is vitally important therefore hydrophilicity is a critical quality attribute.

The hydrophilicity of GO comes at a cost in material conductivity and carbon lattice structure. Oxidation of carbon atoms of the graphene lattice immobilises the π-bond electrons that provide graphene's excellent conductive properties thus increasing the resistance of individual GO platelets compared to pristine graphene. To restore electrical conductivity, GO is commonly reduced, removing the electronegative oxygen atoms, releasing π-bond electrons and restoring π-bonds via strong reducing agents in colloidal solution [94]. Early reduction methods used hydrazine, a powerful reducing agent and highly toxic hydrogen pnictide similar to ammonia [95]. The reduced form of GO remains distinct from pristine graphene, and has been referred to as GO.

1.4.3 Manufacture and application of GO thin films

Spin coating has been used to create several graphene thin films previously, including, organic electrodes [96], osmotic barriers in fuel cells[97], photovoltaic cells [98], humidity sensors [99], resistive memory devices [100], and gas barriers [101]. Spin coating is not unique to GO , but is common in electronics research for creating thin films of molecules

or nanomaterials as resistors, capacitors or memory devices. Spin coating involves high speed rotation of a substrate, upon which a suspension, in this case GO is deposited. The theory of spin coating states, through the conservation of momentum and the surface tension of the suspension, the rotational force imparted by the spinning substrate drives the suspension across the substrate, creating a nanometre-scale thin coat. The sensitivity of the human eye to thin films has been quantified, which suggested that differences of a few nanometres can be resolved [102]. Therefore spin coated products can often be quality assessed with the naked eye, a valuable attribute for any production process. However few tissue engineering studies have been conducted using this technique with GO . More commonly GO is evaporatively, compressively or precipitately deposited as a surface, resulting in a variance in surface thickness, orientation and thus surface chemistry. Particularly heating and solution changes have been shown to alter GO chemistry [103]. Previous reports indicate the technique might have promise for biological research [104].

1.4.4 Chemical Modification and Reduction of GO

GO platelets are fragile; parameters including size, surface area, graphene platelet sheet count and folding can be compromised by mechanical disruption in suspension, solution changes and precipitation. Therefore researchers must optimise processing and production protocols to avoid fracturing GO sheets into ever-smaller platelets in suspension [105, 106]. Furthermore graphene and reduced Graphene Oxide (rGO) platelets are able to agglomerate back into graphitic bodies, sticking together via π-bonds [107]. In the case of rGO , often used as an alternative to CVD pristine graphene, agglomeration and fragmentation of rGO results deterioration in the desirable physiochemical properties including conductivity. This confounds attempts to use rGO as an analogue to CVD graphene and assess its properties.

For many applications particularly related to biotechnology the toxicity of hydrazine reduction used to produce rGO necessitates extensive post reduction purification of the rGO product [93]. Recently, alternative biocompatible, non-toxic alternatives such as

ascorbic acid and a variety of biomolecules including melatonin or ginseng extract have subsequently become available and have been shown to preserve critical characteristics such as size and layer number [108, 105, 109]. To date hydrazine and hydrazine analogues remains the most common method of reducing GO in literature [110]. Industrial alternatives include stringently controlled proprietary CE techniques which produce GO with lower initial oxidation ratios. In particular these techniques control the ratio and delivery of oxidant to limit the insertion of oxygen to the graphene sheet. Such control has been demonstrated to produce GO derivatives with a carbon to oxygen ratio of $1 : 0.75$ [92]

Concerning GO and reduction methods, controversy remains around models proposing the presence of oxidative debris; highly oxidised 'carbonaceous debris' generated during the CE of GO sheets from graphite. Such debris is described as highly oxygen rich carbon compounds retained against the graphene lattice and confounds the quantitative measurement of oxygen content in graphene oxide materials [111, 112]. Under the two component model, the previously discussed reduction techniques to reduce GO will also destroy the oxidative debris, and only washing with strong bases has been proposed to detach this debris from the GO surface [113, 114, 115]. Presence of oxidative debris may further explain the differing opinions of GO surface chemistry and physiochemical properties, with the presence of debris confounding attempts at quantification. This contention adds to the variety of GO preparation and reduction methodologies. Some examples of the variety reported in GO preparation methodologies are outlined in Table 1.2.

The varied and numerous production methods for GO materials causes a similar variety or 'grade' of final products. Though all can be classed as GO , and can be characterised to have the features of GO , it is the range of potentially confounding secondary factors introduced during bespoke production which can confound subsequent data. For example, variations in surface chemistry and platelet size have been demonstrated to affect the colour of GO in suspension. Similarly, several interpretations previous to the Lerf-Klinowski model have been proposed from similar spectral characterisation. Empirically, different CE reaction media and oxidants have been demonstrated to widely vary the carbon-oxygen

Table 1.2: Example Graphene Oxide Reduction methods

Graphene product	Exfoliation method	Reduction method	Reference
Conductive rGO	CE, Stirring (>7 days)	Heat cycles (RT to 150°C)	Jung *et al.* (2008)
Conductive rGO modified with Gulcose Oxidase	CE, Sonication	Electrochemical (0.7-1.1V, 50mVs^{-1})	Wang *et al.* (2009)
Highly reduced rGO	CE, Sonication	Electrochemical (0.7-0.87V)	Zhou *et al.* (2009)
Aggregation resistant rGO	CE, Sonication	Melatonin incubation (3 Hours)	Esfandiar *et al.* (2011)
rGO	CE without sonication	Hydrazine (12 hours, 80°C)	Park *et al.* (2011)
rGO foam	CE, Sonication	Autoclave in Hydrazine (10 Hours, 90°C 98%)	Niu *et al.* (2012)
Thiol functionalised rGO	CE, Sonication	Phosphorous Pentasulfide (12 Hours, 120°C)	Pham *et al.* (2013)
Glycylglycerine functionalised rGO	CE, Sonication	Glycylglycerine (9 Hours, 90°C)	Congcong *et al.*(2014)

ratio without dramatically altering the spectrographic profile of GO via commonly used Raman analysis [92]. Indeed, Dreyer *et al.* describe GO as a 'family of materials' rather than one distinct material.

When interpreting this vagueness, one can look at examples in other materials - Steel is produced by infusing metallic iron with specific percentages of carbon. All steel comprises carbon with iron, but steel is graded based on the carbon content and different steels are used for different purposes. No similar grading schema exists for GO , however the current body of evidence suggests such a position might be beneficial to de-convolute data and improve consistency. As discussed in the following section, graphenes have a controversial position particularly in tissue engineering with highly variable results reported for similar models conducted by different groups.

1.5 Graphene as a Biomaterial in Tissue Engineering

Graphene as a biomaterial for tissue engineering has been a subject of intensive research for more than a decade, often closely associated with scaffold design with the intent to control proliferation and differentiation of cell populations. Graphene is often used to tune the topographical, physical and electrical stimulation provided by an engineered extracellular matrix [116, 117, 118, 119]. Other applications in which graphene materials are used to improve scaffolds include drug delivery, mechanical structure and reinforcement, angiogenesis and immunomodulation, and bio-interfacing [120, 121, 122, 123]. Graphene biomaterials are the subject of investigation by many of disciplines in tissue engineering, including musculoskeletal, cardiac and neurological tissues.

A range of both GO and rGO derivatives are currently used in literature as tissue engineering substrates. Generally, research has utilised CE derived GO as a starting material, due to its simpler production and initial hydrophilic properties which can then be modified and/or functionalised post exfoliation. Comparatively fewer CVD pristine graphenes and some nanotube derived graphenes have also been studied. Scaffolds have

been developed and take many forms including 2D - films, and 3D - foams, fibres, hydrogels and bound into existing biomaterials [124, 125, 126, 127, 128, 129, 130, 131, 132, 133].

Graphene materials are introduced to a scaffold to take advantage a specific physiochemical attribute of graphene to enhance existing materials with properties such as mechanical strength or durability and improved conductivity. In more recent cases, effects on cell fate has been reported, attributed to graphene materials present in the substrate. This suggests graphene materials can act as both scaffold and growth factor in tissue engineering. However there are also scaffold constructions which are entirely graphene based. The broad variety found in graphene, GO and rGO based scaffolds for use as substrates in cell culture and tissue engineering is as expansive as the often bespoke methods used to produce the graphene in question. A summary of example scaffold archetypes using graphene materials studied in scaffold engineering encountered during reading for this review is presented in Table 1.3.

1.5.1 Coating Graphenes in Biopolymer

Concerns and controversy often cited in research on nanomaterial enhanced tissue implants include the potential of toxic effects [150]. For example, nanotoxicity has been extensively documented with other carbon nanostructures such as nanotubes [151]. Such reports find conductive debris released into tissues from nanotube implants causing bridging of synapse junctions[152]. Other studies have shown that carbon nanostructures induce oxidative stress in macrophages and interfere with metabolic processes, with some suggestion GO can exhibit a similar property *in vitro* [153].

In literature, commonly reported practices confound the understanding of potential biological effects of both graphene and GO . Specifically, preparations of graphene materials which include adhesive biopolymers as coatings between the graphene material and the cell bio-interface. First reported by Li *et al.* [154] where a pristine graphene film was coated with poly-L-lysine (PLL) prior to cell culture, this use of biopolymer is common and this study often cited. Derivatives of this approach are featured in notable publications

Table 1.3: GO 3D structures

Archetype	Graphene material	3D Assembly	Reference
Monolith	Graphene Oxide	Freeze dried casting	Serrano *et al.* (2014)[134]
Fibre	Graphene Oxide	Nanofibre composites	Shah *et al.* (2014)[135]
Hydrogel	Graphene Oxide	Hydrogel (CSMA, MPEG-PCL-AC, PECA phase)	Liao *et al.* (2015)[136]
Fibre	Graphene Oxide	Nanofibre composite	Song *et al.* (2015)[137]
Coating	Graphene Oxide	Surface coating pulmonary valve conduit	Wilczek etl al (2015)[138]
Foam	Graphene Oxide	Freeze dried foam with UV irradiation	Akhavan *et al.* (2016)[139]
Hydrogel	Reduced Graphene Oxide	Collagen hydrogel composite	Guo *et al.* (2016)[140]
Monolith-Hydrogel	Graphene oxide with Carbon Nanotubes	PEG-Acrylate Cross linked with hydrogel matrix	Liu *et al.* (2016)[53]
Hydrogel	Reduced Graphene Oxide	Gelatine-Methacryloyl hydrogel matrix	Shin *et al.* (2016)[141]
Fibre	Graphene Oxide	Silk-Fibronin composite	Vera-Sanchez *et al.* (2016)[142]
Film	Graphene Oxide	Topographical ridged coating	Yang *et al.* (2016)[143]
Fibre	Graphene Oxide	poly-L-lysine (PLL)A nanofibre composite	Zhang *et al.* (2016)[144]
Monolith	Graphene oxide (from CNT)	Cross linked porus scaffold	Lalwani *et al.* (2017)[145]
Additive Manufacture	Reduced Graphene oxide	3D printing ink (Chitosan Methacrylate)	Sayyar *et al.* (2017)[146]
Hydrogel	Graphene Oxide	Chitosan polymer matrix (with apatite)	More *et al.* (2018)[147]
Casting	Graphene Oxide	Polycaprolactone guidance conduit mouldings	Qian *et al.* (2018)[148]
Hydrogel	Graphene Oxide	Polyacrylicacid hydrogel matrix	Qiao *et al.* (2018)[51]
Monolith	Reduced Graphene Oxide	Freeze dried casting	Dominguez-Bajo *et al.* (2019)[121]
Coating	Reduced Graphene Oxide	Coated silk fibronin nanofibre scaffolds	Wang *et al.* (2019)[149]

such as D'Abaco *et al.* and Tasnim *et al.* who utilise laminin and collagen respectively to pre-coat the pristine graphene material in a layer prior to cell culture, ostensibly to aid attachment [155, 156]. These reports cite excellent biocompatibility of their similar scaffolds, a commercially available CVD layer of pristine graphene arranged as a foam via a sacrificial monolith.

Further examples of graphene oxide scaffolds prepared and subsequently coated with biopolymer include the monolith scaffolds from Serrano *et al.* [134, 157, 121] which describe a coating of Poly-D-Lysine prior to use and report excellent biocompatibility in a range of *in vitro* and *in vivo* situations. Similarly, Akhavan *et al.* [108, 139] report on a number of preparations including thin films and rolled foam scaffolds coated with Laminin and PLL respectively prior to cell culture.

Other models using graphene materials also exhibit a similar effect, though in a less direct way - the graphenes are not described as being specifically or intentionally coated. Suspension of graphenes in hydrogel matrices [78, 158, 53, 159, 141, 51, 156], compositing graphenes with polymer to form electrospun nanofibres [135, 137, 144, 54, 149] and integration with 3D printing ink [160, 146] can all also be described as partially or totally encapsulating the graphene within a biocompatible material. Such encapsulation of graphene within a matrix can also result in altering the graphene surface chemistry. For example in a study by More *et al.*, a complex composite featuring a self assembling, GO reducing, cross linking reaction; the physiochemical properties of the material are simultaneously obstructed and variably modified by the assembly conditions [147]. More *et al.* in particular report preferential binding by cells to GO containing films, posing a question as to what attribute the GO is providing in their complex assembly to support this effect. Specifically, if their material alters the GO surface chemistry, then it is inferred that this effect is spatially constrained to the GO /cross-linking interface. Therefore, cells are either exposed to GO which has not been modified, or the cross linked film which is superior to the GO in the scaffold design, thus obstructing the GO from the cell-material interface.

These designs including coatings or encapsulation of graphenes confounds measurement of the properties of the material. What is common between all these approaches is investigators report good or excellent biocompatibility of their model. However this can also be described as being in line with results expected of the external coating or encapsulation materials. It is proposed here that coatings to enhance cell adhesion to a scaffold result in the coating becoming the functional culture surface whilst the graphene is sealed from the biological system. Therefore these reports do not investigate the biocompatibility, effect or function of their graphene material scaffold, rather the biocompatibility of their bioadhesive polymer and biomaterial coatings. Additionally, controls that include non-graphene substrates exposed to the same coating protocol share similar limitations; graphenes have a highly interactive electrostatic, polar and non-polar surface chemistry moieties which can bond with both polar and non-polar groups on polymer chains. Thus the interaction of the coating with the substrate will be different on the dissimilar surface chemistries of graphene compared to biomaterial, glass or plastic, resulting in differing compositions of coating polymer. In other words, cells are separated from the graphene material and therefore inference of the effect of graphenes on their system is tenuous.

1.5.2 Biocompatibility of Graphenes

The use of coatings is most likely motivated by reports showing graphenes may have poor biocompatibility *in vitro*. Coating of GO leading to separation of the material from the cell interface, thus mitigating any potential for a cytotoxic or nanotoxic effect. Thus far several reports have examined the topic of graphene biocompatibility, particularly GO as the most prevalent graphene in biological research. Thus far the reported mechanisms of GO toxicity are varied. Examples of these toxicity mechanisms are summarised in Table 1.4.

Ali-Boucetta *et al.* raise a notable hypothesis that the GO preparation method has an impact on the biocompatibility profile of the material. Investigators found that a cytotoxic preparation of CE GO in aqueous suspension demonstrated no significant cytotoxic

Table 1.4: Mechanisms of reported toxicity with GO materials

Graphene Preparation	Reported Toxicity	Reporting Cell	Reference
Oxidised Carbon nanotubes, CE GO .	Reactive oxygen species	HepG2 human liver	Yuan *et al.* (2011) [153]
CE GO and purified CE GO	Aggregate perforation	A549 human lung	Ali-Boucetta *et al.* (2012) [161]
GO , GO -PEG, GO -BSA, rGO -PEG, rGO -BSA	DNA Genotoxicity	Human HL7702 liver, MRC5 lung, U937 Macrophage	Li *et al.* (2014) [162]
GO nanoparticles, nanoribbons and nanoplatelets	Dose dependent cell infiltration	Mesenchymal stem cells	Talukdar *et al.* (2014) [118]
rGO surface coating	Contact cytotoxicity	Human Fibroblasts	Wilczek *et al.* (2015) [138]
GO via unzipped nanotubes	ROS generation, autophagy	Human neuroblastoma SK-N-BE(2), SH-SY5Y	Mari *et al.* (2016) [163]
Commercial GO	Membrane ruffling and shedding	RBL, NIH-3T3, MDA-MB-231	Sun *et al.*(2016)[164]
rGO	Concentration dependent ROS generation	PC-12	Yi *et al.* (2016)[165]
CE GO	Concentration independent tissue infiltration	Zebrafish larvae	Soares *et al.* (2017)[166]

reactions once the material has been purified [161]. Talukdar *et al.* found commercially available preparations of graphene nanostructures could exhibit a dose dependent cytotoxic action independent of the incubation time, hypothesised to be a consequence of a secondary contaminant rather than the directly attributed to the nanoparticles [118].

Other causes of cell disruptive effects are specific to the graphene 2D lattice structure rather than a perhaps unknown contaminating factor. Guo *et al.* investigated electrostatic denaturation of protein by the strong electro-potential π-bonds at the surface of pristine graphene. They found a significant change in protein tertiary structure following exposure to graphene and a concentration of protein strongly adhered to the surface [167]. Others have investigated graphene platelets 2D shape for potential to penetrate through cell plasma membranes leading to membrane 'ruffling' and eventual apoptosis [164, 163].

Yi *et al.* report dose dependent increases of reactive oxygen species (ROS) generation in PC-12 cells following exposure to an rGO pristine graphene analogue. In that work, ROS became elevated as concentration of graphene particles increased, however the authors concluded the material had excellent biocompatibility for the material below a threshold of 10µg/ mL in media dispersion [165].

Conversely, other authors report excellent biocompatibility from directly exposed GO and graphene. Tasnim *et al.* suggest GO can reduce the cytotoxic effects of materials such as 316L stainless steel, with *reduced* ROS generation in similar adherent cells, which would not otherwise adhere or proliferate on the stainless steel without the presence of GO . When graphene was used as a surface, Wilczek *et al.* have reported that rGO surface coating can enhance the biocompatibility of traditional valve implants, suggesting that any cytotoxic effect may only be a consequence of prolonged contact with the material [138]. Defterali *et al.* introduced a suspension of rGO *in vivo* to the brain and olfactory bulb and reported no astrocyte or microglial response or change in neurogenesis, concluding the material was therefore well tolerated in their experimental animals [168].

It therefore remains likely that sufficiently purified CE GO preparations can be utilised as biomaterials without secondary coatings with no adverse consequences, allowing the

physiochemical properties of GO to be investigated and exploited in biological systems. In recent years more experiments with graphene materials have been conducted without coatings. Fabbro *et al.* reported that LPE and ME pristine graphene based carbon substrates produced with extensive characterisation did not require adhesive polymers to remain permissive to cell culture *in vitro*[169]. In particular Fabbro *et al.* were concerned with maintaining the electrically conductive connection between the graphene substrate and cell culture. The conductivity of graphene is often an area of interest for studies seeking to influence cell culture using electrical stimulation. A similar electrical stimulation study conducted by Lee *et al.*, though using a CVD pristine graphene surface found similarly enhanced differentiation in mesenchymal stem cells (mesenchymal stem cell (MSC)) [170]. Balikov *et al.* showed electrical stimulation did not result in material changes or alter the culture conditions to compromise biocompatibility [171].

This body of evidence indicating bare carbon nanostructures and graphene materials may or may not be cytotoxic remains a challenge to graphene biomaterials research. It is proposed here following review of these reports that highly varied production methods for graphene materials contribute considerable confounding factors to many assessments of biocompatibility. A lack of consistency between each bespoke manufacture creates variables in the physiochemical properties of each GO preparation. Similarly bespoke manufacture does not often include purification, quality control or quality assurance measures to ensure complete removal of reactants or monitor side product generation. The controversy is similarly found in several reviews of biomedical concerns with graphene materials [172, 120, 133].

The theory that poor biocompatibility is a consequence of bespoke and imperfect GO production is supported by reported findings mentioning contamination and purification of GO products[161, 173, 174, 175, 176, 177, 178]. This proposal is further supported by the theorised two component model of graphene oxide. The two component model remains consistent with the proposed structure of the Lerf-Klewinski model, but holds that particularly during the common CE and sonication production methods, the GO

platelet remains contaminated with highly oxidised carbon debris with hereto unknown and uncharacterised structures [113, 92, 112, 115].

In future work graphene materials for tissue engineering and other cell culture studies should be sourced from more consistent suppliers practising quality control. This would ensure that bi-products of the exfoliation process and any contaminants are removed from the end product, resulting in a more consistent GO physio-chemistry in published sources. Importantly, a shift to a consistent source of GO materials with similar production methods rather than bespoke manufacture, findings would be more directly comparable.

1.6 Central Nervous System Tissue Engineering

When considering the design requirements of tissue engineering construct it is vital to consider the natural structure and complexity of the target tissues and the interactions the system has with the rest of the body. In this thesis, the titular tissue matter is neural tissues, specifically the CNS . In humans and other vertebrates, there are two connected yet morphologically and structurally distinct systems of neural tissue. The CNS comprises the brain and spinal cord, is isolated from the circulatory system by the blood-brain barrier (BBB) and almost totally encased in bone, in contrast to every other organ. The peripheral nervous system connects the CNS to the rest of the body. The CNS is more anatomically complex and comprised of a greater variety of cells than the peripheral system [179]. CNS neurons are multipolar with several synapses, vary in length from micrometers to millimetres and regions of CNS neurons lack myelination. The presence or absence of myelin leads to an anatomical distinction between ‘white‘ and ‘grey‘ matter within the CNS .

Two archetypes of cells exist within the CNS . Neurons are the origin of nervous function and resulting innervation of the rest of the body via the peripheral system. Glial cells include astrocytes, oligodendroglia (in white matter) and microglia to provide mechanical, physiological and immune support to neurons. [180]. Tissues of the CNS are

organised into distinct anatomical structures, which develop during embryogenesis into the complete CNS at maturity. Each anatomical structure is comprised of a specific ratio of neurons and glia, the mechanism by which these structures form from their progenitor cells remains poorly elucidated but is theorised to be a self organising system during differentiation [181].

Nervous system tissues are mechanically among the softest tissues within a human body. The human brain is a mechanically delicate, non-linear and complex viscoelastic solid, with a reported shear modulus of 0.4-1.4kPa [182, 183]. The extracellular matrix of the CNS comprises the basal membrane, perineuronal net and interstitial matrix [184]. These structures are chemically identified as proteoglycans and hyaluronan with a collagen basement membrane resulting in low elasticity [185]. In comparison to other tissues, cells of the CNS generate comparatively little collagenous extracellular matrix within the intracellular parenchyma at 10-20% of the total mass. In place of robust extracellular matrix, physical support and structure of the CNS is provided by networks of interneuronal astrocytes. Lacking elasticity, the brain and spinal cord are unable to withstand tension or compression without disruption and are thus suspended within cerebrospinal fluid as protection from mechanical disruption.

CNS can suffer acute or chronic degenerative damage. Often these are consequential; an acute injury from mechanical disruption, ischaemia or infection can progress to chronic degeneration of tissue surrounding the injury site [186, 187, 188]. Both acute and degenerative damage can cause a loss of cells, and by extension cellular function.

Depending on severity of an injury, inflammation occurs. For comparatively minor impact such as during concussion, this inflammation can lead to temporary disruption of neurological function. However if vasculature and the BBB is compromised such as during severe trauma the structure of white and grey matter is disrupted. Inflammatory reactions during such events causes ‘activation’ of microglia, which in turn leads to astrogliosis [189].

If the BBB is compromised, it can loose integrity and become permeable to the

circulatory system, including immune cells. Initial permeability to blood cells is high whilst immune cells are recruited, by 14 days post injury the barrier is reported to be impermeable once more [190]. Neutrophils, monocytes and lymphocytes accumulate to the lesion site and are activated as part of an immune recruitment cascade [191]. Compromising the blood brain barrier has serious risks for the immune system to become sensitised to the normally immunoprivileged antigens of neural tissue. Such immune system activation can result in degenerative autoimmune responses, particularly towards myelin. This can lead to multiple sclerosis resulting in chronic and progressive loss of myelin from white matter in the spinal cord [192].

Secondary to the initial immune response, normal metabolism of neural tissue is disrupted by the upregulation of pro-inflammatory cytokines [193, 194]. This leads to disruption of the glycocytic pathways and oxidation of the neural proteasome, causing cell dysfunction and death. The inflammatory response to a severe injury involving compromised tissue structure can persist for weeks as a glial scar forms [195, 196, 197]. This reaction lays the biochemical and cellular foundations for remedial healing and protection of the remaining neural tissues, as upregulation of anti-inflammatory interleukins from phagocytic immune cells accompanies clearance of lipid debris [198]. Anti-inflammatory phases typified by anti-inflammatory phenotypes of microglia can persist for far longer than the acute inflammatory phase. It is during this phase that regeneration occurs including recruitment of neural progenitor cells, axonal regeneration and remyelination states [199, 200, 201, 202].

To understand how these system scale responses and tissue engineering technology can be combined, it is important to consider the physiology of the cell types that comprise the nervous systems. By examining the structure and normal function of the cells of the CNS , the following sections explore the potential pitfalls and opportunities as they are currently understood. In particular, the critical outcomes indicative of healthy cell morphology that can be used to measure the relative successes of a potential neural tissue engineering scaffold. Further, the engineering considerations and potential compromises

that must be made to achieve a biomaterial facsimile of neural tissues in the case of tissue substitutes.

1.6.1 Neurons

During embryonic development clusters of stem cells differentiate into the neurons and the foundations of a complex neuronal network [181]. The human brain has approximately 100 billion individual neurons arranged into a heterogeneous series of anatomical structures including the hippocampus, medulla, cerebellum [203]. Neurons form the electrically active networks of the nervous system. The nervous system can be described in terms of two series of neurons - preganglionic neurons have cell bodies within the CNS and postganglionic neurons with cell bodies located in the periphery [204]. For a CNS scaffold, the structure and function of the potentially meter long peripheral neurons are less vital, however neuritic extension, up to the millimetre scale could offer benefits for spanning injury borders.

CNS Neurons have several dendritic extensions terminating in synapses which secrete and detect neurotransmitters from neighbouring neurons [205]. In the CNS neurons can have thousands of synapses from each neuron. These synapses are plastic, changing in number and receptor density throughout life as connections are reinforced, damaged or atrophied. Neuroplasticity is the basis for learning, memory and maintenance of function with plasticity of neurons an area of research for therapeutic recovery of CNS injury [206]. In some cases, new learned pathway formation and synaptic plasticity has the potential to gradually restore neurological function by circumvention of injured tissue [207]. For example this is a therapeutic option for spinal cord injury patients, to re-learn lost neurological function and in doing so form new neural pathways through intact areas of CNS [208]. It is through these highly adaptable neuroplasticity properties by which a CNS scaffold or tissue substitute could become functionally integrated into host tissues. By replacing damaged tissues with a substrate containing or permissive to neurons, function could be restored.

Neurogenesis is the formation of new neurons from precursor cells. The hippocampus generates new neurons throughout life *via* precursor cells in the dentate gyrus, eventually maturing through a neuroblastic stage into terminal neurons identical to other mature neurons [207]. Differentiated mature neurons of the CNS exists in a post mitotic state and do not divide, however are extremely long-lived. Developing neurons are highly sensitive to the extracellular environment, including hypoxia and reactive oxygen concentrations with a decrease in plasticity and neurogenesis under hypoxic conditions [209].

Neurogenesis has three key components; growth factors to stimulate neuritic extension and precursor cell differentiation, chemoattractive factors to increase the density of precursor cells and a permissible extracellular matrix. In mature tissue these components are downregulated , and thus innate neurogenesis is inhibited. Following disruption through injury in particular, the astrogliotic response results in deposition of additional extracellular matrix including inhibitory proteoglycans [195]. In humans the glial scar is a seemingly impassable barrier to neurons preventing regeneration [189]. Cellular therapies have been trialed in reintroducing neuronal progenitor cells to areas of glial scarring, with some success in trials restoring neurological function in the spinal cord [38]. Therefore induction of neurogenesis is a key target for neuronal tissue engineering, particularly for scaffolds. Neurogenesis of new neurons from precursor cells or regeneration of damaged neuritic extensions from the well documented growth cones at glial scar borders are the most promising ways to repopulate an area with host cells.

This three component nature for neurogenesis aligns with the three component model for tissue engineering. Neurons have been successfully regenerated in the peripheral nervous system using conduit scaffolds which deliver nerve growth factors [29]. Similarly the growth cones of regenerating neurons are shown to be guided by release of growth factors by local electrical stimulation [210]. In these studies limited distances of neural defects are shown to be regenerated by supplanting the scar region with a permissible matrix and facilitating natural growth stimulation.

Herein I have discussed the development, structure and inhibitions of neurons in

the CNS . For tissue engineering, successful models should demonstrate the key, yet linked properties of neuronal growth, neuronal maturation and synapse formation. These attributes found in scaffolds and tissue substitutes indicate a permissive environment for neurons, which can enable integration into host tissues. In particular evidence of integration by neurons would suggest similar plastic recovery as seen in natural tissues could be achieved.

1.6.2 Glia

Mechanical structure and physiological support is derived from robust extracellular matrix, circulatory system and endocrine system in most of the body. However in the CNS neurons and neural function are largely supported by a heterogeneous group of cells generalised as glia [211]. Previously it was believed glia outnumber neurons by up to a factor of 10 [211]. It is now believed that glia and neurons exist in a ratio of 1:1 glial cells to neurons within the brain [212, 203].

Glial cells provide the structural, metabolic, myelination, endocrine, and immune surveillance support necessary to maintain CNS neurons. Astrocytes form part of the BBB alongside vascular endothelium and pericytes [213, 214]. As specialised macrophages in the CNS , microglia serve neuroinflammatory, neuroregulatory and immune surveillance functions [215]. White matter neuronal axons are wrapped in myelin provided by oligodendrocytes which results in the distinguishing ‘white’ designation. Myelin enhances propagation of action potentials, by contrast grey matter regions are unmyelinated and as such lack oligodendrocytes [216].

In recent years increasing efforts have been directed at using tissue engineering to substitute glial scar regions with compatible and permissive scaffold materials [217]. At the glial scar border, neuronal processes have been investigated for regenerative potential. In many cases, the neurons terminating at a scar border show active growth cones [218, 219]. Neurons are therefore intact at the periphery and theoretically capable of re-establishing synaptic connections, but are kept dystrophic by the glial scar [220].

1.6.2.1 Astrocytes

Astrocyte density varies throughout the CNS , around 3 times more astrocytes are present in white matter tissue than grey matter tissue [203]. Individual cells can be expansive and have processes enveloping hundreds of thousands of individual synapses. These cells exhibit a sensitivity to GABA neurotransmitters [221, 222]. The synaptic environment is controlled by astrocytes regulating transmitter concentration at synaptic interfaces and contributing to the clearance of transmitters following synaptic transmission [213]. These synaptic astrocytes are permeable to both potassium and sodium ions, feature energy activated calcium channels and are excitable [223]. This sensitivity does not involve propagation of action potentials, rather astrocytes sequester ions and release these ions in response to neurotransmitter increases [224, 223, 225]. In this way neuronal excitability is limited by astrocytes, dysfunction of synaptic astrocyte function is hypothesised to be a contributing factor in disease such as epilepsy [226].

Under normal healthy conditions astrocytes remain static, maintaining the structure and function of tissue. Following traumatic or 'noxious' stimulation this condition changes and reactive phenotypes are induced [227]. Two reactive astrocyte phenotypes are characterised; A1 and A2 [228]. These phenotypes are distinct in their responses and biochemical secretion. A1 phenotypes are induced by neuroinflammatory reactions propagated by inflammatory signalling from traumatised neurons and microglia. This phenotype is also associated with senescence and ageing of neural tissues, as well as commonly in neurodegenerative diseases such as Alzheimer's [229]. In this state astrocyte function changes from homeostasis of the neuron micro-environment to become inhibitory of synapse formation, thereby contributing to loss of neurological function. A2 astrocytes by contrast are neuroprotective and are induced by ischaemic stimuli, releasing trophic factors to regenerate neurons within the micro-environment [230]. Moreover, A2 astrocytes inhibit cell apoptosis, secreting anti-inflammatory cytokines such as transforming growth factor beta (TGF β) contributing to regeneration [231].

Within neural lesions A1 phenotypes can progress to astrocytopathy and astrogliosis,

leading to a glial scar. During astrogliosis, astrocytes become increasingly proliferative and begin to deposit more extracellular matrix. This process results in generation of tissue comprised of inhibitory A1 astrocytes and neuroinhibitory proteoglycans extracellular matrix. As discussed previously, the presence of glial scar tissue suppresses the limited regenerative potential of neurons[189, 232, 197, 219, 231].

Astrocytes share many similarities with neurons. Current research includes gene therapy aiming to induce a phenotypic change into 'induced' neurons. In a study looking at human and mouse astrocytes, Val Cervo *et al.* have reprogrammed cells *in situ* to become dopaminergic neurons [233]. In this way, degenerative diseases could be reversed by transformation of A1 astrocytes into replacement neurons in diseases such as Parkinson's. This work, though a distinct therapy from tissue engineering, could provide the basis for instructive scaffold enhancement providing a mechanism for neuron proliferation through a scaffold. Characterisation of the prolonged fate of induced neurons is needed, beyond initial rescue of a Parkinsons model.

Few *in vitro* scaffolds have been engineered containing astrocytes. Most scaffolds used for neural engineering have well considered the scaffold with neurons and neuronal lineages. Some graphene scaffolds have been shown to be permissible to astrocytes *in vivo*, maintaining healthy phenotypes without astrogliosis [168]. Astrocytes maintain a mitotic state and can proliferate without adopting activated phenotypes, therefore we can assume scaffolds compatible with neuronal culture will be similarly tolerated by astrocyte culture without specific modification [213].

1.6.2.2 Microglia

Microglia are a subtype of macrophage found only within CNS tissues, normally they have dendritic morphologies similar to astrocytes and neurons. Microglia are the most motile and proliferative cell of the CNS , moving through tissue and replicating to maintain population. Microglia are highly specialised to the CNS , including cell surface neurotransmitter receptors in addition to cytokine receptors. They provide immune surveillance

and injury response within the tissues of the brain [215].

Microglia are similar to astrocytes in having a quiescent phenotype and the potential to enter activated phenotypes. Activated microglia can have pro-inflammatory M1, or anti-inflammatory M2 phenotypes[199, 229]. As immune cells, microglia typically become activated first following a traumatic event [200]. M1 is a neuroinflammatory phenotype causing inflammatory reactions in response to noxious stimuli. These reactions are responsible for A1 astrocyte activation through secretion of pro-inflammatory cytokines such as interferon-γ, and ROS to suppress potential infection [234, 227]. M1 pro-inflammatory microglia change shape from elongated, dendritic morphologies to rounded and increase in both size and proliferative rate [235].

In contrast, microglia activated by interleukin-4 and interleukin-13 pathways adopt M2 anti-inflammatory phenotypes. M2 activation includes a similar change in shape but instead of producing pro-inflammatory cytokines and cytotoxic ROS, M2 activated microglia produce anti-inflammatory cytokines such as IL-4, IL-10 and tissue growth factors [236, 237].

The comparison between M1 and M2 microglial reactions can be summarised as M1 being defensive, to mitigate the cause of damage, whilst M2 is restitutive to regenerate tissue neighbouring a lesion [238]. In the absence of M1 activation or an excess of anti-inflammatory M2 expression, injury and infection can progress unchecked through tissue leading to an expansion of the lesion [239]. By contrast without M2 action, apoptosis of damaged tissue may proliferate and lead to increasing endocellular cytotoxin concentrations. This in turn cascades to increased neurodegeneration through progressive apoptosis and A1 astrocyte activation [240]. Some reports suggest that microglia can transition between activation polarities during response to CNS insult resulting in transitional phenotypes expressing both M1 and M2 markers [241].

It is therefore understandable that comparatively more attention has been given to mitigating microglial responses in tissue engineering scaffolds than there is similar research into astrocytes. Particularly with graphene based scaffolds, the microglial response has

been characterised as favourable. In a study conducted by Jiang *et al.*, culture medium conditioned by microglia seeded on a graphene scaffold was found to enhance neural progenitor cell migration and neurosphere formation [202]. In this study the culture environment was modified by the intercellular signalling by microglia allowed to proliferate in a phenotype dictated by the scaffold. This suggests that the graphene material is permissible to the immune system with no stressor or noxious stimuli to the microglia. However this study used a monoculture of microglia to condition media. Results in a co-culture may provide more information as to the suitability of these materials once other cell signalling is included.

1.6.2.3 Oligodendroglia

Neurons are provided with myelination and membrane support by oligodendroglia, primarily within white matter and produce myelin that functions similarly to the schwann cell of the peripheral nervous system, enhancing action potential conduction [216, 242, 243]. Myelin is a lipid heavy compound which ultimately comprises two thirds of the dry weight of neural tissue, however the exact chemical composition of myelin varies between CNS regions [244].

In the CNS Each oligodendroglia may myelinate up to 50 axons. Each axon requires several oligodendroglia to myelinate its length [211]. Almost the entire length of axons in white matter is myelinated, aside from small regions known as Node of Ranvier which expose the axon to the extracellular environment and synapses to allow contact with astrocytes.

Myelination directly results in faster conduction velocities along axon membranes by controlling potassium gradients following depolarisation, as well as lowering the electrical resistance of the axon by reducing its cytoplasmic volume [185]. Because oligodendroglia enclose neuron processes, in white matter oligodendroglia become tertiary regulators of nutrient supply and membrane maintenance to neuron processes, reducing the load on neuronal cytoskeletal function [245, 246].

Demyelinating diseases have highly debilitating consequences. Firstly loss of conductance through white matter areas, loss of myelin within the CNS leads to the loss of the neuronal axons supported by the oligodendroglia [247]. There is evidence that oligodendroglia can be therapeutically driven to remyelination of neurons in adulthood following demyelination events [199, 248, 201, 249]. However myelin itself has neuroninhibitory properties, preventing penetration of neuron growth cones [189]. Myelin is also found within the glial scar.

For this reason it is clear why the initial M1 macrophage reaction drives microglia to consume local myelin. Without such a reaction, myelin debris may impede regeneration. Consumption of myelin is also one of the stimuli that differentiate microglia into the M2 regenerative phenotype. Despite their importance, *in vitro* culture of anatomically relevant models of oligodendroglia is highly challenging. In tissue engineering research, emphasis has been placed on controlling progenitor cell fate towards oligodendroglia [135]. In their study, Shah *et al.* combined a GO -coated PCL nanofibre scaffold with progenitor cells and reported enhanced oligodendrocyte markers in populations cultured on both components. This is a surprising result given other authors reporting neurogenic differentiation in similar conditions. Furthermore Shah *et al.* is one of the studies noted for using a laminin coating atop the graphene, confounding their data as previously discussed. It is speculated that the extremely narrow and porus nanofibre scaffold structure provided a more topographically instructive environment leading to the increase in oligodendrocyte expression. However as the authors note, the exact mechanism warrants further exploration and explanation.

1.6.3 CNS Tissue Engineering

Tissue engineering offers potential to both restore the micro-environment and regenerate or replace lost cells of the CNS . As previously discussed, human CNS injuries are terminal; neurons do not regenerate following injury. Furthermore injuries result in cellular and extracellular changes to the substance of CNS tissue, the glial scar. This results in a non-permissive extracellular matrix, mechanically stiffer and comprised of neuroinhibitory

extracellular matrix components. Therefore in particular the mechanical stiffness, or rather reduced softness, is a contributing factor to the limitation of neuronal progress through scar regions [250].

Many current biomaterials are mechanically insufficient for generation of CNS tissue. Scaffolds using a composite design substrate such as an electrospun polymer are commonly coated with a second softer material to serve as the cell substrate. It is this softer material that is mechanically significant in CNS tissue engineering, as it is the region in which cells must be able to grow and mature. Examples such as collagen, fibrinogen and alginate hydrogels in particular show the most promise of being able to replicate the rheometric moduli of brain and spinal tissues [251]. In work by Bartlett *et al.*, clinical grade material 20% v/v fibrin and 0.6% w/v collagen hydrogels were found to have similar rheometric moduli to cervical spinal cord, however only the collagen gel had a similar Tan-δ elastomeric profile. Similarly, a clinical grade 1% w/v alginate gel had a similar moduli at low frequency ranges, but a significantly lower Tan-δ across the whole range. This indicates that besides the collagen hydrogel material, currently available clinical gels do not well simulate the mechanical properties of neural tissue. Additionally, Bartlett *et al.* did not control for the differences in mechanical characteristics of white and grey matter CNS tissue, which have been shown to be significantly different potentially confounding their data [252].

The gels used by Bartlett *et al.* have limited potential as living tissue engineering scaffolds due to the cross linking mechanisms. The collagen hydrogel required an acidic solubilisation of the collagen macromer followed by a strong base neutralisation to cross link. This use of extreme pH renders the collagen hydrogel unlikely to support a viable cell population following cross linking. Similarly, the alginate hydrogel uses an osmotic gradient comprising calcium chloride to drive the cross linking process. This hypertonic transition would also have consequences for a living scaffold, reducing viability. The fibrin hydrogel is not similarly limited in biocompatibility, able to cross link at natural pH and salinity, the current use of this gel material is as a surgical glue. However the

fibrin hydrogel was found to be a poor mechanical match for neural tissues. Bartlett *et al.* provided a useful platform for determining similarity of hydrogel materials to neural tissues, allowing more suitable hydrogel chemistries to be investigated for mechanical suitability.

Injectable hydrogels containing encapsulated neurotrophic factors have been investigated for inducing functional recovery following spinal cord injury in a mouse model [253]. Such delivery of neurotrophic factors was found to significantly enhance growth cone advance through otherwise neuroinhibitory tissue caused by a model spinal injury. Xu *et al.* used a unique approach to hydrogel formulation by creating a hydrogel from methacrylate cross-linking a molecule analogous to neurotransmitter acetylcholine. The hydrogel was formed into nanoparticles to encapsulate neurotrophic growth factors, and this delivery system was able to cross both *in vitro* and *in vivo* models of blood brain barrier. In this way the biomaterial delivered instructive factors in a targeted manner, and was able to improve the persistence of NGF, contributing to the improved neuroregeneration. In a similarly unique approach to neural engineering, Faust *et al.* constructed a hydrogel scaffold derived from bladder ECM [254]. This transposed material was found to retain micro-RNA (miRNA) rich vesicles bound within the matrix following generation of the hydrogel. In a surprising result, the endocytosis of these miRNA vesicles by developing neurons enhanced survival and axonal growth. These findings suggest that useful extracellular instructive factors are conserved and can be found in a variety of tissue sources. Both Xu and Faust have demonstrated that biomaterial scaffolds are greatly benefited by the addition of instructive factors which could enhance the integration of tissue substitutes.

Current models for CNS tissue simulation for use in research and therapy as tissue substitutes involves generation of micro-tissue organoids [255]. Organoids are derived from differentiation of multipotent stem cells and can be developed to include vasculature and blood-brain barrier characteristics [256]. In Cakir *et al.*, micro-tissue organoids were found to differentiate and become self supporting with characteristics of the blood-brain barrier including pericytes, endothelium, neurovascular interfaces and astrocytes.

Particularly when implanted *in vivo* such organoids were found to become vascularised by the host. These findings show that CNS tissue substitutes can be generated, featuring critical attributes to substitute CNS tissue. Cakir *et al.* also reported initial signs of neurogenesis within these organoids, indicating that if the organoid can be sufficiently maintained, complex neural tissue may be created. However the engineering of these organoids remains limited; differentiation is complex and lacks temporal or spatial control. Organoids are highly constrained in size during generation *in vitro* through lack of active vasculature. Furthermore, it remains to be proven that neurogenesis can progress beyond the initial growth cone state, or that the organoid could be integrated into neural tissue.

A larger tissue substitute model combined biomaterials with self assembled columns of astrocytes, and a collagen hydrogel matrix [257]. Winter *et al.* showed that the astrocyte tissue substitute facilitated neuronal regeneration by simulating progenitor cell guidance in a manner similar to the de novo generation during embryogenesis. In a co-culture *in vitro* model of growth these living scaffolds resulted in both directed and extended axonal growth instructed by the astrocyte column, with neuronal projections following the astrocytes closely.

Biomaterials can be combined with tissue generating cell populations to create viable living scaffold models of neural tissues. The current models of CNS tissue engineering provide a host of useful approaches and models with potential as a therapeutic product. However more work is required; to date materials capable of replicating the neural micro-environment accurately remain elusive. Instructive factors are poorly constrained in temporal and spatial terms, either delivered in one ‘dose‘ or unipolar in purpose. Current tissue substitutes are promising however lack translation potential to a clinical product. Further work into other materials with more broad application may aid in CNS tissue engineering. The next section discusses how graphenes provide more tools to advance this technology.

1.7 Graphene in CNS Tissue Engineering

Despite the continued controversy about the biocompatibility of graphenes *in vivo* and *in vitro*, several successful uses of the material as cell culture and tissue engineering substrates for neural tissue have been reported in recent years. Pristine graphene provides high electrical conductivity however its chemically inert nature, high electrostatic potential and high hydrophobicity are much less desirable attributes for a cellular environment [173]. Pristine graphene has been shown to present differing affinities for neural cell culture based on manufacturing quality [258]. GO is more commonly used as an alternative to pristine graphene. As GO can be prepared, stored and used as a suspension of platelets in aqueous solvent, GO has a number of advantages over pristine graphene for tissue engineering [259].

A range of cell lines, primary cells and tissues have been successfully grown with graphene materials forming the primary or major constituent component of the scaffold substrate. Examples of the variety in success of these graphene-centric experiments is presented in Table 1.5

1.7.1 Graphenes as Instructive Topography

In many of these studies outcomes including neurogenesis and improved neural function are attributed to graphene materials acting as an instructive factor. However the potential of graphene as an instructive factor is highly varied depending on experimental conditions; Das *et al.* used GO inclusion in a composite amyloid scaffold to induce topographical features which were not replicated in control scaffolds without GO . This topography resulted in improved differentiation of neural precursor cells including neurite extension and neurogenesis [264]. Therefore the presence GO altered the assembling chemistry of the amyloid scaffold, resulting in an instructive topography beneficial for neurite growth. In a similar graphene inclusion design, Guo *et al.* enhanced the conductivity of a fibre using graphene and subsequently delivered low-frequency electrical charges to cells at the

Table 1.5: Neural Culture with Graphene *in vitro*

Archetype	Graphene material	Graphene Assembly	Cell	Graphene model Outcome	Reference
Film	CVD Graphene	Film on glass	SH-SY5Y	Improved neurogenesis	Lee *et al.* (2015)[260]
Coating	CE GO	Coating on steel	SH-SY5Y	Improved cell adhesion, decreased ROS expression	Tasnim *et al.* (2017)[261]
Coating	CE GO	Coating on fibres	PC-12	Improved neurogenesis	Zhang *et al.* (2016) [144]
Hydro-gel	GO with nanotubes	Cross-linked hydrogel	PC-12	Improved adhesion and spreading	Liu *et al.* (2017) [262]
Film	CVD Graphene	Film on plastic	Mouse hippocampal neurons	Improved neurogenesis and growth factor expression	Li *et al.* (2011)[154]
Film	CVD Graphene	Film on plastic	Mouse neural stem cells	Improved spontaneous action potential generation	Tang *et al.* (2013) [119]
Film	LPE/ME Graphene	Film on Glass	Mouse hippocampal neurons	Conductive interface between cells and substrate	Fabbro *et al.* (2016) [169]
Foam	CVD Graphene	Foam on nickle monolith	Mouse microglia	Reduced inflammatory reactivity	Song *et al.* (2014) [263]

surface [265]. This electrical stimulation via a graphene scaffold resulted in enhanced neurogenic differentiation compared with unstimulated controls.

These studies utilised different graphenes, embedded within matrices to create scaffolds which otherwise would not have demonstrated neurogenic differentiation, however both achieved a similar outcome. This demonstrates the versatile and varied applications of graphene as a component of tissue engineering scaffolds in controlling the physical properties of other biomaterials. Topographical instruction with graphenes is not limited to scaffold matrices and has also been demonstrated in surface cultures. Kim *et al.* created layers of CVD graphene films resulting in a channel shaped nanostructure topography. Adherent MSC were found to attach and differentiate more successfully into neurogenic lineages on the shaped graphene substrate compared to similar planar substrates [266]. In a similar study Balikov *et al.* could use a single layer of patterned CVD graphene to achieve similar results by comparing patterned and unpatterned graphene topography to induce neurogenic differentiation markers in MSC [171].

1.7.2 Graphenes with Instructive Chemistry

Cell fate can similarly be influenced by the surface chemistry of the graphene surface. In a study using uncoated graphene, Chen *et al.* examined GO and rGO (as a pristine graphene analogue) films on glass substrates with induced pluripotent stem cells (iPSC). Chen *et al.* found increased attachment on the hydrophilic GO compared to hydrophobic glass and rGO surfaces [267]. This study also investigated the differentiation potential of the cells on each surface. In their results, while the GO surface appeared to facilitate differentiation of the potent cell population, the rGO surface had a negative impact on spontaneous differentiation. This result was attributed to differences in signal transduction via cell surface receptors when interacting with the lack of oxygen containing pendant groups on the rGO compared to the GO surface.

A similar study using adipose derived stem cells (ADSC) by Feng *et al.* used a similar though thicker film coatings of GO and rGO and compared to traditional tissue

culture plastic. Feng *et al.* found similar attachment and viability on both GO and rGO in contrast to the earlier study [268]. However this study sought specifically neurogenic differentiation, a fate otherwise exhibited with low efficiency in ADSC populations. Both GO and rGO surfaces produced higher than expected (90% compared to 50%) levels of neurogenic differentiation, the GO surface produced the highest rate of differentiation. Both graphene surfaces induced higher rates of differentiation than glass and plastic controls. In this case, one mechanism proposed is that surface chemistry of the graphene material functions as a concentration platform for chemical inducers as reported by Lee *et al.* [269]. With this mechanism, the higher electrostatic attraction of rGO (and pristine graphene) compared to GO increases the binding efficiency of induction protein. However, this higher attraction simultaneously leads to increased denaturation of protein tertiary structure. Therefore the GO , with a lesser concentration effect but lesser reduction in protein efficacy resulted in higher rates of differentiation induction.

This property of graphene surface chemistry can also be purposefully utilised as a delivery vector. Li *et al.* utilised a patterned GO substrate to perform a gene transfection in a localised manner to a subset of cells within a population on the culture surface. The delivery protocol led to a pre-concentration of a pDNA/PEI complex to GO coated areas only. This led to gene transfection of cells on GO without inducing similar effects in directly adjacent cells on glass [83]. This work again utilised the pre-concentration or adsorption properties of graphenes in a transient manner first proposed by Lee *et al.* to control cell fate [269].

These similar graphene surface studies highlight how the surface chemistry of graphene materials can have direct effects on adhesive cell populations, and indirect concentrating effects on the cellular micro-environment. By demonstrating the capability of graphenes to alter cell fate, these works have shown the importance of understanding the interaction of graphene surface chemistry with a culture environment.

1.7.3 Graphenes with Glia

Current research focuses heavily on outcomes for neurons, such as neuritic length and neuronal differentiation. Comparatively fewer studies have considered the impact of scaffolds and scaffold materials on glial cells. Using an *in vitro* model, Song *et al.* investigated what reactions are induced in microglia when cultured on a graphene foam model [263]. In their work, Song *et al.* report that microglial cells cultured on a graphene foam did not exhibit inflammatory reactions. Rather microglia were found to have an anti-inflammatory phenotype. Similarly neuronal cells exposed to media conditioned by microglia on the foam did not display signs of inhibition. This indicated the microglia did not secrete neuroinhibitors into the media during culture on the graphene foam.

In a rather different study, GO and pristine graphene nanoflakes introduced into an *in vitro* co culture model of rat astrocytes led to internalisation of the nanoflakes within cell membranes. The work by Chiacchiaretta *et al.* found in contrast to previously discussed studies of graphene internalisation causing apoptosis, Astrocytes with graphene internalisation became morphologically distinguished and upregulated ion channels. This led to an increase in the homeostatic functions of astrocytes, overall promoting neuronal function [270]. These surprising findings suggest that graphenes can influence the phenotypes of glial cells, possibly reducing the severity inflammatory responses following injury.

It is clear that graphene materials have a varied instructive potential in biomaterials and cell culture systems which must be carefully considered [125, 126]. Current research lacks a robust and simple platform for creating consistent GO surfaces ready for interrogation by cell culture comparable to those produced by pristine graphene deposition to investigate potential instructive effects from both innate and administered sources.

1.7.4 Graphene Implants

In addition to *in vitro* work, other reports studying graphene based implants *in vivo* report successful implantation, favourable host responses and tissue integration. In a series of

studies by Serrano *et al.*, foam rGO tissue engineering scaffolds are introduced into *in vivo* rat model neural injuries. This freeze dried casting using a reportedly proprietary process combining high concentration rGO with a hydrogel binder has reported successful infiltration and signs of regeneration by native host cells in spinal cord tissue [157, 122, 159, 121]. Additionally, the scaffolds are reported to demonstrate no immune response and successful vascular integration. This indicates the scaffold is well tolerated by the model animal and is a promising sign of further integration. However as yet this model does not demonstrate functional recovery from the injury model beyond histological evidence.

Similarly Wang *et al.* developed a nerve guidance conduit from electro-spun silk and polycaprolactone fibres coated with rGO . In a rodent peripheral nerve model the scaffold demonstrated equivalent nerve regeneration to gold standard nerve graft [149]. These studies indicate graphene materials are robust and favourable for neural regeneration in the rat experimental model.

In another example, a fibrin-MSC living scaffold has been implanted into a rodent hemisection model by Itosaka *et al.*. This hydrogel model demonstrated that cells in combination with hydrogels could improve neurological function recovery, compared to cell therapy or hydrogel scaffold alone[271]. Similarly the cells within the scaffold exhibited longer term survival during the *in vivo* model compared to the same model under *in vitro* conditions.

In a similar study a hydrocolloid hydrogel product with an undisclosed chemistry was used as a material interface with an rGO thermally reduced monolith. This work by Palejwala *et al.* found that the scaffold could be integrated without cyst formation when delivered immediately at the site of the hemisection model [159]. The scaffold showed excellent biocompatibility of the hydrogel and rGO within a spinal lesion, histological assessment showed integration of spinal tissue into the periphery of the scaffold. However this study was qualitative in nature and did not measure neurological regeneration. Its similarity however to the work of Serrano *et al.* lends weight to the finding that a graphene scaffold is permissible to native cell infiltration in hemisection models. Thus far *in vivo*

models have yet to prove the long term safety of scaffolds. Few long term studies have shown neurological improvement[272, 273].

1.7.5 Future with Graphene Scaffolds

It is now clear that graphenes have a place in neural tissue engineering. As detailed above, graphene scaffolds have been shown to enhance neuronal growth and neuronal differentiation. Furthermore, graphenes can be permissible to glia, and do not cause astrocyte dysfunction. Finally, graphenes have been demonstrated to have instructive capabilities for microglia, controlling phenotypes. More work is needed to investigate the potential to create synthetic tissue analogues, and exploit the potential of graphene for neural tissues [130, 116].

1.8 Research Questions

In this literature review, sources were collected from PubMed (MEDLINE), Web of Science (Core Collection) and Google Scholar. Sources were collected between 2016 and 2020 throughout the duration of this research. The nature of biomaterials, graphenes as biomaterials, graphenes for neural tissue engineering and the particular fastidiousness of neural cells as found in published sources has been explored. In summation, extensive excellent research using graphenes in neural tissue engineering has been conducted thus far. Studies range in scope from two-dimensional surface models to complex three dimensional scaffold. Innumerable successes have been reported though challenges and questions remain, particularly de-convoluting the similarly numerous differing designs of scaffolds and culture conditions to understand the underlying material. Comparing studies, many aspects of graphene's utility as a biomaterial has been confounded, or the observed effects not interrogated to the fullest extent. Commonly biological outcomes are characterised extensively with limited connection between the biologic data and material science.

In particular the role of graphene surface chemistry as an attractive factor for *in*

vitro culture components could well explain observations of enhanced attachment and differentiation. The existing bodies of work frequently utilise bespoke preparations of graphenes which have been demonstrated by comparison of results to have highly varied biocompatibility, physiochemical properties and potential as a scaffold material. Similarly a huge variety of scaffold designs have been reported with similar outcomes, though experimental differences such as inclusion and exclusion of bioadhesive coatings and exogenous growth factor stimulation are not consistent.

Some areas for further development of graphene material tissue engineering have been identified for this body of research.

Is graphene oxide from commercial CE sources biocompatible when constructed into a study model allowing for more standardised and comparable future research? Such a step for research away from bespoke manufacture to a more comparable standard of raw material would aid in comparisons between subsequent studies. This would also facilitate a future GMP production of clinically useful graphenes, as current bespoke manufacture would require extensive scale up.

Does sourced graphene oxide have innate instructive potential for neural cell culture? Several existing studies suggest graphene materials have the potential to enhance neural culture. If a more standard source is to be found do these results persist or is the existing data a result of unique physiochemical characteristics that can only be replicated under bespoke processes. Furthermore what more can be learned about the mechanism by which GO enhances culture? Or, can the instructive potential of GO be enhanced for neural cells?

In terms of tissue engineering scaffolds, graphene has been combined with many other biomaterials, many as monolith designs. Can graphene be combined with advantageous photoinitiated hydrogel systems to provide a 3D scaffold which has potential to be minimally invasive? Current scaffolds are produced as macroscale products which would necessitate extensive resection of host tissue to provide as an implant. This is not an obstacle to current rodent hemisection models as such resection is already performed. However a Click chemistry hydrogel scaffold holds potential to be introduced as a therapy without

causing further recipient morbidity. Such a scaffold model would be a step forward for usable regenerative products.

1.8.1 Hypothesis

To provide a testable hypothesis for this project the following proposal has been formulated to encompass the key attributes examined.

Graphene oxide is a biocompatible and modifiable material for use as an instructive neural scaffold, with properties suited to the growth, development and maturation of neural tissues in vitro.

As such this project has set out provide results towards these questions by addressing the following objectives:

- To develop, characterise and present a 2D model for testing of GO of instructive qualities both innate and administered.
- To test the biocompatibility of a commercially available CE GO source as a GO raw material to create the 2D model.
- To explore the ways in which GO can be modified to add or enhance instructive potential.
- To combine GO with a hydrogel for a 3D model and test biocompatible cross linking systems to develop a neural scaffold.

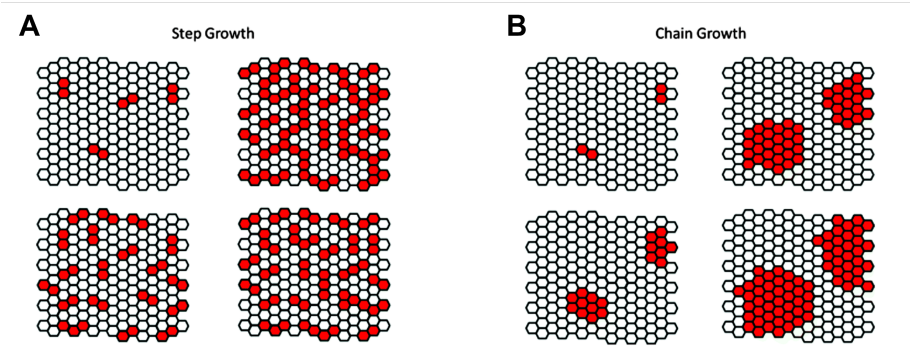

Figure 1.1 | **Illustrated propagation of polymerisation.** (A) Step growth cross linking begins between monomer units connected by a linker molecule, dependent on the presence of the linker, resulting in formation of more, lower weight units in which increase over time. (B) Chain growth cross linking begins between monomer units directly dependent on cross linking groups on the monomer, resulting in formation of few large weight units which become entangled. *Adapted from Payamyar et al. 2016, Two-dimensional polymers: concepts and perspectives [64]*

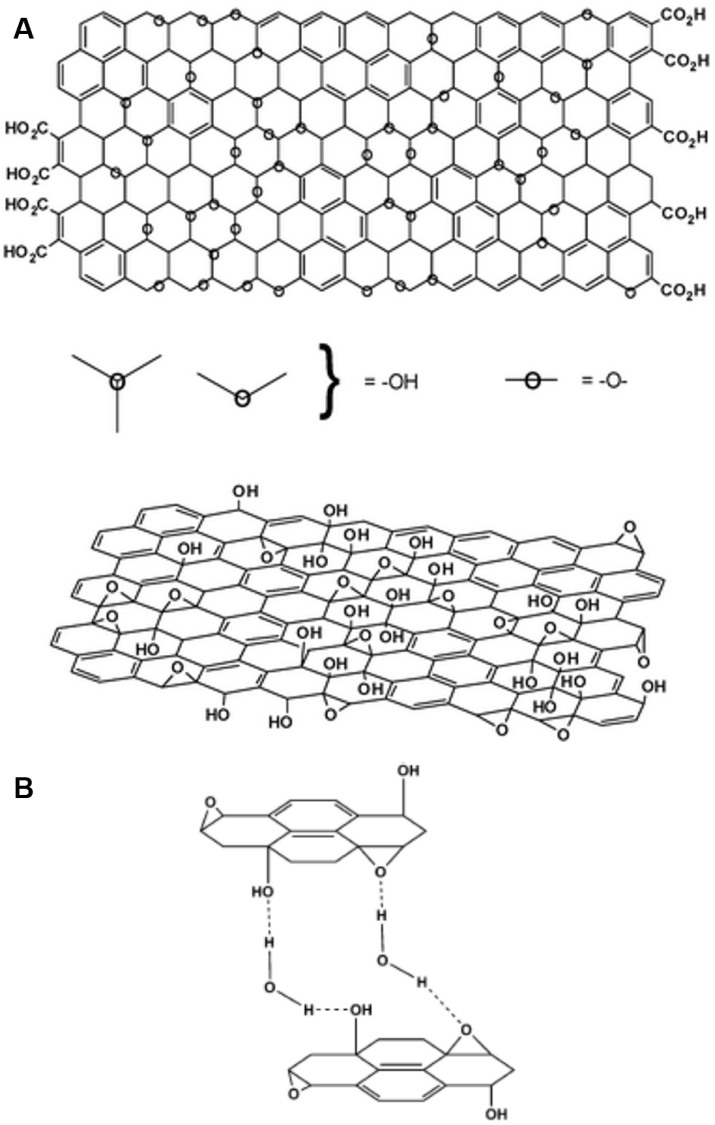

Figure 1.2 | **Illustrated Lerf-Klinowski model of Graphene Oxide.** (A) Lerf-Klinowski model of the chemistry of the graphene oxide carbon lattice illustrated in two perspectives; planar and cross section, showing formula of pendant groups. (B) Illustration of hydrophilic interaction with pendant groups and water molecules under the model. *Adapted from Dreyer et al. 2011, The Chemistry of Graphene Oxide [91]*

Chapter 2

Methods and Materials

2.1 Materials

In this project a range of suppliers were used to obtain reagents as required. Generic chemicals were supplied by Sigma-Aldritch (later Merck) unless otherwise specified. Arranged by supplier, the following key materials and reagents form the non-generic and concentration specific consumables used in this work

- Graphene oxide 1% (w/v) aqueous suspension, 500ml. (GOGraphene, William Blythe ltd, UK)
- Cell culture media, Cell culture media supplements, Trypsin-EDTA 0.05% (w/v), Penicillin-Streptomycin (penstrep), sterile 1X phosphate buffered saline (PBS), Goat serum (Gibco, Thermofisher Scientific ltd)
- Hoechest 33342, Wheat germ agglutinin with Alexaflour 647 conjugate (WGA), EVOS light cubes (Invitrogen, Thermofisher Scientific)
- Ibuprofen powder, Retinoic Acid powder, Polyethyleminine solution (PEI) 50% (v/v) aqueous solution, 1--D-Arabinofuranosylcytosine (AraC) powder, Ruthenium Hexahydrate, Propidium Iodide (Sigma, Merck ltd)

- Calcien-AM (BD Biosciences)
- Friction fit spin coater with customised Delrin spin coater (0.17mm circular recess) optimised to retain a single Number 1.5 round glass coverslip [274] (Osilla ltd, UK)
- Gelatin-Methacryloyl and Gelatine-Norbornene freeze dried macromer (CReaTE Group, University of Otago, Christchurch, NZ)
- Fiji software distribution of ImageJ [275]

2.2 Graphene Oxide

Room temperature stock 1% w/v (10mg/ml) material from GOGraphene was diluted by adding 200 µl to 800 µl of deionised water and mixing via vortex to achieve a homogenous working solution of 0.2% w/v (2mg/ml). Working solution was free of visible clumps and uniform in a dark brown to black colour. Physically, GO platelets measured at least 5±1µm in length, 2±1µm in width and 2±0.2nm in thickness, as per the manufacturer specifications. The manufacturer has conducted characterisation of representative batches of their product and has open source AFM data for the stock material. This can be seen illustrated in Figure 2.1 to demonstrate the typical appearance of a GO platelet. This information is presented to clarify the understanding of the GO models presented in this thesis.

2.2.1 Spin Coating

Number 1.5 glass coverslips were prepared for spin coating by first cleaning with piranha solution (1:3 ratio Hydrogen Peroxide: sulphuric acid) in a fume hood for 30 minutes and stored under deionised water until use. Cleaned coverslips were loaded into spin coater chuck using needle forceps, taking care not to otherwise touch the glass. Next, the spin coater was activated accelerating the chuck to 6000rpm and maintained for 20 seconds to ensure the coverslip was dry. Glass coverslips could be subsequently used as substrates

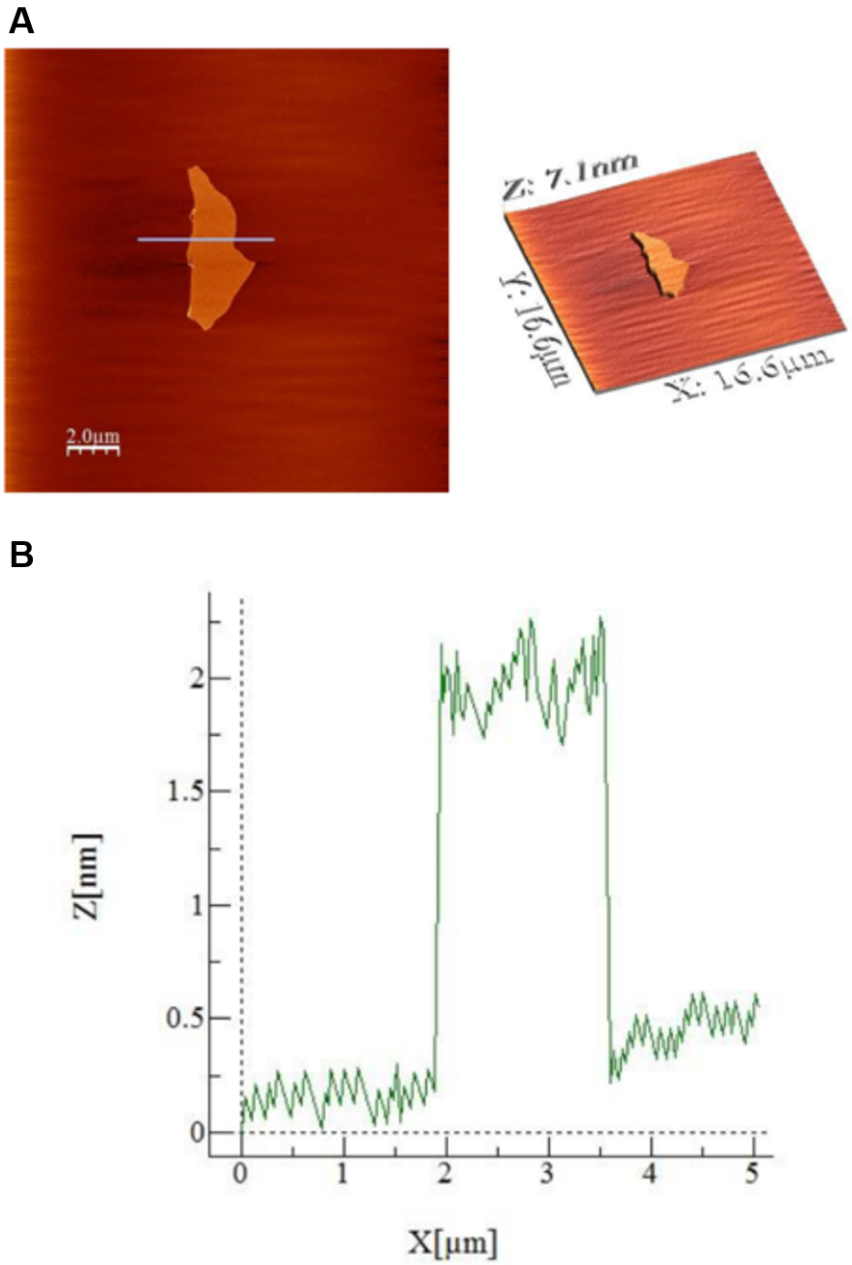

Figure 2.1 | **Atomic force microscopy (AFM) characterisation of GO platelets.** (A) Representative AFM images of GO platelets as provided in GO 1% suspension used in this work. (B) AFM measurement data for representative GO platelet. *GOgraphene. 2016. Graphene Oxide Analysis. Retrieved from https://www.go-graphene.com/pages/graphene-oxide-analysis*

for the GO film. Later to create PEI enhanced glass substrates, coverslips were finally prepared by spin coating 20 µl of 1% w/v PEI aqueous solution at 3000rpm for 40 seconds immediately prior to GO spin coating. Where otherwise specified alternative undercoats were may be used as discussed in Section 2.9 and Section 4.2.2 below.

2.2.1.1 GO Films

Spin coating proceeded according to the schematic outlined in Figure 2.2. 30µl of GO suspension was deposited onto the prepared coverslips before the spin coater chuck was accelerated to 2000rpm and maintained for 40 seconds to spin coat the deposited solution across the coverslip and form the GO film. GO films were accepted following visual inspection for obvious faults, contaminants such as dust or damage such as cracks of the coverslip. Unacceptable GO films were discarded.

GO films were removed from the spin coater chuck with needle forceps and placed into a sterile tissue culture well plates and immersed in 500 µl of 99% ethanol. GO films within culture plates were used following a minimum of 2 hours sterilisation time in ethanol under UV light irradiation, or stored refrigerated under ethanol in well plates and similarly irradiated with UV light prior to use. Ethanol was withdrawn following sterilisation. For characterisation work no further preparation of the GO film was performed. To prepare the sterile GO films for use in cell culture, GO films were washed with sterile PBS and immersed in 250 µl of appropriate cell culture media per film prior to cell seeding.

2.2.2 Adsorption treatment

For adsorption treatment, drugs of interest were dissolved in a 50% ethanol aqueous solution to create an adsorption solution. 250 µl of the solution was applied to the sterile GO films. A minimum of 2 hours and maximum of 12 hours at room temperature was permitted to provide an excess adsorption time. Following adsorption surfaces were prepared for cell culture by washing with sterile PBS and immersion in 250 µl of appropriate cell culture media prior to cell plating.

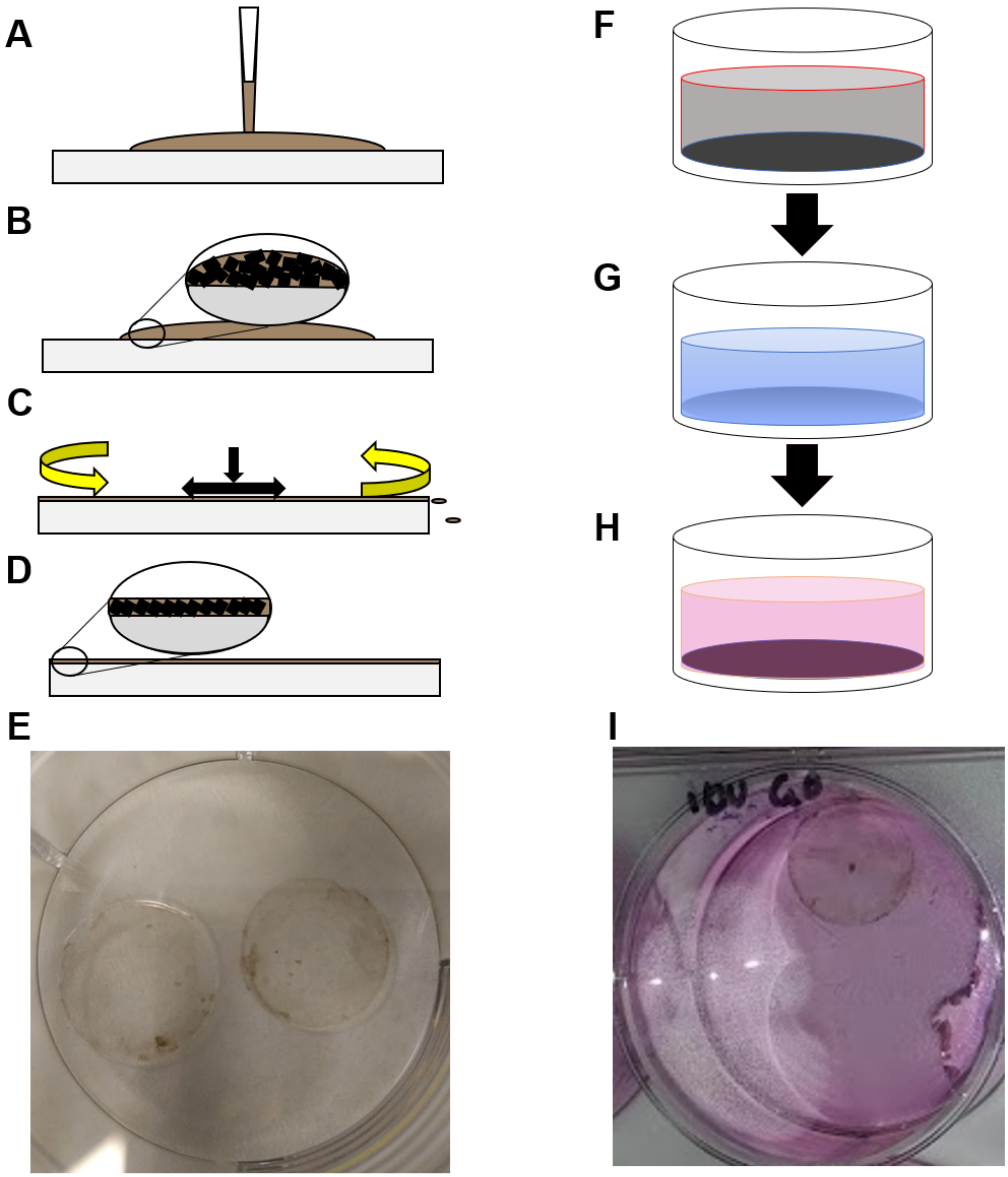

Figure 2.2 | **Illustrated method for spin coating GO thin films..** (A) GO suspension deposited on glass coverslip. (B) GO platelets free in disordered suspension (C) Spin coating by high rpm rotation of coverslip to drive suspension down and across glass surface. (D) GO platelets form plasticised film in an ordered uniform layer. (E) Photograph of GO film as produced by previous steps. (F) GO film immersed in 99% ethanol for sterilisation (G) Ethanol replaced with phosphate buffered saline wash (H) Phosphate buffered saline replaced with cell culture medium prior to cell seeding, (I) Photograph of GO film in culture media ready for cell seeding.

Table 2.1: Comparison of chemical structure in adsorbed molecules

Molecule	Formula	Molar Mass (g/mol)	Solubility (H_2O at 25°C)	Biological action
Ibuprofen	$C_{13}H_{18}O_2$	206.285	21 mg/L	COX-2 Inhibition
Minocycline	$C_{23}H_{27}N_3O_7$	457.483	52000 mg/L	p38 MAPK Inhibition
Vitronectin	$C_{54}H_{84}N_{22}O_{12}$	1233.4	50 mg/L	Arg-Gly-Asp cell recognition sites

2.3 Hydrogel Formulation

Two research grade sterile hydrogel macromers were graciously prepared and supplied by CReaTE group collaborators at University of Otago, New Zealand. Hydrogel macromers were derived from covalent modification of bovine gelatine and supplied freeze dried in 200ml sterile pots. Aliquots were sterile weighed into falcon tubes and dissolved to an initial concentration of 10% w/v in sterile PBS at 37°C over a maximum of 1 hour prior to use, with new preparations made before each series of experiments. Macromer solutions were maintained at 37°C in sealed tubes until use for a maximum of 48 hours. All macromer solutions were diluted to a final working concentration as specified in data chapters using additional warmed PBS or cells in cell culture media.

2.3.1 Gelatine-Norbornene

The step-growth Gel-Nor formulation used a visible light photo-initiated free radical generator, ruthenium hexahydrate. Sodium persulfate was used as the persulfate ion source to catalyse a reaction between norbornene ring moieties on the macromer chain with thiol groups of a dithiothreitol linking molecule. For a 1ml final working volume of hydrogel, $20\,\mu l$ of $50\,\mu M$ ruthenium hexa-hydrate photo-initiator stock and $20\,\mu l$ of $500\,\mu M$ sodium persulfate initiators are combined with $40\,\mu l$ of $500\,\mu M$ dithiothretol for a final volume of $920\,\mu l$ hydrogel solution and mixed until homogenous. Pre-cross-linked hydrogel was pipetted and cross-linked immediately. Visible wavelength light irradiation was used for photo-click reactions. A 1000 W floodlight was positioned 3cm from the pre-cross-linked hydrogel material and allowed 10 minutes for the cross-linking reaction to proceed covered with aluminium foil in at room temperature under sterile conditions.

2.3.2 Gelatine-Methacryloyl

The chain-growth Gel-Ma formulation also used a ruthenium hexahydrate photo-initiator as a free radical generator and sodium persulfate as an ion source to catalyse a reaction between methacrylate moieties on the macromer chain. For a 1ml final working volume of hydrogel, $20\,\mu l$ of $50\,\mu M$ photo-initiator stock and $40\,\mu l$ of $500\,\mu M$ sodium persulfate initiators were combined with $940\,\mu l$ hydrogel solution via pipette and mixed until homogenous. Pre-cross-linked hydrogel was pipetted and cross-linked immediately. Visible wavelength light irradiation was used for photo-click reactions. A 1000w floodlight was positioned 3cm from the pre-cross-linked hydrogel material and allowed 10 minutes for the cross-linking reaction to proceed covered with aluminium foil in at room temperature under sterile conditions.

Alternatively for a redox-initiated reaction between Gel-Ma macromer, photo-initiator was withheld and substituted with a reducing agent as specified to provide chemical reduction of the persulfate and generate ions which catalyse the cross-linking reaction. Redox initiated hydrogels were not irradiated and were instead incubated at 37°Cfor up to 1 hour.

2.3.3 Casts and forms

To create consistent hydrogel shapes with consistent surface area and volume for mass loss characterisation experiments, hydrogel samples were prepared in identical moulds. 2mm thick silicon sheeting was cut into 75mm x 25mm rectangles and then punched with an adjustable hole punch to create 4.5mm holes, for a final cylindrical volume of $30\,\mu l$. The silicon mould was then pressed to a glass microscope slide to create an open topped well which was filled with pre-crosslinked hydrogel and topped airtight with coverglass prior to cross linking to minimise evaporation (Figure 2.3). For rheometry hydrogel experiments, the rheometer plate well was filled with pre-crosslinked hydrogel and cross linked in situ.

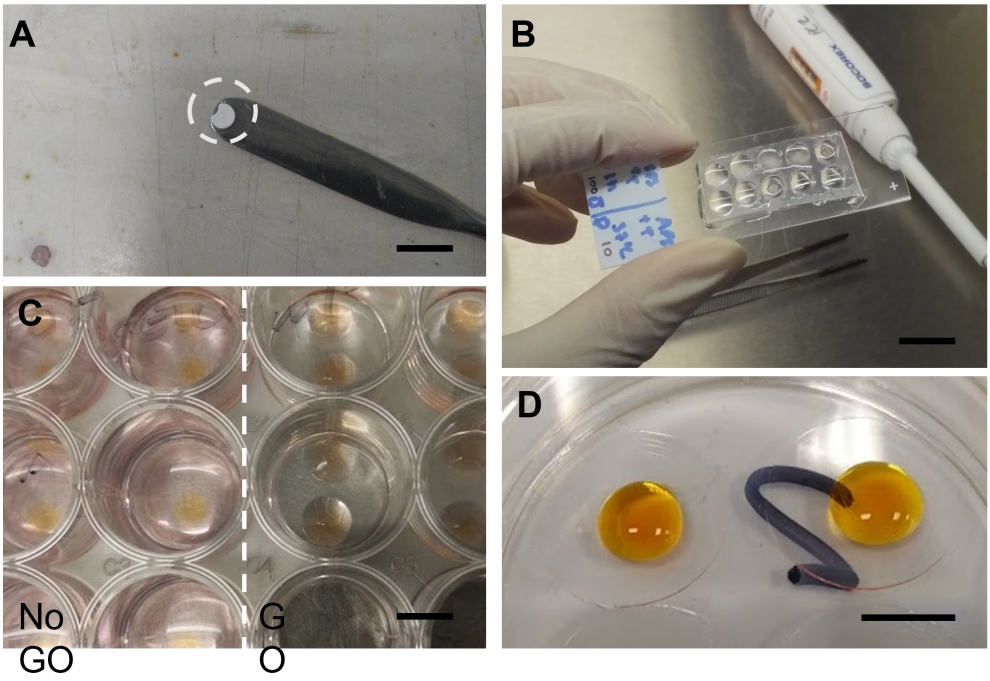

Figure 2.3 | **Photographs of Hydrogel forms used.** Scale bar 2.5mm (A) Freeze-Dried hydrogel (circled) after cross linking without GO, (B) Hydrogels in cast mould during cross linking without GO, (C) Hydrogels in culture with encapsulated cells without (left) and with (right) GO inclusion (D) Hydrogels in droplet form during cross linking without GO on glass substrate

2.4 Cell culture

Neural cells utilised during this project were sourced within the University of Leeds. All cells were handled aseptically within class 2 microbiological safety cabinets. All cell growth and expansion was conducted within sterile tissue culture plastic maintained in cell culture incubators at 37°C, 5%CO_2, 95% humidity Where tissue culture well plates were used, perimeter wells were left unused and loaded with 500 µl sterile PBS to minimise edge effects and evaporative losses from culture wells, experimental wells were maintained with 300 µl media volume. Where tissue culture petri-dish were used, 35mm plates were externally plated in groups of 3 within 100mm plates. Plates were maintained at 1500 µl media volume. Prior to cell seeding all culture surfaces were washed with DMEM:F12 supplemented with 10% v/v foetal bovine serum (FBS) and 100IU/ml penicillin, 100 µg/ml streptomycin (1% penstrep) - hereafter referred to as standard media, unless otherwise specified in data chapters.

2.4.1 Cell lines

Two Immortalised cell line models supplied by University of Leeds were cultured and expanded within 75cm^2 sterile tissue culture flasks. Flasks were monitored using visible light microscopy every 3 days. Cell lines were maintained in DMEM:F12 supplemented with 10% FBS every 3 days during expansion and then treated with specific media during experiments as explained below. Passage numbers were tracked and the range used is specified below

Upon reaching an estimated 70-80% confluence flasks were passaged. To do this cells were detached from the expansion flask by withdrawal of maintenance media followed by a single wash with DMEM:F12. Next flasks were incubated with 3ml of 0.5% trypsin-EDTA solution for 5-10 minutes at 37°C until all cells were visibly detached, observed via bright-field microscopy. Trypsin-cell suspension was subsequently added to 10ml of standard media and immediately centrifuged for 5 minutes at 300*g* to pellet cells from the

suspension. Following centrifugation the supernatant was discarded and the pellet was suspended within 1ml of standard media. A 10 µl aliquot was taken to a haemocytometer to provide a cell count.

2.4.1.1 SH-SY5Y cells

SH-SY5Y cells were used between passage 10 and 14 before being disposed of at passage 15. For experiments, SH-SY5Y cells were seeded at 15000 cells cm^{-2} in standard media. For pseudo-differentiation of SH-SY5Y cells, DMEM:F12 supplemented with 1% N2, 3uM retinoic acid and 1%penstrep was substituted for standard media 24 hours after seeding and maintained every 4 days with differentiated morphologies expected at 10-14 days.

2.4.1.2 BV-2 cells

BV-2 cells were used between passage 8 and 13 before being disposed of at passage 14. For experiments BV-2 cells were seeded at 10000 cells cm^{-2} in standard media for up to 5 days or until confluent. BV-2 cells were not maintained with fresh media following seeding.

2.4.2 Primary cells

Two sources of primary tissue were used to isolate primary cells in this work. 1-3 day postnatal mouse pups were sacrificed to isolate mouse hippocampal neuronal cells, microglia, astrocytes and co-culture tissue suspensions. 1-3 day postnatal rat kittens were sacrificed to isolate rat hippocampal neurons and co-culture tissue suspensions. Primary cells were maintained in specific media appropriate to their lineage during experiments and no passage was performed. Where tissue culture flasks were used, plates were first coated with poly-L-lysine (PLL) and stored refrigerated in the dark for up to 48 hours before use.

In all cases, animals were sacrificed under Schedule 1 by dislocation of the cervical spine. Subsequently the skull was opened with a scalpel blade and the whole brain removed with forceps to a 100mm petri dish dissection area containing sufficient Hibernate-A medium to cover the surface of the dish. Tissue is therefore partially floated and supported within the media during dissection and kept hydrated. Brains were dissected with assistance of dissection microscope lenses under sterile laminar airflow using fine tip forceps. Prior to further dissection the meninges and olfactory bulbs were removed and discarded. Where separation of tissue was required, pinching and pulling actions were used to gently separate the structures of neuroanatomy apart instead of using bladed instruments. All retained dissected tissue was stored in ice-chilled Hibernate-A medium in 15ml falcon tubes prior to further dissociation.

2.4.2.1 Microglia

To isolate microglial cultures the hemispheres of the brain were separated and the mid-brain region removed and discarded. The cortex tissue was retained and pooled into tubes containing 2-4 brains. Collected tissue tubes were transferred to a sterile class 2 micro-biological safety cabinet and Hibernate-A medium was replaced with 1ml of trypsin per brain and incubated for 20 minutes at 37°C. Next, trypsin was withdrawn and replaced with 1ml per brain standard media. Tissue and media was aspirated with a pipette tip into a bacteriological grade 35mm pipette dish inclined at 15° from horizontal using the dish lid. Media and tissue were gently, repeatedly aspirated 30 times to the top of the inclined dish to dissociate the tissue into individual cells. Dissociated cell suspension was then filtered through a $70\,\mu\mathrm{m}$ nylon cell strainer into a 50ml falcon tube and the strainer washed through with up to 1ml per brain additional standard media. Cells in suspension were centrifuged at 300*g* for 5 minutes to pellet cells and the supernatant was discarded. Cells were gently re-suspended within 2ml per original brain of standard media. 2ml of suspended pellet was to (PLL) coated 75cm^2 tissue culture flasks and supplemented with standard media to a final volume of 15ml and incubated for 3 days.

After 3 days, 50% of the flask volume (7.5ml) was collected and centrifuged at 300*g* for 5 minutes. The supernatant was collected and supplemented to 15ml with standard media to create conditioned media. The remaining media inside the flask was discarded and the flask refreshed with 15ml of conditioned media.

Between 9 and 13 days *in vitro*, flasks were monitored via brightfield microscopy for the appearance of spheroid microglial bodies protruding and loosely bound to an astrocyte layer. Upon observation of these features, flasks were placed upon an orbital shaker and agitated for 30 minutes at 180rpm to detach microglia from the cell layer into the media. Following shaking the entire media volume of the flask was aspirated down the culture layer twice to collect any remaining loosened microglia and transferred to a 15ml falcon tube. A microglial depleted astrocyte enriched layer remains adherent to the flask and was maintained with conditioned media for use in astrocyte isolation as below.

Tubes were centrifuged at 250*g* for 5 minutes and the supernatant retained to conditioned media as above. Pellets were resuspended in 2ml of conditioned media. A 10 µl aliquot was taken to a haemocytometer to provide a cell count. Microglial preparations were seeded at 20000 cells cm^{-2} in conditioned media and maintained for up to 5 days. To induce microglial activation, LPS was used at 1 µg/ml introduced into the culture media at 6-12 hours after cell attachment.

2.4.2.2 Astrocytes

To isolate astrocytes, the monolayer cultures left over following the above microglia preparation maintained with conditioned media for a further 24 hours to recover following microglia harvest. Flasks were incubated with 3ml of 0.5% trypsin-EDTA solution for 5-10 minutes at 37°C until all cells were visibly detached via bright-field microscopy. Trypsin-cell suspension was subsequently added to 10ml of standard media and immediately centrifuged for 5 minutes at 300*g* to pellet cells from the suspension. Following centrifugation the supernatant was discarded and pellet re-suspended in 1ml of standard media. A 10ul aliquot was taken to a haemocytometer to provide a cell count. Astrocytes

from suspension were seeded at 10000 cells cm^{-2} in standard media and maintained every 4 days.

2.4.2.3 Neurons

To isolate neurons both structures of the hippocampus were separated from the each cortical hemisphere of the brain, with the cortex, thalamic tissue and midbrain discarded. Subsequently hippocampal tissue was pooled into tubes containing 2-4 brains. Collected tissue tubes were transferred to a sterile class 2 microbiological safety cabinet and Hibernate-A medium was replaced with 1ml of trypsin per brain and incubated for 20 minutes at 37°C. Next, trypsin was withdrawn and replaced with 500µl per brain standard media. Tissue and media in the collection tube was gently aspirated with a sterile pipette tip into a bacteriological grade 35mm pipette dish inclined at 15° from horizontal using the dish lid. Media and tissue were gently aspirated 30 times to the top of the inclined dish to dissociate the tissue into individual cells. Dissociated cell suspension was filtered through a $70\,\mu m$ cell strainer into a 50ml falcon tube and the strainer washed through with up to $500\,\mu l$ per brain additional standard media. A $10\,\mu l$ aliquot was taken to a haemocytometer to provide a cell count. Cell suspension was seeded at between 8000 and 10000 cells cm^{-2} in standard media.

After 6 hours, attachment of cells was confirmed with brightfield microscopy and standard media was withdrawn and replaced with Neurobasal media supplemented with 1%v/v B27, $2\,\mu M$ Glutamine and 1%v/v penstrep as maintenance media.

48 Hours after seeding $5\,\mu M$ of cytosine arabinoside (araC) was added to the media to inhibit non-neuronal cell proliferation. Every subsequent 3 days 50% of maintenance media was refreshed with fresh maintenance media, araC concentration was maintained for up to 1 week. Subsequently araC was not added to media during maintenance resulting in a cumulative 50% decrease in concentration following each maintenance period. Cultures were maintained for up to 3 weeks with neuronal measurements and images taken at between 7 and 21 days.

2.4.2.4 Co-culture

For neuron-glia co-cultures, hippocampal tissue was collected and prepared as for the neuron isolation above. Two methods of neuron-astrocyte co cultures were performed. In the first method, isolated cells from hippocampus tissue was seeded to surfaces identically to neuron preparations, however araC was withheld.

In the second method, at 48 hours post seeding, 1 μM of araC was added to the media to reduce proliferation of non-neuronal cells. Every subsequent 3 days 50% of maintenance media was refreshed with fresh maintenance media however araC concentration was not maintained to allow the concentration to begin reducing from 5 days post seeding. Therefore a lower initial araC concentration decreased by 50% each 3 days, which was observed allowing glial cells to proliferate more slowly than in araC absent cultures. Cultures were maintained for up to 3 weeks with neuronal measurements and images taken at 14 or 21 days.

2.5 Characterisation of Materials

Characterisation of 2D and 3D materials used facility resources within the University of Leeds and established techniques from literature to acquire the data.

2.5.1 Raman spectral analysis

Raman microscopy was performed with the kind use of School of Earth and Environmental Sciences, University of Leeds equipment using an inVia confocal Raman microscope spectrometer (Renishaw PLC) with a 514-nm laser and 1800 l/mm diffraction grating. The peak range was calibrated using a silicon wafer standard immediately prior to use.

Individual GO films prepared for characterisation as above were loaded onto the stage atop a glass slide and a 50x objective lens manually focused onto the film surface by resolution of visible film features. Raman spectra were acquired using a 50 pass laser scan short programme and compiled. Normalisation, smoothing of background spikes,

peak identification and labelling processes were performed using Spectragryph (Friedrich Menges) software.

2.5.2 Scanning electron microscopy

Scanning electron microscope (SEM) images of GO films were acquired with the kind assistance of Stuart Micklethwaite of the Leeds Electron Microscopy And Spectroscopy centre (LEMAS) using a Helios G4 CX dual beam FIB-SEM (Thermofisher Scientific).

Individual GO films prepared for characterisation as above were first mounted to SEM holder stubs with adhesive pads on the underside of the substrate and applied with a 1-nm thick iridium sputter coat to prevent charge build-up. Planar SEM images were acquired first in 10000x magnification.

To acquire cross-section SEM images a reinforcing platinum support was deposited via ion deposition to minimise damage to the GO film during FIB beam milling, to a depth of 2000nm [276]. Ion polishing of the milled edges revealed the cross sectional interface between the GO film, glass coverslip and platinum support. Images of the cross section were acquired at 25000x magnification at an angle of incidence of 20°from the sample surface. Images were analysed and the distance between the glass surface and top GO layers was acquired digitally in situ using Amira-Avizo (Thermofisher Scientific) software during acquisition of images to allow for correction of the angle of incidence automatically and obtain a true measurement.

2.5.3 X-Ray photon spectroscopy

Near ambient pressure X-ray photon spectroscopy (NAP-XPS) spectra of GO films with and without SH-SY5Y populations were acquired with the kind assistance of the Elizabeth Willneff of the Versatile X-ray Spectroscopy Facility (VXSF) using an EnviroESCA (SPECS GmbH).

Where spectra of GO films were acquired, samples were stored in PBS in a cell culture incubator for 14 days. Where spectra GO films with SH-SY5Y cells were acquired,

films were first seeded with 5000 or 15000 cells cm^{-2} and maintained as described in Section 2.4.1.1 above for 14 days. Where spectra GO films with SH-SY5Y cells removed were acquired, SH-SY5Y seeded GO films identically prepared to the above were incubated with Trypsin-EDTA for 10 minutes immediately prior to analysis. Films were washed with deionised water and mounted to SEM holder stubs with adhesive pads on the underside of the substrate and loaded onto the EnviroESCA stage as seen in figure 2.4.

Once loaded the sample chamber and scanning chamber were evacuated of ambient atmosphere and charged with H2O to a pressure of 11mb for NAP-XPS. NAP-XPS was conducted with an Al Kα source and electrons collected with a Slit of 4:7x20 in a grid scanning pattern using Fixed Analyzer Transmission mode, an Excitation Energy of 1486.71 eV, Detector Voltage of 1600 V and a Bias Voltage: 90.00 V.

Graphical analysis of XPS data arranged as ISO14976 VAMAS block files was performed with CasaXPS software (Casa Software Ltd). Survey peaks were identified using CasaXPS element libraries and elemental atomic percentage was calculated in software assuming that all detectable peaks formed the totality of elements present. Charge correction was performed using a distinct oxygen peak at 536eV attributed to the oxygen component of H_2O High resolution spectra peak component models were constructed to a residual error of <1 standard deviation using Tougaard background approximations. The same peak model construction was kept with consistent constraints and propagated to all samples prior to specific fitting involving adjustment of peak height, adjustment of peak position was conducted with all peaks relative to maintain distribution.

To compare peak models between samples, proportional change between component areas were calculated as reciprocals from the ratio of each similar component. Therefore a value of Proportional change at 0 denoted no change in the component area, positive values of Proportional change indicated an increase in the component relative to the reference sample. A negative value of Proportional change indicated a decrease in the component relative to the reference sample. For given samples the calculation to determine the relative proportional change in component peaks is as follows:

$$\text{Proportional Change} = 1 - \frac{Component_{reference}}{Component_{comparator}}$$

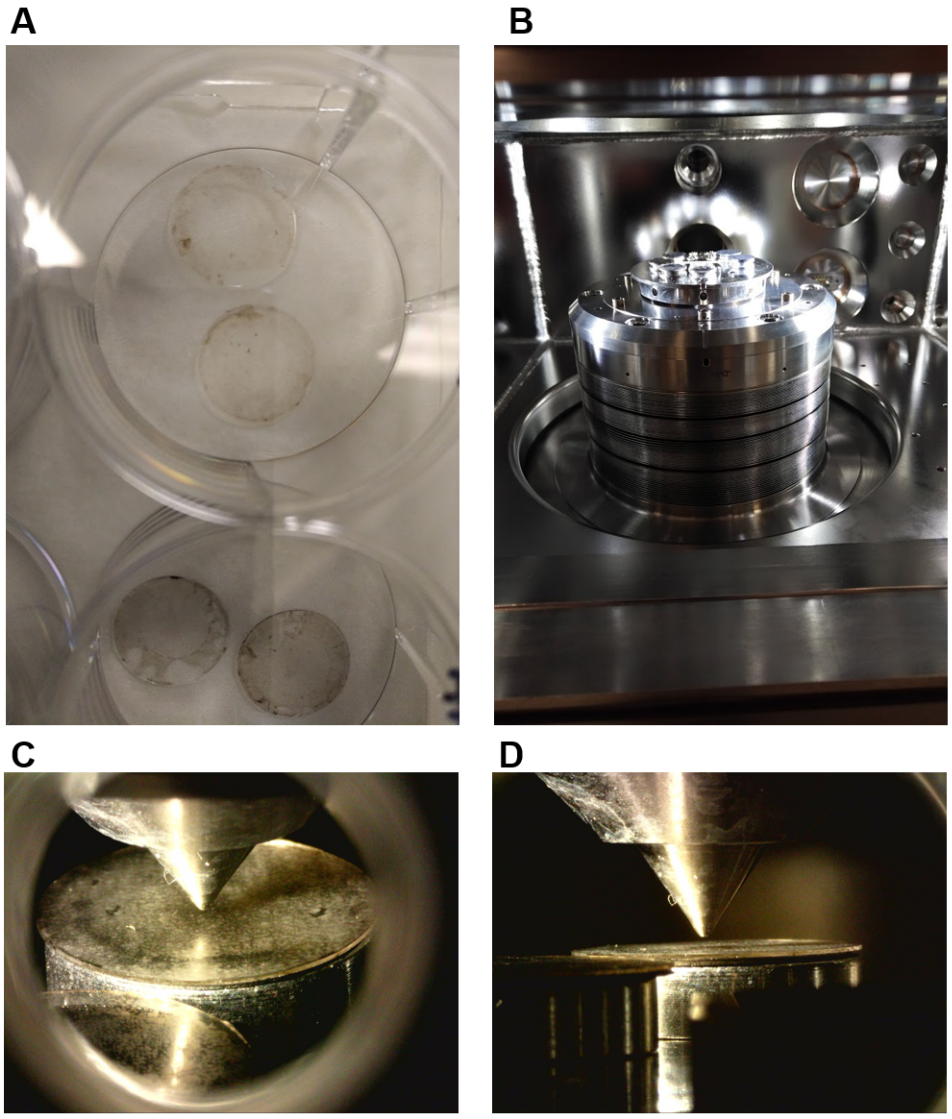

Figure 2.4 | **Photographs of XPS experimental setup.** (A) GO film washed prior to mounting in XPS stage. (B) Films mounted in XPS stage during initial evacuation of atmosphere for NAP measurement. (C-D) XPS nozzle during measurement at flat GO film surface. Working distance 250±50μm to achieve 1x103 CPS

2.5.4 Mass loss and swelling

Characterisation of hydrogel samples included swelling and mass loss experiments. This was performed according to works published by the macromer manufacturers CReaTE group and Lim et al [75, 76, 73]. Identical cylindrical casts prepared in batches using silicon moulds were weighed for initial wet mass ($m_{initial,t=0}$) following cross linking. A subset of half the original samples were frozen and lyophilised immediately and weighed to obtain a dry mass ($m_{dry,\ t=0}$).

$$\text{actual macromer fraction} = \frac{m_{dry,t=0}}{m_{initial,t=0}}$$

The remaining subset was instead incubated in a bath of 37°C PBS for 24 hours, blotted dry and weighed to obtain a swollen mass ($m_{swollen}$) before being frozen, lyophilised and weighed again to obtain a dried mass with any soluble fraction removed (m_{dry}). The soluble fraction is defined as the lost mass during the swelling incubation.

$$m_{initial,dry} = m_{initial} * (\text{actual macromer fraction})$$

$$\text{Soluble fraction} = \frac{m_{initial,dry} - m_{dry}}{m_{initial,dry}} * 100\%$$

The mass swelling ratio (q) is defined by the fractional difference in mass between the swollen mass and the subsequent dried mass to remove any influence of soluble components.

$$q = \frac{m_{swollen}}{m_{dry}}$$

Which is then used to calculate the actual swelling ratio (Q) including the density of the gelatin macromer (1.369)

$$Q = 1 + 1.369(q - 1)$$

The cross-linking density is estimated by calculating the cross linked mass without the soluble fraction and correcting for the Higgins parameter of gelatin (0.49) and the density of the gelatin macromer.

$$\text{Cross Link Density} = \frac{-ln(1-q) + (q) + 0.49(q)^2}{Q(Vo)\frac{(Vr)(1/3)-(q)}{2}}$$

where: Vo is the molar volume of solvent, and Vr is the reciprocal of swelling ratio

2.5.5 Rheometry

Rheometry of hydrogel materials was conducted with the kind assistance of Daniel Secker at University of Leeds IMBE St James campus using an Anton Paar bench-top rheometer with a 22mm parallel plate with a gap size of 0.1mm. Hydrogel samples were mixed to final concentrations, cast and cross-linked in silicone moulds as described previously with dimensions equal to the rheometer geometry. Samples were swollen overnight to equilibrium in PBS and tested the next day. Rheometry testing first comprised an amplitude sweep which determined the optimal testing amplitude to be 0.1% shear strain, with testing and data collection conducted using frequency sweeps between 0.1 and 1 rad/s

2.6 Imaging

Images of cell cultures were taken with the kind use of Protein Production Research Facility, University of Leeds equipment using an EVOS™ FL Auto 2 imaging system

(Thermo Fisher Scientific). Software automated image acquisition of at least 10 fields per sample were acquired and were automatically stitched into single large images and individual channel images retained for figure purposes. For 3D samples, z-stacks of at least 15 fields were collected and compiled into maximum intensity projections and individual images similarly retained. Images of fibroblasts in hydrogel cultures were taken manually using a Zeiss Axio imager Z1 at CReaTE group facilities (Christchurch, NZ).

2.6.1 Staining

During this work both live and fixed cells were stained. Combinations of stains were used as specified in figure captions. For cytoplasmic staining of live cells, 1mg Calcien-AM powder was dissolved in $201\,\mu l$ anhydrous dimethyl sulfoxide to create $5\,mM$ stock solution. Stock solution was added to culture media for a final working concentration in media of $10\,\mu M$ and incubated for 20 minutes at 37°C, culture media was refreshed prior to imaging with an EVOS microscope using a GFP light cube.

For counter-staining of nuclei, 1mg Hoechst 33342 powder was dissolved in 1ml deionized water to create 1mg/ml stock solution. Stock solution was added to culture media for a final working concentration of $10\,\mu g/ml$ and incubated for 20 minutes at 37°C, culture media was refreshed prior to imaging with an EVOS microscope using a DAPI light cube

For nuclear staining of dead cells, 1mg Propidium Iodide powder was dissolved in 1ml deionised water to create 1mg/ml stock solution. Stock solution was added to culture media for a final working concentration of $10\,\mu g/ml$ and incubated for 20 minutes at 37°C, culture media was refreshed prior to imaging with an EVOS microscope using a Texas Red light cube

For pre-fixation staining of cell membranes, 1mg of WGA powder was dissolved in 1ml PBS to create 1mg/ml stock solution. Stock solution was added to culture media for a final working concentration of 10ug/ml and incubated for 20 minutes at 37°C, before fixation for immunohistochemistry, and was imaged with an EVOS microscope using a

Cy5 light cube.

2.6.2 Immunohistochemistry

Table 2.2: Antibodies for Immunohistochemistry

Antibody	Usage	Species	Dilution ratio
Anti-Tau	Primary	Rabbit	1:1000
Alexafluor 488 anti-rabbit	Secondary	Goat	1:500

Where immunohistochemical (IHC) staining was performed, antibodies were used following optimisation at the specified dilutions in Table 2.2. Fixed cells were used for IHC staining To fix cells, media was withdrawn and replaced with 3.7% v/v Formalin with 0.1% v/v methanol in PBS and incubated at room temperature for 2 minutes. To permeabilize cells, ice cold 100% methanol was applied for 60 seconds, subsequent wash with PBS followed by application of 1%v/v goat serum, 1% Tween-20 in PBS (blocking buffer) for 30 minutes at room temperature with gentle agitation. Blocking buffer was replaced with primary antibodies suspended in blocking buffer and applied to the sample for an overnight incubation at 4°C, during this step the sample plate was wrapped in foil to minimise evaporative loss.

Primary antibody buffer was washed off in three volumes of blocking buffer to remove unbound antibodies and replaced with secondary antibodies suspended in blocking buffer with a working concentration of Hoechest 33342. Secondary antibody buffer was incubated for 1 hour at room temperature in the dark with gentle agitation. Secondary antibody buffer was washed off in three volumes of blocking buffer to remove unbound antibodies and finally replaced with PBS and imaged immediately. Primary antibody was omitted for negative control of non-specific secondary antibody binding signal. Rabbit IgG control antibody was used for an isotype control to validate the staining protocol and specificity of primary antibodies.

2.7 Quantification of images

Images of cell cultures were assessed using Fiji software, its functions and packages to transform, count and measure the features within individual images. Macro functions were used to automate analysis where possible and permit efficient processing of high numbers of images into numerical data. Automated processes were checked and validated with manual quality assurance using representative images from each microscopy session before use.

2.7.1 Viability assay

Live and dead cells were differentially stained in unfixed samples by addition of working concentrations of Hochest 33342 and propidium iodide to the culture media followed by incubation for 20 minutes at 37°C to allow dyes to bind. Following incubation culture media was refreshed to remove unbound dye and any debris and samples were imaged under PBS. Images were analysed with Fiji using the Find Maxima function to automatically count hoechest ($count_{total}$) and propidium iodide ($count_{dead}$) stained nuclei separately within the blue and red channels respectively.

$$count_{live} = count_{total} - count_{dead}$$

$$\text{Cell Viability } \% = \frac{count_{live}}{count_{total}} * 100$$

2.7.2 Morphology

To assess gross cell morphology, cells were stained with Calcien-AM to elucidate the living cytoplasm and subsequently acquire images in the green channel. To assess gross morphology of glia in co-cultures, WGA staining was performed and images acquired in

the red channel, counterstained with Hoechst. To assess neuritic lengths in tau-positive cytoskeletons of differentiated SH-SY5Y, primary neurons and neurons in co-cultures, fixed cultures were stained with anti-tau antibody to preferentially stain tau protein within axonal projections and between projection plasma membranes. Use of Alexafluor-488 secondary antibody allowed collection of this signal in the green channel. Morphology assessments were performed on stitched images to ensure the largest possible field of view and normalise signal intensity across the plane.

2.7.3 Shape analysis

To quantify morphological features of cells from culture images of cytoplasm and cytoskeleton stained cells were analysed with Fiji. For measurement of length of the neurites, immuno staining of Tau positive neurites was performed and the NeuronJ package [277] was used to fit and measure splined lines to bright tau positive neurite like projections visible on images. For cytoplasmic cell area and perimeter data as well as derivatives of circularity, solidity and roundness, green channel images of Calcien-AM images were isolated, converted to 8-bit images and processed into binaries via manual threshold to create masks of cell cytoplasm.

Shape analysis [278] used the particle analysis shape descriptor measurement functions within Fiji and are defined as:

$$\text{Circularity} = 4\pi * \frac{Area}{Perimeter}$$

$$\text{Roundness} = 4 * \frac{Area}{\pi * (Major\ Axis)^2}$$

$$\text{Solidity} = \frac{Area}{Convex\ Area}$$

Where:

- *Circularity* describes a perfect circle with a value of 1.0.
- *Roundness* can also be considered the inverse of aspect ratio and describes a score for elongation of a bounding ellipse fit to the cell body, describing a geometrically even object at a value of 1.0.
- *Solidity* describes the ratio between the true area and the convex area, describing a smooth perimeter at a value of 1.0.

Circularity and roundness describe similar yet distinct morphological attributes, however roundness is more sensitive to elongation of an objects area whilst circularity describes the shape as a smooth perimeter, independent of protrusions. Solidity describes the complexity of the perimeter shape by encompassing any smaller protrusions of otherwise negligible area.

2.8 Data analysis, presentation and statistics

R (The R Foundation, CRAN) was used for statistical analysis, data processing and data presentation. Packages were downloaded from CRAN via RStudio. Data from Fiji output as .csv files were parsed into R data-frames and manipulated entirely within the R environment. Measurement data from XPS, SEM, rheometry outputs, balances and other instruments recorded in lab book was directly compiled within R into data frames.

Tidyverse package was used for graphical interpretation of data, removal of outliers and summarisation, whilst base R was used for ANOVA statistical testing with Tukey's Honestly Significant Difference post-hoc correction applied. Significance was determined at adjusted $P<0.05$. Where only two groups are tested, Students T-Test for difference of means was substituted for ANOVA.

2.9 Optimisations

Initially to prepare the 2D GO thin film model commercial 10mgml^{-1} GO stock suspension was diluted with deionized water to create a 2mgml^{-1} working solution. 30µl volumes were spin coated across glass substrates to create the film. Spin coating was performed according to the method demonstrated in Figure 2.2. Initially it was observed that the spin coating process could fail with incomplete coverage of the substrate, this was attributed to the lack of a cleaning step prior to spin coating. Therefore to create repeatable GO films, glass substrates were subsequently piranha cleaned with a 1:3 ratio of hydrogen peroxide and sulphuric acid for 20 minutes prior to spin coating. This cleaning noticeably increased the hydrophilicity of the glass and removed any potential contaminants present as supplied. Following the addition of this cleaning, spin coats were reliably produced using the specified spin coater settings. Bare glass coated with GO surfaces were subsequently referred to as GO/None coats.

Next, batches of GO/None coats were observed to have inconsistent and intermittent damage macroscopically following at most 1 maintenance period in culture conditions following production, increasing at subsequent maintenance periods. To improve robustness of the films and to limit detachment from the substrate, adhesion between the GO film and glass substrate was enhanced with application of a molecular polymer undercoat. This undercoating was applied to the bare glass substrate before GO via spin coating under the same conditions as the GO ink. Undercoating effectively eliminated the occurrence of GO film damage and improved efficiency.

The choice of polymer undercoat was informed by a conservative view of potential biological confounding effects. Thus initially Gelatine, PEI and PLL were chosen for their established biocompatibility and general use in cell culture. However when considering ease of use and practicality for the spin coating process, differences exist between Gelatin, PEI and PLL. Each polymer considered has differing requirements for storage and handling, and additional consideration was paid to the material source with subsequent effect on

material reliability. The handling particulars for each polymer are summarised in Table 2.3. In this work, the key criteria for efficient production during the spin coating stage included easy availability of ink from stock solution, ease of deposition by pipette to the substrate, acceptable coating efficacy and an adhesion improvement of the GO film compared to the GO/None model.

Table 2.3: Comparison of production considerations for polymer undercoats

Polymer	Stock @20°C	Storage	Source
Gelatine	Solid	Room Temperature	Bovine/porcine Collagen
Polyethyleminine (PEI)	Viscous Liquid	Room Temperature	Synthetic
Poly-l-Lysine (PLL)	Liquid	Frozen -20°C	Bacterial Fermentation

Following production of 80 useful samples, 60 with an undercoat, it was noted that the discard rates seen in Table 2.4 were lower for PEI and PLL than for gelatine. For GO films prepared with an undercoating polymer, incomplete coverage resulting from uneven ink deposition was the most common cause of sample loss during production. For GO/None, replacement samples were required following detachment of the GO from the glass surface during sterilisation.

Table 2.4: Comparison of acceptance failures for polymer undercoats

Polymer	Successful coats	Total coats	Failure mode
Gelatine	20	27	Incomplete coverage (6), Handling error(1)
Polyethyleminine (PEI)	20	21	Incomplete coverage (1)
Poly-l-Lysine (PLL)	20	21	Incomplete coverage(1)
None	20	40	Detachment during sterilisation(20)

In this optimisation the following observations were made; poly-lysine was stored frozen and required defrosting prior to spin coating. PLL also had the shortest useable lifetime. Similarly gelatin required heating prior to spin coating to melt the polymer and decrease its viscosity. Furthermore as gelatin is thermo-sensitive, it provided the weak-

est bond between GO film and glass and could detach in culture conditions similar to GO/None. PEI, provided both the most convenient handling characteristics requiring no specific storage conditions or steps besides dilution to prepare ink from the stock solution. Additionally, as a synthetic molecule comprising a short repeating monomer, consistent molecular weights and branching options are available from several manufacturers. Finally PEI presented the lowest chance for harbouring or introducing microbiological contamination to the model [279]. Therefore for the majority of subsequent work, PEI undercoats were used following a validation of the biological compatibility within the model.

Chapter 3

Characterisation of GO Films

3.1 Introduction

In this thesis it was important to comprehend the physical properties of the 2D GO thin film model as prepared by spin coating. Spin coating as a manufacturing process is has several variables including, spin speed, initial solution evaporation rate, solution viscosity and shear thinning behaviour therefore spin coater settings to create films consistently were determined experimentally. Additionally, it was important to characterise the chemistry of the commercial GO material and film construction. By understanding the model construction and chemistry, these attributes could be used to later contextualise results from cell culture.

In this work we examined how changing the spin coating speed conditions and how changing the GO suspension concentration used to create the film model resulted in variation of the GO film thickness and structure. GO films were initially detected visually without aid of a microscope; the films were visible as a grey-brown yet transparent colouration on the transparent clear glass surface. Compared to the uncoated glass surface of the substrate, the GO film was less reflective to incident light resulting in a less lustrous appearance. The film was resistant to touch but could be removed by abrasion by a sharp

or hard object such as needles or tweezers without scratching the glass. To explore this film structure in more detail, first, the thickness, structure and appearance have been characterised with SEM. Both planar and cross section views of the model were acquired to visualise the micrometre to nanometre scale features. The cross section images were used to measure the thickness of the GO film and thus derive the number of GO layers within the film. Additionally the film surface topography was qualitatively assessed.

Next, films were examined under phase contrast microscopy to see how this film structure appeared through the microscope, as microscopy images are a key source of data in later chapters. Subsequently films were characterised using Raman spectroscopy illustrate the chemical structure by examining the spectral fingerprint created by different vibration states within the molecular bonds. This was used to justify the surface chemistry present on the GO film model, including the purity of the surface and detect if the substrate was exposed.

Finally, to further investigate the chemical structure of the GO film and then any changes to the film surface resulting from use as a cell culture substrate, a set of samples was prepared and investigated with near-ambient pressure x-ray photon spectroscopy (XPS). XPS measures the excitation emission spectra of chemical bonds following exposure to high energy x-rays. In addition by using near-ambient pressure XPS (NAP-XPS) this work presented the unique opportunity to acquire spectra from intact cell cultures.

The aim of the research presented here was to characterise the GO film model structure and surface chemistry. This developed to include an aim to detect the way in which the film surface and surface chemistry could interact with a cell culture environment. This would then inform what characteristics might have an affect on a cell culture in later chapters.

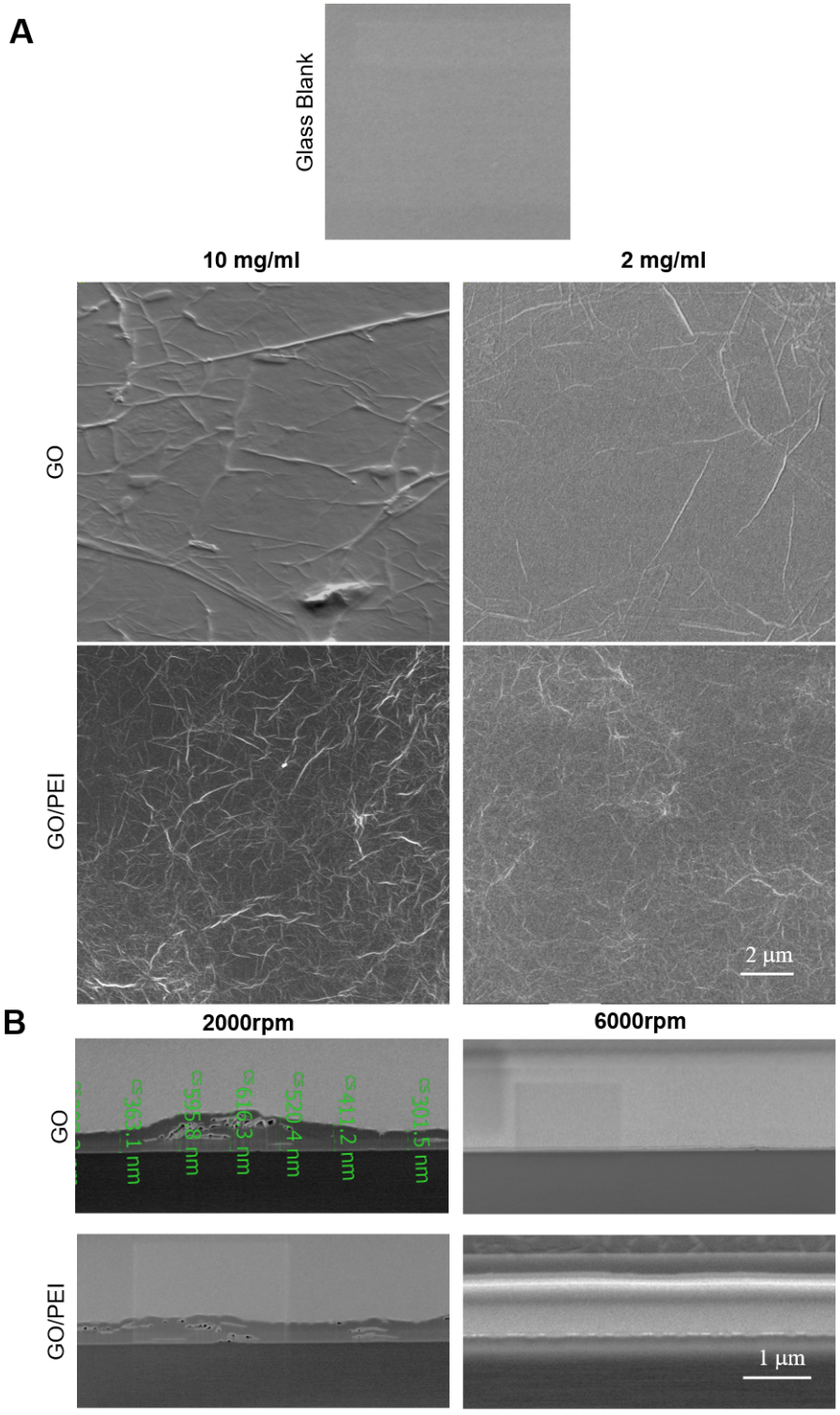
A
Glass Blank
10 mg/ml
2 mg/ml
GO
GO/PEI
2 µm
B
2000rpm
6000rpm
GO
GO/PEI
1 µm

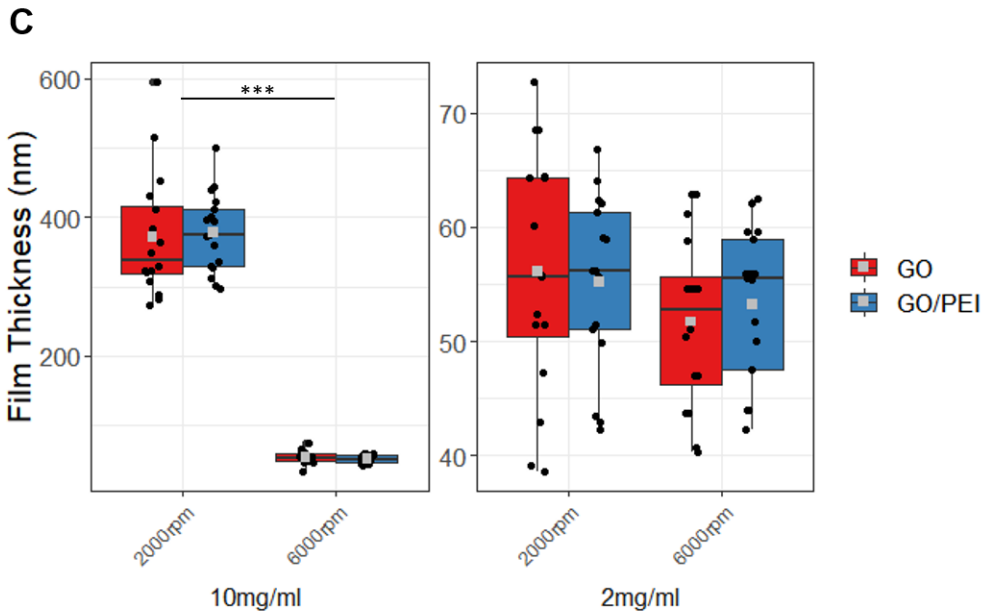

Figure 3.1 | **Scanning Electron Microscopy of GO films.** (A) Plan view images of bare glass substrate, GO film on bare glass, and GO film on PEI coated glass. Films were created at 6000rpm from 10 mg/ml or 2 mg/ml GO suspension, respectively. (B) Representative cross section images of GO film following ion beam milling showing 10mg/ml GO suspension films on bare glass or PEI coated glass, spin coated at 2000 rpm or 6000 rpm respectively. Green annotations are example measurements. (C) Mean (grey point), Range (box and whisker), and Distribution (jitter points) of film thickness measured from cross sections in n = 3 samples for GO and n = 3 samples for GO/PEI. *** $p < 0.001$

3.2 Results

3.2.1 Planar and cross-section SEM

By examining the the film with electron microscopy, the way in which the GO platelets assembled during different spin coating conditions could be observed. The cross section was investigated to describe the physical parameters of the GO film, including how thin the ‘thin film‘ actually measured. Additionally, films on each substrate were compared to see if any difference in film thickness or morphology was introduced by the PEI undercoat.

Planar topography and cross-section thickness were investigated using Electron Microscopy (Fig 3.1), as described in Section 2.5.2. To investigate how the GO film was constructed, films were created with different GO suspension concentrations and spin

conditions; The GO suspension was used at either the working concentration of 2mg/ml or as the stock concentration of 10mg/ml. The expectation was that the higher concentration of GO would lead to a thicker film. Additionally the spin speed of the spin coater was adjusted to either 2000rpm or 6000rpm as indicated. The lower spin speed was expected to produce a thicker film than the higher speed.

In Figure 3.1(A) the creation of GO films was shown to create a surface with noticeable topographical texture in comparison to the smooth featureless glass substrate. These features comprise small wrinkles or folds, the result of layering and folding of individual GO platelets (lateral dimension 3-5μm). The wrinkles in the GO films created from either concentration of suspension were smaller, shorter, less linear and more frequent in films on the PEI coated substrate compared to the bare glass substrate. There is no pattern or geometry to the features indicative of a random consistent deposition pattern consistent with the theory presented in Figure 2.2 and the organic polygonal shapes seen in Figure 2.1.

In Figure 3.1(B) the cross-section differences between films created from 10mg/ml GO suspension at both spin speeds is presented. The GO films made at 2000rpm produced a substantially thicker, more disorganised film, with voids and inclusions within the film. These features had no defined structure, and measured up to 5nm in major axis. In comparison the GO films made at 6000rpm produced an even and consistent layer with no visible features in cross section. The thick 2000rpm film had a more rough appearance and a less consistent structure compared to the thin 6000rpm film. There was no regularity to the features, which again suggests a random deposition during spin coating.

In Figure 3.1(C) these film thickness differences separated by GO concentration (mg/ml) at both spin coater speeds (rpm) are quantified and summarised. With 2mg/ml GO in suspension the films are consistently thin and statistically similar. At 2000rpm films measure 56±11nm (Mean±SD) and 55±8nm on bare glass and on PEI coated glass respectively. At 6000rpm films measure 52±8nm (Mean±SD) and 53±7nm on bare glass and on PEI coated glass respectively. With 10mg/ml GO in suspension the films are

significantly different when comparing between spin speeds ($p<0.001$). At 2000rpm the film is less consistent, increasing in thickness to 372±90nm and 378±56nm on bare glass and on PEI coated glass respectively. This is compared to films created at 6000rpm, which measure 54±10nm and 52±6nm on bare glass and on PEI coated glass respectively, and are similar to films created with the lower 2mg/ml GO suspension. Furthermore at 10mg/ml the interquartile range of measurements is increased tenfold from approximately ±10nm to ±100nm.

3.2.2 Characterisation of chemistry by Raman spectra

The GO film model was inspected to visually characterise the surface in more representative conditions to which it would be used used in later chapters than SEM. If the films had any visible common topography, or that the features seen in the SEM images were also visible with light microscopy that could be considered as a factor in later chapters. Furthermore in quantifying the raman spectra, the surface chemistry of the film could be elucidated. This would provide validation that the PEI undercoat was not present at the surface of the film, therefore the manufacturing method in Section 2.2.1 was reliably producing a GO film on PEI coated substrates.

The visible features of the film were simply imaged using phase contrast microscopy. For collection of Raman spectra as per Section 2.5.1, three batches totalling 72 individual films were prepared as per Section 2.2.1. Spectra were acquired from 5 random areas of each film providing a high degree of confidence that the surface was consistent. Finally, the peaks in spectra were identified positionally and the peak structure compared to a existing characterisation of the constituent materials.

Under phase contrast microscopy, GO films appeared as a rough and dark surface compared to the bare glass (Figure 3.2(A)). The features are dissimilar to the lines and creases resolved in SEM images and appear rounded at this scale. Similar to the planar view seen in SEM images, the GO film surface features do not have any regular or consistent pattern to the visible features. This is continuous with earlier results indicating

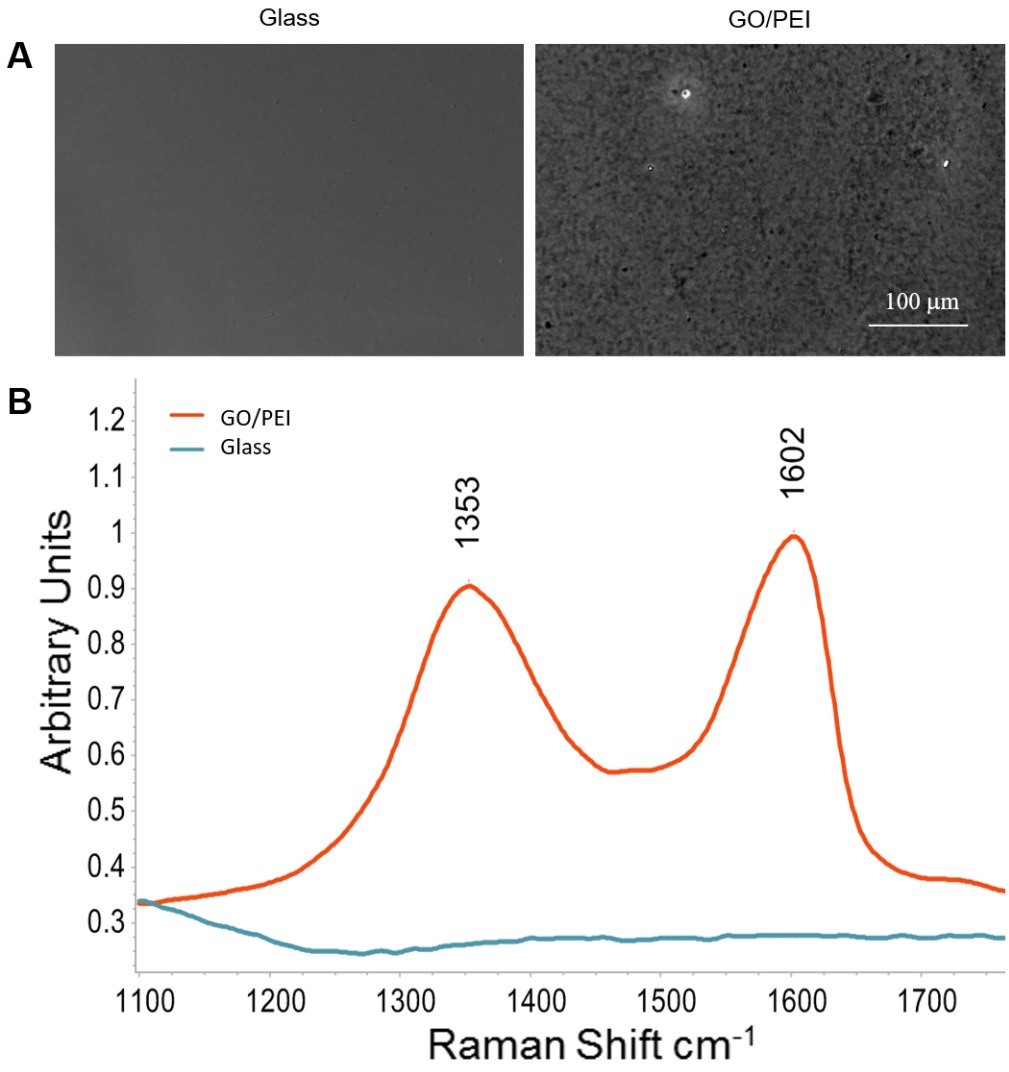

Figure 3.2 | **Representative microscopy and Raman shift of GO film.** (A) Plan view phase contrast images of Glass substrate and GO film surface (B) Mean Raman spectra of GO film (red line) with peaks at 1353cm-1 and 1602cm-1 marked compared to glass blank substrate (blue line) with no defined peaks. Mean of 5 random locations from each of 72 individual films and 24 individual glass coverslips from n = 3 independent preparations

the model film is randomly rough compared to the bare glass surface, without structure or organisation. The Raman spectra of three batches of GO films (Figure 3.2(B)), shows two peaks were detected; the first a distinctive D band peak at 1353cm^{-1} characteristic of the disordered oxygen containing species on the GO surface and the second G band peak at 1600cm^{-1} is typical of graphitic material, attributed to the sp_2 C-C bonds. These peaks were detected across all locations of the GO film.

3.2.3 Quantification of atomic ratio by XPS

To understand the surface chemistry of the GO film model, and to begin to investigate how the surface changes when exposed to cell culture, NAP-XPS survey spectra were used to characterise the atomic concentration. NAP-XPS is different from traditional XPS as it can be conducted in an atmosphere rather than a vacuum within the sample chamber, including humid conditions. In this way, not only was the opportunity to examine the GO film with XPS available, but novel examination of SH-SY5Y cells with XPS.

NAP-XPS does not require total vacuum which would dry and crystallise molecules changing the surface chemistry, NAP-XPS spectra therefore present measurement of surface chemistry more similar to biological conditions. Spectra from a confluent layer of SH-SY5Y cells after 14 days in vitro (Cells Confluent), or a sparse layer of SH-SY5Y cells after 14 days in vitro (Cells Sparse) were also collected. Finally spectra were collected from duplicate Cells Confluent preparations which had subsequently treated with trypsin for 30 minutes (Removed Confluent) and a duplicate Cells Sparse sample also treated with trypsin for 30 minutes (Removed Sparse). These spectra were collected to highlight any changes to the GO film surface chemistry without the cell structures present. For comparison of opportunistic carbon, spectra collected from a blank glass cover slip were also included. All spectra were collected in the same (11mb H_2O) atmospheric conditions. For all preparations, oxygen, carbon and nitrogen peaks were expected, with the differences in the atomic ratio of these components providing insight into the present chemistry.

XPS survey spectra for the experimental set of Graphene oxide thin films are illustrated

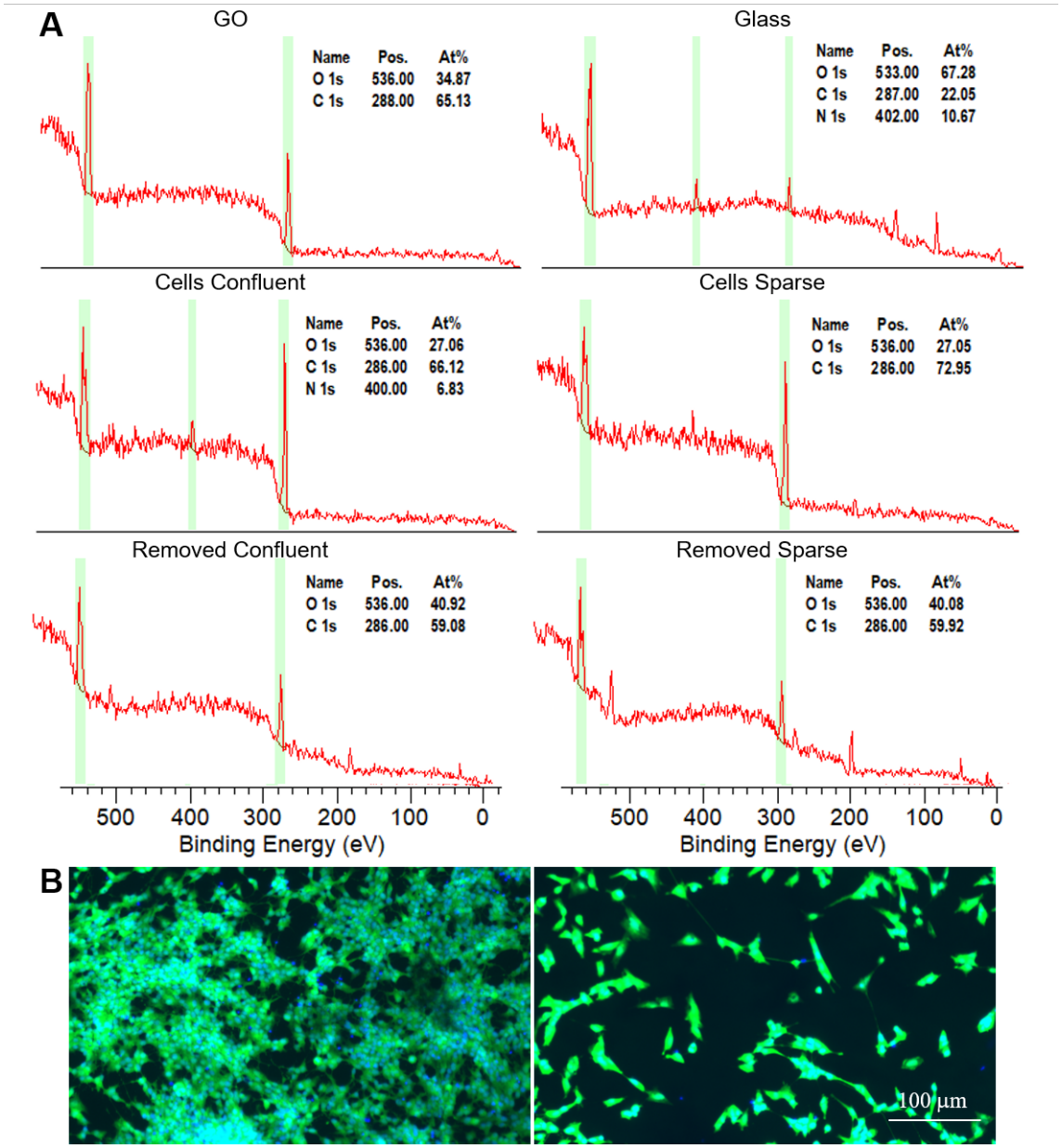
A
GO
Name Pos. At%
O 1s 536.00 34.87
C 1s 288.00 65.13
Glass
Name Pos. At%
O 1s 533.00 67.28
C 1s 287.00 22.05
N 1s 402.00 10.67
Cells Confluent
Name Pos. At%
O 1s 536.00 27.06
C 1s 286.00 66.12
N 1s 400.00 6.83
Cells Sparse
Name Pos. At%
O 1s 536.00 27.05
C 1s 286.00 72.95
Removed Confluent
Name Pos. At%
O 1s 536.00 40.92
C 1s 286.00 59.08
Removed Sparse
Name Pos. At%
O 1s 536.00 40.08
C 1s 286.00 59.92
500 400 300 200 100 0
Binding Energy (eV)
B
100 µm

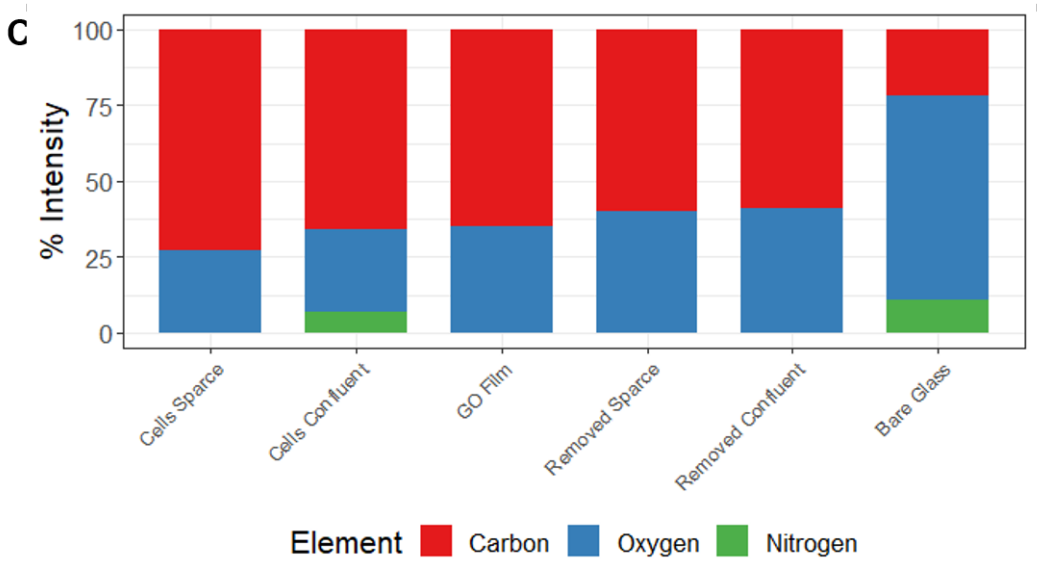

Figure 3.3 | **XPS Survey Spectra of GO films and GO films from cell culture.** (A) Survey spectra conducted at Near Ambient Pressure (11mb H2O) of GO/PEI film, Bare Glass substrate, GO/PEI film with a confluent layer of cells, GO/PEI film with a sparse layer of cells, GO/PEI film following enzyme removal of a confluent layer of cells and GO/PEI film following enzyme removal of a sparse layer of cells. Individual film used for each spectra, collected over 60 passes with dwell time 0.1s, step size 1eV, pass energy 100eV. (B) Representative fluorescence images of Confluent and Sparse layer of cells at 14 days in standard medium stained with Calcien AM (Green) and Hochest (Blue). (C) Relative percentage intensity of survey spectra peaks arranged in order of decreasing carbon signal.

in Figure 3.3(A). All survey spectra have similar distinctive peaks for carbon and oxygen, highlighted on each survey. Carbon peaks are detected at 286eV, with oxygen peaks at 536eV. A nitrogen peak at 400eV is resolved in both the glass blank and cells confluent spectra but is not resolved elsewhere. There is a suggestion of a nitrogen peak in the spectra of sparse SH-SY5Y, however this peak was not sufficient to meaningfully resolve from the background during analysis. The inconsistency of a defined nitrogen peak indicates the nitrogen emission was at the limit of detection in the NAP humid atmosphere. In the high signal density of confluent SH-SY5Y cells and the low total signal intensity of bare glass, the nitrogen peak is resolved. In confluent SH-SY5Y this is due to the higher protein density, whilst on bare glass the nitrogen element must inevitably be supplied by the aliphatic contamination signal.

Figure 3.3(B) demonstrates the difference between cell culture conditions. The con-

fluent SH-SY5Y cell layer (Left image) presented 79.2±2.6% (Mean±SD) coverage of cell bodies at the surface. By contrast the sparse SH-SY5Y cell layer (Right image) presented 15.6±4.3% coverage of cell bodies at the surface. This represents a 5 fold increase in cell coverage in the Confluent condition compared to the Sparse condition. In the removed conditions, the cell coverage is 0%. These differences in cell coverage are detected as differences in atomic percentage.

Figure 3.3(C) summarises the atomic percentage of each element within the spectra. The adventitious carbon on bare glass has a carbon to oxygen ratio of 0.32, this indicates a higher amount of oxygen compared to carbon. This is consistent with the understanding of aliphatic, short hydrocarbon chain contamination from the atmosphere. The presence of a nitrogen component to this spectra indicates that some of this aliphatic contamination has nitrogen containing groups, indicating this contamination most likely originates from airborne pollution.

GO films have a higher carbon content with a 1.86 carbon:oxygen, this can be attributed to the presence of the carbon lattice with oxygen containing groups. For SH-SY5Y surfaces the carbon content is increased relative to the aliphatic background and the GO film, with a carbon:oxygen ratio of 2.44 with confluent cells and 2.66 for sparse cells. The increased carbon content can be attributed to the presence and detection of organic carbon chain at the surface and within cells which are not highly oxidised such as proteins, polysaccharides and lipids. There is more oxygen per carbon in the cells confluent condition compared to the cells sparse condition. This is due to the presence of hydrophilic oxygen containing end groups in the greater area of phospholipid membrane. Following enzymatic removal of cells the carbon:oxygen ratio is consistently 1.48, below the ratio of GO films. This indicates that the oxygen content of the surface is higher following the enzymatic digestion of the cell culture. This is attributed to trypsin protease resulting in exposure of additional oxygen species from hydrolysed peptide bonds.

3.2.4 Characterisation of chemistry by XPS spectra

Table 3.1: Corrected Component Peak Intensity Fig 3.4 (RSF*CPS/eV)

Spectra	C-O	C=O	sp3	sp2	O2	C-O(Aliphatic)	H2O
O1s	23.3	1.7	-	-	1.7	2.9	18.8
C1s	35.0	10.2	19.3	19.7	-	-	-

XPS data from GO preparations have commonly been analysed to indicate the binding groups present within the GO platelets. Fitting expected peak distances based on predicted binding groups and model compounds by method analysis has been previously reported as useful for NAP-XPS [280]. In this work, component spectra for GO were assembled based on previously reported component positions in spectra of GO and rGO [103]. This work explored the chemical states of carbon and oxygen which form the substance of the GO film..

Oxygen specific spectra were collected between 528 and 238 electron volts, following charge correction Fitting of O1s spectra peak models is an interpretive process, within the O1s spectra the peak is broad and several possible oxygen binding states are very close in (eV). Carbon specific spectra were collected between 282 and 291 electron volts, following charge correction. The C1s spectra peak models were constructed and constrained based on position relative to the first sp_2 (lowest energy) component.

High resolution O1s and C1s spectra for the GO film are presented in Figure 3.4(A-B). The O1s spectra (Fig 3.4(A)) shows two distinct peaks at 532.09 and 534.47eV. The higher eV peak is mainly comprised of a strong water oxygen peak and oxygen gas peak from the NAP atmosphere at the surface. The lower peak is dominated by the aromatic C-O bonding peak consistent with the expected structure of GO featuring extensive epoxide bonding. A second component of C-O from linear carbon is also present at 530eV. This is suggestive of the aliphatic carbon component. Consistent with the expected structure of GO, the C-O aromatic bonding is the most prominent non-atmospheric component in this spectra.

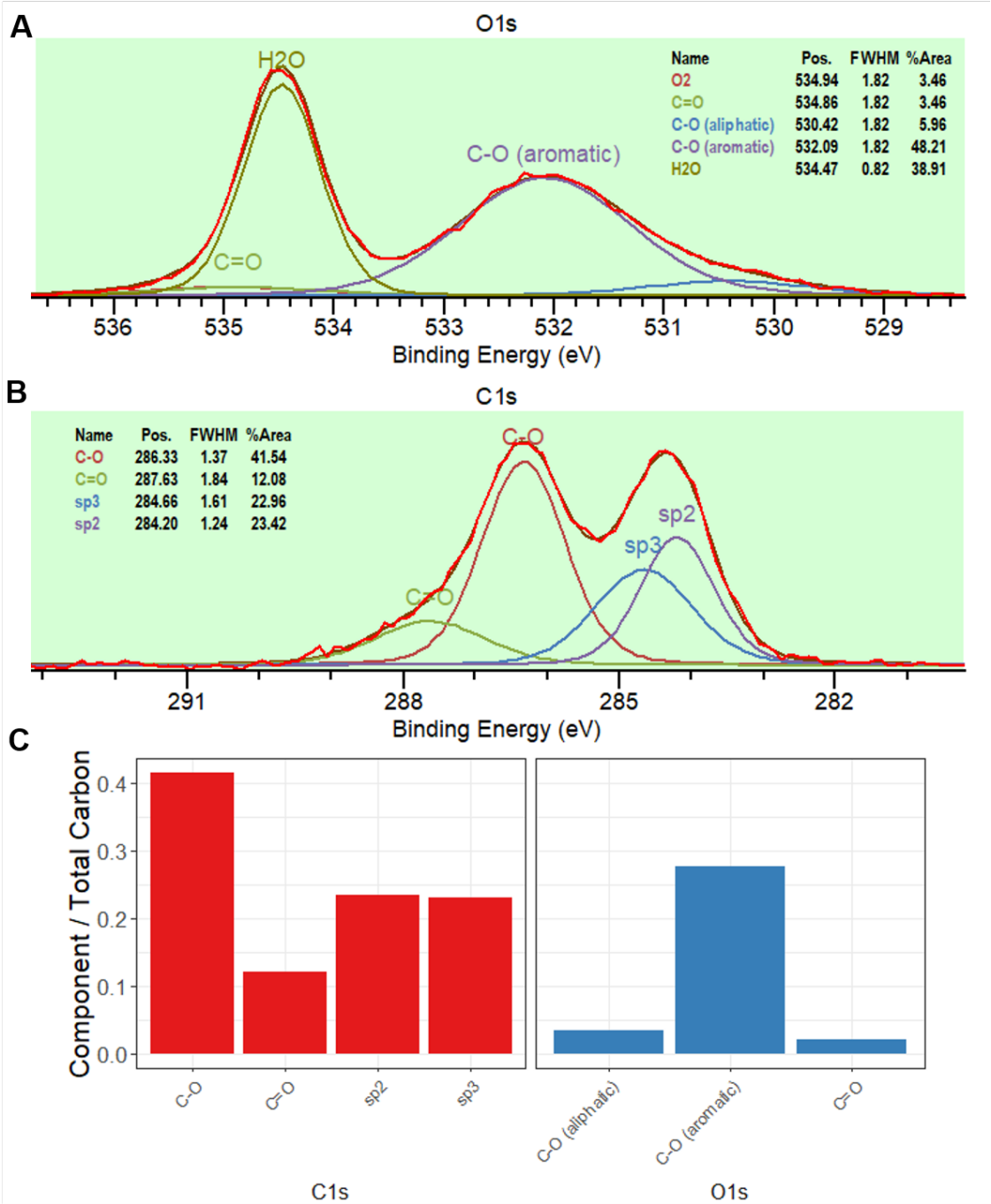

Figure 3.4 | **High resolution O1s and C1s spectra of GO film.** (A) Quantified O1s peak spectra with fit component peak model for GO film showing identified component peaks based on position. (B) Quantified C1s peak spectra with fit component peak model for GO film showing identified component peaks based on position. (C) Graph to show each component in A-B as a ratio of the total carbon signal. Spectra collected over 60 passes with dwell time 0.25s, step size 0.1eV, pass energy 50eV. Peak models fit to within ± 1 residual standard deviation using Tougaard background estimation.

The C1s spectra is illustrative of the GO carbon structure (Fig 3.4(B)). Here a doublet peak is found to comprise four component groups consistent with previously reported characterisation of GO. The carbon sp_2 component is found at 284.2 with the sp_3 located 0.46eV higher. This sp_3 is lower in binding energy than expected according to previous reports. Here this discrepancy is attributed to a reduction in binding energy caused by surface moisture when comparing to high vacuum experiments. Particularly the sp_3 component is broader than the sp_2 component with a larger full-width-half-maximum. This is because the sp_3 component includes all tetragonally bonded carbon which can encompass a wider range of possible bonds between carbon, oxygen and hydrogen, whilst the sp_2 component describes only planar bonded carbon-carbon. Of note, in this GO film preparation, the relative ratio of sp_2 (Carbon lattice) and sp_3 (Defect Carbon) bonded carbon as a proportion of the total carbon signal is nearly identical (Fig 3.4(C) C1s). This indicates that the GO film material is evenly comprised of lattice carbon and carbon defects consistent with high quality GO.

The positions of the C-O and C=O components are as expected at 2.1 and 3.3 eV higher than the sp_2 component. The largest component is the C-O group, and comprises nearly half of the total carbon signal. A C=O component from carboxylic acid is completes the bonding group and is responsible for the asymmetric tail region of the C-O component. Table 3.1 provides the corrected peak intensities for the component peaks in Figure 3.4, thus the quantities of each group are tabulated.

3.2.5 Characterisation of surface chemistry following cell culture

Table 3.2: Corrected Component Peak Intensity Fig 3.5 (RSF*CPS/eV)

Surface	C1	C2	C3	C4
Cells Confluent	59.4	13.5	8.4	1.2
Cells Sparse	46.9	18.1	9.2	3.0
Removed Confluent	38.8	20.9	7.4	2.0
Removed Sparse	35.6	21.7	8.6	2.6

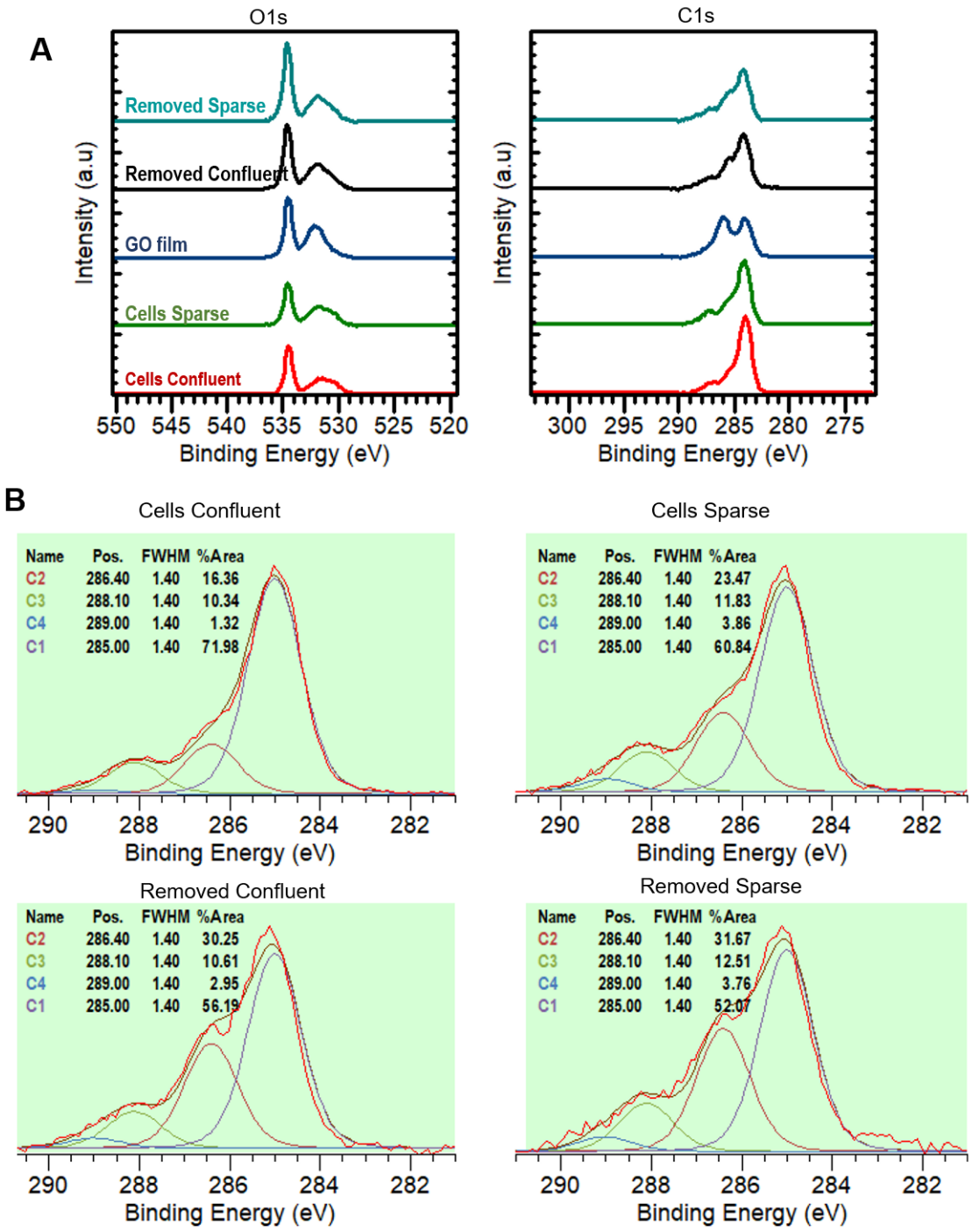
A
O1s
C1s
Removed Sparse
Removed Confluent
GO film
Cells Sparse
Cells Confluent
Intensity (a.u)
550 545 540 535 530 525 520
300 295 290 285 280 275
Binding Energy (eV)
B
Cells Confluent
Name Pos. FWHM %Area
C2 286.40 1.40 16.36
C3 288.10 1.40 10.34
C4 289.00 1.40 1.32
C1 285.00 1.40 71.98
Cells Sparse
Name Pos. FWHM %Area
C2 286.40 1.40 23.47
C3 288.10 1.40 11.83
C4 289.00 1.40 3.86
C1 285.00 1.40 60.84
Removed Confluent
Name Pos. FWHM %Area
C2 286.40 1.40 30.25
C3 288.10 1.40 10.61
C4 289.00 1.40 2.95
C1 285.00 1.40 56.19
Removed Sparse
Name Pos. FWHM %Area
C2 286.40 1.40 31.67
C3 288.10 1.40 12.51
C4 289.00 1.40 3.76
C1 285.00 1.40 52.07
290 288 286 284 282
Binding Energy (eV)

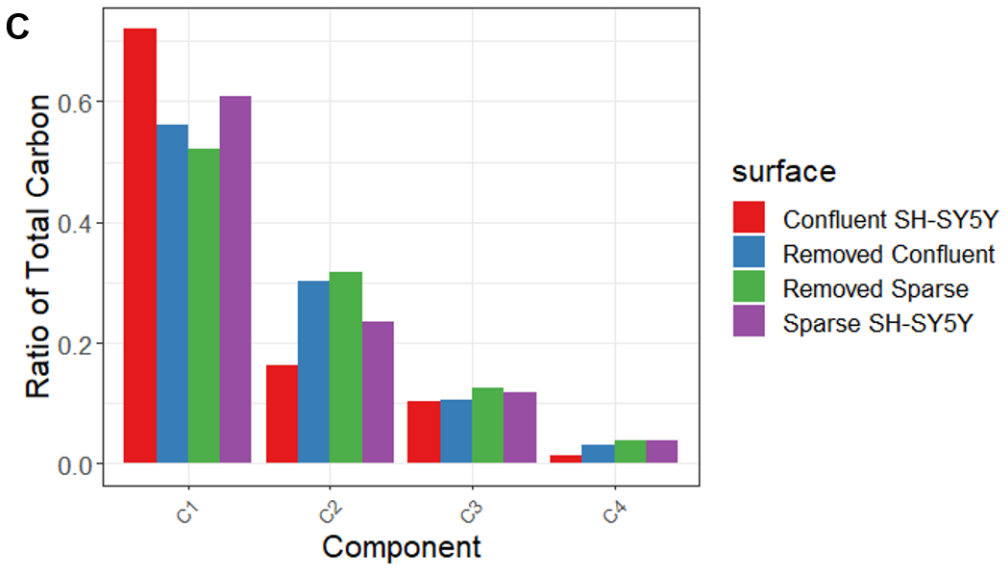

Figure 3.5 | **XPS High Resolution C1s Spectra of GO films from cell culture .** (A) Relative intensity peak shapes for O1s and C1s spectra collected from the indicated samples. GO film spectra (Blue line) included for reference. Individual film used for each spectra, collected over 60 passes with dwell time 0.25s, step size 0.1ev, pass energy 50ev. (B) Quantified peak spectra for each of the indicated samples with fit component peak models showing raw peak area. Peak model fit to within ś 1 residual standard deviation using Tougaard background estimation. (C) Component peaks expressed as a ratio of the total carbon signal for each surface as indicated.

Table 3.3: Attribution of Fig 3.5 component peaks according to their position in binding energy (eV)

Component	Binding energy (eV)	Binding Groups	Proposed source
C1	285	Linear Carbon Chains (sp_3)	Unsaturated lipid chains
C2	286.4	Single Bound Carbon (C-O, C-N)	Proteins
C3	288.1	Double Bound Carbon (C=O, O=C-N, O-C-O)	Amino groups
C4	289	Complex Bound Carbon ([C=O]-O-R, R=C)	Carboxylic acid, Ester bonds

This work aimed to characterise the molecular structure of SH-SY5Y cell surface or ex-cell culture trypsin digested surfaces in a similar manner to characterisation of the GO film. The spectra of each surface was again de-convoluted into a set of artificial component peaks representing of likely chemical components. Differences in these ratios would provide insight into how the surfaces differ in carbon bonding states. Furthermore this work provided the novel opportunity to explore the complexity of the C1s spectra of intact SH-SY5Y cells.

Carbon specific spectra were collected between 282 and 291 electron volts, following charge correction. A total of four component peaks were used to construct the models. The first component (C1), established at 285eV was used as a positional constraint for all subsequent peaks. Using fewer components did not adequately fit these data, whilst more components described unrealistic bonding states. Components were fit according to peak separation [280]. Positions of component peaks were compared against an XPS library to provide a likely identification as listed in Table 3.3 [281].

The shape of the high resolution spectra for both oxygen and carbon normalised for intensity is illustrated in Figure 3.5 (A). The surfaces from cell culture had distinct C1s spectra compared to the GO film, indicating different binding states. Additionally the range of binding energies is marginally narrower in the GO film compared to the cell culture spectra However, the O1s spectra remain similar in shape and range. Furthermore the Cells confluent/sparse, Removed confluent/sparse conditions are similar in C1s shape. Finally the SH-SY5Y surfaces (Cells confluent/sparse) have a higher signal intensity than companion surfaces following cell removal. This furthers the observations made from the survey spectra above in Section 3.2.3 that the cell surfaces contained relatively more carbon.

Figure 3.5(B) shows the high resolution spectra collected for each surface detailed with the component peaks. Table 3.2 provides the corrected peak intensities for the component peak. Figure 3.5(C) quantifies the component peaks as a ratio of their respective total carbon signal in each condition. These data show how the distribution of carbon bonding

states is changed by changes in cell density. The contributions to the C1s spectra from the different biological conditions can be derived with reference to Figure 3.3(B).

Confluent cells have the highest proportion of total carbon supplied by the C1 component. This is due to contribution of linear carbon from the phospholipids of cell membranes and other tetragonal carbon with hydrogen. Component C2 is increased compared to the confluent SH-SY5Y surface once cells are removed with trypsin, suggesting a relative increase in carbon bonded with nitrogen or oxygen within protein is present in the digested surfaces, relatively more than present on the cellular surface. This is also seen in the Sparse SH-SY5Y sample indicating this pattern is indicative of a layer on the GO film rather than a cell component. Conversely the component C3 is approximately equal in all conditions, indicative that amino groups are similarly present in all samples. Similarly component C4 is the lowest in all surfaces, indicating a low proportion of free carboxylic acid groups. Additionally this carboxylic acid component is lower in these biological samples than in the original GO film (Table 3.1).

3.3 Discussion

The present study examined if spin coating could create a thin film model that would be useful for testing GO as a biomaterial. The results of this work indicate that spin coating could create films, contiguous in structure and consistent in thickness. Furthermore the surface created by spin coating with the GO suspension is measurably consistent with the known spectra of GO [282, 283]. In this model, pre-coating the glass substrate with PEI, an enhancement to GO film adhesion, did not result in a detectable change to film thickness increases or surface spectra. The spectra of GO films from SH-SY5Y cell culture conditions have also been observed and characterised, indicating adherence biomolecules to the GO film which resisted washing during sample preparation. This study also presents the first characterisation of the XPS C1s spectra of SH-SY5Y cells in hydrated conditions.

3.3.1 Spin Coating and GO Film Thickness

In agreement with previous research indicating GO surfaces are often topographically featured, GO films have complex surfaces with nanometre scale wrinkles and creases [284]. These features, caused by the folding and creasing of GO platelets in suspension during spin coating, are random in appearance. On PEI coated substrates, the frequency of these features increases while the length decreases compared to the glass substrates (Fig 3.1(A)). The thickness and cross section of the GO film is dependent on manufacturing conditions. Specifically, the films can be created from GO suspension concentrations between 10mg/ml and 2mg/ml, however the spin coater speed must be adjusted to account for the viscosity of the GO suspension. With slow spin coating conditions the film form with a thickness in excess of 500nm with a variability (Fig 3.1(B)). This is explained by the increased density of GO in the suspension at 10mg/ml, compared to the diluted 2mg/ml working solution. As part of spin coating optimisation, it is now known to avoid the combination of slow spin speeds with concentrated GO suspension. Fortunately, both increased spin coater speed and lower concentrations of GO suspension are shown to produce similar films (Fig 3.1(C)) Within this thesis, the 2mg/ml concentration was selected to maximise stock efficiency, combined with the 2000rpm spin coater speed to reduce risk of substrate damage, as specified in Section 2.2.1. Using these optimised ranges manufacture of the 2D GO film model can reliably produce films in under 3 minutes. Comparing the thickness of these films to the reported platelet dimensions (Fig 2.1 suggests the GO films used for the rest of this work have a structure 15 to 20 GO platelets thick.

It is interesting to consider the variation observed in film thickness and morphology; - uniform, thin and homogenous for high speeds or low concentrations compared to variable thickness with inclusions at high suspension concentrations with low speed. In suspension GO platelets are able to move, fold and disperse freely whilst in suspension both before and during the spin coating process. The principle of spin coating is to spin the substrate and use the surface tension of the solvent to drive the suspension laterally, thus also reducing

the vertical volume and concentrate the GO against the surface, drying away the liquid phase in the process via evaporative loss and hydraulic action (Fig 2.2) [285, 274, 104]. During spin coating, if the suspension is not stretched across the substrate due to either insufficient rotational force or increased density of platelets, the liquid phase will become trapped between the layers of GO platelets. This is consistent with known properties of spin coated GO structures being impermeable to liquids [97]. In this case the result was a thick and porous film structure in the 10mg/ml, 2000rpm condition presented here (Fig 3.1(B). Conversely, when the suspension concentration is reduced, a range of spin coating speeds can produce thin and consistent films. High spin coating speed can produce similar films to the low concentration suspension. This indicates an optimal combination exists of suspension concentration and spin speed. Further investigation into this relationship could be used to model the fluid dynamics of GO in H_2O suspension during spin coating. It is reasonable to assume from the observed evidence that a sharp transition exists between overcoming the surface tension for a given suspension concentration. This limit could lead to maximising efficiency of the spin coating process in terms of energy and materials. In this work such an investigation was beyond the scope of this project as materials were plentiful in relation to time, however for a more industrialised process such an optimisation would be desirable.

3.3.2 GO Film Surface Chemistry

The film surface returns Raman scatter spectra consistent with reported GO spectra in literature [286]. In Raman microscopy, laser energy photons are directed at the sample and are inelastically scattered by molecular bonds within the sample, loosing energy in the process. Measurement of the resulting energy shifts of these photons form Raman spectra describing the vibrational and rotational low frequency modes of the bonds within the bulk of a material. GO is an amorphous material within the context of Raman spectroscopy, typically presenting a wide doublet peak comprised of the D-band sp^2 carbon lattice and G-band sp^3 carbon defect shifts [86]. This is in contrast to pristine graphene or

graphite spectra which present single sharp peaks, or reduced graphene oxide which also features higher shift peaks not seen in the present GO film. Raman spectra reported elsewhere have been conducted on powdered samples. This work presented spectra of GO material as a stacked, plasticised thin film thus increasing the conformity of platelets during analysis. This could have the potential to amplify the signal from other bonding states or carbonaceous debris. However this increased order did not reveal any further features within the spectra.

In this work, the D-band peak was detected at 1353cm^{-1} and the G-band peak at 1602cm^{-1} consistent with their reported positions in literature (Fig 3.2(B)). Similarly the ratio of the bands was as expected at $\tilde{0}.9$, featuring a higher signal intensity but a narrower peak shape from the G-band. Previously, this ratio was used to describe the quality of the GO, a measurement of the ratio of defects to the carbon lattice and thus oxygen content. However recently, it is now known that this G-band includes a superposition of two components; the G-band and D'-Band, corresponding to sp_3 carbon structures [287]. Despite this, the absence of other spectral features indicated the surface was graphene oxide. No peak shapes in the Raman shift spectra suggested detection of the polymer indicating the GO provided a functionally opaque layer to the laser photons. No higher peaks such as the 2D-band at Raman shift 2700cm^{-1} or the D+G combination signal at 3000^{-1} reported for materials such as rGO were observed in this work. These results indicate the spin coating and sterilisation methods do not result in a change of the spectra for GO compared to previously reported studies [282].

XPS spectra of the film has been collected and found to be consistent with literature [283]. In XPS x-ray energy photons are directed at the sample and photons are absorbed by electrons within the atomic orbits of elements. This causes electrons which are sufficiently energised to become liberated from the atomic orbit. These electrons retain a signature kinetic energy related to the bonding state from which the electron escaped. In other words, different bonding states of elements and different elements release electrons with different kinetic energies. Elemental survey spectra (Fig 3.3(A)) from GO film revealed

the atomic concentration of carbon and oxygen (C:O Ratio) was 1.86 : 1 similar to reports of high quality graphene oxide produced through Hummers method [92, 283]. This is also consistent with the theoretical oxidised carbon lattice of the Lerf-Klinowski model seen in figure 1.2.

Similarly, in the high resolution spectra of the GO film (Fig 3.4(A-B)) revealed a single O1s peak accompanied by an atmospheric peak and a characteristic GO doublet C1s peak. The spectra were fit to within 1 residual standard deviation with peak models suggesting the presence of at least 4 different carbon bonding states. The bonding states attributed in Table 3.1 included the sp_2 carbon lattice (Component C1), sp_3 carbon defects (Component C2), epoxide carbon-oxygen bonds (Component C3) and carboxylic acid, (Component C4). The ratio of these components indicates the GO film has an even distribution of carbon lattice and carbon defect bonds. These component peaks described a set of bonding states which were consistent with the expected structure of GO from the Lerf-Klinowski model and of high quality GO [91, 92, 283].

Previous XPS characterisation of GO has been conducted on powder, under high vacuum [283]. These spectra were collected from a plasticised thin film under 11mb H_2O atmospheric conditions presenting a more conformal and concentrated platelet arrangement, but a hydrated chemical environment subject to hydrophilic polar hydrogen bonding. Furthermore the information distance - that is the penetration distance of x-rays within this material - is estimated to be 10nm of thickness in these NAP conditions [280]. This is wholly within the measured GO film depth. There was a possibility that these factors would result altered spectra relative to previous powder analysis, such as additional peaks revealed by the hydrated atmosphere exposing previously unseen bonding states. The only difference observed compared to expected spectra is the reduced interposition distance of the sp_2 and sp_3 component peaks.

3.3.3 GO Film Characteristics and Cell culture

Two critical attributes have thus far been described with the potential for the GO film to effect cell culture; The surface is rough when viewed with SEM and phase contrast microscopy, with nano-scale and micro-scale topography derived from inter-platelet folding. This roughness provides an increased surface area relative to flat glass substrates. Chemically, the film surface has a heterogeneous composition including an equal portion of sp_2 and sp_3 carbon bonding states in addition to the expected oxygen functional groups. This chemistry provides both polar and non-polar intermolecular regions suitable for hydrophilic and hydrophobic residues. This indicates the GO film is likely to exhibit adsorption properties, particularly for complex molecules comprising both polar and non polar regions such as protein. Furthermore the roughness suggests the surface will be suited to adhesion of cell culture [288].

3.3.3.1 XPS Characterisation of GO Films After Cell Removal

Data acquired from surfaces which have had cells removed with trypsin and subsequently washed to remove debris reveal the presence of an adhered protein on the GO film. Figure 3.5(B) shows a distinctive pattern of component peaks and peak ratios within the ‘Removed‘ condition spectra consistent with the XPS spectra of vitronectin [289]. Vitronectin is an adhesive molecule known to bond to glass and plastic readily and thus facilitate cell culture, serving as a binding cite for integrins and thus enabling cell adhesion. During seeding of cells to the GO film surface, cells are delivered in a medium containing a 10% v/v foetal bovine serum, which is abundant with vitronectin and a vital part of cell attachment in cell culture [290].

This work showed that vitronectin becomes robustly bonded to the GO film in a layer at least 10nm thick, indicated by the obscuration of the GO peak structure. This layer is not disturbed by cell activity, remaining consistent between ‘Removed Confluent‘ and ‘Removed Sparse‘ conditions. Similarly the vitronectin peak structure is visible in the

'Cells Sparse' condition. The presence of vitronectin layer is not in itself surprising, as vitronectin deposition is an expected part of cell adhesion during cell culture. However the persistence of this layer is interesting, as the vitronectin source was only maintained for a short time during the establishment of the culture. The implication is that the GO film can be passively and simply prepared as an adsorbed substrate for cell culture, which will not be dislodged during prolonged maintenance. The initial aim of this work was to identify how the GO film is altered by cell culture, the data showed the GO film becomes thickly and robustly adsorbed with vitronectin when exposed to standard media.

3.3.3.2 XPS Characterisation of SH-SY5Y Culture

The surface chemistry of cells during XPS will be influenced by hydration and vacuum. Previous work has been previously reported examining e-coli bacterial cells on a silicon substrate using similar NAP-XPS conditions [280]. In that study, the bacterial cell wall and capsule surface chemistry was characterised using NAP-XPS. In their report, Kjaervik et al determined the information depth of the assay to be 10nm, sufficient to capture the entire thickness of a phospholipid bilayer, surface protein and polysaccharide. This may be the first study to perform a similar analysis on the SH-SY5Y neuronal cell line.

In the study by Kjaervik et al, cell membrane structures were described in their NAP spectra based on the changes observed during incremental drying. In the present study, changes in the spectra were induced by altering the amount of the cell coverage. Phospholipids are comprised predominantly of linear carbon chains, lipid bilayers which comprise the cell membrane are approximately 5nm thick. Several of these membranes are present covering the extent of each cell and within reticulum. It is therefore unsurprising to observe that linear carbon content is higher in confluent cells than sparse cells, as the cell coverage is higher. By contrast, components of the spectra corresponding to peptide bonding are similar between cell densities, indicating that though the lipid content is dependent on cell density, the amount of protein remains similar at different densities.

However this work also provides other insights; In previous XPS characterisation of

biological samples, the extracellular environment was not considered, because cells were separately prepared onto an XPS substrate such as silicon independent of cell culture. The GO film in this chapter was used as both the XPS sample surface was also the original adherent cell culture substrate. SH-SY5Y cells and their extracellular environment on GO films have been characterised, showing differences based on cell coverage which relate to the changes in cell membrane coverage, and a vitronectin extracellular environment. Therefore this work has demonstrated a method in which both the extracellular environment and resident cells can be resolved during NAP-XPS. With further development this method could be leveraged to examine changes in extracellular chemistry following biological interventions. Further work to characterise deposited peptide and protein structures would benefit from a systematic protocol of dehydration following NAP measurement [280]. However, because the GO film surface has become coated in a layer of vitronectin, the underlying GO film chemistry could not be resolved. This has limited determination of any changes to the structure of GO by cell culture. To further work in determining if any changes are induced in GO surface chemistry, a protocol to strip deposition from cell culture would be required. This will require overcoming the adsorption forces between the GO film and surface layer.

3.4 Conclusions

GO can be successfully prepared into thin films via spin coating, to 15-20 layers thick with an adhesive polymer undercoat and characterised with a range of spectroscopy. GO films have been characterised, displaying classically expected spectra for carbon and oxygen bonding as reported for high quality graphene with a high level of oxidation and no detectable contaminants. Finally, the GO film can adsorb and become coated in a thick layer of vitronectin during cell culture which remains robustly attached for a prolonged period. This indicates the GO film is likely to adsorb molecules during culture which will result in an enhanced environment compared to non GO surfaces.

Chapter 4

Biocompatibility of Graphene Oxide in a 2D Film Model

4.1 Introduction

In this thesis understanding the biocompatibility of the 2D GO thin film model was an important step for the development of GO as an instructive biomaterial. Previous reports had suggested GO could have cytotoxic [291], nanotoxic [150] and oxidation state dependent effects on cell culture [176]. Other reports were confounded by the application of tertiary coatings to graphenes prior to cell culture, isolating the material from the cellular micro-environment [162]. The last chapter demonstrated that this film model is measurably GO, and interacts with cell culture passively becoming coated in vitronectin. However this does not exclude the possibility of contamination [161], or adsorption and concentration of toxic cell waste at the surface [292].

In this chapter, GO films were used as a substrate for cell culture, and investigate the cell morphology and cell survival on this material. By using GO as the growth substrate without additional coatings as reported elsewhere, this work aims to investigate the biocompatibility of GO, the film model and the surface chemistry in interface with

the cellular micro-environment. Commercial GO stock was used in the 2D film model, therefore there is a risk of contamination from manufacture which would be detected in the present study. The overall aim of this thesis is to investigate GO for potential with neural tissue engineering, thus in this work neural lineage cells were used. These cells included cell lines SH-SY5Y and BV-2, as well as primary wild type mouse and rat neurons, hippocampal tissue co-culture, mouse microglia and astrocytes. Cells were plated and grown on GO films as described in Section 2.4. Fluorescent microscopy imaging of live cells and immunofluorescent imaging of fixed cells was used to record cells as described in Section 2.6.1. Finally the number, viability and morphology of the cell populations on the GO film were quantified as described in Section 2.7. Of particular interest were any morphologies or discrepancies in the cell populations on GO films which differed from paired populations on traditional glass substrates.

The aim of the research presented here was to explore the biocompatibility of the GO film model, and by extension the commercial GO stock. This included identification of any apparent influence of GO on adhered neural cells and the cell culture environment. These outcomes would then provide a basis for further modification of the GO to improve the instructive properties.

4.2 Results

4.2.1 Effects of GO films on SH-SY5Y cell viability

The SH-SY5Y cell line is commonly used as an immortalised model for neuron growth and differentiation. By using this cell line, both the initial biological responses to the GO film model, and model neuron specific responses could be observed and serve as a basis for predicting the responses of primary neurons. Additionally, the SH-SY5Y cell line has an inducible differentiation morphology, which could be subsequently measured to quantify the differentiation response of these cells on the film.

Individual GO films were constructed on glass substrates according to Section 2.2.1,

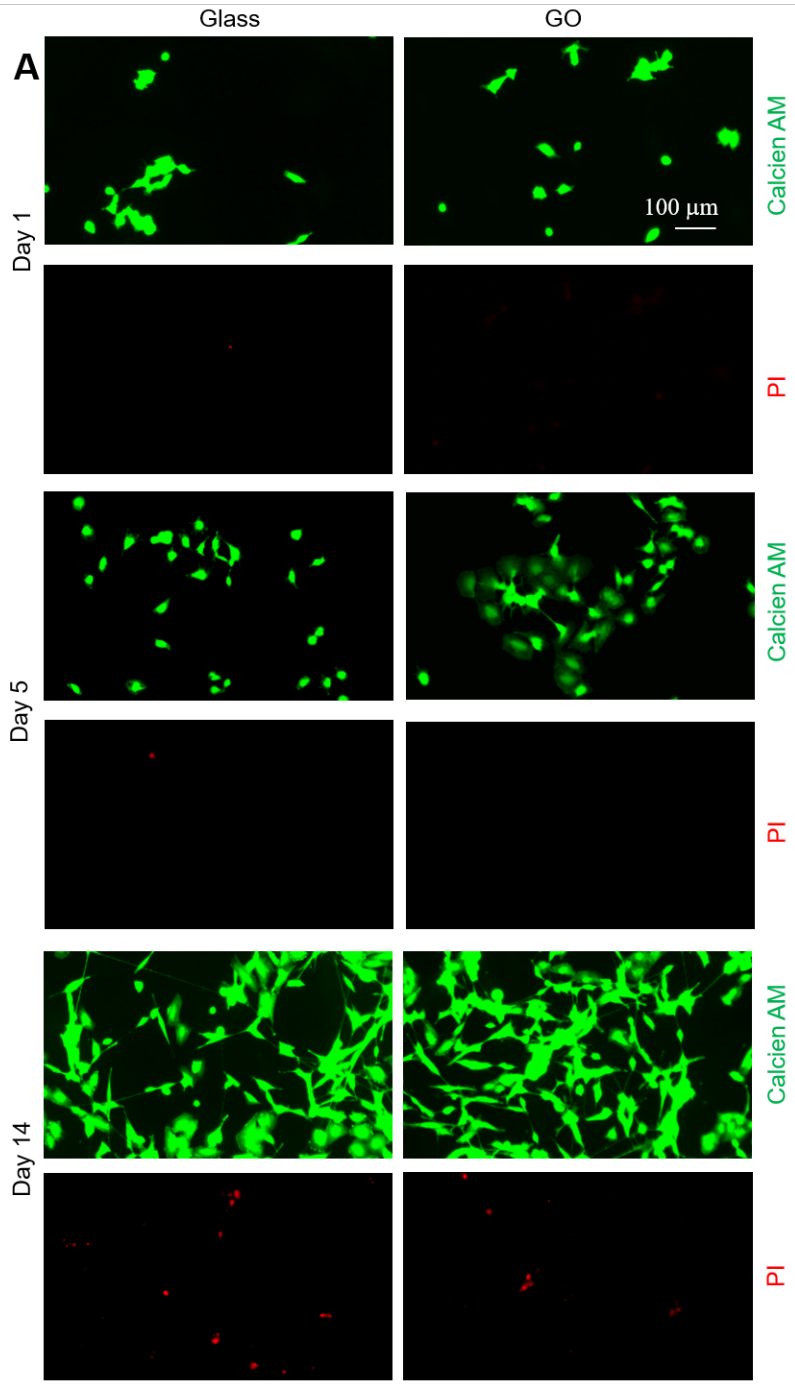
Glass
GO
A
Day 1
Day 5
Day 14
Calcien AM
PI
100 µm

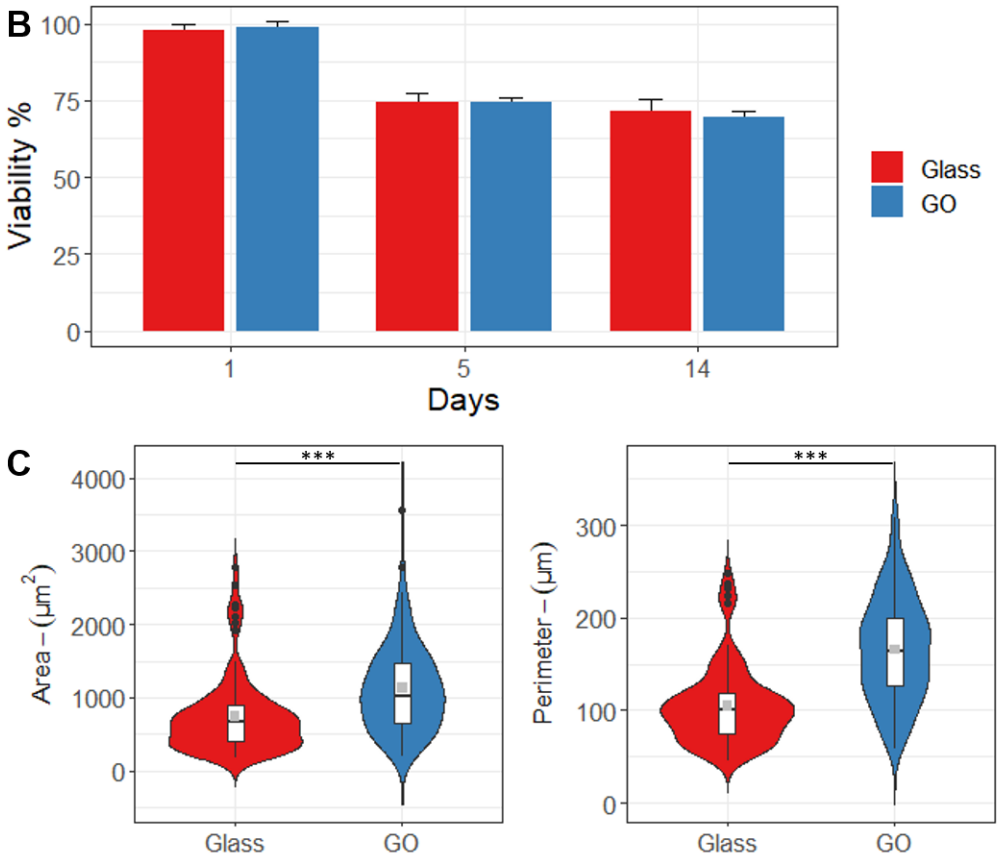

Figure 4.1 | **Effect of GO on SH-SY5Y cell growth and attachment.** (A) Representative fluorescence images showing cells on glass surface or GO film on day 1, day 5 and day 14, respectively, cultured in differentiation medium. Cells were co-stained by calcien-AM (green) and propidium iodide (PI) (red). (B) Mean cell viability under indicated cultured conditions from n = 3 independent cell preparations. (C) Mean (grey point), Range (white box), and Distribution (Violin) of area and perimeter of individual cells under indicated conditions at day 1, 110 cells for glass and 110 cells for GO from n = 3 independent preparations. *** $p < 0.001$

plated and maintained with SH-SY5Y cells according to Section 2.4.1.1. Identical preparations of cells plated to glass substrates without GO films were used as control comparisons. Glass surfaces are commonly used in cell culture as inert substrate. To investigate the viability and appearance of these cells over time, representative samples were taken at each time point and supplemented with Hoechst 33342 (Hoechst), Propidium Iodide (PI) and Calcien-AM (C-AM) to reveal nuclei, nuclei within permeable membranes (otherwise considered dead-cells) and live cell cytoplasm respectively. The GO film was expected to support cell attachment, however a question remained about long term cell survival.

In Figure 4.1(A), images of SH-SY5Y cells at three time points on Glass and GO surfaces are shown to be similar in number, size and shape at all 3 time points. Cells are also similar to expected SH-SY5Y morphology. Initially on day 1 single cells and small clusters of cells with a round morphology are seen staining positive with Calcien-am. By day 5, cells spread apart on the surface, no longer closely clustered, and small neurite like projections were now visible. This is the beginning of the differentiated morphology. By day 14, differentiation had progressed with longer neuritic like extensions visible. Cell bodies have adopted elongated morphologies. At day 14 cell number had also increased on both surfaces, consistent with the expectation that not all cells respond to differentiation media and remain proliferative in both the glass control and GO film condition [293].

In Figure 4.1(B) the percentage viability at each presented time point is shown as determined by the calculation in Section 2.7.1. Cells on glass and GO surfaces had similar viability at all three time points. On day 1 cells had high viability suggesting no immediate cytotoxic effects from the GO film or the control glass surface. Following this time point, cells are maintained in differentiation media as detailed in the protocol in Section 2.4.1.1 By day 5 cells have increased in number, viability has decreased slightly on both surfaces, though remains high. Viability remains consistent between day 5 and day 14, suggesting the decrease in viability can be attributed to the change from standard media to differentiation media after the day 1 time point. Both surfaces showed consistent viability with no significant differences, suggesting no benefit or hindrance by the GO film

surface compared to glass.

Figure 4.1(C) shows the mean area and perimeter determined by particle analysis after Calcien-AM staining of cytoplasm for cells at day 1. This quantitative explores the size of cells following initial attachment, but before differentiation. In n=3 preparations this data shows a significant increase in the overall size of cells on the GO film compared to the glass control. Mean area of cells on GO is 34% larger than cells on glass, similarly mean perimeter of cells on GO is 36% longer than cells on glass. This suggests cells have attached to both surfaces, but cells on the GO surface are spreading out and increasing in planar dimensions faster on GO.

4.2.2 Effects of GO film undercoats on SH-SY5Y cell viability

Early during work with the GO film model, it was observed that the GO film could in some cases become detached from the glass substrate (Figure 4.2(A)). This phenomena was simply replicated by rapidly pipetting liquid onto the film surface several times, simulating the turbulence of repeated media changes. To counter this and improve adhesion between the GO film and the glass substrate, an undercoating method was developed. The method development considerations of this is detailed in Section 2.9. To confirm the biocompatibility of the GO film is not negatively impacted by the addition of this undercoat, and detect any confounding factors introduced by the addition of an undercoat, further biocompatibility tests were conducted with the selection of potential polymers. Identical GO films without undercoats (GO), with Polyethyleminine (GO/PEI) or with alternative Gelatin (GO/Gelatin) or Poly-L-Lysine (GO/PLL) undercoats were prepared.

The undercoating layer was applied by spin coating onto the glass surface before the GO suspension was applied to create PEI, Gelatin or PLL coated substrates. Subsequently the GO film was created on top of these coated substrates. This undercoat reinforces the adhesion between GO and the substrate making for a more robust model which better resists turbulence during maintenance periods and thus is better suited to cell culture. Physical nano-scale and micro-scale differences caused by this improved adhesion between GO

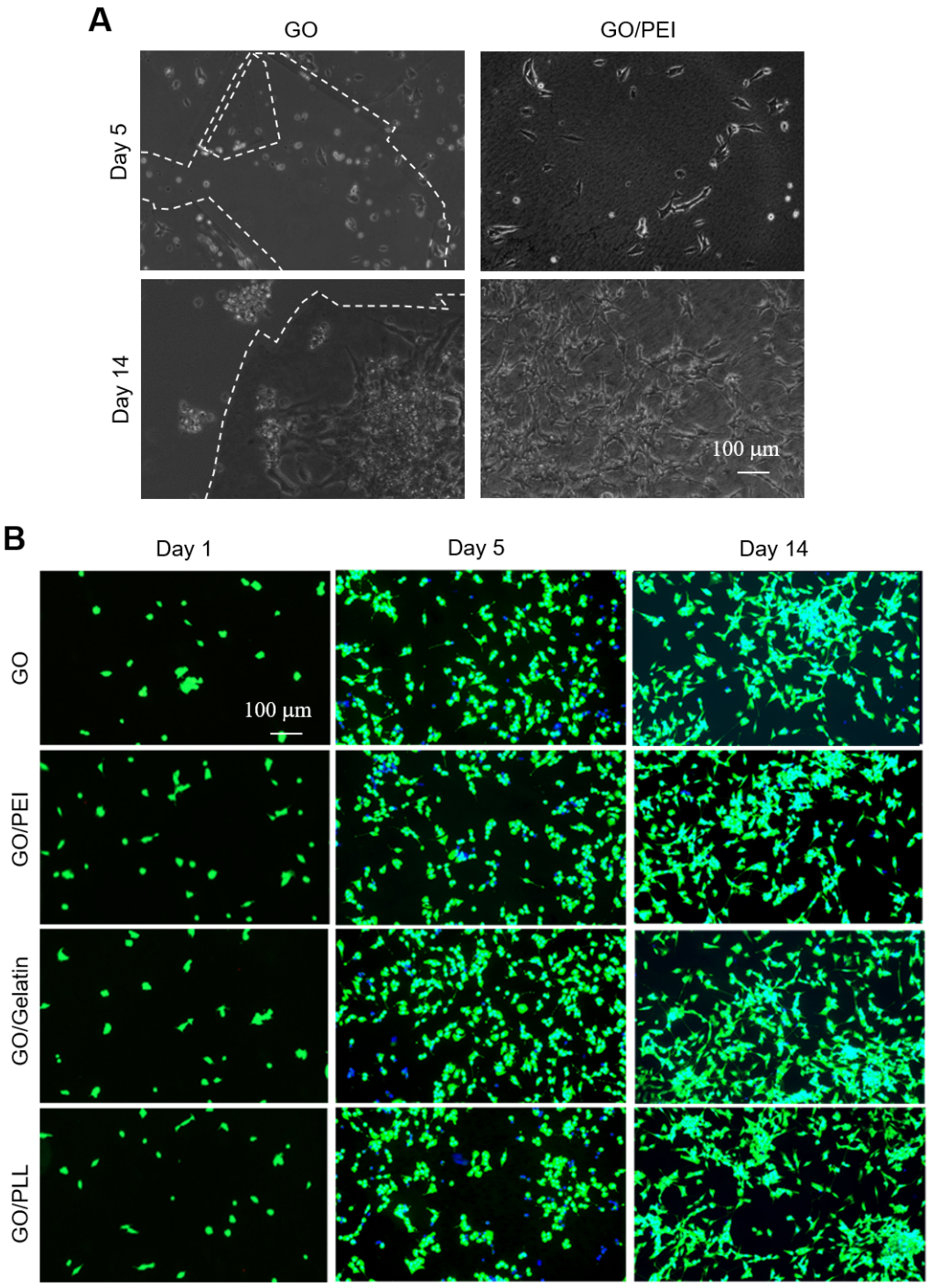
A
GO
GO/PEI
Day 5
Day 14
100 µm
B
Day 1
Day 5
Day 14
GO
GO/PEI
GO/Gelatin
GO/PLL
100 µm

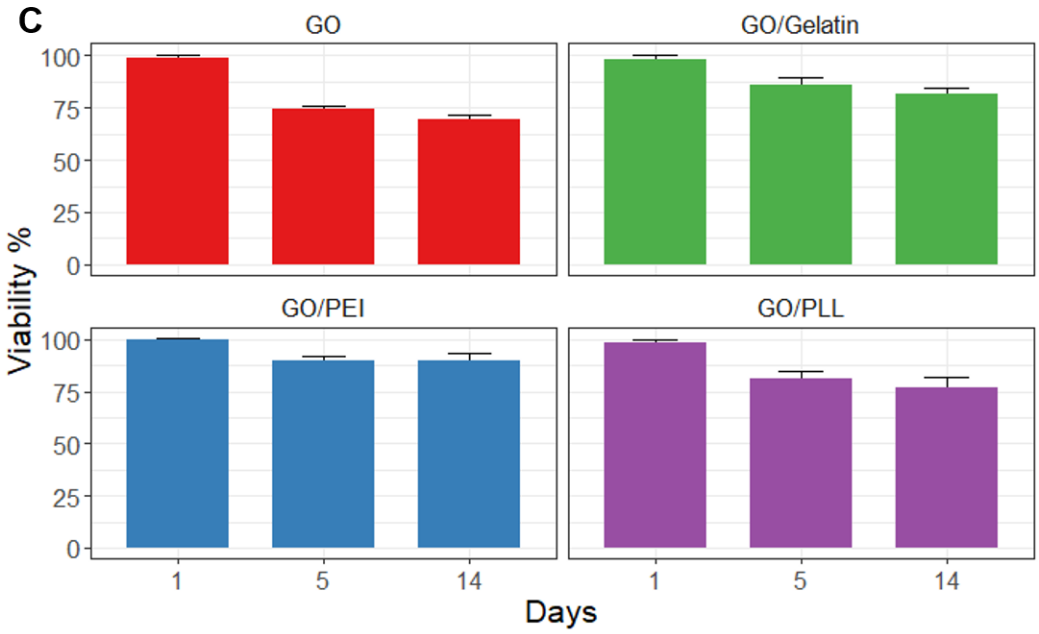

Figure 4.2 | **Effect of GO with different undercoating on SH-SY5Y cell viability.** (A) Demonstrative phase contrast images of cells growing on GO film without (left) or with undercoating polyethyleminine (GO/PEI; right) at 5 and 14 days respectively under differentiation medium. Areas with GO film detached are marked with dashed lines. (B) Representative fluorescence images showing cell growth on GO film without or with undercoatings of polyethyleminine (PEI), Gelatin, or poly-L-lysine (PLL) on day 1, day 5 and day 14 respectively. Cells were co-stained with calcien-AM (green) and Hochest (blue). (C) Mean cell viability under indicated conditions from n = 3 independent preparations.

films without and with undercoating have been explored in Section 3.2.1. No difference was expected in viability between GO films and any undercoated film.

In Figure 4.2(B), representative images of SH-SY5Y cells at 1, 5 and 14 days in differentiation conditions are presented. Cells are seen to be similar in number, size and shape at each time point on each model condition. SH-SY5Y were observed to proliferate over 14 days with differentiation media introduced after day 1 leading to formation of neuritic like structures visible at 5 and 14 days on all models consistent with previous data. In Figure 4.2(C) the mean cell viability over n=3 preparations is presented. No significant difference between undercoats is found in viability of SH-SY5Y cells at any time point. All undercoats sees a small decrease in cell viability over time with no condition performing notably better or worse than any other in these data. Furthermore cells showed no morphological sign of contact cytotoxicity, growth inhibition, apoptosis or stress on any surface combination. This indicated any of the polymers would be biologically suitable for use as an undercoat without negatively impacting cells.

4.2.3 Effects of GO films on SH-SY5Y cell differentiation

When maintained in differentiation media as outlined in Section 2.4.1.1, SH-SY5Y undergo a phenotype change effecting a pseudo-differentiation to a phenotype similar to dopaminergic neurons [293]. To test the progression of this differentiation on the GO film and detect any differences in differentiation response introduced by the GO film surface, SH-SY5Y cells were cultured on glass surfaces compared to the GO film. An additional condition of glass with only the PEI undercoating was included to investigate any influence a surface with improved adhesion would have on differentiation compared to the glass surface and confirm any increase could be attributed to the GO rather than the polymer (Figure 4.3).

This change in phenotype includes growth of neurite-like extensions which stain positively for Tau cytoskeleton components and can be measured from fluorescence images. By measuring the length of these neurites a metric of the progress and success of neurite

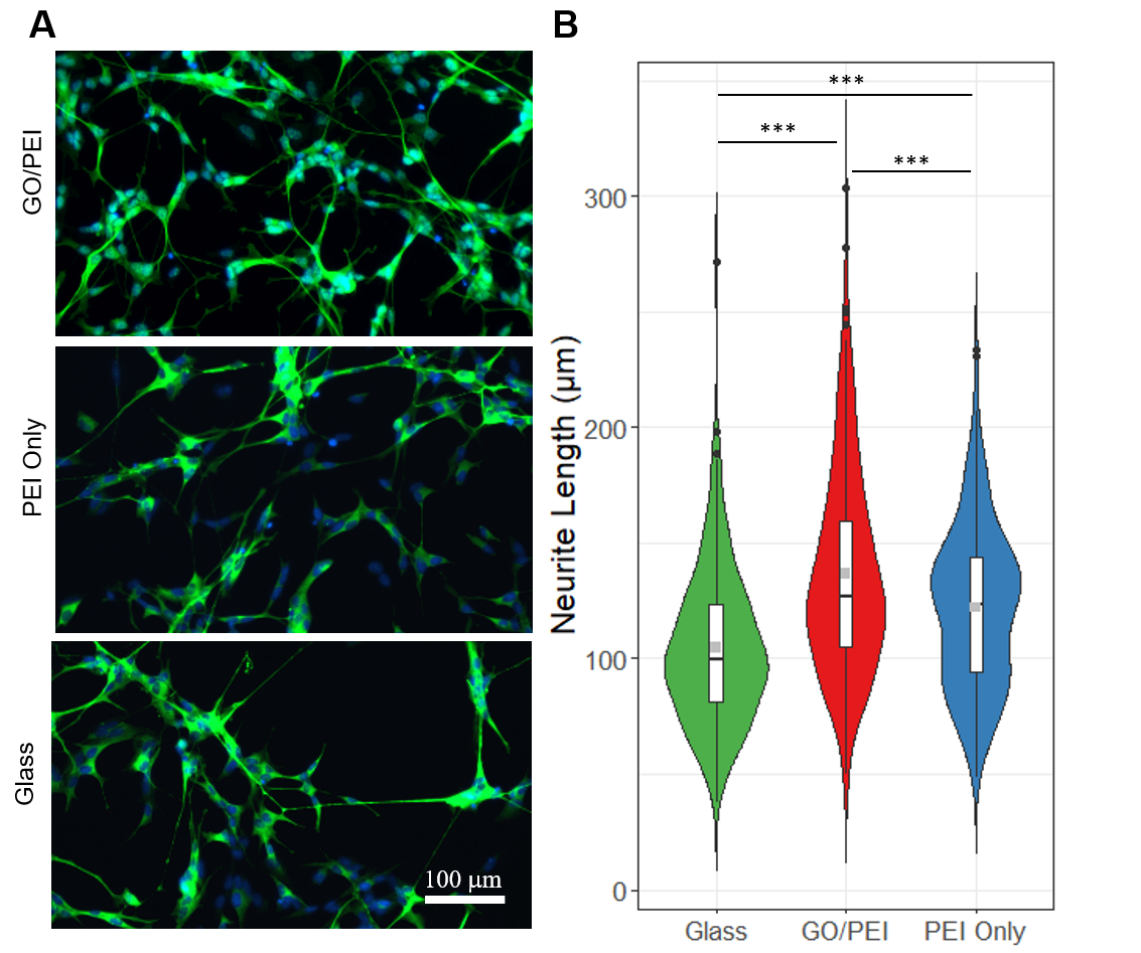

Figure 4.3 | **Effect of GO on neurite growth of SH-SY5Y cells.** (A) Representative fluorescence images showing cells on glass surface, polyethyleminine (PEI) surface or GO/PEI film on day 14, cultured in differentiation medium. Cells were co-stained by neuronal marker Anti-TAU with Alexafluor-488 (green) and Hochest (blue). (B) Mean (grey point) Range (white box) and Distribution (Violin) of measured neurite lengths under indicated cultured conditions in 200 cells (GO/PEI), 200 cells (PEI only) and 200 cells (glass), from n = 5 independent cell preparations. Neurites are longer on GO/PEI *** $p < 0.001$ compared to cells growing on Glass and are longer on GO/PEI ** $p < 0.01$ compared to PEI only.

growth was available. Longer growth indicated a better surface for neurite generation, whilst reduced growth would indicate an inhibitory effect.

In Figure 4.3(A) representative IHC images of SH-SY5Y cells in differentiation conditions stained for the TAU cytoskeleton on GO/PEI films is presented compared to similar cultures on PEI coated and bare glass substrates. Cells in all images produced visible neurite-like projections across the extracellular spaces bridging between clusters of cells. Fine diameter projections were resolved in all images with longer fine projections per cell visible on GO film compared to PEI or glass surfaces.

In Figure 4.3(B) neurite length data is presented per culture surface for cells after 14 days under differentiation conditions. Neurites were measured by fitting NeuronJ splines to the neurite projection on green-channel images. A significant increase in mean neurite length is seen on GO films compared to both PEI and glass groups. A smaller but still significant increase in mean neurite length is seen on PEI compared to Glass. The range of neurite lengths is the largest on GO film between 50 and 240μm provided by a mixture of small blind ended projections and large cell connecting projections which spanned considerable distance between cells. Median neurite lengths is similar for GO/PEI and PEI only. Range and median values for glass group is the smallest of the sample population with cells concentrated in clusters with less expansive projections between clusters.

SH-SY5Y cells display the expected pseudo-differentiation in response to retinoic acid differentiation stimuli on all surfaces. Longer neurites are generated by SH-SY5Y cells cultured on GO films compared to PEI only or Glass surfaces. The longest neurite projection measured was observed in the GO film group. Importantly the GO film was superior to the PEI only condition. This suggests the GO film is superior for SH-SY5Y neurite growth than glass or polymer alone.

4.2.4 Effects of GO films on BV-2 viability

The BV-2 cell line is commonly used as an immortalised model for microglial growth and reactivity. In this work, using this cell line is a complement to the previous work with

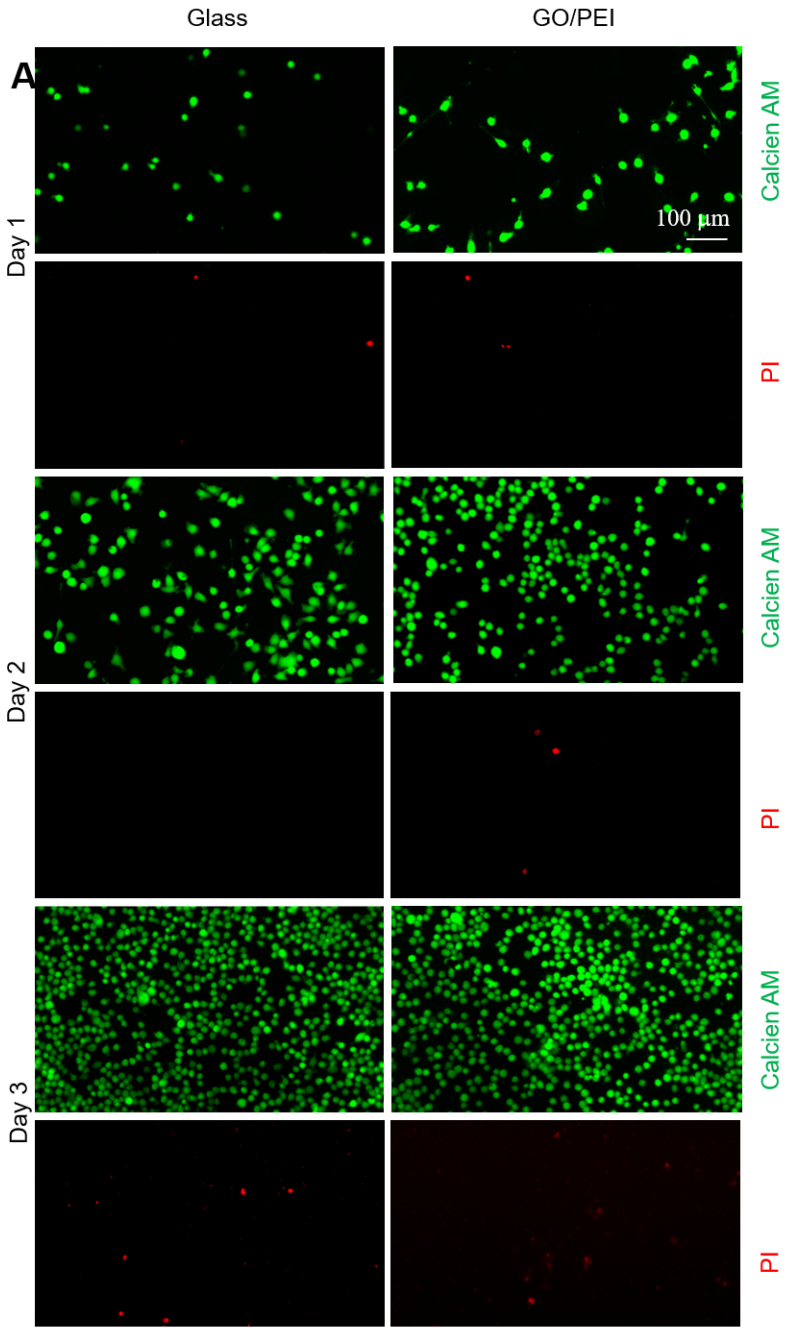
Glass
GO/PEI
A
Day 1
Day 2
Day 3
Calcien AM
PI
100 µm

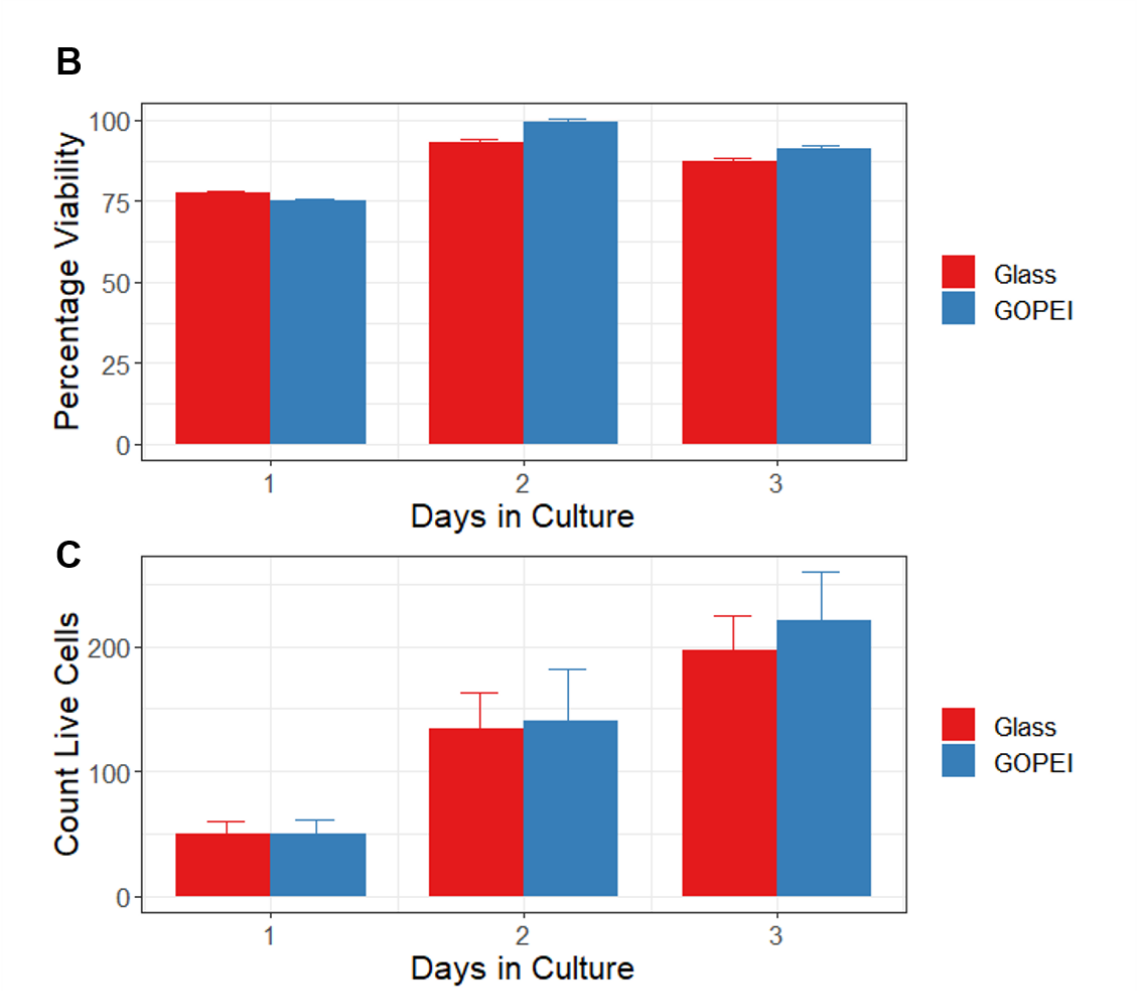

Figure 4.4 | **Effect of GO on BV-2 microglial cell growth and proliferation..** (A) Representative fluorescence images showing cells on glass surface or GO film on day 1 to 3, respectively, cultured in standard medium. Cells were co-stained by calcien-AM (green) and propidium iodide (PI) (red). (B) Mean cell viability under indicated cultured conditions from n = 5 independent cell preparations. (C) Mean count of green stained (live) cells under indicated conditions, from n = 5 independent cell preparations.

SH-SY5Y cells, providing a different lineage of cells with a different proliferative rate and fastidiousness with which to test the initial biological response to the GO film model. Furthermore the BV-2 cell line could be used as a basis for predicting the response of primary microglia to the GO film.

Individual GO films were constructed on PEI coated glass substrates according to Section 2.2.1. The films were plated with BV-2 cells according to Section 2.4.1.2. Identical preparations of BV-2 plated to glass substrates without GO films were again used as control comparisons in a parallel to the previous SH-SY5Y work. To investigate the viability and appearance of these cells over time, representative samples were taken at each time point and supplemented with Hoechst, PI and C-AM to reveal nuclei, dead-cells and live cell cytoplasm respectively. The GO film was again expected to support attachment, however BV-2 are a highly proliferative cell line in standard media, thus a short 3 day scale was used to prevent the cells reaching confluence and confounding data. Thus the main outcome of this experiment was to identify any differences in proliferative rate between the surfaces over this time period. In this way, promotion or inhibition of the cell replication rate caused by the surface could be identified.

In Figure 4.4(A), images of BV-2 cells over three time intervals on glass and the GO/PEI model were shown to be similar in number, size and shape. Initially on day 1 single cells with a round morphology are seen staining positive with Calcien-AM. On day 2 cells proliferated and approximately twice as many cells were visible. By day 3 cells were numerous and reached confluence. On each day the number of PI positive dead cells remains similar and isolated, indicating no dense areas of cell death. These images suggest both the glass and GO surfaces are suitable for BV-2 cell culture. At all time points, BV-2 cells were rounded on the GO film, however cells on the glass surface were ramified. This suggests the BV-2 cells have an activated morphology [294].

In Figure 4.4(B) the viability at each presented time point is shown. Cells on glass and GO surfaces have similar viability at all three time points, with a comparative increase after day 1. On day 1, cells had high viability, further suggesting no immediate cytotoxic

effects from the GO film, in agreement with the previous SH-SY5Y data. At day 2 and day 3, viability appears to increase due to the increase in total cell number, as explored in Figure 4.4(C). BV-2 cells were proliferating rapidly, approximately doubling each 24 hours. BV-2 were not PI positive suggesting death at the same rate, resulting in an relative increase in viability. In terms of cell proliferation, the surfaces were not significantly different.

4.2.5 Effects of GO films on BV-2 morphology

In the previous experiment, the BV-2 cells are seen to proliferate rapidly on both glass and GO film surfaces. However a qualitative difference was noted in the morphology of BV-2 cells on GO compared to glass, under the same conditions. On glass the BV-2 cells had a ramified morphology with dendritic projections, indicative of a resting or quiescent phenotype. In contrast BV-2 on the GO film were smaller, and more round, indicative of an activated or reactive phenotype. This suggested BV-2 were became activated by the GO film. To investigate this further, the size and shape of BV-2 cells on both surfaces was investigated.

Identical preparations on glass and GO films were stained with C-AM and Hoechst and quantified for perimeter, area and shape descriptors. The differences between shape descriptor calculations are detailed in Section 2.7.3. In this work, higher scores of circularity, solidity and roundness were indicative of a more activated phenotype with fewer or no dendritic projections.

In Figure 4.5(B) the difference in BV-2 is quantified as a significant difference in cell size in n = 3 preparations. Mean cell area was twice as large and perimeter was twice as long on glass surfaces compared to GO film. Furthermore, range of sizes was substantially greater on glass surfaces compared to GO film, indicating BV-2 were more uniform on the GO film. This difference was further explored in Figure 4.5(C) and described in terms of cell shape descriptors. Cells on GO films are significantly more circular, more rounded and have a higher solidity than similar cells on glass at the same time point. This suggests cells

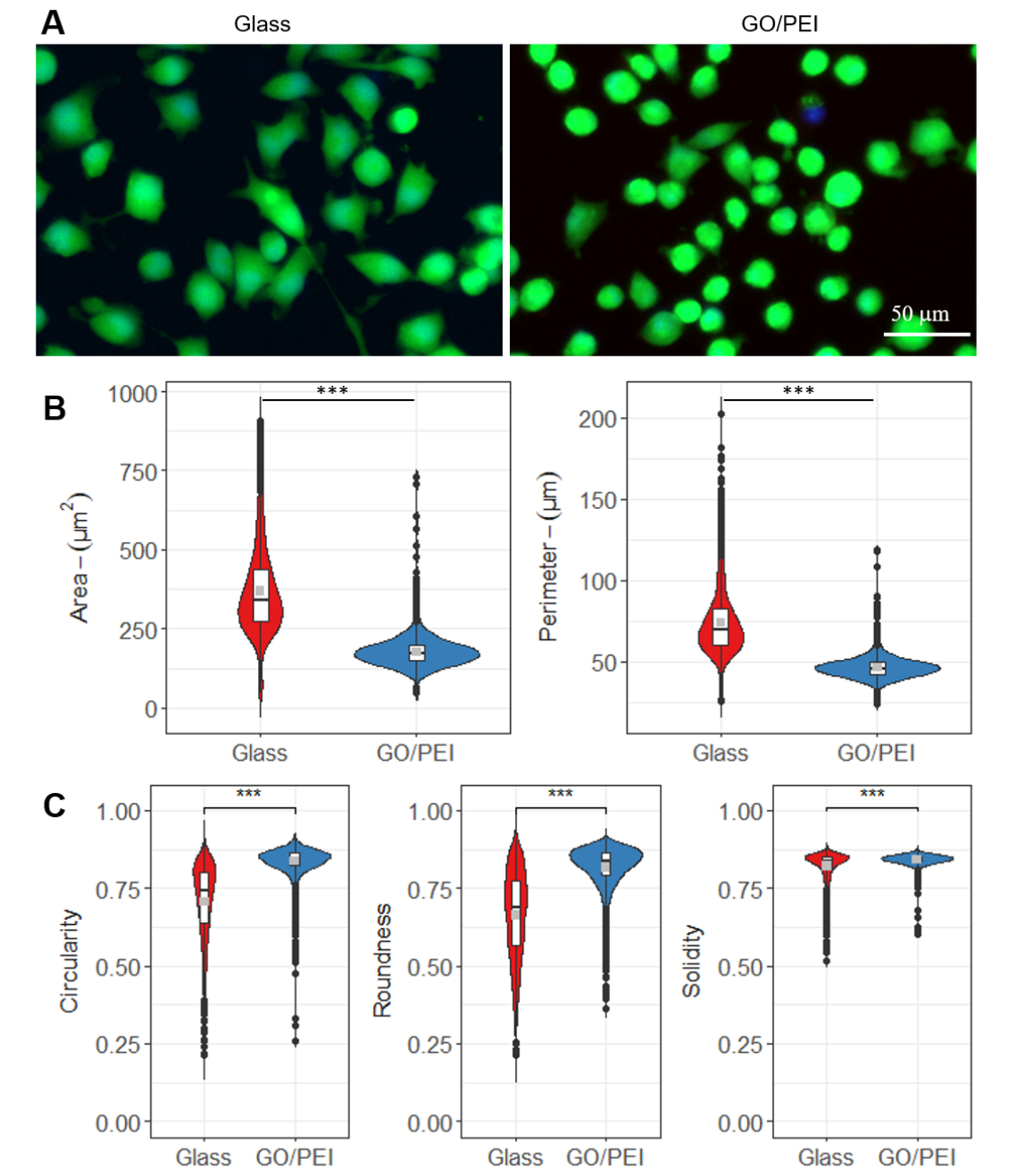

Figure 4.5 | **Effect of GO on BV-2 cell morphology.** (A) Representative fluorescence images showing cells on glass surface or GO film on day 3, respectively, cultured in standard medium. Cells were stained by calcien-AM (green). (B) Mean (grey point), Range (white box) and Distribution (Violin) of individual cell area and perimeter measurements under indicated culture conditions from n = 3 independent cell preparations. (C) Mean (grey point), Range (white box) and Distribution (Violin) of individual cell shape descriptors under indicated conditions, 2000 cells for glass and 2000 cells for GO from n = 3 independent cell preparations. *** $p < 0.001$.

on GO films are less ramified and therefore more consistent with the activated phenotype seen in BV-2 cells.

4.2.6 Effects of GO films on mouse neuron survival

Following evidence that the GO film is biocompatible using the SH-SY5Y neuronal cell line, the next step was to test the response of primary neuronal cells to the GO film model. The responses of primary neurons would confirm if the GO film model was a viable platform for further development. Primary neuronal cells are post mitotic and are highly fastidious, and therefore were expected to be more sensitive to any stressors in the surface previously reported from GO such as reactive oxygen species (ROS), or contaminants. Furthermore, the development of neuronal morphology would indicate if neuronal maturation was inhibited on the GO film surface.

Hippocampal neuronal cells were isolated from mouse brain tissue and applied to glass surfaces or GO films in a replication of previous work with the SH-SY5Y neuronal cell line. Neuronal cells were expressed as a count of live cells within the same area, in this case the entire cover-glass surface. In this way changes in cell numbers are expressed, because neuronal do not proliferate any significant increase in cell number between time points would indicate the proliferation of non-neuronal cells such as glia.

In Figure 4.6(A), cells on Glass and GO surfaces were similar in size and shape on day 7, and grown long dendrites by day 14. In Figure 4.6(B) the cell count at each presented time point is shown. Neuronal cells on glass and GO film have similar counts at both time points, indicating no proliferative cells remain within the preparations. On day 7 neuronal cells were seen to have attached to both surfaces. In the mean of n = 3 repeats, more neuronal cells had attached to the GO film compared to glass, this was not found to be a significant difference. By day 14, neurons had matured developing dendrites, and cell count remained similar to day 7. GO films remained higher in mean cell count compared to glass surfaces, however the standard deviation had increased by day 14 indicating more variability between mature cell count. Both surfaces showed good viability with

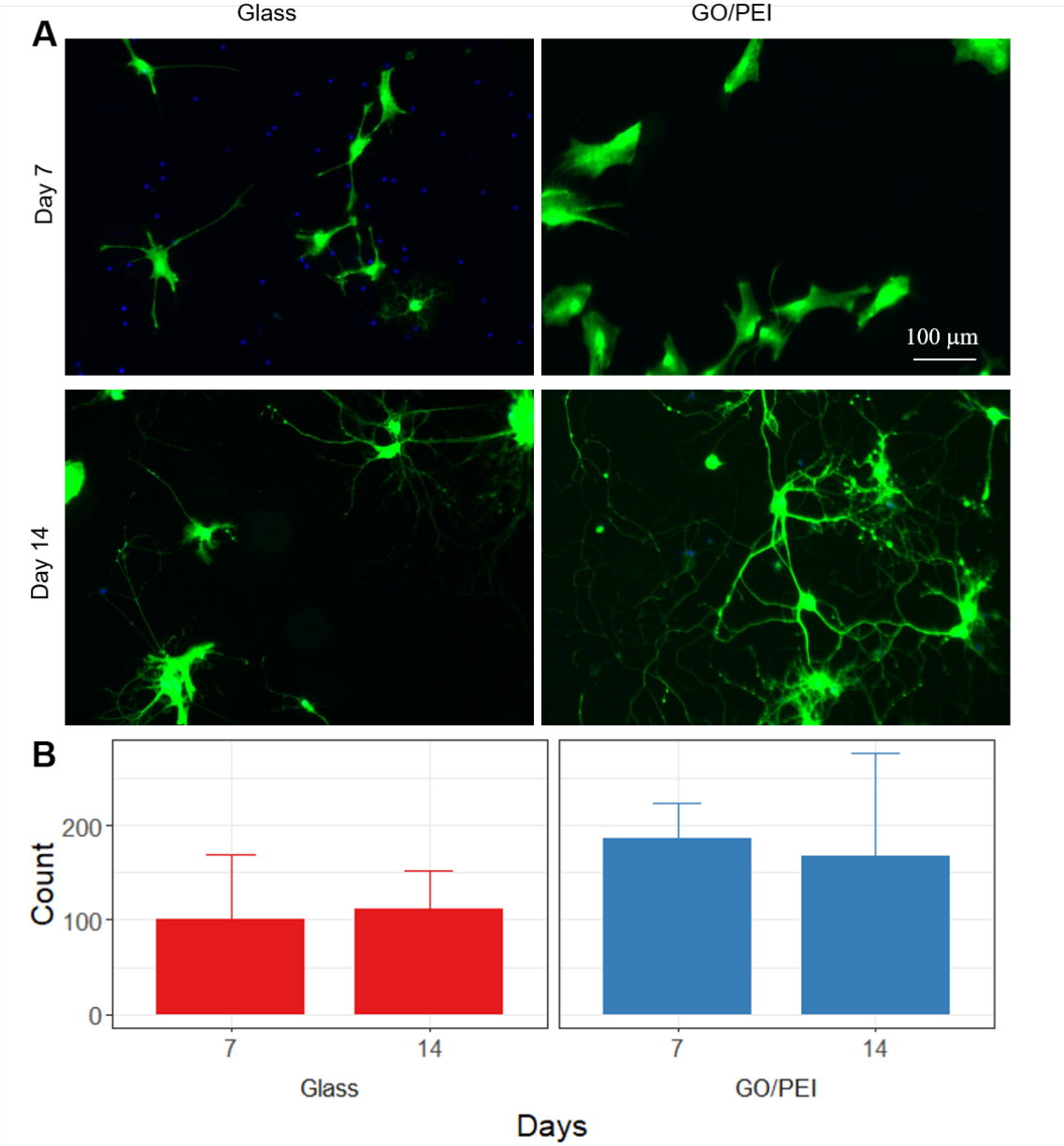

Figure 4.6 | **Effect of GO on mouse hippocampal neuron viability..** (A) Representative fluorescence images showing cells on glass surface or GO film on day 7 and day 14, respectively, cultured in neurobasal medium. Cells were co-stained by calcien-AM (green) and Hochest (blue). (B) Mean cell count under indicated cultured conditions from n = 3 independent cell preparations.

no PI positive cells detected at any time point indicating plated cell membranes remained impermeable.

Therefore, the GO film was comparable to the glass surface as a substrate for the growth of mouse neurons, possibly superior in initial cell adhesion. Additionally, the GO film did not result in cell death, and supported the expected growth and maturation of neurons.

4.2.7 Effects of GO films on rat neuron survival

Hippocampal rat neurons are similar post mitotic cells to primary mouse neurons, from a similar but alternative species of common laboratory animal. Therefore by repeating this work with the rat cells, further exploration of the compatibility of GO as a culture surface for primary neurons can be made. Additionally, this work would identify if there was a difference cell response to the GO film and conditions.

Primary hippocampal neuronal cells were isolated from rat brain tissue and applied to glass surfaces of GO films in an identical manner to previous work with mouse neurons. Change in cell count was again used to explore both the attachment and survival of neuronal cells, the presence of any proliferative cells.

In Figure 4.7(A), cells on Glass and GO surfaces remain similar in size and shape at both 7 and 14 days. Interestingly, rat neuronal cells appeared to be clustered together more than mouse neuronal cells prepared in the same conditions (Figure 4.6(A)). On day 7 rat neurons were observed as small clusters of cells with a ramified morphology and many small dendrites stained with C-AM. By day 14 these cells had become isolated, and had developed fewer, longer and intricate dendrites which span between cells and appeared interconnected.

In Figure 4.7(B) the cell count at each presented time point is shown. Rat neuronal cells on both glass and GO surfaces showed a similar trend in count at both time points, cell count showed similar decreases between the day 7 and day 14 time points on both surfaces In particular between day 7 and day 14 cells on glass there was a significant decrease in

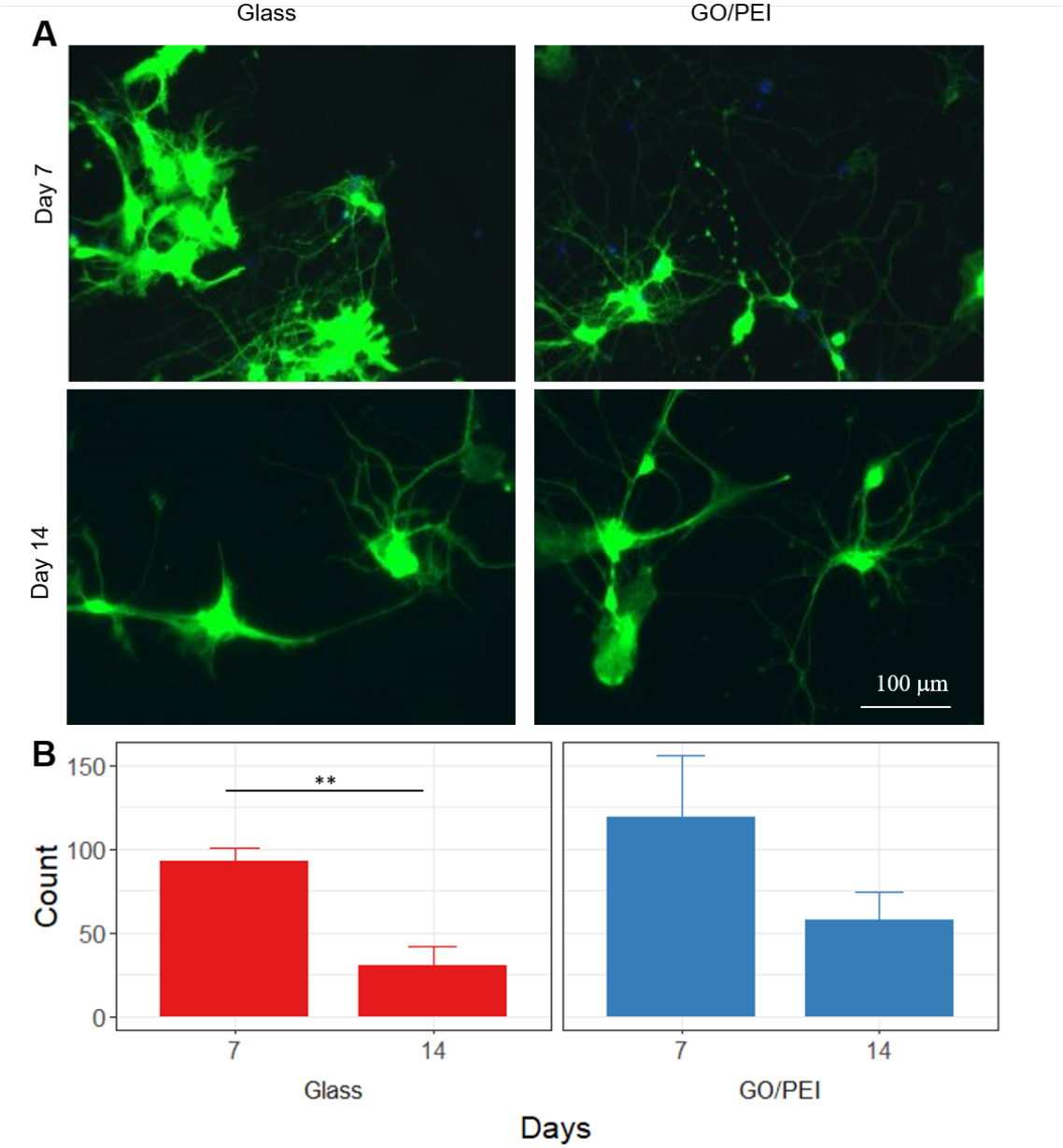

Figure 4.7 | **Effect of GO on rat hippocampal neuron viability..** (A) Representative fluorescence images showing cells on glass surface or GO film on day 7 and day 14, respectively, cultured in neurobasal medium. Cells were stained by calcien-AM (green). (B) Mean cell count under indicated cultured conditions from n = 3 independent cell preparations. ** $p < 0.01$

cell count. A similar decreasing trend was seen between day 7 and day 14 on GO films however this was not found to be significant. Because a similar decrease was observed on both surfaces, the most likely explanation for this decrease is that rat neuronal cells are less well maintained by the culture conditions compared to mouse neurons. Alternatively, as the distribution of cells appears to change between days 7 and 14 on both surfaces in Figure 4.7(A), it is possible the cell clusters contained surviving rat glial cells which had persisted longer than mouse glial cells, but had been depleted by day 14. Both surfaces show good viability with no PI positive cells detected at any time point indicating cell membranes remained impermeable.

The GO film remained similar in performance to the glass surface as a substrate for the growth of rat neuronal cells, cell count showed a significant decrease between 7 and 14 days. The GO film did not result in measurable cell death or alter the formation of dendritic projections compared to glass.

4.2.8 Effects of GO films on mouse astrocyte proliferation

GO films have been shown to be biocompatible substrates for neuronal cells not resulting in cell death, however other neural cells such as astrocytes have important CNS functions. Therefore the compatibility of the GO film with astrocyte cultures is also of interest and importance. Furthermore, this work served as an important step to characterise astrocyte growth on GO films, and thus how best to optimise culture conditions for future co-culture experiments between glial cells and neuronal cells. Primary astrocytes were isolated from mouse brain tissue by culturing cortical layers and then depleting the culture of microglial cells as described in Section 2.4.2.2 and plated to glass and GO films. Astrocytes are highly proliferative and were expected to form confluent layers over time. This work was therefore considered a preliminary step and conducted with n = 1 repeat on glass. Previously reported studies have demonstrated that astrocyte cells are dependent on extracellular matrix attachment and thus would have poor attachment without prior coating of the glass in bioadhesive such as laminin [295]. Thus far no surface was intentionally prior coated

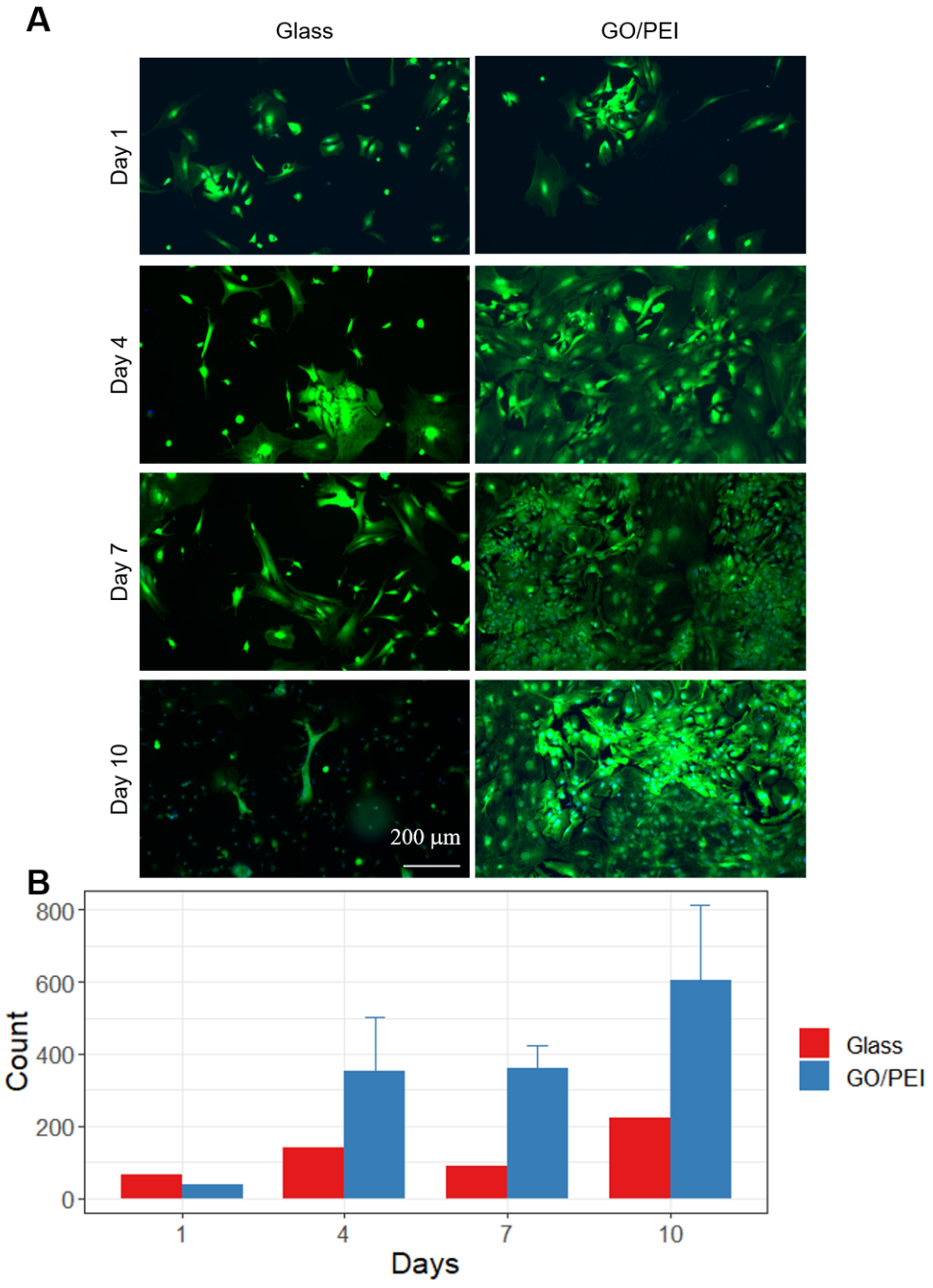

Figure 4.8 | **Effect of GO on mouse astrocyte proliferation..** (A) Representative fluorescence images showing cells on glass surface or GO film on day 1, 2, 3 and 4, respectively, cultured in standard medium maintained every 3 das. Cells were stained by calcien-AM (green). (B) Mean cell count under indicated cultured conditions from n = 1 independent cell preparation for Glass and n = 3 preparation for GO/PEI.

with bioadhesives as the interaction of the surface with the cellular micro-environment was of paramount interest.

As seen in figure 4.8(A) on day 1 cells are similar in count and appearance on both glass and GO films. However differences in cultures were observed at subsequent time points; On day 4, cells on glass remained isolated or in small clusters, whilst cells on GO films have expanded to confluence. This pattern is repeated on day 7 and day 10, cells on glass remain isolated whilst cells on GO films remain confluent. On GO films at day 7 cells have reduced cell area compared to day 4, with larger cells becoming visible again on day 10. This was confirmed with the preliminary preparation and its replicates. Repeats were performed with GO films to confirm the observations of proliferation to a confluent layer and continued high viability.

On GO films astrocytes were seen to increase in number at each time point (Figure 4.8(B)). At days 4 and 7 there were 4 times as many cells as on day 1, with a further increase to 8 times as many on day 10. This data indicates that astrocytes cultured on GO films would proliferate and obscure neurons quickly if used as a co-culture, making quantification of neurons in a co-culture model challenging. Therefore, astrocytes on a GO film in a co-culture model should be initially inhibited to reduce the speed of proliferation. Additionally, this confirmed that for comparison of co-cultures, a coated glass substrate would be required to support glial cells, however neurons have previously been demonstrated to survive on bare glass.

4.2.9 Hippocampal tissue co-culture on GO films

Neural tissues of the CNS are a composite structure of both neurons and glial cells, with intercellular signalling instructing growth. Previous data shows GO films were compatible substrates with the component cell types in isolation, and that astrocytes could reach confluence in faster than neuronal cells would mature. As previously introduced, astrocyte phenotypes typically support neuronal growth. However, these cells can also express inhibitory phenotypes when activated by noxious stimuli. To understand if glia on

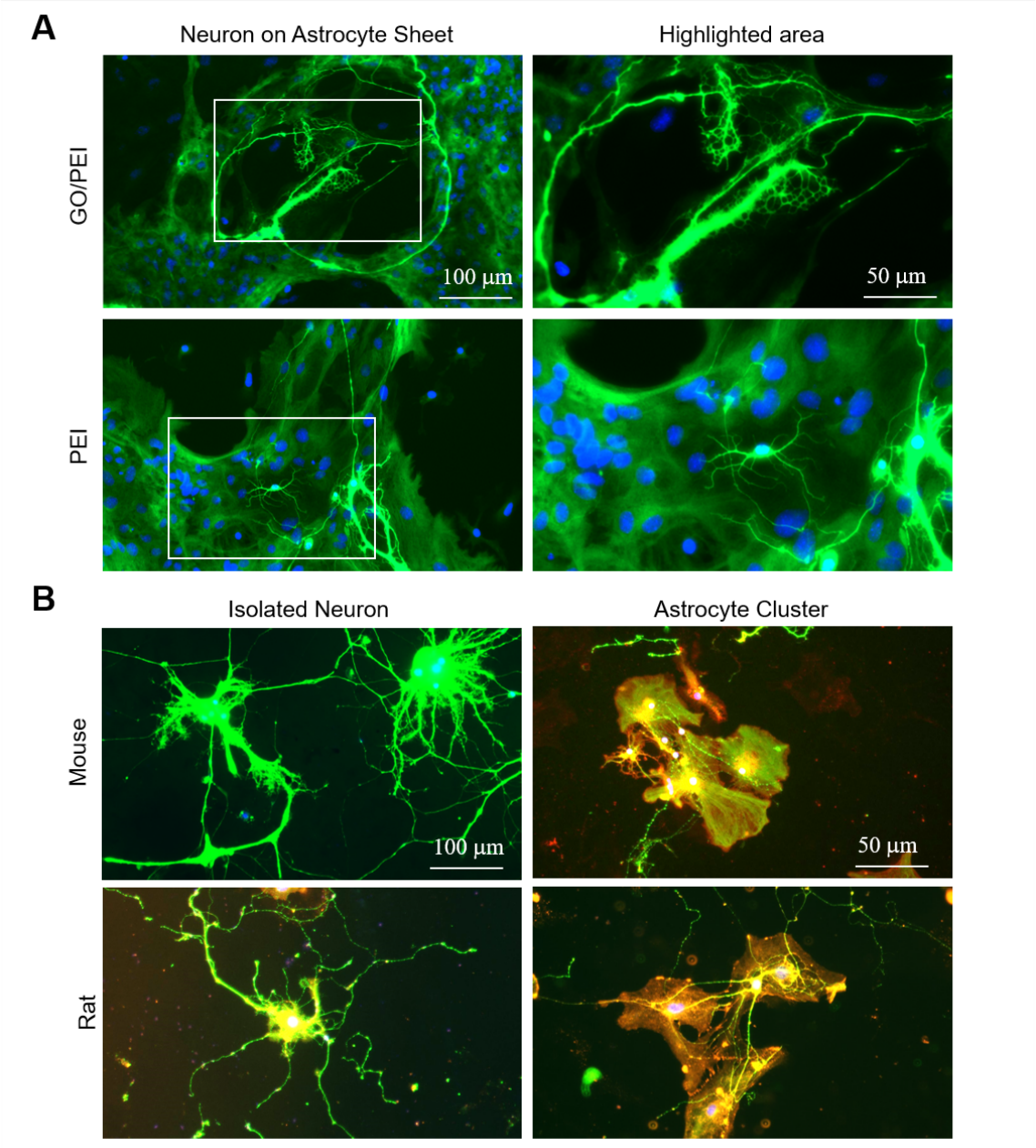

Figure 4.9 | **Qualitative morphologic similarity of Neurons in co-culture..** (A) Representative fluorescence images showing cells on GO film or Glass substrate coated with PEI. Neurons and astrocytes allowed to develop in co culture. Highlighted areas show normal neuron morphology and fine architecture supported by glia layer. Cells co-stained with Anti-Tau antibody for neurites and Hochest for nuclei (B) Representative fluorescence images showing mouse or rat cells on GO film without and with local glia. Cells co-stained with Anti-Tau antibody for neurite cytoskeleton and WGA for glia and neuron membranes

GO films remain supportive of neuron growth, co-culture of neuronal cells and glia from dissociated hippocampal tissue was performed.

Building on previous results, both mouse and rat tissue was used in this work. The concentration of araC was varied to ensure its inclusion did not alter neuronal maturation; araC was either withheld entirely or used at a lower concentration to reduce the proliferation of glia. GO films on PEI coated substrates were prepared as previously. A comparison surface included a PEI coated substrates without a GO film following on from the above evidence that glia would not adhere well to bare glass.

In Figure 4.9 examples of neurons growing in cultures containing glia are illustrated demonstrating the typical growths of neuronal cells staining positively for Tau with differing local glial cell populations and araC content. Figure 4.9(A) shows co cultures prepared by withholding araC entirely from cultures prepared from isolated mouse hippocampal tissue. Here, GO film was compared against the PEI substrate to observe neurons within confluent glial layers. Neurons were observed stained for Tau cytoskeletal protein against a background of glia. Under low magnification neuron dendritic projections are observed following the topography of the glial membranes. Under higher magnification, the dendrites are observed to have highly intricate termini consistent with synapses. The co-culture preparation on both GO films and PEI substrate are seen to behave similarly. There was a wide variety of neuronal morphologies observed on both surfaces comprising multipolar neurons, looped dendrites and fine synapses. No pattern or structure was observed in the dendrites besides constraint to the glial cell layer.

Figure 4.9(B) shows co cultures on GO films prepared by decreasing araC concentration prepared from mouse or rat hippocampal tissue. Using this inhibitor condition, neurons within the same GO film can be observed growing either isolated without local glia, or with clusters of glia. Isolated neurons grew similarly to neurons from cultures with araC inhibition of glial cells (Fig 4.6, Fig 4.7), with many long neurite projections featuring a branching and expansive morphology. Where neurons are found with glia, neurites become entrained between the glia membrane and do not extend away, similar to the observations

in Figure 4.9(A) above. Therefore neuron development is independent of araC. Glia are seen to control the distribution of neuronal projections, constraining dendrites to the glial membrane. There is no noticeable difference in neuronal cells in these conditions on GO films or PEI substrates, with cells developing mature morphology on both surfaces.

4.2.10 Effects of GO films on mouse microglial viability

As the immune cell of CNS tissues, microglia respond to noxious stimuli by entering reactive phenotypes. Therefore the compatibility of the GO film with microglial cultures is of interest and importance. In the above work with the BV-2 cell line as a model of microglial culture, there is evidence that the GO film may induce such reactive phenotypes in microglial cells, loosing their ramified morphology and proliferating quickly. Therefore this work aims to characterise the response of primary microglia to GO films and investigate similar effects.

Individual GO films were constructed on PEI coated glass substrates according to Section 2.2.1, plated with mouse microglia according to Section 2.4.2.1. Identically prepared microglia populations on glass substrates were used for comparison in a parallel to the above BV-2 work.

In Figure 4.10(A) the appearance of microglia cultured on glass or GO films is presented. At day 1, differences appeared between the surfaces, with cells on glass appearing smaller and more rounded than cells on GO films. By day 2, cells on GO films appeared to produce dendritic projections consistent with a ramified morphology, compared to cells on glass which remain more rounded. By day 3, cells on glass were seen in a ramified morphology with dendritic projections, cells on GO films had longer projections. By day 4, cells on GO films were obviously more numerous and had numerous dendritic projections whilst cells on glass appeared larger in area. Under the same capture conditions cells on glass appeared less bright, possibly indicative of cells spread more in the planar direction compared to cells on GO films.

In Figure 4.10(B) the mean count of live cells on both surfaces is presented. Microglial

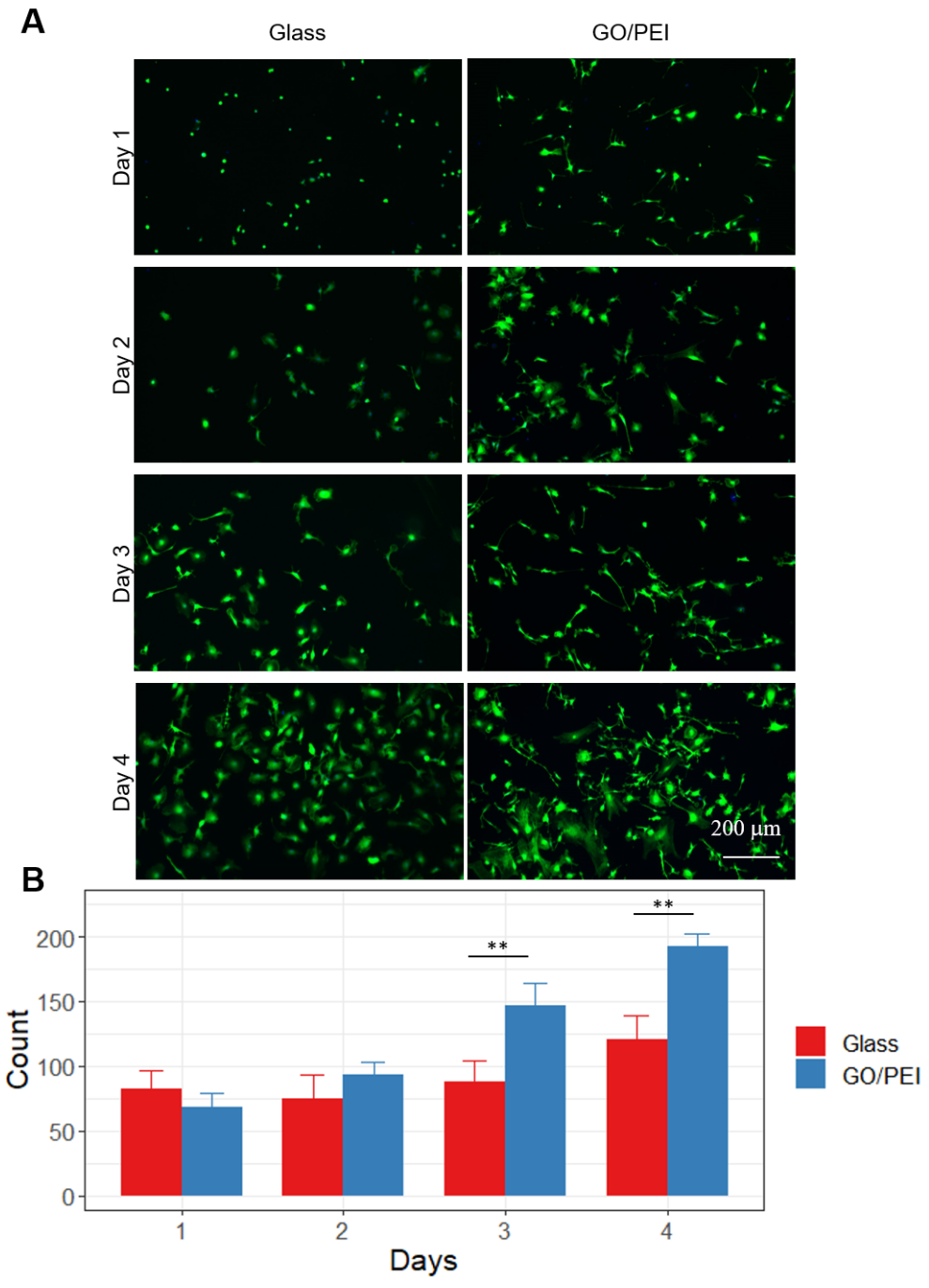

Figure 4.10 | **Effect of GO on mouse microglia proliferation..** (A) Representative fluorescence images showing cells on glass surface or GO film on day 1, 2, 3 and 4, respectively, cultured in 50:50 conditioned : fresh standard medium. Cells were stained by calcien-AM (green). (B) Mean cell count under indicated cultured conditions from n = 4 independent cell preparations. ** $p < 0.01$.

cells were seen to proliferate steadily on both glass and GO film surfaces, doubling in number after 4 days. However a significant difference was detected in the rate of proliferation between the surfaces. Cell count remains similar for the first two days ($p>0.05$), however from day 3 there were significantly more microglia detected on GO films compared to glass surfaces. This indicates the cells on GO films are proliferating faster compared to cells on glass.

As previously discussed, the glass surface is less ideal for expansion of primary cells which benefit from a coating of extracellular matrix or a bioadhesive substrate. Microglia are observed to proliferate more at 3 and 4 days on GO films compared to glass, but remained similar during the earlier time points. This suggests the GO film cultivated a more permissible substrate for microglial proliferation than glass. Furthermore, microglia on GO films appeared to remain ramified, suggestive of a non-activated phenotype. This is dissimilar to the BV-2 microglial model which appeared to enter an activated phenotype on GO films.

4.2.11 Effects of GO films on mouse microglial activation

The above data suggested microglial cells were dissimilar to the BV-2 microglial cell model and did not enter an activated phenotype on GO films. To better understand the responses of microglia on GO films, a model of microglial activation was created using lipopolysaccharide (LPS) stimulation, a method known to induce microglial reactivity. This work would aid in developing an investigative model for later adsorption treatment of the GO film. To do this, microglia on GO films (Control) were compared with identical preparations where LPS was introduced to the media at as described in Section 2.4.2.1. Cultures were then stained with C-AM to reveal any changes to live microglia morphology on GO films when treated with LPS. These changes in morphology were quantified in terms of shape and size.

In Figure 4.11(A), the appearance of microglia without and with LPS treatment is presented from 4 time points. At day 1 the Control cells were ramified with dendritic

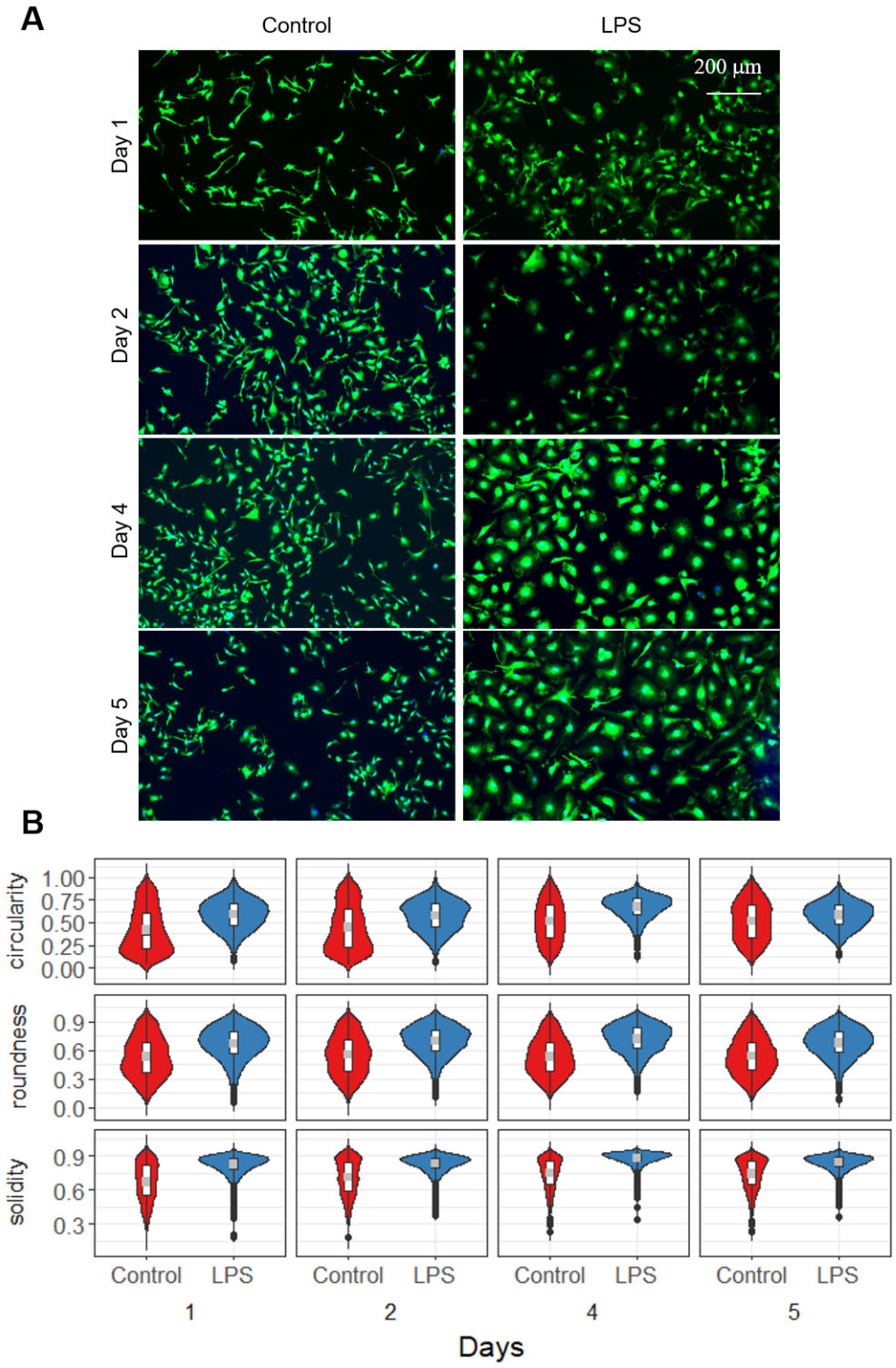
A
Control
LPS
200 µm
Day 1
Day 2
Day 4
Day 5
B
circularity
1.00
0.75
0.50
0.25
0.00
roundness
0.9
0.6
0.3
0.0
solidity
0.9
0.6
0.3
Control
LPS
1
2
4
5
Days

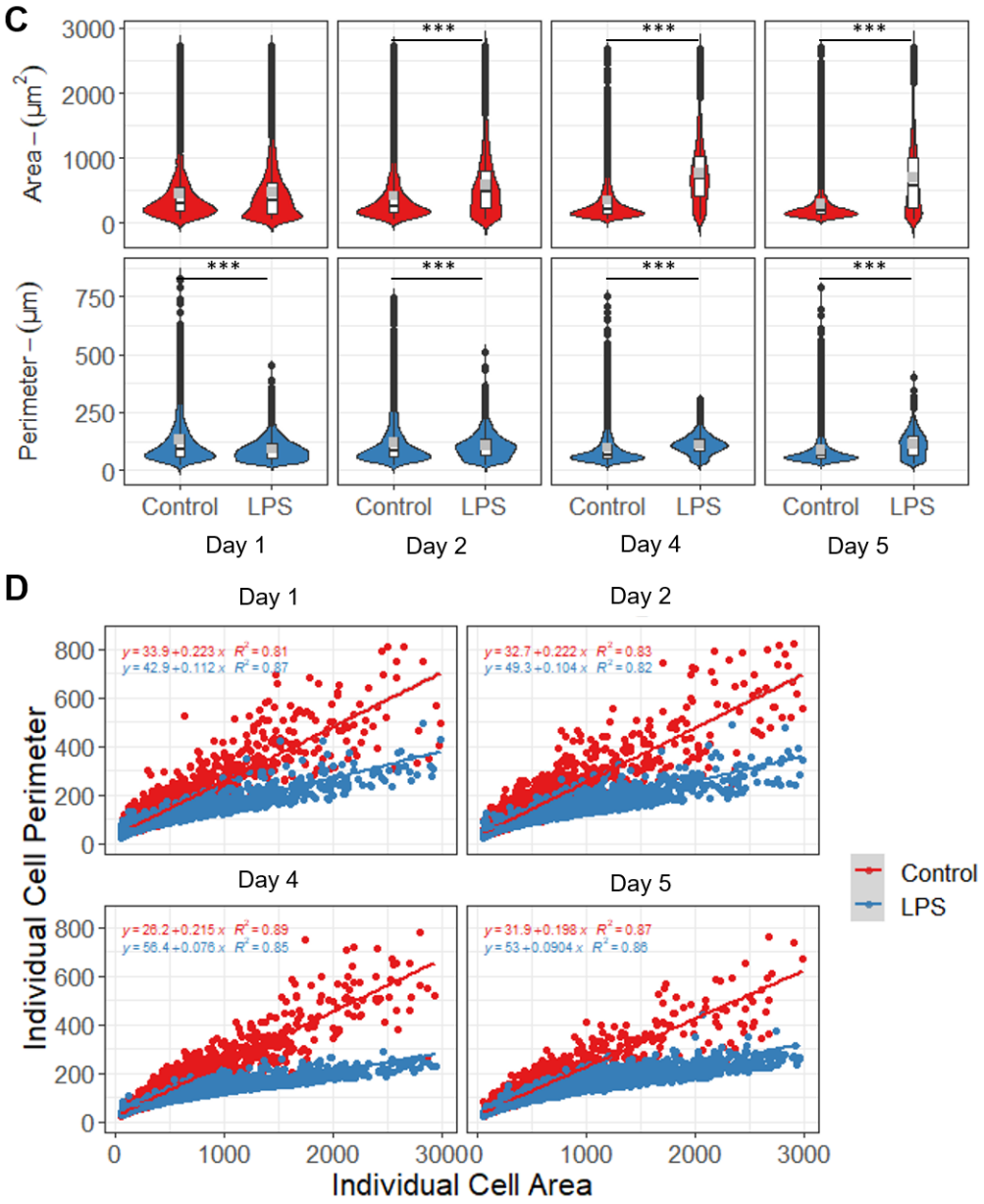

Figure 4.11 | **Effect of LPS treatment on primary mouse microglia on GO surface.** (A) Representative fluorescence images showing cells on GO film without and with LPS treatment on day 1, 2, 4 and 5 respectively, cultured in standard medium. Cells were stained by calcien-AM (green). (B) Mean (grey point), Range (white box) and Distribution (Violin) of individual cell shape descriptors under indicated conditions, 10000 cells for glass and 10000 cells for GO from n = 3 independent preparations. (C) Mean (grey point), Range (white box) and Distribution (Violin) of individual cell area and perimeter measurements under indicated culture conditions 10000 cells for glass and 10000 cells for GO from n = 3 independent cell preparations.. *** $p < 0.001$. (D) Scatter plots of area and perimeter for individual cells under indicated conditions with a linear line of fit.

projections, whereas the LPS treated cells appeared larger, more spread in planar dimension with fewer projections. This difference continued at day 2, 4 and 5. Control microglia remained ramified whilst the LPS treated microglia on GO films continued to increase in size and decrease in number of projections. These morphological differences were quantified and characterised as shape descriptors in Figure 4.11(B). At all time points LPS treated cells are significantly more circular, more round and more solid in shape than the control condition cells ($p<0.05$). This is in agreement with expectations that microglia adopt an activated morphology following LPS stimulation.

These morphological differences were further explored as differences in size (Fig 4.11(C)). Mean cell area for LPS treated cells were significantly larger than control cell area at days 2, 4 and 5 confirming that cells became larger in area when treated with LPS. Mean cell perimeter showed an interesting trend. At days 1 and 2, cells in the control condition have significantly longer perimeters than LPS treated cells. However this changes at days 4 and 5, where cells in the LPS treated condition have significantly longer perimeters. This is a result of the change in morphology. At days 1 and 2 the dendritic projections of the control microglia contribute to a longer perimeter. At days 4 and 5, the LPS activated microglia cells have expanded in planar dimensions thus have a higher perimeter. The change in distribution of area against perimeter observations is illustrated in Figure 4.11(D).

Overall, primary microglia have been shown to attach and proliferate on the GO film. Microglia retain a non-activated morphology during proliferation, retain responsiveness to LPS stimulation and change morphology consistent with an activated phenotype on GO films. This includes an increase in circularity, roundness and solidity compared to the resting state, and also comprises changes in cell area and perimeter. Therefore microglia behaved differently to the BV-2 cell line on the GO film, and do not adopt an activated morphology on GO films without external stimulation.

4.3 Discussion

The present study examined if the 2D GO film model was a biocompatible substrate for the culture of neural cells. The GO film was robust and suitable for prolonged culture, particularly when the film adhesion to the glass substrate is enhanced by an undercoating polymer. In all cases, cells were found attached to the GO surface and had high viability, indicating there is no negative effects of this GO material, or its undercoat. Various polymers can be used as undercoating without difference to GO film integrity or cell adhesion. PEI was selected as the most efficient and easy to use of the available alternatives. GO films in this chapter were conducted without applying any bioadhesive treatments to the GO surface. All cells therefore experienced a GO film surface modified only by the microcellular environment and culture media. Differences are seen in cell counts comparing GO films with glass surfaces, which suggests cell adhesion on the GO film is superior to cell adhesion on glass. The SH-SY5Y neuronal cell line showed longer neuritic growth during differentiation with retinoic acid, similarly mouse and rat neurons matured and produced intricate dendritic projections on GO films. Astrocytes on the GO film proliferate to confluence but retain phenotypes permissive to neuronal growth as seen in co-culture experiments. In microglial models, BV-2 showed an altered morphology on the GO film which indicated an activated phenotype. By contrast, mouse microglia did not show an activated morphology on the GO film, but retained sensitivity to LPS resulting in an induced activation state. In general the GO film is a biocompatible substrate which does not cause cell death or dysfunction in a range of neural cells.

4.3.1 Demonstration of GO biocompatibility

As characterised in the earlier chapter, the film model presented a continuous, rough GO surface for cell culture. By immobilising the GO platelets as a film, this model limits the risk of GO penetrating cell membranes [164]. The film model was not coated with tertiary coatings, this leaves the GO surface chemistry exposed to the cell culture micro-

environment. Therefore this work provides evidence that this commercial GO of high purity, and is free of potentially cytotoxic contaminants [161]. Similarly the excellent cell viability and differentiation performance demonstrates no biomolecule disrupting electrostatic effects are detected [167, 292]. The observation of fine cell process morphologies suggest no disruption of the plasma membrane such as ruffling is detected, no nanotoxic effects are induced by the GO film [164, 163, 165]. Finally, the resting morphology of microglia suggests ROS generation by the GO film is low or absent [165].

4.3.2 Neuronal development on GO films

SH-SY5Y neuroblastoma cell line is used as a model for neuronal development on the GO film. Compared to inert control surfaces and the undercoating polymer, neurite growth by retinoic acid differentiated SH-SY5Y cells is enhanced on the GO film model. Previous reports have identified the potential for electro-conductive carbon surfaces to result in enhanced neurite generation in neural lineage cells [158, 139, 51]. It is tempting to consider this explanation for the enhanced neurite generation seen in this work. However during electrostatic investigation of the 2D GO film model during this work, the resistance of the surface was found to be high, making a conductive explanation unlikely. Furthermore, enhanced neurite growth was also observed in SH-SY5Y cells grown on an adhesion enhanced, non-conductive PEI coated substrate. This does not support an explanation based on conductive enhancement. Instead, these data point to adsorption from media to the GO film as a likely explanation of the increased SH-SY5Y growth. To induce differentiation of SH-SY5Y, FBS containing media is withdrawn after cell attachment in favour of retinoic acid differentiation media. The observed enhanced neurite extension on GO film surfaces may then be explained by improved nutrition of SH-SY5Y through adsorption by GO of protein from media causing localisation of media components proximal to cells at the GO surface [269].

Hippocampal neurons of both the rat and mouse also develop long neurite projections on GO films, though unlike the simple neurite like projections of SH-SY5Y cell line these

projections feature high architectural complexity and a range of expansive or looping structures on GO films. In co-culture experiments a neurite supporting phenotype of glia is observed demonstrated by the changes in neuronal morphology caused by the presence of proximal glia. In isolation, neurons extend projections in all directions across the GO film. In the presence of glia within 50-100μm of the neuronal cells results in neurites becoming localised and conformal with the glial membrane. Glia with reactive phenotypes are known to exhibit neuroinhibitory and neurotoxic phenotypes and induce these phenotypes throughout glia [227]. The close and supportive association between glia and neurons observed in this work indicate that astrocytes are instead displaying neuron-supporting phenotypes and generating an extracellular micro-environment permissive to neurite growth on the GO film. This is consistent with previous reports that astrocyte homeostatic function is not modified by GO materials [270]. Neuronal cells in co-culture with glia appear to form more complex dendritic termini consistent with synapses, which are not seen in isolated neurons.

This data shows that the GO film is a permissible substrate for culture of neuronal cells and neurons in co-culture. Neuronal cells are are not inhibited by the GO film, and are instead enhanced by the interaction of the surface with the cellular micro-environment. However the GO film was a passive component of these cell cultures, the film did not directly effect or lead to neuronal differentiation or maturation independent of maintenance conditions beyond providing an enhanced substrate. Thus the instructive capacity of the GO film in this case is best considered as a delivery platform for other molecules. This suggests a GO material surface provides a basis for generation of neural tissue with mature neurons and supportive glial phenotypes.

4.3.3 Microglial reactivity on GO films

Comparing primary microglia on GO films to BV-2 microglial cell line on GO films, an activated phenotype is observed on in BV-2 cultures which is not observed in microglia. In particular, without external stimulation BV-2 cells proliferated rapidly doubling in number

every 24 hours and developed a round morphology on GO films. In comparison, BV-2 on glass maintained a ramified morphology. However this is not observed in primary microglial cultures. Microglial cells proliferate more quickly on GO films than on glass, but slower than BV-2 doubling in number after 4 days. Importantly, primary microglia remained ramified on the GO film . This suggests primary microglia do not become activated when cultured on the film, which is a positive outcome in contrast to the preliminary findings with the BV-2 model. Quiescent microglia retain process forming, elongated and dendritic morphologies, characterised by a relatively high membrane perimeter accompanied by a low score of solidity indicating complex shape formation, low cell area, low cell roundness and low circularity typical of an elongated body with short processes. Primary microglia are observed to remain sensitive to activation by LPS treatment when cultured on the GO film. The activated primary microglia are distinct from the resting morphology featuring higher circularity, roundness and solidity indicative of a loss of membrane dendritic projections. This confirms that microglia respond as expected when cultured on a GO film, and that LPS activation is an effective method of inducing a reactive phenotype on GO films. Previous reports have stated that graphene substrates can have anti-inflammatory effects on microglia [263]. On the contrary, the GO film induced a reactive pro-inflammatory phenotype in BV-2, but had no effect on the reactivity of mouse microglia.

4.4 Conclusion

In this research a viable 2D model to investigate the performance of graphene oxide as a thin film culture surface has been developed. This model of GO thin films supported by PEI on glass substrates are found to have good biocompatibility with neural culture, no investigated cell type failed to attach, develop and/or proliferate on the model surface. This data demonstrates that the neuronal cell line SH-SY5Y, microglial cell line BV-2, mouse and rat primary neurons, astrocytes and microglia all demonstrate high viability

and functional development on GO films.

The GO film is shown to be an enhancing platform for dendritic extensions, particularly in the length of neurite extensions from the SH-SY5Y cell line, though primary neurons also produce extensive and well developed neurites on GO. Furthermore the GO film does not adversely effect astrocytes or microglia in culture, and does not induce reactive neuroinhibitory phenotypes in either glial cell.

In summation, GO films created by spin coating are a biocompatible model for the investigation of GO in neural culture, with the potential to be instructive to certain cell types by modulation of the cellular micro-environment.

Chapter 5

GO Films as a Delivery Vector

5.1 Introduction

In this thesis the capacity of the GO material to provide an instructive material for cell growth is of importance and interest in the development of GO as a biomaterial. Previous reports have suggested that graphene surfaces can adsorb biomolecules and thus alter cellular micro-environments for plated cells compared to otherwise identical but untreated surfaces [269, 83]. Further reports have shown GO is predicted to have the capacity to retain proteins [296, 133]. Others reports have demonstrated that GO can reversibly adsorb other molecules including pharmaceuticals to graphenes [297, 127, 298]. In the last chapter, the GO film model was biocompatible and cells plated on the GO film continued to display expected morphology and responses to stimuli. When characterised, it was observed that the GO film surface became coated in vitronectin following exposure to cell culture. Therefore this incidental coating may preclude any further adsorbed factors or instructive capacity from effecting cell populations.

In this chapter, the GO film model was developed further as a substrate for cell culture by exploitation of the adsorption properties of the GO film. In this context, adsorption was used as a delivery vector to introduce molecules into the culture micro-environment.

This work aims to provide new ways in which scaffolds could be engineered to control cell responses to a potential implant. Neural cells were used, specifically SH-SY5Y neuronal cells, BV-2 microglial cells and mouse microglial cells for their established measured normal responses on the film model. Cells were plated and grown on GO films as described in Section 2.4. Fluorescent microscopy imaging of live cells and immunofluorescent imaging of fixed cells was used to record cells as described in Section 2.6.1. Finally the number, viability and morphology of the cell populations on the GO film were quantified as described in Section 2.7. Microglial activation was a particular target in this work. As the immune cell of the CNS, control of microglial activation would could aid implant integration and limit rejection.

The aim of the research presented here was to explore if adsorbed molecules remained sufficiently bioavailable to alter cell responses to expected stimuli. This included identification of likely mechanisms by which adsorption proceeds. These outcomes could provide a facile and novel method to use GO as an *in vitro* vector to deliver pharmaceuticals to local cells.

5.2 Results

5.2.1 Effects of adsorbed vitronectin on SH-SY5Y attachment

In the previous chapter vitronectin was detected in XPS spectra on GO films following digestion of cell culture with trypsin (Section 3.2.5). Vitronectin, a component of the FBS used in standard media and the primary component by which cell attachment is assisted during seeding. This layer was resilient to being washed away during sample preparation for XPS, which suggests the vitronectin was adsorbed to the GO film during cell plating where the GO surface was exposed to FBS. This coating may be responsible for some of the enhanced cell adhesion and proliferation on GO films in the previous chapter, if vitronectin was concentrated into a more robust layer by GO compared to non-adsorpative glass.

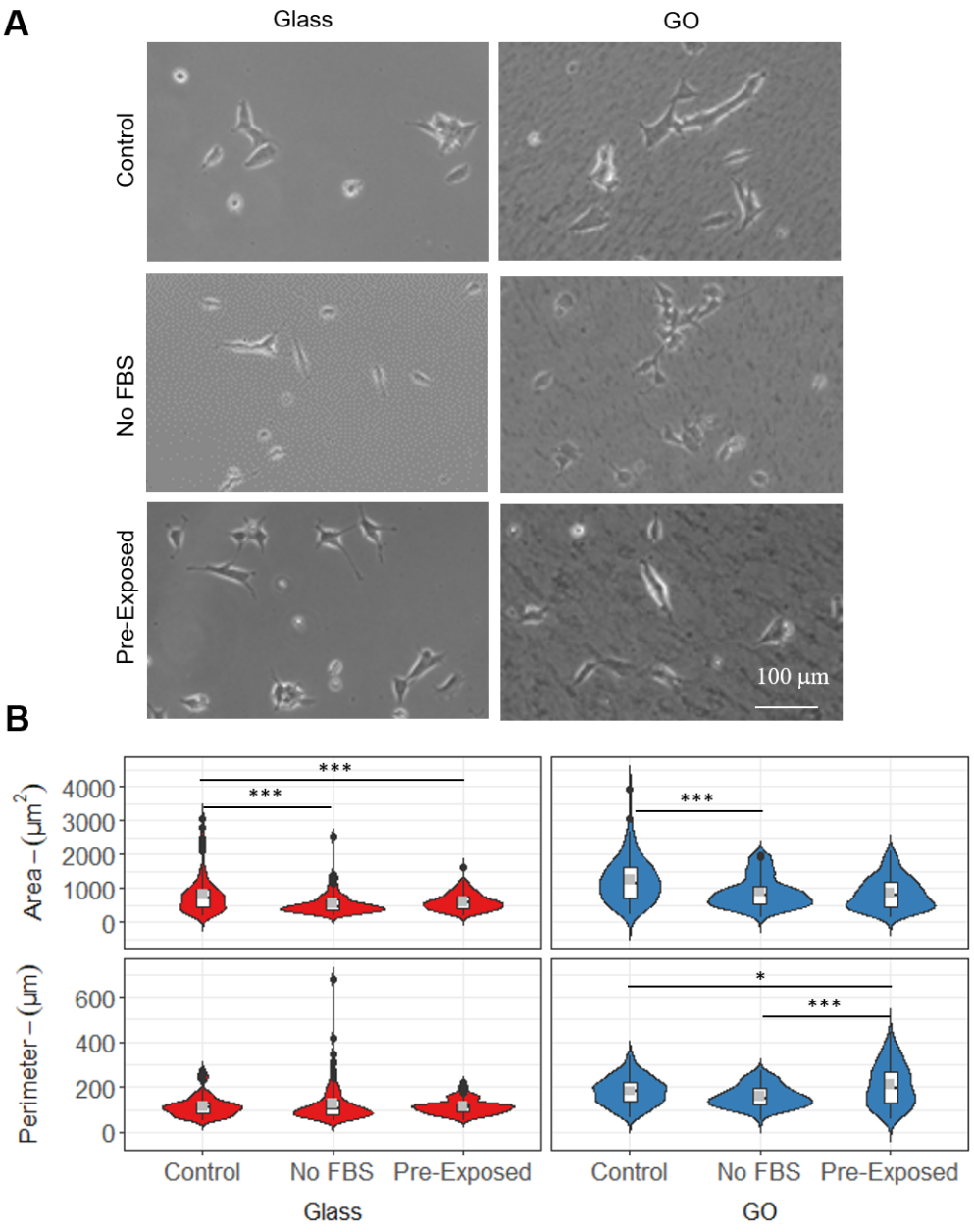

Figure 5.1 | **Effect of serum treated GO surfaces on SH-SY5Y initial attachment.** (A) Representative phase contrast images showing SH-SY5Y cells on Glass surface or GO/PEI film on day 1. Cultured in standard media (Control) or Serum free media (No FBS, Pre-Exposed). Cells were not stained and imaged in culture conditions (B) Mean (grey point), Range (white box) and Distribution (Violin) of individual cell area and perimeter measurements under indicated culture conditions, from 100 cells for glass and 100 cells for GO from n = 3 independent preparations. *** $p < 0.001$, *$p < 0.05$ compared to cells growing on glass.

To investigate this, the initial attachment of SH-SY5Y cells to GO films and glass surfaces was investigated under 3 conditions; A Control condition of SH-SY5Y cells plated in standard media containing 10% FBS onto surfaces prepared in accordance with Section 2.4. A 'No FBS' condition of SH-SY5Y cells plated in serum free media onto surfaces that were not exposed to standard media or FBS. A 'Pre-Exposed' condition of SH-SY5Y cells plated in serum free media onto surfaces prepared in accordance with Section 2.4 and then washed with serum free media three times prior to seeding to attempt to detach any protein which is not robustly adsorbed. The glass surface expected to have limited vitronectin retention, while the GO film predicted to show increased cell adhesion. Samples were placed in a tissue culture incubator for 8 hours following seeding before phase contrast images were acquired and the cells measured.

In Figure 5.1(A) representative phase contrast images of SH-SY5Y cells adhering to the surfaces under each experimental condition are presented. The GO film surface was visible beneath the cells in the images of cells on the GO film. SH-SY5Y cells were seen to initially attach in all cases and began to spread small processes, expanding in planar area. However differences were seen in cell morphology between the preparation conditions. Cells in control conditions were broadly rectangular and appeared healthy on both glass and GO films. By contrast, cells under the No FBS conditions were smaller, rounder and appeared to have shrunken cell volumes on both surfaces compared to the control condition. SH-SY5Y cells on the Pre-Exposed condition GO film were different when comparing surfaces. Cells on Pre-Exposed glass are similar to cells from the No FBS condition with visibly shrunken cell bodies. However cells on Pre-Exposed GO film showed a less shrunken morphology, were similar to the control condition, and dissimilar to the No FBS condition.

In Figure 5.1(B) the differences in cell size is summarised in terms of cell area and cell perimeter. On glass, cells had the largest areas in the control condition, significantly higher than either the No FBS or Pre-Exposed conditions, cell perimeter was similar in all conditions. On GO films, cells had the largest areas in the control condition,

significantly higher than the No FBS condition, however the Pre-Exposed condition had a similar mean area to the control. On GO films the pre-exposed condition is found to have significantly increased mean perimeter compared to the no FBS condition on the GO film. Furthermore a significant increase in mean perimeter on the pre-exposed condition compared to the control condition was observed. This may be explained by an increased length and number of projections visible in the pre-exposed condition compared to the control condition, which contribute perimeter but negligible area.

5.2.2 Effects of adsorbed ibuprofen on SH-SY5Y cell proliferation

The potential for GO to adsorb pharmacologically active molecules remains to be explored. Pro-inflammatory reactions are a limiting factor in neuroregeneration therefore this work has targeted delivery of anti-inflammatory COX-2 inhibitor 2-(4-Isobutylphenyl)propanoic acid otherwise known as Ibuprofen to limit neuroinflammatory reactions in stimulated by the COX-2 pathway [299]. First, to investigate what effect adsorption treatment with ibuprofen has on the previously established biocompatibility of GO, the attachment, viability and proliferation of SH-SY5Y was investigated on adsorption treated surfaces compared to untreated surfaces. In particular, if the adsorption treatment compromised the biocompatibility of the surface, it was predicted this effect would become evident during following plating. GO films were prepared as described in Section 2.2.1, and treated with ibuprofen as described in Section 2.2.2 to allow the ibuprofen to adsorb to the GO. For this work, to reduce possible dilution of effects from the adsorption treatment, culture media was not refreshed following plating, thus once cells had attached the system was not supplemented or changed.

In Figure 5.2(A), the appearance of SH-SY5Y cells grown on GO films and GO films which have received the adsorption treatment is presented. Cells on GO films appeared similar in both the control and adsorbed condition at all time points; cells begin isolated or in small clusters and are observed to gradually proliferate over 4 days. At day 4, which would mark the first maintenance period, cells appear identical, have formed clusters and

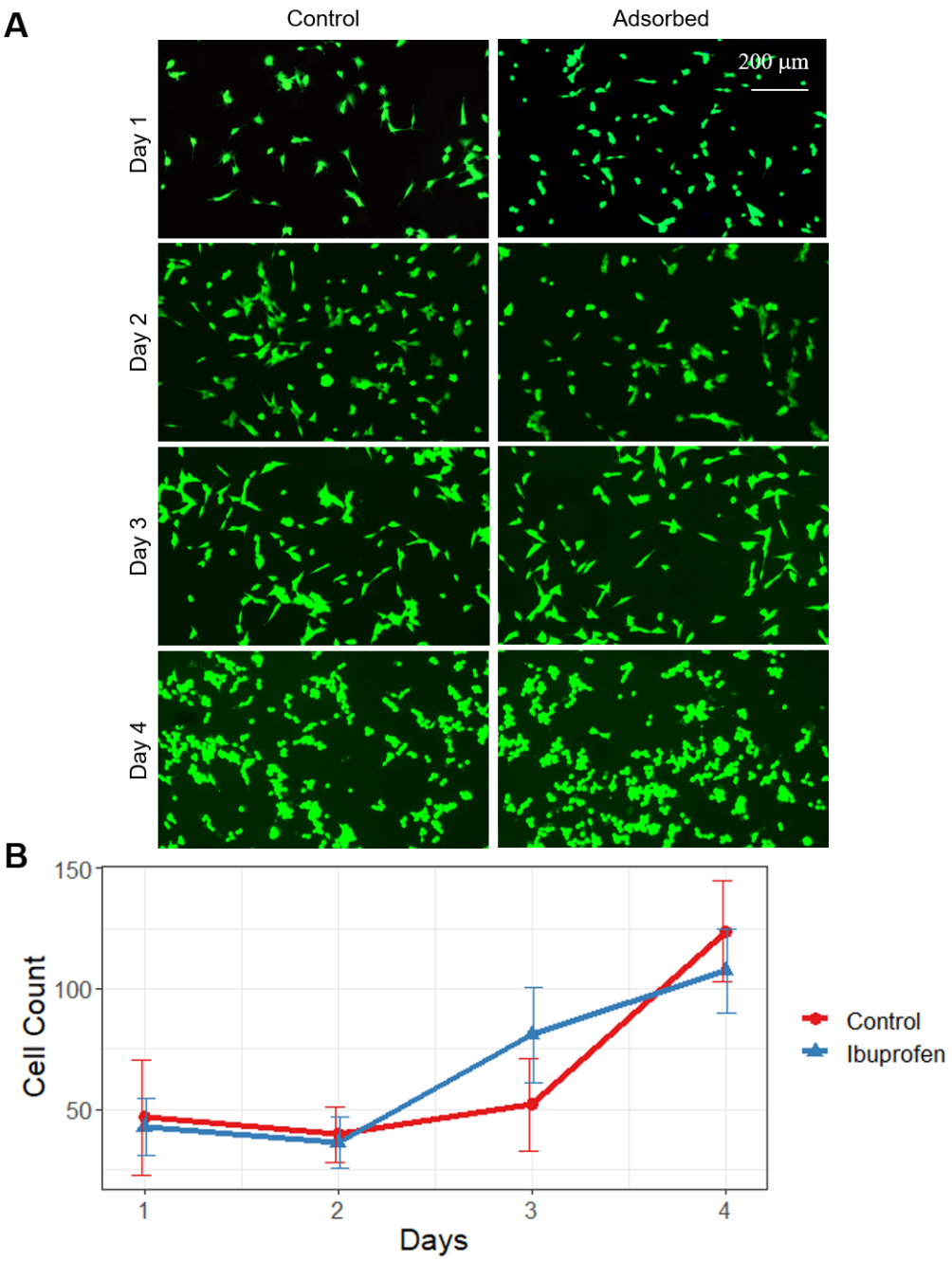

Figure 5.2 | **Effect of ibuprofen treatment on SH-SY5Y proliferation on GO film.** (A) Representative fluorescence images showing cells on GO/PEI film without or with pretreatment with ibuprofen on day 1, 2, 3and 4 days respectively, cultured in standard medium. Cells were stained by calcien-AM (green). (B) Mean cell count under indicated cultured conditions from n = 3 independent cell preparations.

have increased in number relative to day 3. Cell proliferation is quantified in Figure 5.2(B) which shows mean cell count follows a similar trend on both surfaces with no significant differences between the control or ibuprofen adsorbed surface at any time point. In line with expectations, the cell number increases over the 4 days with a significant increase ($p<0.05$) between days 2 and 3, and days 3 and 4 for both surfaces, indicating cells are proliferating normally after initial attachment to the ibuprofen-adsorbed surface. This is important as the adsorbed surface can be reasonably expected to have the highest availability and thus the highest concentrations of ibuprofen during these early time points.

5.2.3 Effects of adsorbed ibuprofen on SH-SY5Y cell differentiation

Following on from evidence that in the initial proliferation of SH-SY5Y is not affected by the adsorption treatment, the differentiation response of SH-SY5Y was investigated. Differentiation of SH-SY5Y is not a COX-2 pathway dependent process, therefore no interaction of this adsorption treatment with SH-SY5Y was predicted. However ensuring that cell response to stimuli remains as expected is important in confirming the biocompatibility of the adsorption modification.

Two sets of surfaces were used in this work. Films were prepared as previously without ibuprofen treatment were used as the Control condition for GO films. Identical GO films treated with ibuprofen as previously were used as the Adsorbed condition. Glass substrates were treated identically to GO films without or with the ibuprofen adsorption treatment. SH-SY5Y neuronal cells were plated in standard media and maintained with retinoic acid media to induce differentiation as previously described. Glass surfaces have been shown earlier to result in shorter neuritic projection from SH-SY5Y cells compared to the GO film, thus longer projections were expected on the GO films. In this work, C-AM was used to highlight the cell cytoplasm and neurite projections of live cells.

In Figure 5.3(A) cells on control and adsorbed GO film and glass surfaces are presented at day 10 and day 14. SH-SY5Y displayed the typical differentiation morphology, with cells in small clusters producing fine single branched neurite projections, which spanned

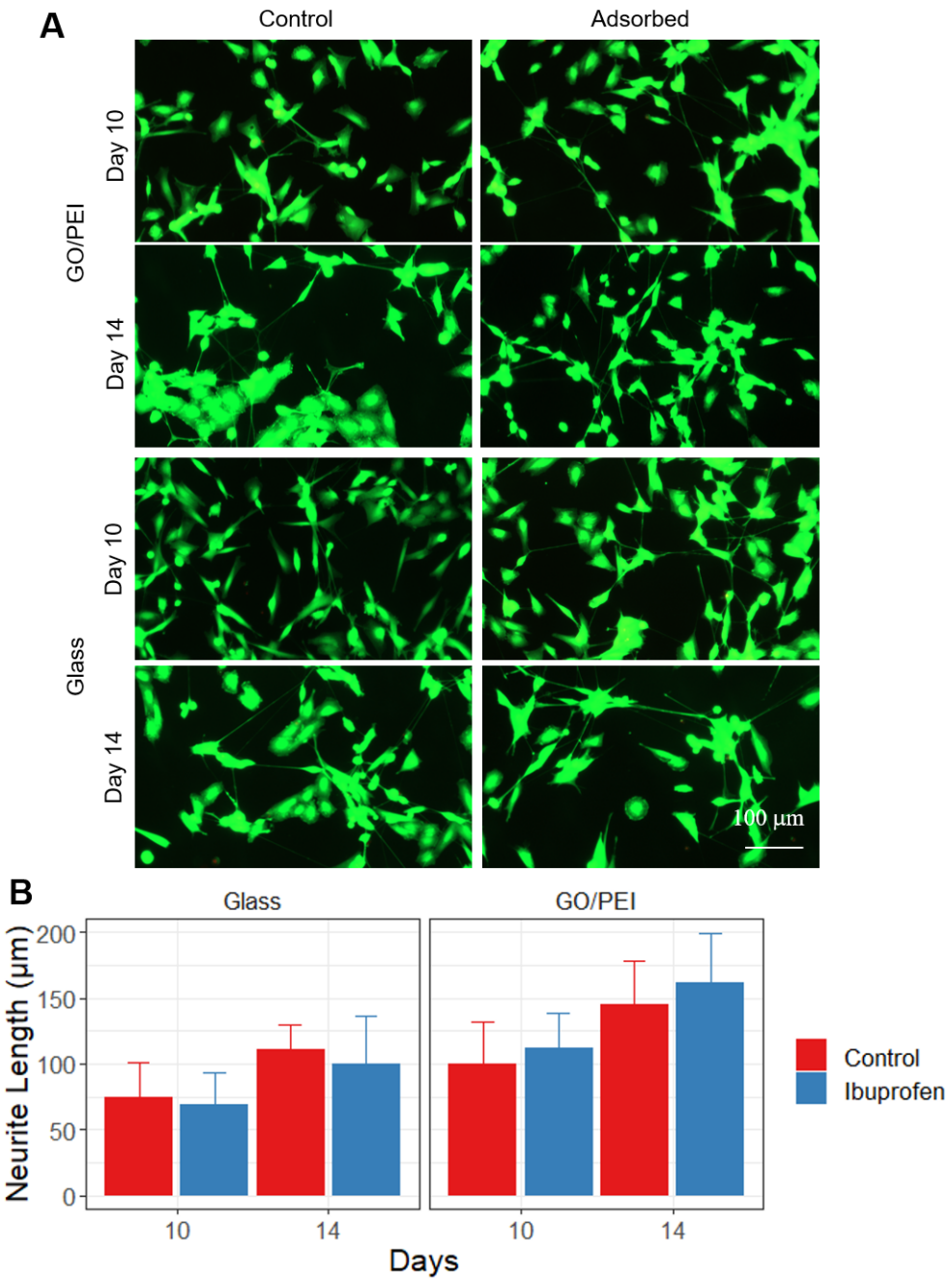

Figure 5.3 | **Effect of ibuprofen treatmet on neurite growth of SH-SY5Y cells..** (A) Representative fluorescence images showing cells on GO film or Glass surfaces without or with ibuprofen treatment on day 10 and 14 days respectively, cultured in retinoic acid differentiation medium, maintained every 4 days. Cells were stained by calcien-AM (green). (B) Mean neurite lengths in 200 cells from n = 3 preparations under indicated conditions.

between clusters. This was consistent with differentiation to the neuronal phenotype induced by retinoic acid. Cells in both treatment conditions on GO films appeared similar, fine neurite projections were apparent between cell clusters, comparatively longer at day 14 than day 10. Cells in both treatment conditions on glass also appear similar at both time points, with similar neurite morphology and again longer at day 14.

In Figure 5.3(B) the mean neurite lengths on each surface under each condition are presented. Cells on glass had shorter mean neurite length compared to cells on the GO film, in agreement with earlier data. On both surfaces, mean length increased between day 10 and day 14, showing differentiation had progressed. Importantly, no significant difference is seen between the ibuprofen adsorbed condition and the control condition on either surface at either time point. This confirmed the differentiation of SH-SY5Y remained unaffected by ibuprofen treatment of the GO film.

5.2.4 Effects of adsorbed ibuprofen on BV-2 cell proliferation

Following on from the evidence that the ibuprofen does not alter the proliferation or responses of SH-SY5Y cells GO film, the treatment was also investigated with BV-2 cells. In Section 4.2.4 BV-2 cells proliferated rapidly on GO films, in Section 4.2.5 the morphology of BV-2 cells on GO films was suggestive of an activated phenotype. Microglial cell activation involves the COX-2 pathway, thus the inhibitor treatment was expected to have a measurable effect in BV-2 cells on the GO film. The results of the present study would indicate if the adsorption treatment was sufficient to control BV-2 activation on the GO film.

Two surfaces were used in this work; GO films without (Control) and with (Adsorbed) ibuprofen treatment were prepared as above. BV-2 cells were plated to these surfaces in a parallel to the previous experiment described in Section 4.2.4. To investigate the viability and appearance of these cells over time, representative samples were taken at each time point and supplemented with Hoechst, PI and C-AM to reveal nuclei, dead-cells and live cell cytoplasm respectively.

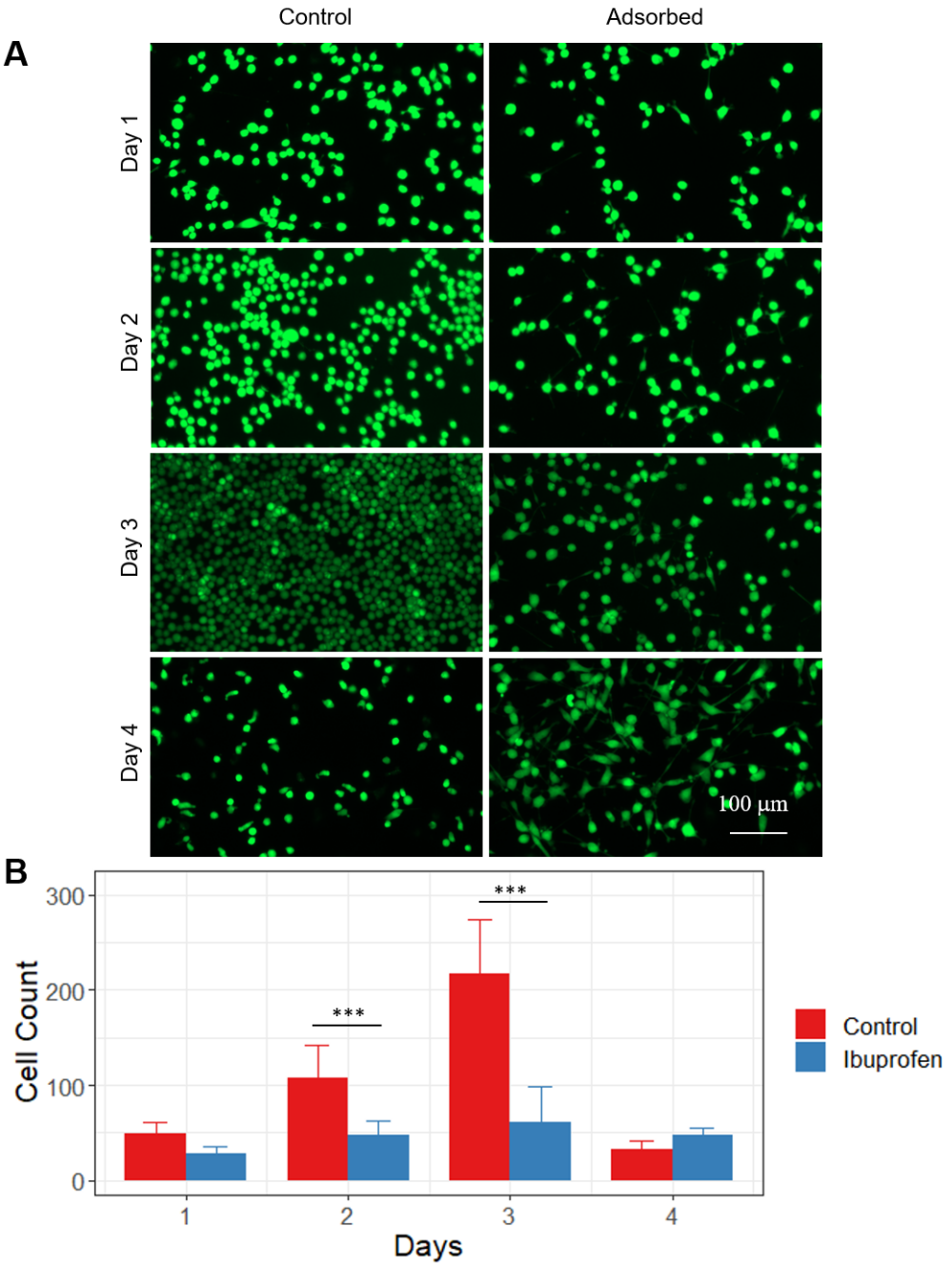

Figure 5.4 | **Effect of ibuprofen treatment on BV-2 cell proliferation on GO film.** (A) Representative fluorescence images showing cells on GO/PEI film without or with pretreatment with ibuprofen on day 1, 2, 3and 4 days respectively, cultured in standard medium. Images show cells stained by Calcien-AM (green). (B) Mean cell count under indicated cultured conditions from n = 3 independent cell preparations *** $p < 0.001$

In Figure 5.4(A) cells on control and adsorbed GO films are presented. There were noticeably more cells visible at day 2 and day 3 on the control surface compared to the adsorbed surface. This was most apparent at day 3, where cells on the control condition are approaching confluence, whilst cells on the adsorbed condition remain sparse and spaced apart. Additionally, BV-2 cells on the control surface were uniformly circular at all time points, consistent with the earlier reported activated morphology. In contrast, BV-2 cells on the adsorbed condition had a ramified morphology with a higher incidence of cells producing dendritic extensions. This morphology was best noticed at the day 4 time point where cells on the adsorbed condition have a noticeably ramified morphology compared to the control condition. Additionally, between day 3 and day 4, cells on the control surface showed a dramatic decrease in cell number, which was not observed on the adsorbed surface

This difference in cell count over is quantified in Figure 5.4(B). BV-2 were seen to be similar in number at day 1, and day 4. However at day 2 and day 3 there was significantly more cells present in the control condition compared to the ibuprofen adsorbed condition. The observed increase in cell number in the control condition is consistent with previously reported data on the proliferation of BV-2 cells on GO films. This indicates that the ibuprofen adsorption treatment has reduced the proliferation of BV-2 on the GO film. These findings are interesting, indicating that the ibuprofen has an effect on BV-2 when delivered via the GO film surface. There were also changes in morphology which are explored below.

5.2.5 Effects of adsorbed ibuprofen on BV-2 cell morphology

The above Section 5.2.4 showed that BV-2 microglial cell line proliferation was modified by ibuprofen treatment of the GO film. Additionally, the morphology of BV-2 cells on the GO film treated with ibuprofen was noticeably different To further understand this reaction, the morphology of BV-2 cells on these surface is explored here. In Figure 5.5(A) higher magnification images of cells from Figure 5.4 on control and adsorbed GO films at day 3 are

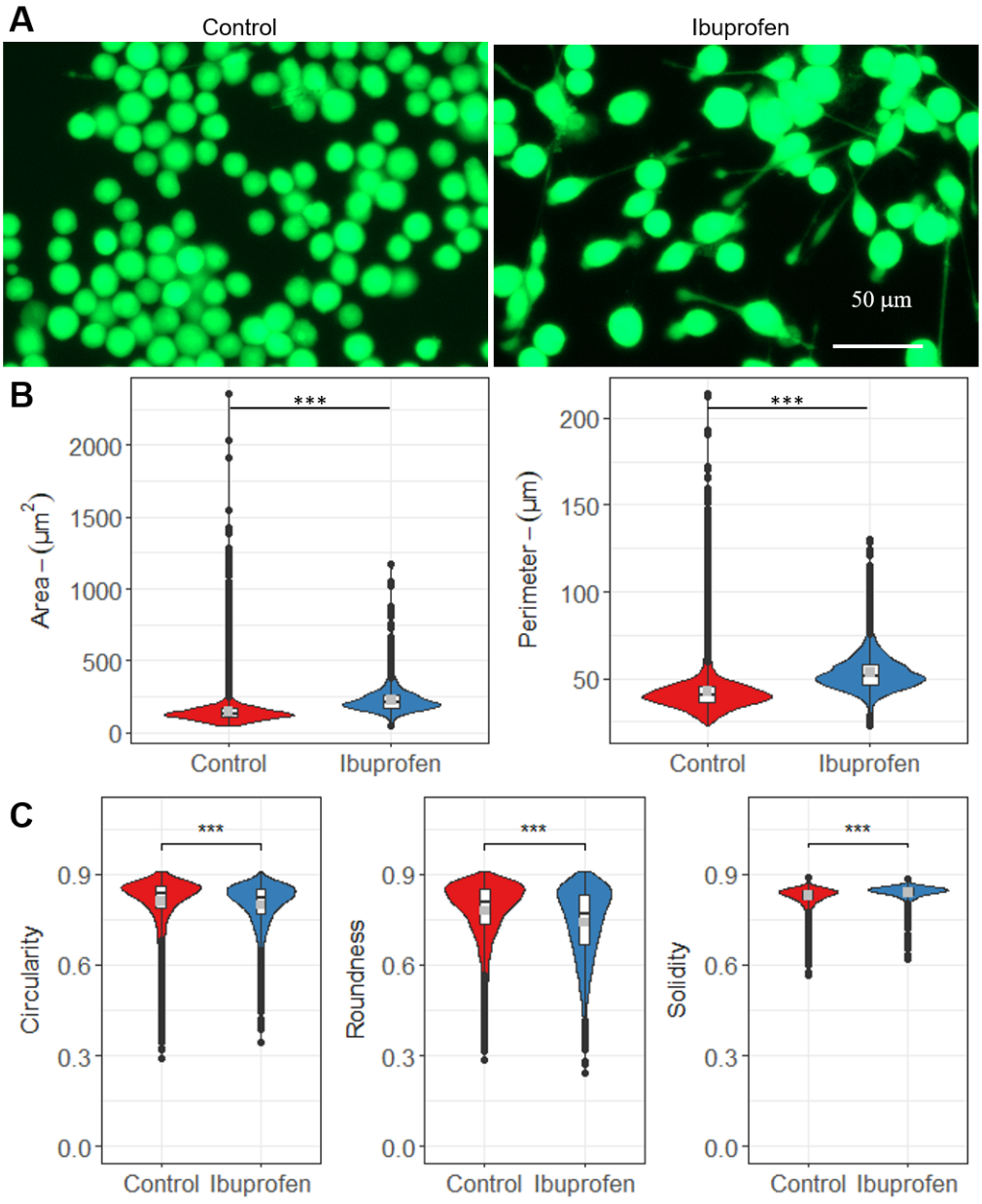

Figure 5.5 | **Effect of ibuprofen treated GO surface on BV-2 cell morphology..** (A) Representative fluorescence images showing cells on GO film without and with ibuprofen adsorbtion treatment on day 3, respectively, cultured in standard medium. Cells were stained by calcien-AM (green). (B) Mean (grey point), Range (white box) and Distribution (Violin) of individual cell area and perimeter measurements under indicated cultured conditions from n = 3 independent cell preparations. (C) Mean (grey point), Range (white box) and Distribution (Violin) of individual cell shape descriptors under indicated conditions, 2000 individual cells for glass and 2000 individual cells for GO from n = 3 independent cell preparations. *** $p < 0.001$.

presented. On the control surface BV-2 were uniformly round, tightly clustered and small. In contrast, cells on the adsorbed surface were larger, and had some dendritic projections. Figure 5.5(B) quantifies the differences in morphology in terms of cell size. BV-2 cells on the ibuprofen adsorbed surface were found to have significantly ($p<0.001$) larger mean areas, and longer mean perimeters, than cells on the control surface. Furthermore the range of cell area and perimeter observed was larger in the ibuprofen adsorbed condition.

In Figure 5.5(C) the shape of these cells is quantified. Cells on the ibuprofen adsorbed condition are significantly less circular, rounded and solid than cells on the control condition. This was due to the observed dendritic projections resulting in cells with more complex shapes. This shows ibuprofen had an effect, reducing the activation state of the BV-2 culture on GO films. Therefore adsorbed ibuprofen significantly decreases the proliferation rate and increases dendritic morphology of BV-2 cultured on the GO film model.

5.2.6 Effects of adsorbed ibuprofen on mouse microglial proliferation

Above, treatment of the GO film with adsorbed ibuprofen has been shown to alter the proliferation and morphology BV-2 microglial cells This is indicative of a shift from an activated, proliferative spheroid phenotype to a ramified morphology with reduced proliferation. In Section 4.2.10 microglia reacted differently than BV-2 to the GO film as a culture surface; where BV-2 appeared activated, mouse microglia appeared quiescent in a non-activated phenotype. Therefore it is important to confirm microglia remain unchanged by the ibuprofen treatment of the GO film.

GO films were prepared as above, with untreated GO films serving as the Control surface, compared against ibuprofen treated GO films as the Adsorbed surface. Microglial cells isolated from mouse brain tissue as described in Section 2.4.2.1 were identically plated to the untreated and ibuprofen treated films. To investigate the viability and appearance of these cells over time, representative samples were taken at each time point

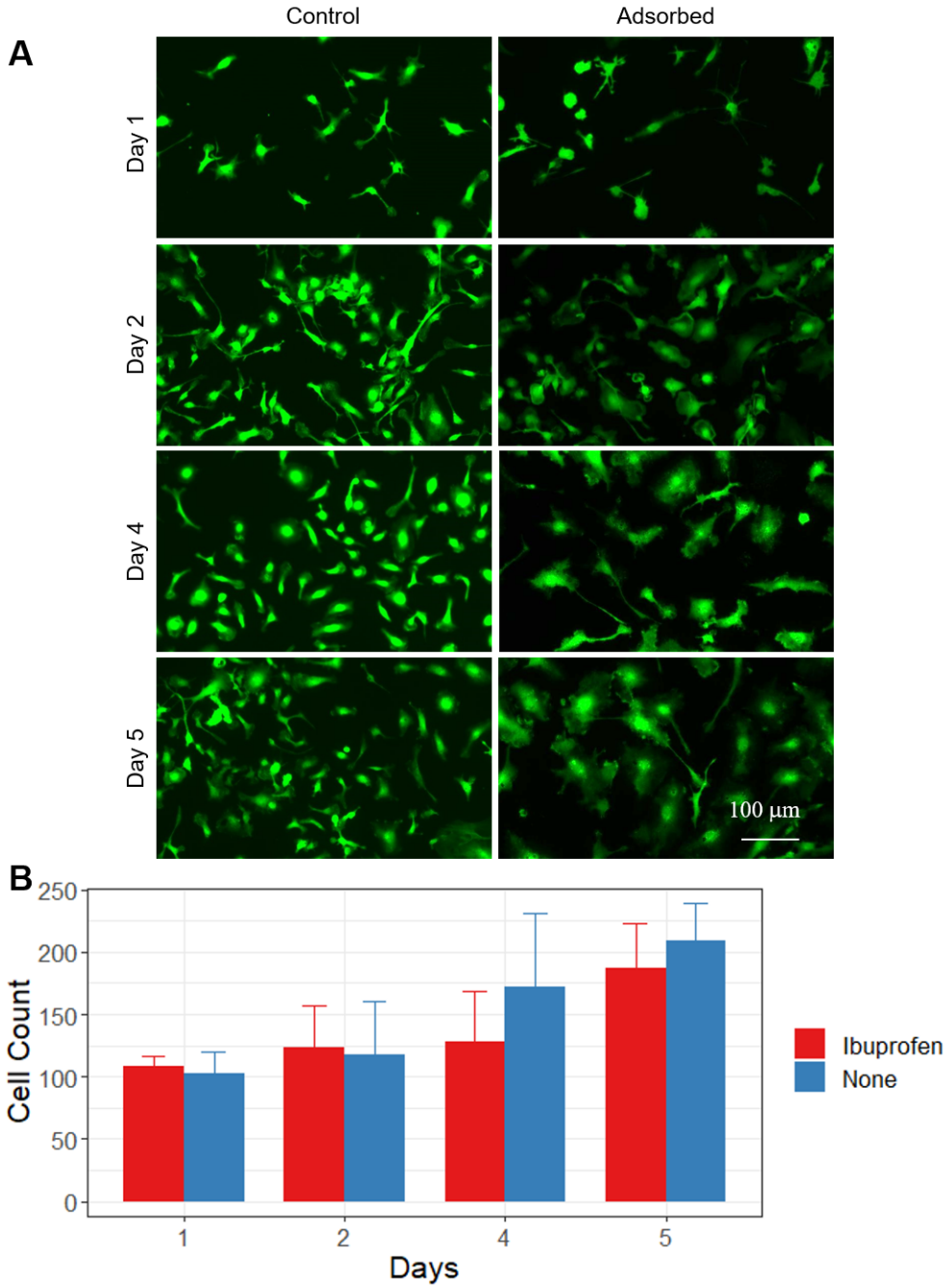

Figure 5.6 | **Effect of ibuprofen treatment on mouse microglia proliferation on GO film..** (A) Representative fluorescence images showing cells on GO/PEI film without or with pretreatment with ibuprofen on day 1, 2, 4 and 5 days respectively, cultured in 50:50 conditioned : standard medium. Cells were stained by calcien-AM (green). (B) Mean cell count under indicated cultured conditions from n = 3 independent cell preparations

and supplemented with Hoechst, PI and C-AM to reveal nuclei, dead-cells and live cell cytoplasm respectively.

In Figure 5.6(A) primary microglia on Control and Adsorbed GO films are presented. Microglia were similar at each time point on either surface, ramified with dendritic projections and closely clustered. In Figure 5.6(B) the mean cell count is presented for each surface. No significant difference in mean count was seen between the control and adsorbed conditions, cells increased in number in a similar way on each surface. This indicates the ibuprofen treatment does not effect the proliferation of microglia, unlike the effect seen above in the data from the BV-2 microglial cell line presented above (Fig 5.4).

5.2.7 Effect of adsorption treatments on mouse microglial activation

Ibuprofen adsorption treatment did not effect mouse microglia in a manner similar to the BV-2 microglial cell line. One key difference between the behaviour of these cells on untreated GO films, is BV-2 exhibited an activated while the mouse microglia did not. In Section 4.2.11 mouse microglia on the GO film were induced to an activated phenotype by addition of LPS. Therefore the present study aimed to investigate how adsorbed GO films effects this LPS induced activation of microglia. To diversify the potential adsorption treatments, minocycline has also been included in this work in addition to ibuprofen. Minocycline is a tetracycline antibiotic minocycline and a well characterised inhibitor of LPS induced microglial activation through inhibition of the p38 MAPK pathway [300, 301]. The physiochemical properties of minocycline and ibuprofen are summarised in table 2.1 [302, 303]. This work explored three objectives; if the ibuprofen adsorption treatment could effect microglial activation, if adsorption could be used with other known inhibitors of LPS activation, and if the effect was specific to the GO film or if other components of the system, specifically the undercoat, was responsible for adsorption.

To do this, two parallel experiments were conducted: First, mouse microglia have been plated to GO films with and without adsorption treatments at t=0 (Fig 5.7). Microglia on GO films without LPS treatment or adsorption treatment were used as a control showing

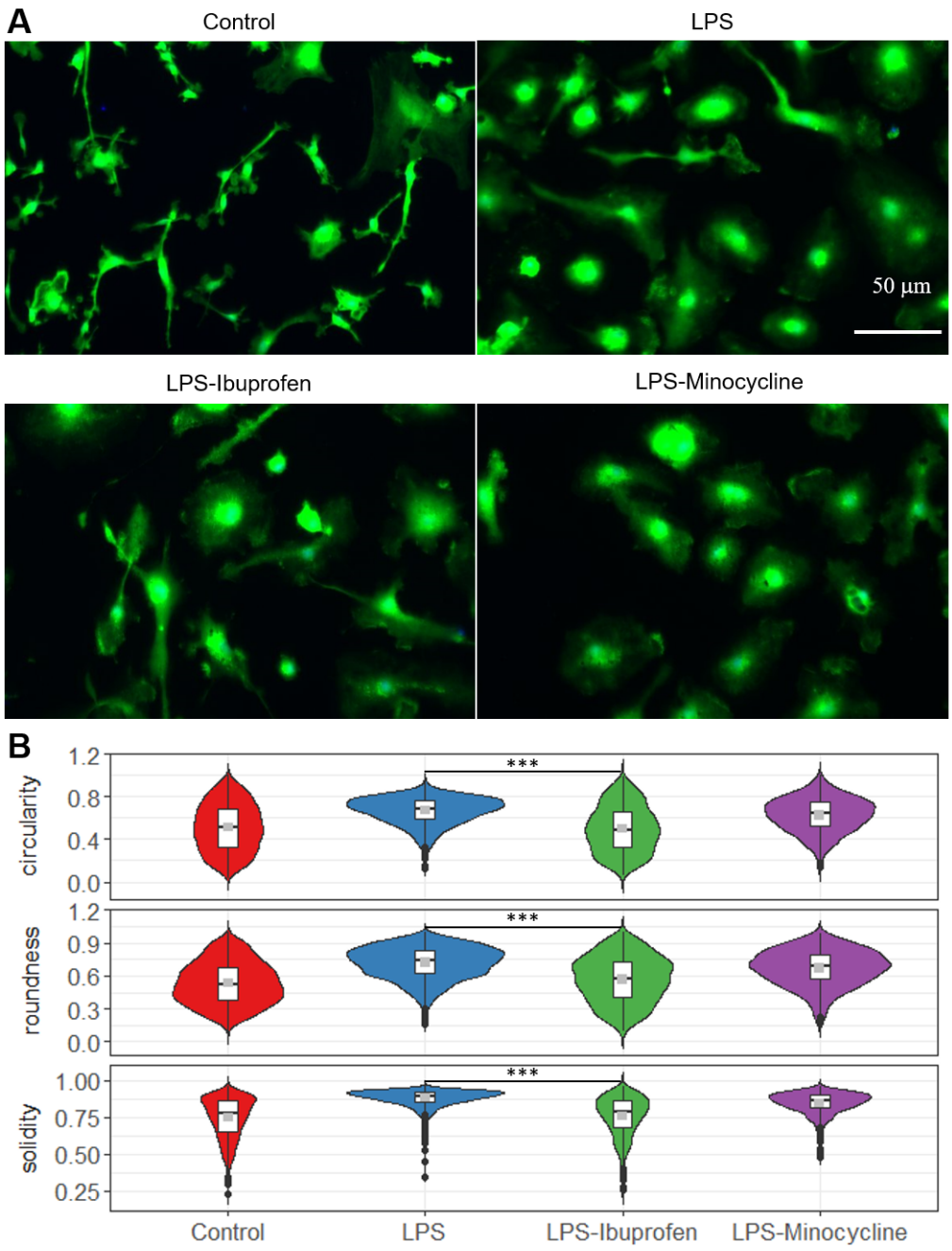

Figure 5.7 | **Effect of adsorption treated GO surfaces on primary mouse microglia morphology.** (A) Representative fluorescence images showing cells on GO film without and with LPS treatment, and LPS treated cells with ibuprofen or minocycline adsorption treatment on day 4, respectively, cultured in standard medium. Cells were stained by calcien-AM (green). (B) Mean (grey point), Range (white box) and Distribution (Violin) of individual cell shape descriptors under indicated conditions, 480 individual cells for each condition from n = 3 independent cell preparations. *** $p < 0.001$.

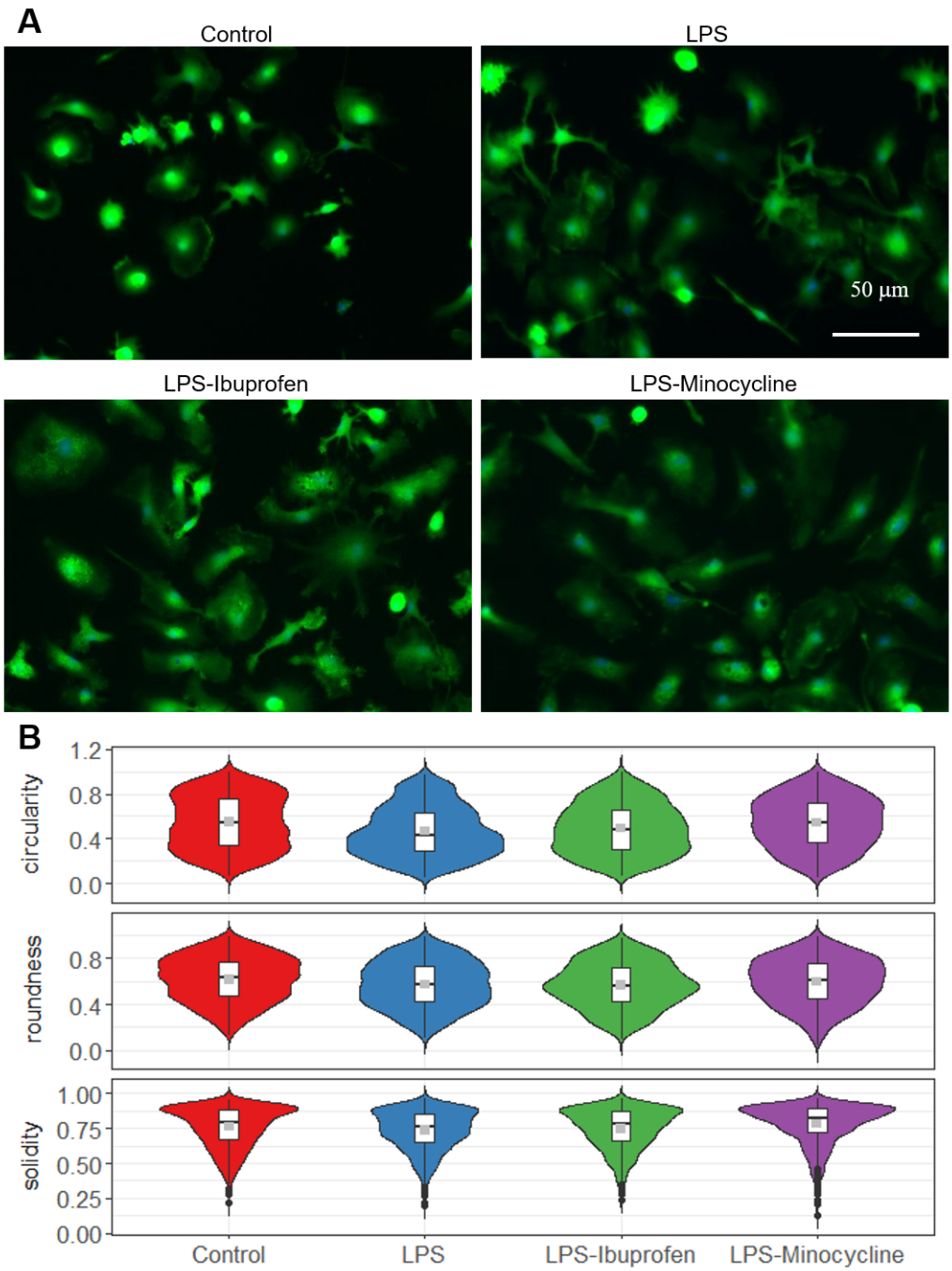

Figure 5.8 | **Effect of adsorption treated PEI surfaces on primary mouse microglia morphology..** (A) Representative fluorescence images showing cells on PEI without and with LPS treatment, and LPS treated cells with ibuprofen or minocycline adsorption treatment on day 4, respectively, cultured in standard medium. Cells were stained by calcien-AM (green). (B) Mean (grey point), Range (white box) and Distribution (Violin) of individual cell shape descriptors under indicated conditions, 480 individual cells for each condition from n = 3 independent cell preparations.

the ramified microglial morphology (Control). Identical cultures subsequently treated with LPS at t=0.5 days to induce an activated phenotype were used as a control for the activated microglial morphology (LPS). A set of GO films treated with ibuprofen, plated with microglia, and treated with LPS provided the first experimental condition (LPS-Ibuprofen). An identical set of GO films were treated with minocycline, plated with microglia, and treated with LPS provided the second experimental condition (LPS-Minocycline).

At the same time, identically plated microglia on PEI coated substrates with the same adsorption treatments as above were identically treated with LPS (Fig 5.8). In this way the differences between adsorption treatments on microglial LPS reactivity, and adsorption treatments with and without the GO film on microglial LPS reactivity were explored. Cells were stained with C-AM to highlight the cytoplasm of live cells.

In Figure 5.7(A) shows microglia on non-adsorbed GO films without LPS treatment, microglia on GO films with LPS treatment leading to activation and microglia treated with LPS on ibuprofen or minocycline adsorption treated GO films at day 3. In the control condition the normal ramified and dendritic morphology of microglia is visible. When treated with LPS microglia lost their ramified morphology and cells have become larger, and rounded, indicating these microglia have adopted an activated phenotype. When treated with LPS on Ibuprofen adsorbed GO film, the ramified morphology remained similar to the control condition. Treated with LPS on the minocycline adsorbed GO film the ramified morphology was again lost and cells became rounded, similar to the LPS activated condition.

These morphological changes are quantified as shape descriptors in Figure 5.7(B). A significant difference was seen in the circularity, roundness and solidity of microglia on the ibuprofen adsorbed GO film compared to cells on the GO film without any adsorption treatment when treated with LPS. LPS-Ibuprofen samples were less circular, less round and less solid indicating they retain more complex shapes than the LPS treated cells on GO films. Interestingly the LPS-Ibuprofen cells were not statistically different from the

Control condition cells without LPS activation, indicating the reactive phenotype was being inhibited by the ibuprofen adsorbed GO film. In contrast, the LPS-minocycline condition is not significantly different from the LPS treated cells on GO films. This suggests the minocycline adsorbed GO film did not inhibit the reactive phenotype.

In Figure 5.8(A), without the GO film, microglial cells cultured on PEI adopted more rounded morphologies with fewer dendritic projections, and respond to LPS stimulation by increasing size. Figure 5.8(B) again quantifies the morphology as shape descriptors. Neither adsorption treatment was seen to have any effect on subsequent cell response to LPS stimulation. This indicates the adsorption of treatment is only effective in modifying microglial activation in the presence of the GO film, and is not dependent on the film undercoat.

5.3 Discussion

With a high surface roughness and heterogeneous polar and non-polar surface chemistry, adsorption of proteins and other organic molecules to GO surfaces has been previously explored in literature [174, 292, 304]. The present study examined how the 2D GO film model could be modified through adsorption and effect *in vitro* neural cell attachment and morphology. The GO film was found to adsorb protein and pharmaceutical molecules from solution to the surface, in this way the surface served as a vector to deliver these molecules to the plated cells. This adsorption was performed via incubation with with molecules in suspension prior to cell plating. Adsorption treatment with 10% FBS standard media was seen to provide enhanced cell attachment to the GO film in serum free plating conditions. GO film biocompatibility was not negatively affected, and adsorption of ibuprofen did not alter the expected responses of non-microglial cells. However in the BV-2 microglial cell line, proliferation was significantly reduced by adsorbed ibuprofen. This reduced proliferation was accompanied by a restoration of the ramified BV-2 morphology from a rounded-activated morphology previously observed on the GO film. Interestingly, adsorbed ibuprofen produced measurable effects in LPS activated mouse microglia, but minocycline did not, indicating a difference in the adsorption process based on the molecular chemistry. In general, the GO film will adsorb molecules from solutions during incubation, and these molecules can subsequently effect neural growth and morphology during culture.

5.3.1 Effects of vitronectin adsorbed to GO films

GO films exposed to 10% FBS containing media become coated in a robust, detectable layer of biomolecule characterised as vitronectin with a distinctive XPS spectra. Vitronectin coating is commonly used to promote cell adhesion for plastic surfaces, and is an important part of initially seeding cells within serum-containing media [290]. In traditional cell culture practice and elsewhere in this thesis, cells are plated in 10% FBS containing media

to provide vitronectin and aid in attachment of cells to surfaces. In this chapter we have shown that GO films exposed to 10% FBS containing media are capable of supporting better SH-SY5Y cell attachment than untreated GO films, or identically prepared glass surfaces as shown by Figure 5.1. In this study, cells were plated in serum free conditions to remove this source, thus only vitronectin deposited on the surface during the adsorption treatment was available. Thus, the adsorption of vitronectin by GO films produced a measurably superior cell attachment surface. This finding contributes to the understanding of other observations in this thesis; for example the higher count of initial mouse neuron and astrocyte cells attached to GO films compared to glass surfaces of identical area seen in the previous chapter. It is clear this vitronectin coating derived from the culture environment provides immediate benefit to the attachment of primary cells. Importantly, this passive coating consequence was not found impact the maturation or reactivity of primary cells on the GO film.

In comparison with other sources, other reports do not characterise the deposition of media components to GO or graphene scaffolds. This is an important factor in the initial cell attachment and growth of neural cells relative to surfaces with limited adsorption capacity. Importantly, this cannot be considered a source of systematic error as the GO film is demonstrably superior at passively adsorbing and retaining molecules from solution. Thus any study comparing a non-adsorbing surface against a GO enhanced surface must consider this as a contributing factor in cell growth, attachment and differentiation.

5.3.2 Effects of pharmaceuticals adsorbed to GO films

Though the adsorption of vitronectin to the GO film is interesting and of academic use as a research tool, it is of limited therapeutic utility. To enhance the instructive capability of GO, adsorption of cell modifying molecules is desirable. In this chapter, I have presented the adsorption of a COX-2 inhibitor (RS)-2-(4-(2-methylpropyl)phenyl)propanoic acid (Ibuprofen) to the GO film. This adsorption treatment is observed to produce a significant effect on the reactivity of microglial cells. Importantly this effect is shown to be specific,

with no detected effects in the development of SH-SY5Y neuronal cells.

In the previous chapter, BV-2 cultured on the GO film surface had an activated phenotype and high proliferation similar to published literature on BV-2 cells [294]. In this chapter, ibuprofen adsorption treated GO films reduced the proliferative rate and restored a ramified morphology for BV-2 cells on the GO film characteristic of a non-activated phenotype. This is accompanied by significantly reduced proliferation, indicating the ibuprofen adsorbed GO film is having an effect on BV-2

Mouse microglia on the GO film remained quiescent with a complex dendritic morphology. In this work, microglia were induced into an activated phenotype using LPS. As explored in the previous chapter, following LPS treatment microglia remained viable increased in cell area and with higher roundness, circularity and solidity, indicating the cells were now no longer elongated but instead truncated and amorphous. GO films with adsorbed ibuprofen reduced the activated morphology caused by LPS. This restored the ramified dendritic microglial shapes seen on GO films without LPS treatment. Specifically, the roundness, solidity and circularity were significantly different from LPS activated microglia, statistically similar to microglia without LPS treatment. Therefore the GO surface can be adsorbed with ibuprofen to control and reduce microglial reactivity. Interestingly, Minocycline, another known inhibitor of microglial activation shows no effect as an adsorbed molecule [300]. This difference is explored below in discussion about the mechanism of the adsorption effects.

5.3.3 Mechanisms of adsorption and bioavailability via GO films

The molecular structures of ibuprofen, minocycline and vitronectin are summarised in table 2.1. Vitronectin is a large and complex globular protein with a high affinity for hydrophilic surfaces such as the GO film [305]. Vitronectin adsorbs via conformal changes in the protein structure [306]. As shown in the earlier chapter, the GO film has a wrinkled and topographically random surface with an increased surface area compared to smooth glass substrates. Following adsorption treatment, vitronectin is therefore adsorbed to the

complex surface topography of GO film, with more contact between the protein and GO surface than the protein and smooth glass surface. Thus more vitronectin is adhered to GO films than glass, providing adhesion sequences for subsequently plated cells.

The adsorption mechanism between GO and ibuprofen comprises spontaneous physiosorption of ibuprofen from solution and sequestering via Van-Der Waals forces and electrostatic interaction to the GO surface between carbon ring structures [307]. This bond is strong, methods for detaching organic contaminants similar to ibuprofen from GO platelets reported in literature has involved concentrated nitric acid [304]. Ibuprofen has a non-polar benzene ring structure and carbon chain conjugated to a polar propanoic acid. The bulk of the ibuprofen molecule is therefore non-polar, resulting in a low solubility in aqueous solution. Following adsorption treatment in the alcohol buffer, ibuprofen remains robustly adhered to the surface topography of the GO film as a precipitate, resistant to solubilisation. Ibuprofen is a lipid soluble molecule able to enter cells directly via diffusion across the plasma membrane leading to inhibition of and subsequent disruption of the COX pathway [308]. Importantly, adsorbed ibuprofen remains locally bioavailable via direct contact with the extracellular membrane.

Like ibuprofen, minocycline has an aromatic carbon ring structure. Adsorption between GO and minocycline therefore also comprised a spontaneous physiosorption of minocycline from solution and retention via Van-Der Waals forces, however a greater portion of this is polar interactions and hydrogen bonding between GO and minocycline polar groups. Minocycline has a higher solubility in aqueous solutions, with extensive polar groups on the tetracycline carbon structure. Thus, following adsorption treatment, minocycline adsorbed to the GO film solubilises during wash steps into culture media depleting the surface of adsorbed minocycline. Adsorption in this case is therefore less robust and equilibrium dependent, resulting in a decrease in adsorbed minocycline during washing and cell culture [309]. Therefore in cell culture minocycline is depleted from the cellular micro-environment and is therefore not able to suppress the LPS induced inflammatory reaction.

The differences in these adsorption behaviours and the detectable biological effects point to low solubility, lipid soluble carbon rich molecules such as ibuprofen being ideal candidates for pharmacological enhancement of the GO film surface for scaffold engineering. Furthermore, complex protein molecules such as vitronectin are readily adsorbed by the GO film, and do not impact the bioavailability of adsorbed ibuprofen. However molecules with extensive polar interactions such as minocycline are easily solubilised from the GO surface and thus are poor options for scaffold enhancement.

5.4 Conclusion

In this research the adsorption of ibuprofen to GO films has been used to reduce microglial reactivity to LPS *in vitro*. Adsorption treatment does not alter the biocompatibility of the GO film, including the cell attachment or viability, however leads to changes in proliferation rate and morphology of BV-2 cell line, and morphology of mouse microglia. The adsorption of ibuprofen does not alter neuronal cell lines, however adsorption can be used to enhance attachment in culture conditions that do not include FBS or attachment enhancing molecules. In summary, the GO film model can be used as a platform for investigation of low solubility carbon rich pharmaceuticals in direct cell culture, with the potential for other drug-cell interactions to be developed.

Chapter 6

Hydrogel Models supplemented with Graphene Oxide

6.1 Introduction

In this thesis the understanding of GO biocompatibility has been developed in the context of use as a 2D surface. The progression to advance this material for tissue engineering is to compound GO into a 3D model. Therefore this chapter presents the characterisation, progression and development of hydrogel models for use with GO and eventually neural cells.

Cross linking of macromer molecules to form hydrogels can progress along one of two pathways either involve linking macromer chains directly (chain growth) or via use of a secondary cross linking molecule (step growth). In the present study, two hydrogel macromers have been formulated and kindly provided by K.S Lim of the University of Otago. The first hydrogel system was Gelatin-Norbornene (Gel-Nor), a modified gelatin macromer with a bridged cyclic hydrocarbon group for step-growth hydrogel formation. This system requires a thiol rich cross linker such as Dithiothreitol, however alternative thiol rich target groups could be used as cross linkers. Previous reports have

demonstrated that thiol modified molecules heparin could be used as cross linkers in thiol-norbornene hydrogel matrices, posing the possibility that step-growth hydrogels could be better integrated with GO by modification of GO with thiol groups [67, 114].

The second hydrogel system was Gelatine-Methacryloyl (Gel-Ma), a gelatin macromer with pendant methacrylate groups for chain growth hydrogel formation. This system requires no cross linking molecule, rather macromers cross link via reaction between methacrylate groups. Chain growth hydrogels are more prone to cyclisation - where macromer pendant groups combine within a single gelatine molecule instead of between different molecules, making the chain growth system potentially more unpredictable than step growth hydrogel systems. However, because chain growth hydrogel does not depend on a cross linking molecule, toxic exposure for cell culture during cross linking is reduced.

To explore the potential of the hydrogels as scaffolds, the biocompatibility of alternative cross linking systems independent of ultraviolet light were characterised. The first alternative was a redox system, in which a chemical reaction was used to drive cross linking propagation between the macromer. The second alternative was a visible light irradiation based free radical system.

Furthermore, the mechanical properties and cross linking characteristics of hydrogel formulations were investigated. Mechanical stiffness of two formulations of Gel-Ma have been characterised via rheometry to determine the storage and loss moduli and therefore the viscosity. The viscoelastic properties of the hydrogel formulations are important attributes for providing an environment suitable to the growth and development of structurally complex neural cells. Brain tissue has been characterised in literature using the elastic storage component (G') and plastic deformation loss component (G") moduli expressed as the ratio (tanδ) [310] as an elastic solid with a G' between 1e+02 - 1e+03 Pa and G" between 1e+01 - 1e+02 Pa.

Finally, two different models for compounding cells into hydrogels to form a 3D culture model have been explored, including encapsulation of the cells within the pre-crosslinking formula and a layering system utilising the existing 2D GO model. This led to two different

ways of combining graphene oxide with the hydrogel, exploring how graphene oxide with the hydrogel affects cells.

The aim of this study was threefold. First, characterise the present hydrogels including the mechanical properties, *in vitro* durability and biocompatibility of the formulations, and the morphology of cells cultured with the system. Next, GO was combined in two ways with hydrogels to investigate how GO could be combined with hydrogel, and if the positive effects of GO reported in earlier chapters translated into a 3D scaffold. Finally, this study aimed to provide a route for which the GO material could be advanced as a neural scaffold.

6.2 Results

6.2.1 Redox initiated Gel-Ma hydrogels

Reductants	Oxidants
Tetramethylethylenediamine (TEMED)	Sodium Persulfate
Dithiothreitol (DTT)	Ammonium Persulfate
Ascorbic Acid (ASC)	Potassium Persulfate

Table 6.1: Reductants and Oxidants used as part of the redox generated free radical cross linking system. All combinations of reductant and oxidant were investigated.

To first identify if a redox initiated hydrogel system could be a biocompatible alternative to the existing visible light initiated system, a series of redox initiated hydrogels were characterised for cell viability and soluble fraction. The visible light initiated system previously and extensively characterised by Lim et al was used as the standard to which this redox system was compared.

The oxidants and reactants comprising 9 redox initiator combinations used to generate free radicals and catalyse the cross linking reaction are listed in table 6.1. Each oxidant was used with each reductant and vice-versa. Formulation of the hydrogel macromer was conserved across initiators as described in Section 2.3 and contained $1x10^6$ human

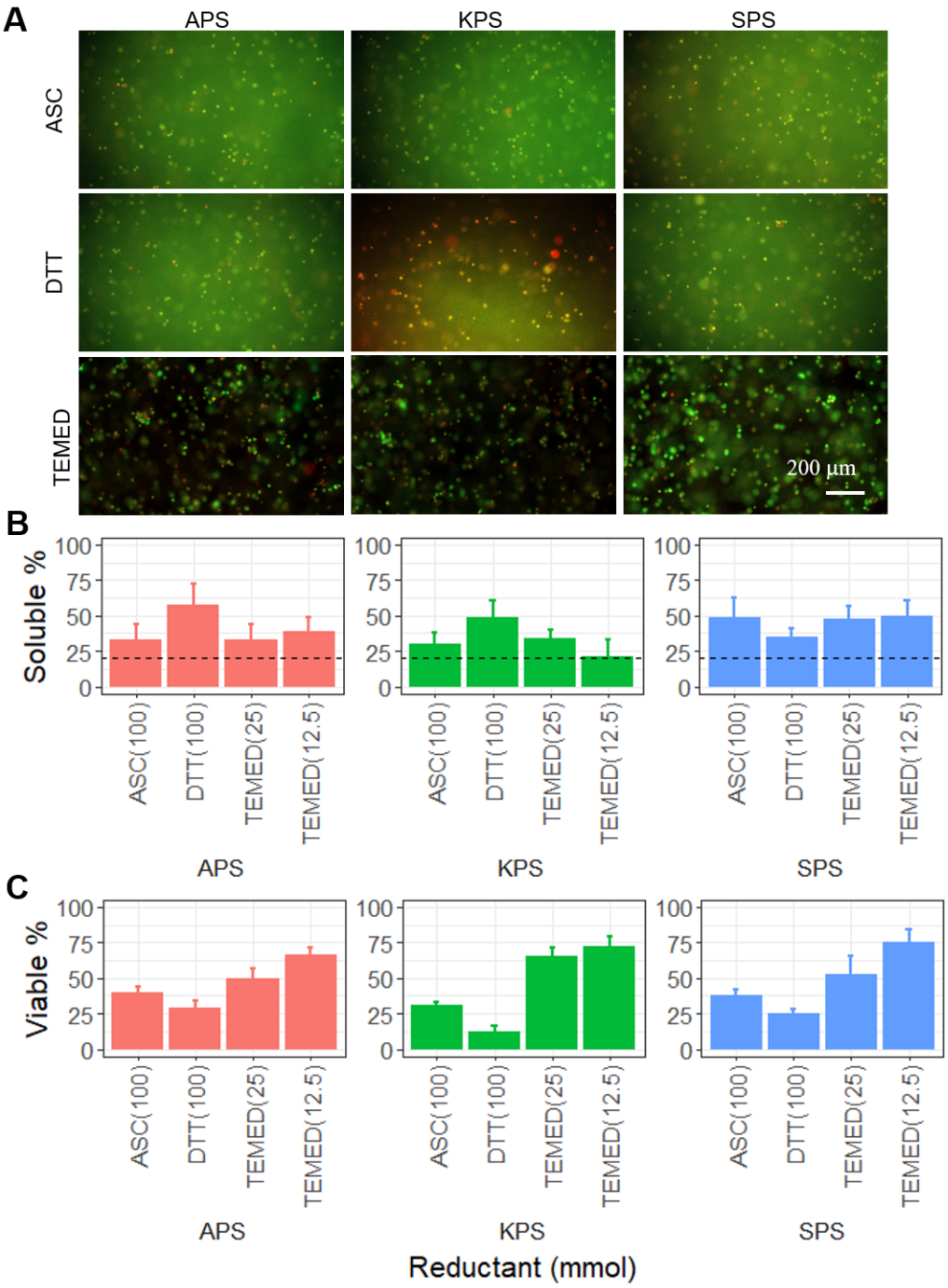

Figure 6.1 | **Comparing solubility and biocompatibility of redox cross linked Gel-Ma Hydrogel..** (A) Representative fluorescence images of human foreskin fibroblasts encapsulated within 10% w/v Gel-Ma hydrogel cross linked with indicated initiator conditions. Images taken at 48 hours after cross linking, cells are co-stained with Calcien-am (Green) and Propidium Iodide (Red). (B) Mean soluble fraction for indicated reductants with each oxidant. Dashed line indicates 20% soluble fraction acceptance level. (C) Viability of encapsulated cells under indicated conditions at 48 hours after cross linking from n=3 independent preparations.

foreskin fibroblasts per ml of pre-crosslinked hydrogel mixture. 30uL aliquots of the pre-crosslinked hydrogel were pipetted into silicon moulds, shielded from the air with coverslips and incubated in a cell culture incubator at 37°Cfor 1 hour. These conditions were chosen to accelerate the rate of reaction compared to cross linking at room temperature, in addition to more closely imitating in vivo conditions. Following cross linking, gels were characterised for viability as before, and soluble fraction as described in Section 2.5.4

Figure 6.1(A) shows fibroblasts were successfully encapsulated into the hydrogel formulation and remained intact following cross-linking. Cells were observed throughout the gel structure evenly distributed. Interestingly, several cells were observed to dual stain with C-AM and propidium iodide, indicating permeability of cell membranes.

Figure 6.1(B) shows the soluble fraction performance of the redox initiator systems, with the minimum acceptance criteria of 20% soluble fraction marked. No redox initiator combination resulted in <20% soluble fraction. Only the TEMED/KPS at [12.5mmol] formulation approached this acceptance level, after an hour in cross-linking conditions.

Finally, in Figure 6.1(C), viability of the encapsulated fibroblasts is presented. Mean viability for all redox initiated hydrogels was below 75%, which is partially explained by the high number of dual stained cells, which for purposes of analysis were assumed to be cells undergoing cell death. This low viability indicates the redox initiator systems were not a biocompatible alternatives to irradiation approaches using Gel-Ma. Furthermore the low gel efficiency indicates this redox initiator system was not a reliable alternative for creating acellular gel samples. Finally with a cross-linking time of 1 hour, the redox initiator system was not fast or efficient for research. The visible light initiator system reported by Lim et al was available as an alternative for progress with future work [73]

6.2.2 Gel-Nor and Gel-Ma durability in culture conditions

Next, it was important to identify which visible light initiated hydrogel system was suitable for prolonged cell culture, as maturation of the neuronal cell cultures used in this thesis require up to 14 days. The same formulation of ruthenium visible light initiator system was

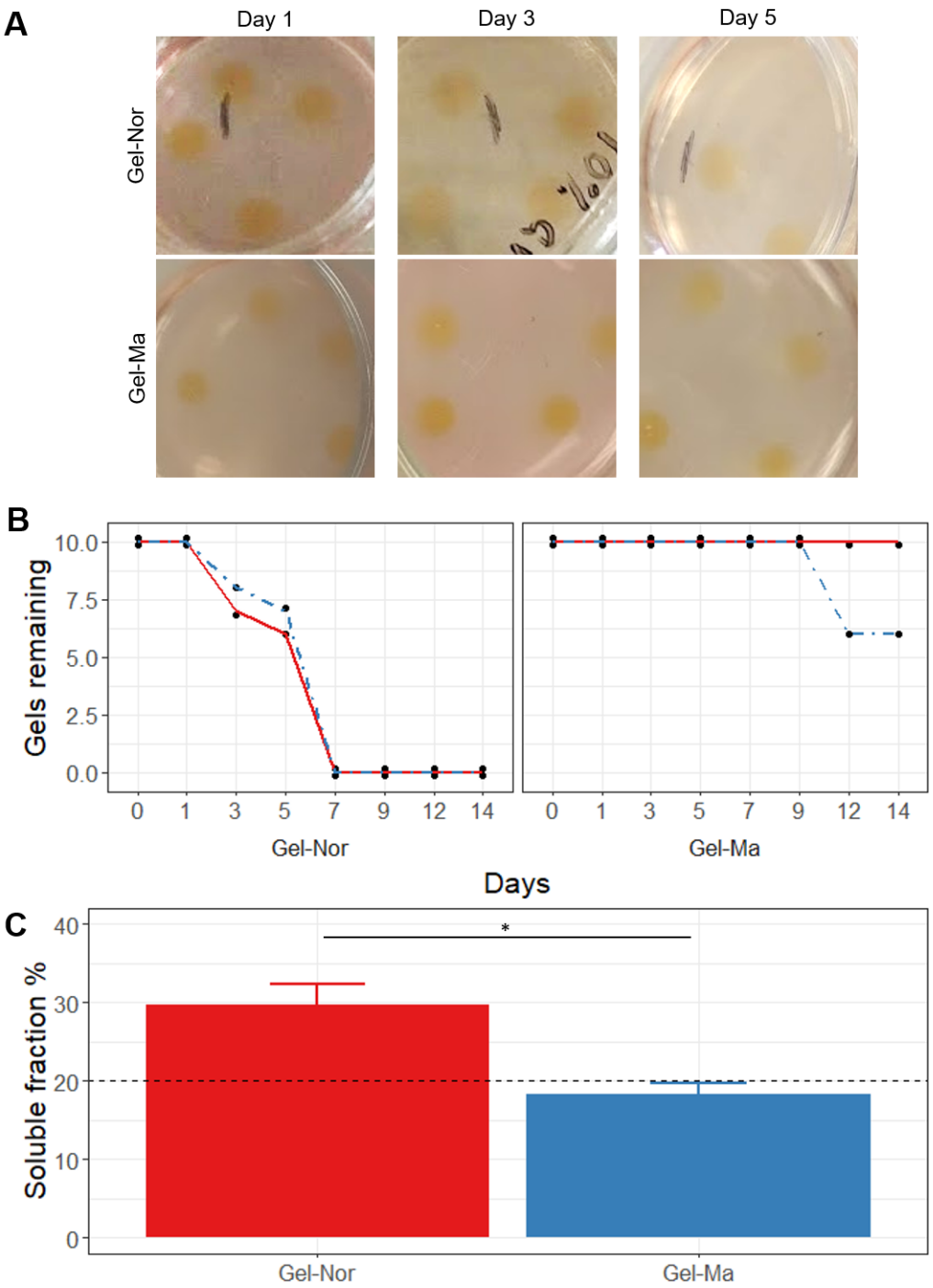

Figure 6.2 | **Comparing survival in culture conditions over time of Gel-Nor and Gel-Ma Hydrogel.** (A) Representative photographs of Gel-Nor and Gel-Ma hydrogels kept in culture media in culture conditions at 1, 3 and 5 days respectively. (B) Survival curves for gels without (red line) and with graphene (blue dashed line) inclusions observed every 2 days. (C) Soluble fraction data for 10% w/v Gel-Nor and 3% w/v Gel-Ma Hydrogels after cross linking in for 60 samples from n = 3 independent preparations * $p < 0.05$.

suitable for both Gel-Nor and Gel-Ma, thus the variable in this work was the macromer.

Hydrogels were prepared as casts as described in Section 2.3. Casts were at 10% w/v or 3% w/v final macromer concentration for Gel-Nor and Gel-Ma respectively. Following cross linking, gels were immersed in standard media in 6 well plates and stored in a cell culture incubator for up to 14 days. Samples were inspected visually every 2 days starting at 1 day and intact gels in each well counted. To simulate cell culture, media was maintained every 4 days. For soluble fraction quantification,

Figure 6.2(A) shows images of gels at 3 early time points. Over this period, Gel-Nor samples were seen to dissolve compared to Gel-Ma samples. Particularly, Gel-Nor hydrogels were seen to become larger and less well-defined compared to Gel-Ma. The number of samples remaining at each survey is illustrated as survival curves in Figure 6.2(B). By day 7, no Gel-Nor samples remained, dissolving completely and leaving a yellow discolouration of the culture medium from the ruthenium heptahydrate initiator. In contrast, the majority of Gel-Ma samples remained intact until day 14. Figure 6.2(C) characterises the difference between macromers in terms of soluble fraction, again the minimum 20% minimum acceptance is marked. Gel-Nor hydrogels did not reach the minimum acceptance of soluble fraction, the higher soluble fraction explains the loss of samples during the survival data. By contrast the Gel-Ma hydrogel demonstrated significantly lower and thus acceptable soluble fraction.

From these data, it is clear that the step-growth Gel-Nor system has poor durability in prolonged culture conditions. Gel-Ma by contrast is durable for 14 days and has good soluble fraction performance at much lower w/v % concentrations corresponding to a wider range of optimisation possibilities for gel stiffness and water content.

6.2.3 Effect of GO on Gel-Ma swelling

Next, it was important to characterise how including GO in the affected the cross linking of Gel-Ma. Additionally, the effect of changing the hydrogel macromer concentration was characterised in the same terms. If GO resulted in significantly different hydrogel

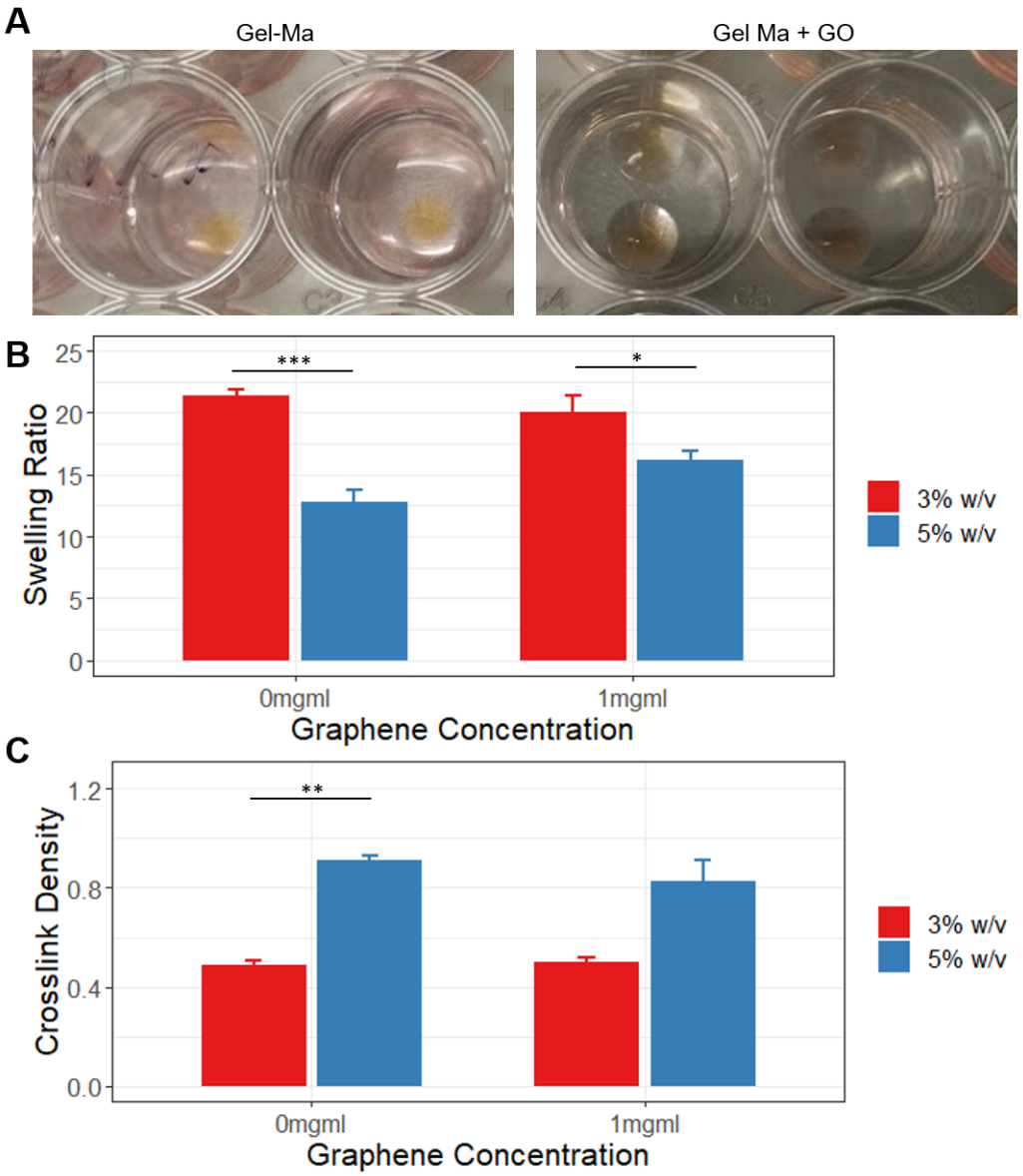

Figure 6.3 | **Comparing gel performance characteristics without and with GO inclusion in two concentrations of Gel-Ma Hydrogel. .** (A) Representative photographs of Gel-Ma hydrogels without and with GO inclusion respectively. (B) Swelling ratio for gels with indicated formulations following cross linking (C) Cross linking density estimation for gels with indicated formulations following cross linking. 10 gels measured per formulation for a total of 40 gels in each of n = 3 independent preparations *** $p < 0.001$ ** $p < 0.01$ * $p < 0.05$.

characteristics then this would provide a basis to understand any differences observed with cell inclusion. In particular if the GO resulted in less efficient cross linking this would require modification of the formulation to compensate.

Two concentrations of Gel-Ma hydrogels were prepared as casts as above but without or with inclusion of 1mgml GO. Casts were at 5% w/v or 3% final macromer concentration. Following cross linking, and characterised by mass loss and swelling as described previously.

Examples of gel appearance without and with GO inclusion is shown in figure 6.3(A). Addition of GO changes the colour of the gel from yellow to dark brown, however gels remained transparent and therefore permeable to visible light. In Figure 6.3(B) the mean swelling ratio of gels was seen to decrease as macromer w/v concentration is increased. However addition of GO did not significantly alter the swelling ratio of the gel. In Figure 6.3(C), the mean crosslinking density of the hydrogel was not affected by the addition of GO to the hydrogel. Cross-linking density was significantly increased at the higher macromer concentration without GO. When GO was included the difference in means remains but significance is lost ($p = 0.373$).

6.2.4 Effect of GO on Gel-Ma rheology

The Gel-Ma system was adapted from a method using 10% hydrogels as chondrogenic scaffolds and 3D printed bioinks. In this thesis, the gels were reduced in w/v concentration to produce in softer gels more suitable for neural culture. Above, the cross linking characteristics of Gel-Ma without and with GO at two concentrations has been characterised mathematically. In the present study, the rheology of these formulations has been characterised.

In Figure 6.4 the moduli across the whole testing range are presented for each gel formulation. Reducing the hydrogels to 5% and below resulted in very soft gels. Addition of GO to the hydrogel does not significantly change G' or G" as seen in Figure 6.4(A-B), however reducing the hydrogel w/v to 3% does significantly reduce both moduli. In

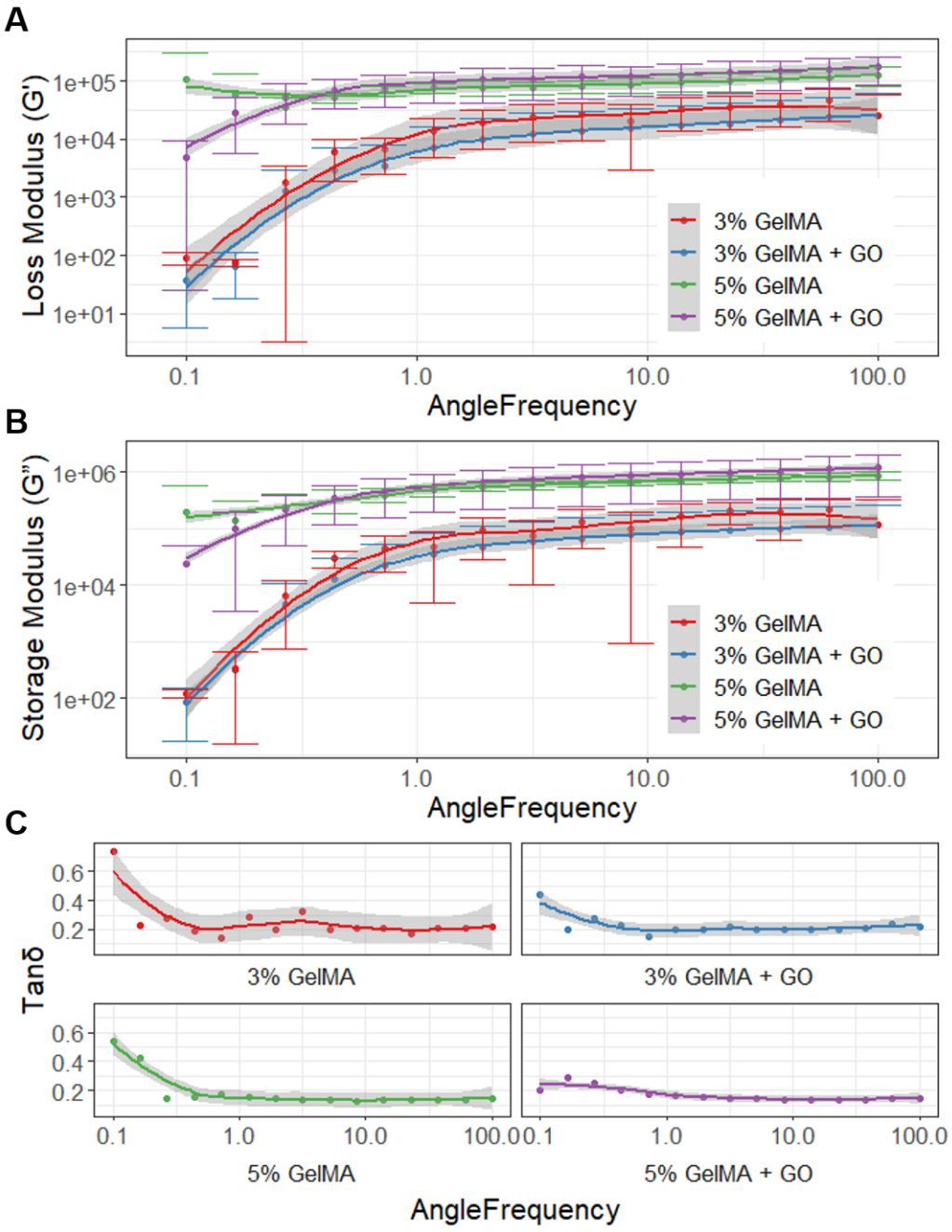

Figure 6.4 | **Comparing rheometry characteristics without and with GO inclusion in two concentrations of Gel-Ma Hydrogel. .** (A) Loss modulus of gels without and with GO inclusion at 3% and 5% w/v as indicated. (B) Storage modulus of gels without and with GO inclusion at 3% and 5% w/v as indicated. (C) Tan ratio (G/G) for gels with indicated formulations

Figure 6.4(C) the tanδ calculated by taking G''/G' remains less than 1 for all formulations indicating that the gel microstructure is behaving as an elastic solid rather than deforming plastically. Moduli follow the same profile in 5% vs 3% gels, however 3% gels have lower moduli across the whole angular frequency range indicating the gel is softer.

In published sources of brain tissue rheology, tanδ increased as frequency increases, indicating the material became increasingly plastic at higher frequencies and dissipates more energy. Here, Gel-Ma samples remained highly elastic at higher frequencies resisting energy dissipation and instead reflex elastically under shear. The 3% w/v Gel-Ma hydrogel has the most similar magnitude of G' and G" moduli to brain tissue as reported by Canovic et al, though remains 10 times higher than native tissue.

6.2.5 Effect of GO on Gel-Ma biocompatibility

The 3% formulation of Gel-Ma was chosen for biocompatibility experiments following the above optimisation. This formulation was the softest gel available thus most likely to support neural growth, whilst the mechanical and chemical properties were not significantly different when combined with GO.

In this work, cells were included in the pre-cross-linked mixture to produce hydrogels with cells encapsulated within the hydrogel matrix. This is similar to the preliminary Gel-Ma work with fibroblasts. In this study, GO was included in the hydrogel formulation at 1mg/ml and compared against gels without GO to identify what effects GO inclusion had on the hydrogel biocompatibility and cell morphology. Cell cultures were prepared as in the previous chapter. Mouse hippocampal tissue preparations maintained araC, isolated mouse neurons maintained with araC and SH-SY5Y neuronal cells maintained with retinoic acid differentiation media were encapsulated individually and maintained for 21 days.

Figure 6.5(A) presents the morphology and appearance of neural cells in Gel-ma hydrogels without and with GO inclusion at 21 days in culture. Gel-Ma demonstrated good biocompatibility with no sign that the cross linking process caused damage to the

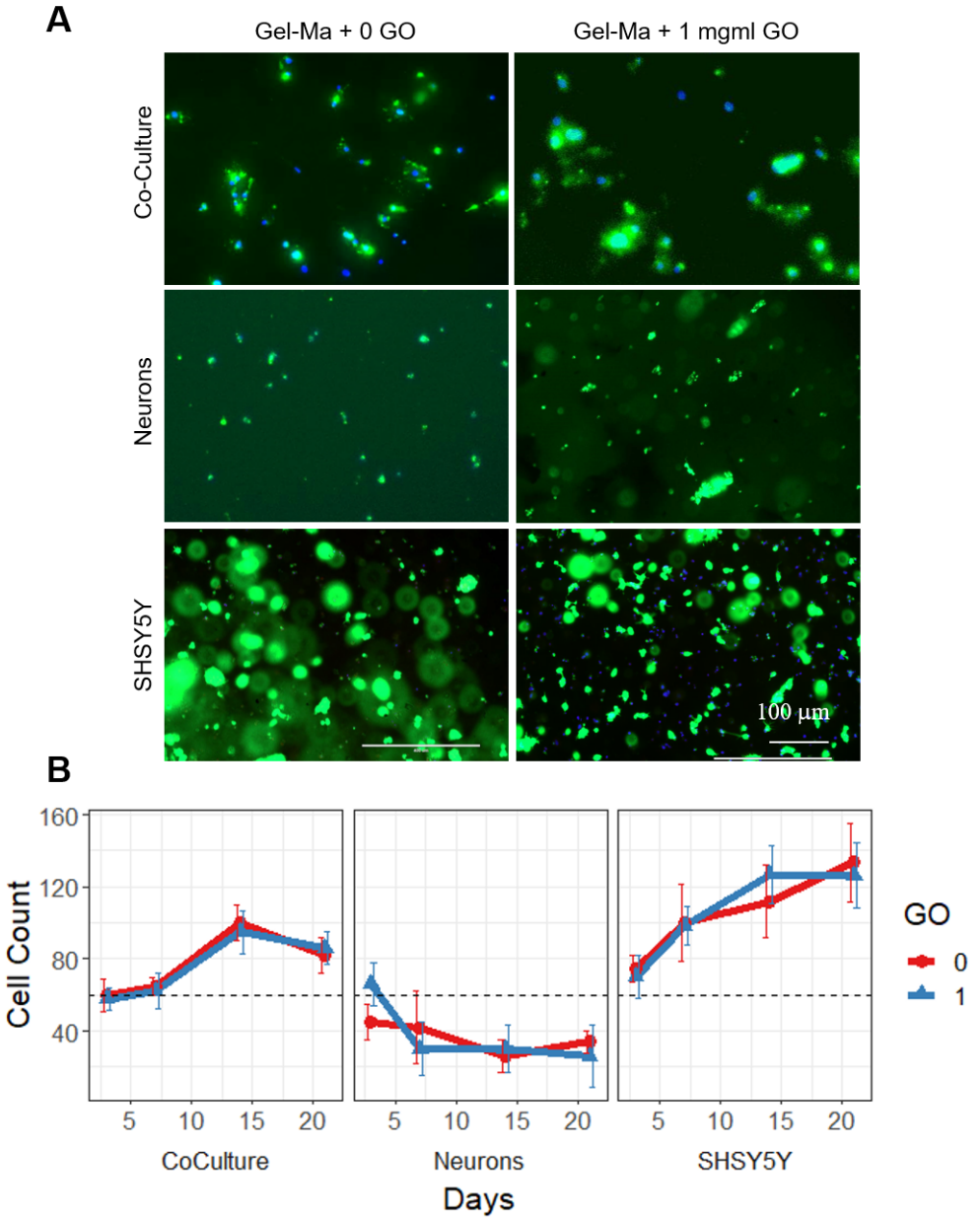

Figure 6.5 | **Effect of encapsulation Gel-Ma hydrogel without and with GO on cell proliferation..** (A) Representative fluorescence images showing cells encapsulated by Gel-Ma without or with GO on day 21 respectively, cultured in neurobasal medium for primary co-culture and neurons and differentiation medium for SHSY5Y. Cells were co-stained by calcien-AM (green) and hochest (blue). (B) Mean cell count under indicated cultured conditions from n = 3 independent cell preparations. Dashed line marks normalised initial cell count.

cells such as the dual-staining observed in redox initiated gels above. In both gels without and with GO cells were similar, all cell populations remained spheroid throughout, with no visible extension of processes.

Figure 6.5(B) quantifies cell number across 21 days. SH-SY5Y neuronal cells in-

creased slowly in cell number at each time point, with no difference between the gel conditions observed. Mouse neurons decreased in number relative to the starting point however from day 6 to day 21 remained consistent, suggesting the initial count contained glial cells which subsequently died. The co-culture from hippocampal tissue began to increase in cell count between 6 and 14 days, but then stopped in both gel conditions. Cells were spheroid, but viable throughout culture, regardless of cell type or gel formulation indicating cells within the hydrogel matrix did not extend processes during encapsulated 3D culture as expected from similar time periods on 2D culture environments. It is remarkable that the addition of graphene oxide as part of the scaffold did not significantly alter the biocompatibility of the gel formulation or significantly effect cell proliferation.

6.2.6 Presentation of a layered Gel-Ma with GO as a neural culture substrate

Cells showed no progress towards typical morphologies when encapsulated within the hydrogel matrix as part of the initial formulation. However, inclusion of graphene within the hydrogel matrix resulted in no significant difference in cell viability or proliferation. Therefore an alternative scaffold design combining the successful spin-coat GO film developed in the earlier chapter with the 3%w/v Gel-Ma hydrogel matrix was developed as the next stage of this work. This design utilised the GO film as an initial substrate with hydrogel added following cell attachment to the GO film to create a three-layer design with a 3D hydrogel 'above' the cell culture. This design was used with hippocampal tissue preparations to explore if neuronal morphology developed as expected within a layered scaffold

2D GO films were prepared as described in the earlier chapters. Briefly, 50nm spin-coated GO layers have been deposited on PEI coated glass cover-slips and seeded with a preparation of mouse hippocampal tissue. Following an overnight attachment period in standard media, media is withdrawn and immediately a 1mm thick layer of Gel-Ma macromer with the visible light initiators formulated is deposited on top of the GO film and allowed to cross-link under 1000w visible white light for 10 minutes. Following cross linking, cultures were maintained every 4 days and allowed to grow to maturation at t=14 days in culture. Neuronal morphology was investigated and compared against encapsulated neurons as well as SH-SY5Y cells encapsulated to explore if neurons could develop matured morphology in the layered model.

In Figure 6.6(A) cells in each condition are presented. Encapsulated neurons and SH-SY5Y cells show the as described spheroid morphology with no extension of processes. In contrast, the hippocampal preparation in the layered model shows increased cell size and extension of neurite processes, staining brightly with anti-Tau immunocytochemistry.

In figure 6.6(B) the difference in morphology is quantified in terms of shape descriptors.

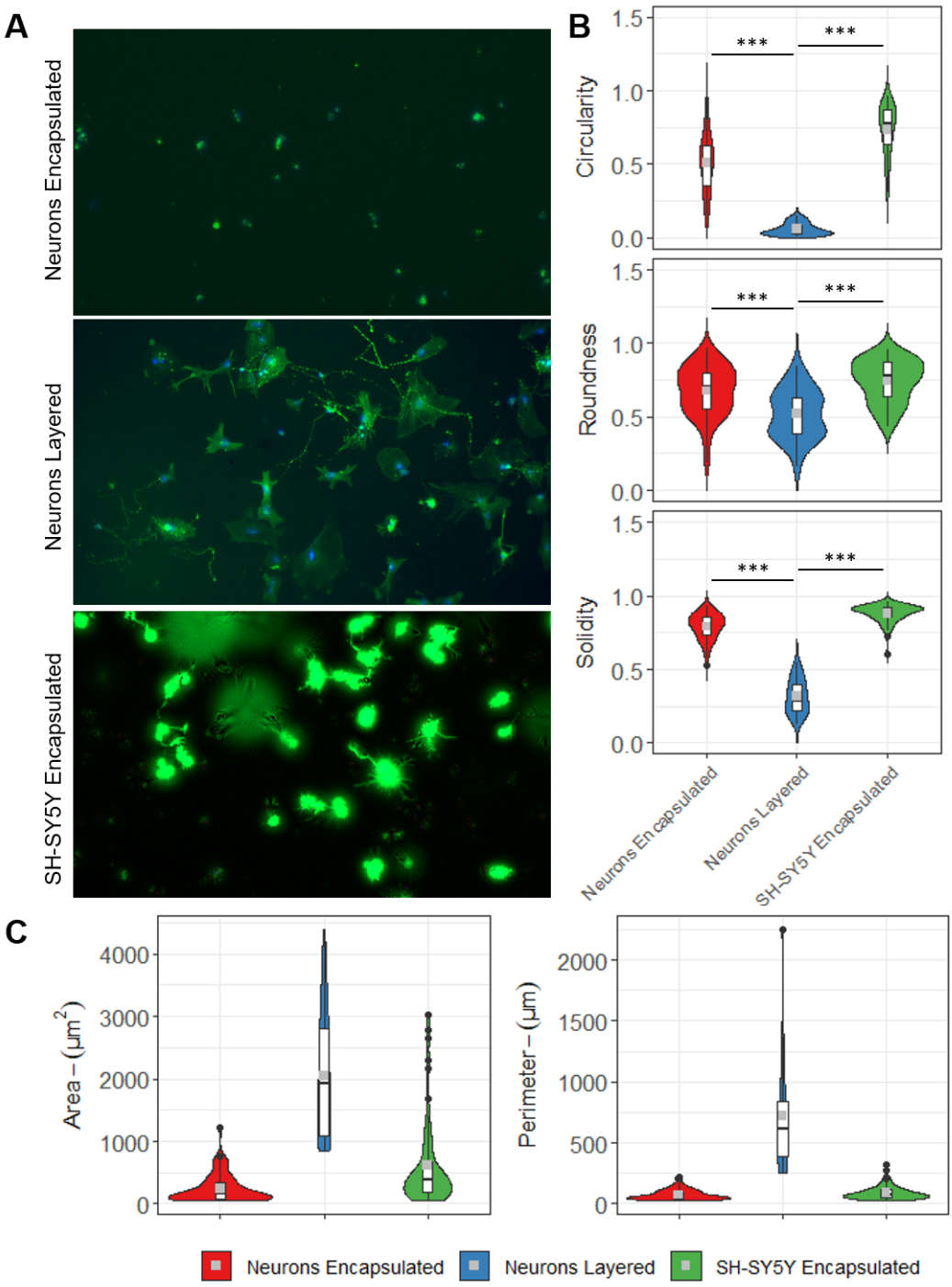

Figure 6.6 | **Layered compared to encapsulated culture models for neural cells..** (A) Representative fluorescence images showing cells encapsulated by Gel-Ma or layered with Gel-Ma on day 14 as indicated, cultured in neurobasal medium for primary neurons and differentiation medium for SHSY5Y. Cells were co-stained by Anti-Tau (green) and hochest (blue). (B) Mean (grey point), Range (white box) and Distribution (Violin) of individual cell shape descriptors under indicated conditions, 40 individual cells for each condition from n = 3 independent cell preparations. (C) Mean (grey point), Range (white box) and Distribution (Violin) of individual cell area and perimeter measurements under indicated conditions from n = 3 independent cell preparations. *** $p < 0.001$.

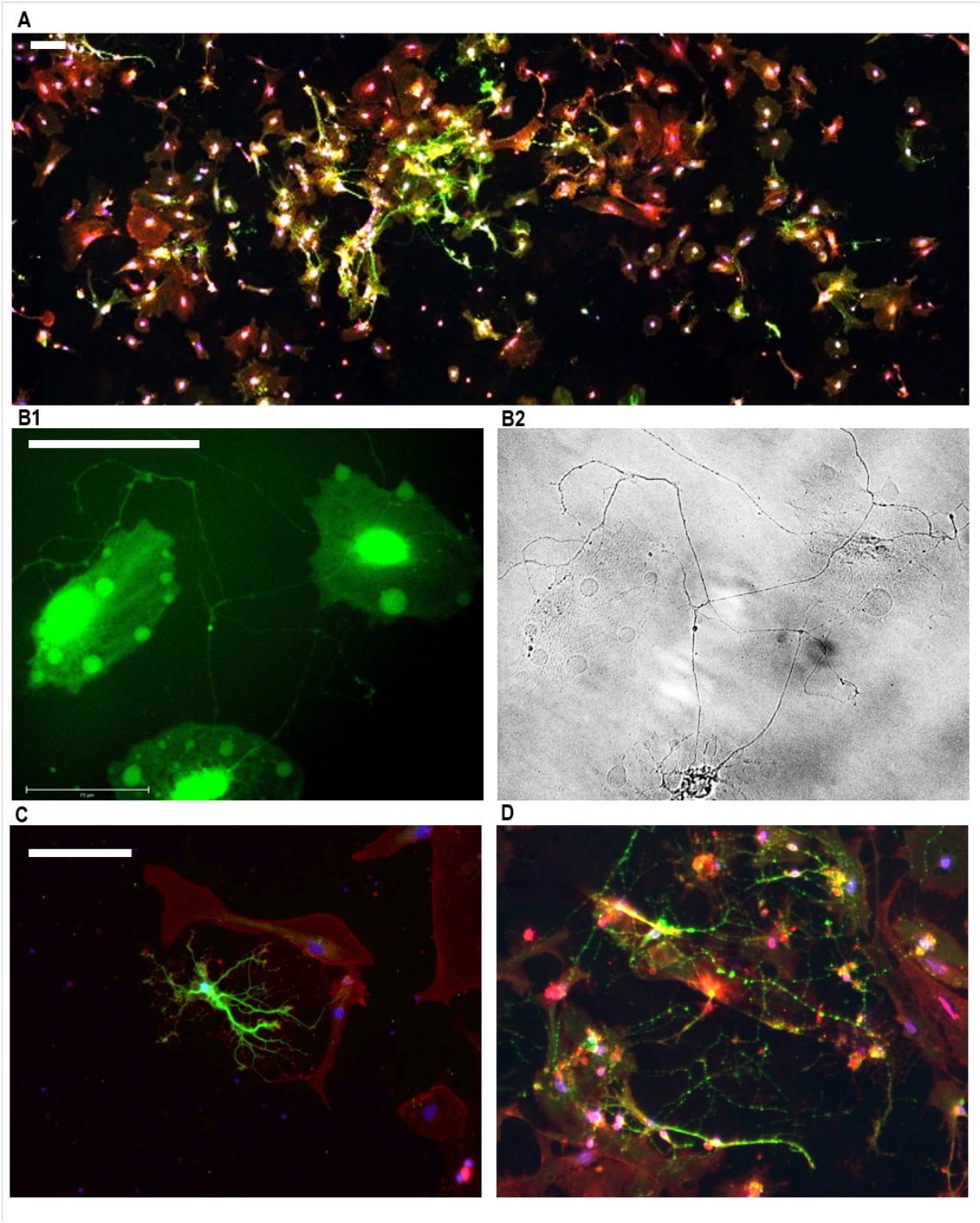

Figure 6.7 | **Qualitative display of co culture morphology in the layered model..** (A) Wide field projection of co culture co stained with Anti-Tau (green) and WGA (red) (B1) Calcien-AM stained neurons with neurite projection passing between (B2) Phase contrast channel of B1 showing depth of field and z-direction of neurite feature. (C) Interaction of neuron (green) with glia (red) showing directional growth of neurites. (D) Interaction of neurons (green) with glia (red) showing complexity.

Cells in the layered model show significantly lower scores of circularity, roundness and solidity compared to cells in the encapsulated model, indicating the cells are much more complex in shape.

In figure 6.6(C) these differences are further explored in terms of area and perimeter. Cells in the layered model have a higher mean area and a higher mean perimeter, with a greater range of both metrics. This indicates cells have successfully spread and are producing processes.

The layered culture model shows more mature cell morphology compared to the encapsulated model, with cells displaying morphology consistent with the 2D model, indicating the layered design does not impact the ability of cells to mature. Neurons in layered culture have significantly longer perimeter values compared to encapsulated culture corresponding to the reach of processes through the culture environment. Neurons in layered culture also spread in area following initial attachment to the GO film and thus have significantly higher area values.

In Figure 6.7(A) neurons and glia develop complex architecture and form interdependent networks, similar to the 2D culture model. Here again as previously reported, neurites preferentially extend towards glia and become constrained within the local clusters of glial cells, however neurites are also observed reaching into the fore-field. This 3D complexity is illustrated in Figure 6.7(B1-B2) with a Calcien-AM and phase contrast image of a neurite extension moving towards a cluster of glial cells located away from the GO film within the hydrogel layer. In Figure 6.7(B1) the intricacy of live neurite and glial bodies was resolved clearly through Calcien-AM staining. In Figure 6.7(B2)the depth of field can be better appreciated as the foreground objects and blurred background GO film beneath, with sharp illumination of the neurite in the plane of focus. In Figure 6.7(C) isolated neurons were seen to still grow preferentially towards local glial cells with the hydrogel layer. Similarly when glial cells were numerous, Figure 6.7(D) shows neurites become constrained and begin moving along glial membranes through the 3D culture.

6.3 Discussion

The overall aim of this study was to characterise and develop a 3D hydrogel which could be combined with GO to create a neural scaffold. This study presents the development and characterisation of gelatin hydrogels, and refinement of a formulation which was with GO and neural cell culture. The results of this work indicate that Gel-Ma can be successfully combined with the 2D GO film to produce a layered scaffold which can support the maturation and migration of neural cells. Importantly, inclusion of GO within the hydrogel matrix does not impact the biocompatibility or cross linking efficiency of Gel-Ma at up to 1mg/ml.

6.3.1 Alternative redox initiator systems

Redox initiation of hydrogel polymerisation allows for a radiation independent cross linking of Gel-Ma hydrogels. As characterised in this work the cross linking performance of this initiator system is poor and leads to hydrogels with high soluble fractions. Previous work in this area had been conducted with synthetic polymers such as polyvinylacetate, a synthetic polymer rather than gelatin, it is evident that the biological motif of gelatin quench the redox reaction [69]. To overcome this limitation, the redox reagent concentration was increased, however this came at a cost in cell viability. This was particularly apparent in the high incidence of dual staining between Calcien-AM and propidium iodide in cells encapsulated by redox-initiated Gel-Ma. The fluorescent calcein component of C-AM is a product of esterase metabolism following uptake of C-AM by cells, and thus only live cells fluoresce when treated with C-AM. However, propidium iodide cannot traverse intact cell membranes, thus only stains cells with permeable membranes, usually dead cells. Thus cases of dual staining indicate active esterase metabolism in cytoplasm, but in cells with permeable membranes, therefore the dual stained cells had been damaged by the redox initiator reaction. However this is not conducive towards a viable encapsulated cell population.

The objective in investigating radiation independent cross linking systems was to potentially simplify a future treatment options using a cell containing self assembling all-in-one formulation of hydrogel as an in-situ treatment. Though the redox initiator system was characterised on robust fibroblast cells, the reduced biocompatibility makes it clear that this initiator system would not be suitable for a neural scaffold with frangible and fastidious neuronal cells.

6.3.2 Visible light initiated gelatin hydrogels as encapsulation based scaffolds

Gelatin macromers have been previously shown to produce biocompatible hydrogels with excellent cell binding performance allowing maturation of complex cell morphologies [73]. During this research, gelatin derived hydrogels macromers elsewhere used for 3D printing have been translated for use as a supporting matrix for neural cell culture. Two cross linking chemistries were evaluated for potential as neural scaffolds. Gelatin cross linked with a thiol-norbornene chemistry (Gel-Nor) [67], had high soluble degradation. This resulted in loss of gels before 14 days, too quickly for maturation of neural cells as seen in earlier chapters. The potential advantage of the Gel-Nor step-growth gel system was to enable covalent integration of thiol modified GO [311]. During optimisation for this thesis, Gel-Nor was reduced to a minimum of 10% w/v macromer concentration [76]. However by reducing the concentration, the cross linking efficiency was compromised resulting in inadequately robust matrix formation during the photo-click initiated polymerisation reaction.

The second hydrogel chemistry was gelatin cross linked with methacryloyl chemistry (Gel-Ma). This hydrogel was used earlier in the investigation with redox initiators. When combined with the visible light wavelength photo-click initiator system, Gel-Ma had much lower soluble degradation. The visible light photo-click Gel-Ma hydrogels demonstrated good durability at low w/v % formulations. Viscoelastic properties of 3% Gel-Ma gels represented an optimised concentration of G', G" and tanδat 1000, 10000 and 0.2 re-

spectively. These rheological properties of Gel-Ma were approximately 10 times more resistant than the reported values for brain tissue [310].

Biocompatibility of the Gel-Ma visible light system with neural cells and cell lines *in vitro* is good with viable cells visible up to 21 days. Encapsulated SH-SY5Y cells maintained in differentiation media did not extend processes as expected or adopt the expected dopaminergic neuron-like morphology seen on GO films and other surfaces. Similarly, mouse hippocampal neurons and glial cells did not spread to the normally expected morphologies when encapsulated within the hydrogel matrix, instead remaining largely round and circular with high degrees of roundness, circularity and solidity. This persistent spheroid morphology whilst still accompanied by high viability during encapsulated cell culture was curious, as previous reports indicated cells produced expected morphologies in stiffer, higher w/v Gel-Ma hydrogels [312, 73]. In contrast to the successful cells encapsulated and reported by others, neural cell cytoskeleton is not developed for penetration of robust extracellular matrix. Although the Gel-Ma material is rheologically similar to brain tissue, it remains higher in elasticity, additionally the rheology data for brain tissue considered whole brain tissue including the glial matrix and neural network rather than the scant extracellular matrix in isolation. It is therefore reasonable to conclude that these optimised hydrogels at 3% w/v still remain too dense and elastic to harbour morphological development of neural cells *in vitro* when the gel is fully enclosing the cell.

Inclusion of GO suspension at 1mg/ml within the hydrogel matrix resulted in no significant differences in hydrogel biocompatibility or stability, a small difference is observed in the low rad/s range of rheometry data including the G' and G" moduli and tanδ, suggesting the addition of GO reduced plasticity during low torque measurements. However this dissimilarity is not present at higher values of rad/s where Gel-Ma with GO and Gel-Ma followed the same trend. Furthermore, GO added into the Gel-Ma hydrogel formulation had no consequences to viability of the encapsulated cells but similarly no significant benefits either.

6.3.3 Gel-Ma combined with GO films as a layered scaffold

To characterise neural cell growth on a layered scaffold, the GO film model from earlier chapters was combined with the optimised 3% w/v Gel-Ma photo-click hydrogel. Addition of hydrogel following cell attachment produced a three-layered scaffold comprising a contiguous GO base layer, mouse hippocampal co-culture, with an upper hydrogel 3D layer providing a new axis for cell expansion. This design was similar to previous Gel-GO heterogeneous scaffolds which combined sequential assembly of graphenes with supporting matrix [139]. However this work presents a system which contains viable tissue between layers, at the GO-hydrogel interface, rather than the scaffold surface.

Neural cell co-culture in the layered scaffold demonstrated cell morphologies consistent with expected maturation, including visible neurite extension between cells, and greater numbers of neurite projections than cells within encapsulated culture. Layered scaffolds also supported glial cells with evidence of inter-cellular interactions typical of a supporting relationship localised to the GO-hydrogel interface similar to the 2D GO film co culture though with visible evidence of neurites beginning to penetrate the hydrogel material towards glial cells higher within the gel. In comparison to the 2D cultures in earlier chapters, cells on the layered scaffold produced more fine neurites, neuronal cells expanded further atop glial groupings and spread further.

6.4 Conclusion

Gel-Ma has shown potential as a neural scaffold, including excellent biocompatibility, efficient cross linking and durability in neurogenic culture. Gel-Ma has been combined with the GO film and shown to support maturation of mouse neural tissue in three dimensions. This leads to possibility to develop both the GO instructive properties and scaffold in parallel. Future work should bring the existing adsorption modification of GO films into the layered scaffold. Similarly, this layered design should be developed further to detach the GO film from the original glass substrate onto the hydrogel following cross linking

and permit more layers to be added.

Chapter 7

Summary and future directions

The original hypothesis of this project was:

Graphene oxide is a biocompatible and modifiable material for use as an instructive neural scaffold, with properties suited to the growth, development and maturation of neural tissues in vitro.

In this project, a commercially sourced chemically exfoliated graphene oxide stock has been used to assemble 2D and 3D model environments suitable for the culture of neural cells including neurons and glia. The model culture environments have been characterised to elucidate the model design, surface chemistry of GO as a film, interaction of GO with the cell culture environment, mechanical performance of GO containing hydrogels, and the biological reactions to these materials. The overall project objectives have been addressed and evidenced with data and analysis from the data chapters.

7.1 Development of the 2D GO model

In this thesis, a spin coating method was developed and used to generate a 2D GO film surface [285, 104]. Spin coating was found to be a simple and ergonomic technique allowing the direct use of GO from suspension to reliably create thin films of GO. Spin coating requires no further specialist equipment or knowledge besides access to a spin

coater, beneficially the technique is also highly intuitive, scalable and adaptable. In this work the creation of GO films was found to progress and iterate quickly by adjusting spin coater conditions until reliable coats were manufactured. Importantly, this spin coating could be performed on a range of materials and substrates provided the substrate can be fit to the spin coater, for this project an interference fit spin coater chuck designed for glass cover-slips was manufactured and used throughout.

Interference fitting has a number of advantages over other vacuum spin coater designs including no requirement of a pump to maintain a vacuum, thus allowing the coater to be operated bench-top within normal lab space without issue. Compared to other methods used with graphenes to create flat surfaces such as drop casting, evaporation or vapour deposition, spin coating has a number of advantages; GO films were able to be produced quickly, up to 20 per hour at room temperature and without further drying. Additionally, GO stock could be used as aqueous suspension without modification from the stock suspension, such as freeze drying or re-suspension which might compromise the platelet quality, differentially modify the surface chemistry, or introduce confounding factors [161, 106].

In this work, GO films following were produced of 30-50nm in thickness, which was calculated to be 15-20 layers of GO platelets. GO films are robust as a simple creation between the GO stock and glass substrate, however the GO stock can be diluted to increase efficiency and reduce the amount of stock used during coating by up to 5 times without compromising the film thickness. Adhesion between the GO film and glass substrate became an issue during preliminary work, with incidence of the film detaching from the substrate during hydrostatic pressures of media changes. To improve robustness of the film, adhesion between GO and glass was enhanced by addition of a PEI polymer coat to the glass substrate before GO film construction. This enhancement was deposited to the glass surface via spin coating in a single extra step, which eliminated GO films detaching from the substrate. Other polymers were considered and evaluated including gelatin and poly-l-lysine however both alternative polymers had stringent handling requirements not

shared by PEI which most ergonomically and effectively fit into the spin coating workflow.

Addition of the PEI coat between the glass substrate and the GO film did not alter the measured properties of the GO film. When analysed for Raman spectra, both GO films with and without PEI support produced the same characteristic twin peak spectra at the same Raman shift with no discrepancies. PEI support did not lead to changes in film thickness but did appear to change the nanoscale topography of the planar surface when viewed with SEM, resulting in more, smaller wrinkle like features compared to longer, fewer such structures for GO films without PEI support. The significance of this observed change in topographical features was not quantified, but no differences were noted in cell growth or attachment. The simplicity with which this adaption could be implemented to the model and lack of consequences to the surface chemistry further highlights the adaptability of the spin coating technique for the study of GO films, and that the GO film was a contiguous solid layer capable of obscuring the adhesive coat entirely.

The surface chemistry of the GO film was characterised in detail using XPS. These data demonstrated that the GO material was of high quality, and consistent with the accepted theoretical model structure of GO. The GO film had a similar quantity of polar and non polar carbon bonding states, suitable for the adsorption of both polar and non polar molecules. Moreover, these XPS data did not indicate that oxidative debris, reduced GO or graphitic bodies were present within this GO stock material [112, 115]. The GO film structure, nor the hydrated NAP-XPS conditions presented did not provide any further insights or alternate perspective into the chemistry of GO than was otherwise reported previously in powder preparation and traditional high vacuum XPS conditions [283].

7.2 Biocompatibility of GO

GO has most often been produced bespoke by researchers for each individual publication, leading to a great deal of confounded data regarding the biocompatibility of GO. Particularly, variance in exfoliation methods causes variance in surface chemistry, platelet

dimensions, layer number and purity [92]. In this context, it is unsurprising that previous reports have catalogued biocompatibility consequences in cells exposed to GO, counter-balanced by similar studies reporting opposing outcomes. Similarly, common practice has seen GO surfaces and GO coated materials subsequently further supplemented by layers of bioadhesive polymer [154]. It is the supposition of this work that these coatings obfuscate the GO surface, and subsequently the studies in question are evaluating biological performance and cell behaviour on the biopolymer, rather than a GO surface.

This work aimed to prove commercial GO was inherently biocompatible, providing an easily accessible raw material in an effort to open scope for others to use more standardised material sources for tissue engineering applications. The GO film did not include any tertiary coating in bioadhesive polymer, to evidence that these treatments are unnecessary with high quality GO. It is therefore clear that commercial GO can be of equal or better quality than bespoke manufacture. With greater standardisation, more progress can be made in GO biomaterial development through greater comparability.

GO assembled as films directly from the stock solution were first sterilised with ethanol and before being used as cell culture substrates with no intentional bioadhesive coating. Any cytotoxic contamination of the GO, or intrinsic cytotoxic properties of the GO material would be detectable in experiments that followed the principles of cytotoxicity testing as practised in the medical device industry via microscopic validation of cell growth and morphology on a potentially cytotoxic source [313]. No lineage of cells cultured in this project failed to adhere and grow directly atop the GO surface, including neuronal and microglial cell lines, mouse and rat neurons, astrocytes and mouse microglia. All cell types also had excellent viability on the GO films, developed, matured and responded to stimuli as expected. This excellent biocompatibility performance of the GO prepared without additional bioadhesive coatings highlights that high quality GO as available from commercial sources does not have cytotoxic behaviour, does permit cell attachment and thus does not require coatings to allow study in cell culture.

7.2.1 Neuronal phenotype responses on GO

The SH-SY5Y human neuroblastoma cell line was used as a model of neuronal differentiation. This cell line has a proliferative undifferentiated phenotype resembling neuroblasts during expansion and undergoes a pseudo-differentiation to a phenotype resembling neurons in response to exposure to retinoic acid [293]. Differentiation treatment has a number of advantages for the study of the GO surface and its effect on neuronal type cells including a reduction of proliferation, increase in extension of processes resembling neurites, and a synchronisation of the cell cycle.

The GO film when used as a culture surface is shown to significantly enhance the length of neurites expressed by SH-SY5Y cells compared to controls following differentiation stimulation with retinoic acid. Though initially this effect could be considered a consequence of the conductive properties of graphenes, as reported in other literature showing electrical stimulation can enhance neuronal development, in this work this theory has been discounted: Though GO in a reduced state can conduct electrical fields through sp^2 carbon and liberated πbond electrons, in this work showing enhanced neurite length, no reduction treatment had been applied. Reduction of the surface by SH-SY5Y cell culture could also be considered, however no known mechanism for biological reduction of GO by mammalian cells exists [314]. This work does not provide evidence to suggest such a revolutionary theory.

Instead, an alternative theory for the enhanced neurite development on the GO film is considered here. The GO film surface provided an enhanced cell attachment environment through adsorbtion of vitronectin from FBS containing cell culture media. Additionally the GO film surface retained detectable protein even once a cell culture environment is enzymatically digested and washed away. It is therefore supposed by this work that GO adsorbs protein during cell culture which remains locally available during differentiation. This adsorbed protein leads to the GO film surface becoming an enriched environment for adherent cells, a conclusion supported by the work of Lee et al who proved a GO culture

surface could adsorb 25 times more serum protein than inert control surfaces [269]. The protein enriched GO film surface provides a number of benefits, firstly providing an improved cell adhesive surface for migration of neurite processes during differentiation. Secondly by providing a localised concentration of media nutrients at the culture surface close to the adherent cells. In this way, SH-SY5Y neuronal cells differentiating on GO films are better supported compared to the non-GO surfaces, thus neurite extensions become longer through improved adhesion and nutrition.

By comparison primary neurons during differentiation form expansive networks of primary neurites which then branch into numerous smaller secondary and tertiary neurites, making measurement and accurate quantification difficult. For primary neurons, neurite length is strongly affected by the number of cells in proximity, degree of cyclisation and branching between cells. This is compounded when comparing co-cultured glia and neurons with isolated neurons. Due to these confounding factors with measurement, it is more not possible to conclude that the GO surface benefits mouse neurons in terms of quantitative neurite length in a similar manner to SH-SY5Y. However, by observing the morphology of neurons on GO films, it is possible to observe the development of the mature morphology and synaptic terminals. Primary neurons on GO films show matured morphology within 14 days. Particularly when cultured alongside glia, these neurons produce fine synaptic terminals and have highly developed cytoskeletal complexity. This indicates neuronal maturation progresses on GO films, and is similar and qualitatively more complex than on the inert surfaces presented in this project.

7.2.2 Microglial reactivity on GO films

On GO film, BV-2 cells showed a high proliferation rate and reached confluence inside of 4 days. Compared with identical cells on inert surfaces, BV-2 showed a characteristic activated phenotype suggesting an inflammatory reaction was induced by the GO film [294]. This is contrary to previous reports which have shown GO and graphene functionalised scaffolds can have anti-inflammatory effects in microglial cells [263, 315] However,

a similarly activated phenotype was not seen in mouse microglia on GO films which remained quiescent and had a resting phenotype. Mouse microglia could be induced into an activated phenotype using 1μg/ml LPS, showing microglia reacted normally on GO films with no sign of reactivity suppression. It is therefore possible that the adsorptive properties of the GO film concentrate pro-inflammatory factors, which have previously been shown to be higher in BV-2 cells than microglial cells [316]. This results in an activated pro-inflammatory propagation through BV-2 on the GO surface which is not similarly seen in mouse microglia or BV-2 on inert surfaces.

7.3 Instructive adsorption on GO films

In this project, GO film has been modified during preparation with adsorbed factors to control the phenotype of cells. Previous reports have shown evidence of GO can adsorb pharmaceutical molecules [307, 298, 304]. In this work the GO film was shown to adsorb and concentrate protein from cell culture and produce measurable effects in neuronal and microglial cells. Microglial activation was used as a reporter for successful instructive adsorption when using the GO film as a vector for ibuprofen. The biocompatibility and neuronal cell response was not changed by the adsorption treatment. However BV-2 cells showed a significant difference in proliferative rate and morphology on the GO films with an adsorption treatment compared to those without. BV-2 cells on the adsorption treated GO films exhibited significantly different morphology appearing ramified with processes extending from the cell body, rather than the expected largely round morphology seen earlier on GO films This modified biological reaction in the BV-2 cell line is consistent with COX-2 inhibition reducing an inflammatory reaction, which is the expected outcome of treatment with ibuprofen. Additionally, this confirmed the earlier rounded and highly proliferative BV-2 phenotype seen on GO films was an activated phenotype.

Primary microglia remain ramified and proliferate slowly when cultured on the GO film, with or without adsorption treatment with ibuprofen. However the LPS induced

inflammatory phenotype was inhibited on the ibuprofen adsorption treated GO film. Ibuprofen adsorption treatment had a significant effect on mouse microglia, inhibiting the inflammatory reaction.

The success of this adsorption treatment appears to be limited to molecules with low solubility in aqueous solutions such as ibuprofen. Minocycline, another known inhibitor of microglial inflammatory reaction induced by LPS treatment [300, 309, 301] was similarly dissolved in separate adsorption buffer and used to treat surfaces for a comparative study between adsorbed ibuprofen and adsorbed minocycline in mitigating microglial activation. Unlike ibuprofen treated surfaces, the minocycline treated surfaces showed no significant difference in microglial activation. This negative result indicates that the adsorption of minocycline to the GO film is less successful relative to ibuprofen.

Tetracycline antibiotic minocycline has 4 carbon ring structures featuring electropositive double bonds in each, in comparison to the single benzene ring structure of ibuprofen. However minocycline has a number of polar groups with potential for hydrogen bonding relative to its molecular mass with a possible 14 hydrogen bonds and molecular mass of 457.5 g/mol. Thus adsorption of minocycline to GO was dependent on polar interactions and thus vulnerable to solubilisation. By comparison ibuprofen which can only form 3 hydrogen bonds with a molecular mass of 206.28 g/mol. The hydrocarbon chain of ibuprofen therefore is insoluble in polar solvents and remains adsorbed to the GO film via non-polar interactions and resistant to solubilisation.

Following adsorption treatment, surfaces were washed several times to remove the adsorption buffer, which leads to a reduction in the concentration of minocycline at the GO film surface. Thus during cell culture as any remaining minocycline becomes diluted into the culture media, below an effective concentration to inhibit microglial activation. By contrast ibuprofen remains adsorbed to the GO film until contact with microglial plasma membranes [127, 317]. The ibuprofen molecule is lipid soluble, therefore during cell adhesion to an area adsorbed with ibuprofen the molecule is free to diffuse through the cell membrane and become bioavailable, in a sufficient concentration to inhibit microglial

activation.

7.4 GO films as an XPS substrate for analysis of cells and cell micro-environments

Able to be operated in a near ambient pressure mode, at 11mb with a hydrated water atmosphere rather than hard vacuum, NAP-XPS presented an opportunity for acquiring spectra of biological material that had not been dessicated, dried or otherwise fixed. In this way, NAP-XPS can produce spectra of chemical structures as they exists in biosimilar conditions. As a part of this work the GO film has been used as a platform for novel XPS characterisation of SH-SY5Y cells *in vitro*. The GO film was biocompatible, cell adhesive without requiring polymer modification, and can support cells in prolonged culture. Additionally, during XPS the GO film required minimal charge correction and showed no signs of excitatory degradation. Furthermore, the spectra of GO is well known as discussed earlier. Prior work using NAP-XPS on biological samples has previously focused on precipitates of bacterial cultures on silicon substrates [280].

Changes in cell density were clearly shown in the XPS spectra, with corresponding changes in both atomic concentration and differences in the structure of carbon spectra. These changes reflected the differences in emissions between SH-SY5Y cell body structures and the extracellular environment. Phospholipid membranes contribute a high linear carbon signal in XPS spectra of dense cell coverage compared to in sparse cultures. Furthermore, in this work vitronectin adsorbed to the GO film surface has been characterised, reflecting a measurement of the extracellular environment. The vitronectin spectral structure becomes increasingly apparent as cell density decreases. This presents an additional use for the GO film as an all-in-one culture substrate for XPS analysis. These findings present an opportunity for future work to characterise changes in the *in vitro* cell and extracellular environments.

7.5 Combining GO with hydrogels

To finally explore how the commercial GO material could be translated into a neural scaffold, I began to develop a GO-hydrogel model. Two hydrogel systems were investigated in this work, with two initiator systems considered and two deployments of graphene oxide within the hydrogel system.

The initial investigation into a step-growth Gel-Nor system using a thiol cross linker, was motivated by the prospect of covalent cross-linking of thiol modified GO into the hydrogel system [311]. However the Gel-Nor system was prone to dissolution under cell culture conditions and could not be adequately controlled without increasing gel concentration and therefore stiffness. Furthermore, the chemistry to affix thiol groups to GO via epoxide ring opening remained elusive. Quantification of reaction products via ultraviolet-visible spectrophotometry revealed only free thiol within the samples, with no GO-Thiol bonds. Thus two critical issues had arisen with the planned Gel-Nor material, so an alternative hydrogel was used.

In this project work progressed instead with the more reliable and simple Gel-Ma system. Using Gel-Ma, two approaches to initiation of the cross linking reaction were investigated; radiation independent redox initiation and visible light initiated ruthenium hexahydrate cross linking. The redox system was characterised by formulating persulfates as both the oxidant molecule and source of sulfate ions to catalyse the cross linking reaction, with various reductant molecules to generate the ions [69]. The redox system produced hydrogels with a high soluble fraction and poor cell viability compared to the visible light system. This confirmed the best option for cross linking the gel-ma system was the visible light ruthenium hexahydrate system [73].

Gel-Ma hydrogels were optimised to a 3% w/v macromer content, which had rheological properties approximately ten times stiffer than normal brain tissue, but a similar viscoelastic profile [310] Neuronal cells encapsulated in the hydrogels showed showed a constricted, spheroid morphology with no extension of the dendritic processes expected

for matured cells. This indicated that the gel was too stiff for encapsulated cultures to generate normal matured morphology. Gel-Ma was then combined with graphene oxide in two ways. First the GO suspension was diluted into the pre-crosslinked hydrogel to create a hydrogel mixture containing up to 1mg/ml of GO in suspension. Compared to hydrogel without GO inclusion, the Gel-Ma with GO at 1mg/ml had no significant benefit or consequence to encapsulated cells, with similar viability and morphology.

Instead of encapsulating cells and GO, hydrogel was used as a layered scaffold combination with the GO film model. This new design led to significant improvements in neurite growth compared to the encapsulated cultures with cells becoming much larger, less spheroid and producing neurites extending into the hydrogel upper layer, demonstrating a 3D growth. In this layer design cells were adhered to GO films and then combined with hydrogel layers to create stratified scaffolds. In combination with the instructive and vector properties of the GO film this provides a platform for further development of intelligent scaffolds for generation of complex neural tissue with anti-inflammatory and neurite enhancing qualities. The layered scaffold approach represents the pinnacle of the work achieved in this project.

7.6 Conclusions

In conclusion, the work presented in this thesis has demonstrated that GO available from a commercial source can be biocompatible, and should be considered for any GO tissue engineering project before making a bespoke batch of indeterminate quality. GO can be easily and quickly assembled into a study surface from suspension, using spin coating, which is an excellent investigative platform for cell culture and spectral analysis.

GO films are innately supportive of cell adhesion and cell development through adsorption from media, and shows significant improvements in neurite extension. Furthermore, GO can be used as a vector to deliver pharmacologically active molecules with a low solubility in media. In this work the GO film was used to deliver anti-inflammatory molecule

ibuprofen to microglial cells and successfully inhibit microglial activation via the COX-2 pathway. Other molecules can be adsorbed to the GO film including vitronectin for cell attachment.

The GO material can be incorporated into 3D scaffolds, with a benefit when assembled into a stratified design. Cells pre-supported on a GO film can be provided an enhanced culture environment by subsequent addition of a hydrogel layer providing a 3D culture environment following adhesion to the GO film. In the layered culture the GO film appears to provide a topographical feature for the development of basal cell attachment with subsequent protrusion of the cells into the hydrogel originating at the GO film.

Summation: This project has created a solid foundation for future researchers to continue the investigation into GO for neural scaffolds.

7.7 Evaluation

This project has laid the foundations for several areas of further research that can be performed to build upon the work herein. **2D GO film model:** The 2D GO film model is the most well explored area of this research, and provides a platform for others to use. The model has been investigated for adsorption performance and cell culture compatibility, this work can be expanded and investigated for performance with other adsorbed molecules. Additionally rGO was considered as part of this work including the potential of reducing the GO film in situ to create a more conductive surface and investigate these properties in this model. Preliminary work with ascorbic acid and electrochemical reduction required further optimisation

The GO film model would also benefit from more investigation with XPS. In particular this work was limited by time for spectral acquisition, further spectra comprising different XPS conditions may better elucidate the nitrogen, oxygen and other elemental spectra. Furthermore NAP-XPS, spectra of solutions can be acquired allowing for direct comparison between the solution and film surface. In this way a comparisons can be made

between the adsorbed surface and adsorption buffer.

Cell culture: Neuronal length quantification on GO films could be enhanced by introducing a topographical substrate beneath the GO film, resulting in a patterned GO film. This work did attempt to create such a substrate using recycled polycarbonate from DVD's in a replication of the work of Lu et al [318]. However the method used to prepare the polycarbonate in this project (Laser cutting) resulted in a cytotoxic leach-able contaminant from the thermally denatured edges which impeded cell growth in culture. To improve this outcome, instead of repurposing and recycling another material, instead GO films should be prepared purpose ground glass cover-slips to ensure no confounding variables.

Regarding the adsorption qualities of the GO film, a good direction for future research would be to perform sequential cultures on the same GO film. In this way, the extracellular environment that adsorbs to the film may result in a conditioned culture surface to further enhance the instructive properties. For example this could comprise an initial culture of an astrocyte layer to create an astrocyte extracellular micro-environment, followed by a neuronal culture to investigate cell maturation and neurite extension.

3D Hydrogel with GO: Though this work used a Gel-Ma hydrogel to form the 3D component of this scaffold, Gel-Ma may not be the best choice of hydrogel. The mechanical properties of Gel-Ma are poorly suited to simulating brain tissue, the material remains too stiff and elastic at the lower limit of its useable range. Hippocampal tissue co-culture developed 3D neurites within the layered scaffold design. Future work should seek to combine multiple layered scaffolds together to provide a multi-stratified composite. In particular, each layer could include a different cell type to test migratory signalling through the layers.

References

[1] Buddy D. Ratner, Guigen Zhang, William R. Wagner, Shelly E. Sakiyama-Elbert, Guigen Zhang, and Michael J. Yaszemski. 1.1.2 - a history of biomaterials. In *Biomaterials Science (Fourth Edition)*, pages 21–34. Academic Press, 2020.

[2] Celeste M. Abraham. A brief historical perspective on dental implants, their surface coatings and treatments. *The open dentistry journal*, 8(24894638):50–55, May 2014.

[3] Monika Saini, Yashpal Singh, Pooja Arora, Vipin Arora, and Krati Jain. Implant biomaterials: A comprehensive review. *World journal of clinical cases*, 3(25610850):52–57, January 2015.

[4] J. B. Murphy. Factors of resistance to heteroplastic tissue-grafting : studies in tissue specificity. iii. *The Journal of experimental medicine*, 19:513–22, May 1914.

[5] Clyde F. Barker and James F. Markmann. Historical overview of transplantation. *Cold Spring Harbor perspectives in medicine*, 3(23545575):a014977–a014977, April 2013.

[6] Fergal J. O'Brien. Biomaterials and scaffolds for tissue engineering. *Materials Today*, 14(3):88–95, 2011.

[7] Erin Lavik and Horst von Recum. The role of nanomaterials in translational medicine. *Acs Nano*, 5(5):3419–3424, 2011.

[8] Ramón Torrecillas, José S Moya, Luis A Díaz, José F Bartolomé, Adolfo Fernández, and Sonia Lopez-Esteban. Nanotechnology in joint replacement. *Nanomedicine and Nanobiotechnology*, 1(5):540–552, 2009.

[9] N. P. Pampaloni, M. Giugliano, D. Scaini, L. Ballerini, and R. Rauti. Advances in nano neuroscience: From nanomaterials to nanotools. *Frontiers in Neuroscience*, 12:16, 2019.

[10] M. O. Riehle. Biocompatibility: Nanomaterials for cell- and tissue engineering. *NanoBiotechnology*, 1(3):308–309, 2005.

[11] Amy K. Madl, Monty Liong, Michael Kovochich, Brent L. Finley, Dennis J. Paustenbach, and Günter Oberdörster. Toxicology of wear particles of cobalt-chromium alloy metal-on-metal hip implants part i: physicochemical properties in patient and simulator studies. *Nanomedicine : nanotechnology, biology, and medicine*, 11:1201–15, Jul 2015.

[12] Eyal Bar-Kochba, Mark T. Scimone, Jonathan B. Estrada, and Christian Franck. Strain and rate-dependent neuronal injury in a 3d in vitro compression model of traumatic brain injury. *Scientific Reports*, 6:30550, 2016.

[13] Robert Lanza, Robert Langer, and Joseph P. Vacanti. *Principles of tissue engineering*. Academic Press, 2011.

[14] Herve Petite, Veronique Viateau, Wassila Bensaid, Alain Meunier, Cindy de Pollak, Marianne Bourguignon, Karim Oudina, Laurent Sedel, and Genevieve Guillemin. Tissue-engineered bone regeneration. *Nature biotechnology*, 18(9):959–963, 2000.

[15] Maria-Pau Ginebra, Montserrat Espanol, Yassine Maazouz, Victor Bergez, and David Pastorino. Bioceramics and bone healing. *EFORT Open Reviews*, 3(5):173–183, 2018. PMID: 29951254.

[16] Johnna S. Temenoff, Hansoo Park, Esmaiel Jabbari, Daniel E. Conway, Tiffany L. Sheffield, Catherine G. Ambrose, and Antonios G. Mikos. Thermally cross-linked oligo(poly(ethylene glycol) fumarate) hydrogels support osteogenic differentiation of encapsulated marrow stromal cells in vitro. *Biomacromolecules*, 5(1):5–10, January 2004.

[17] Renata G. Rosa, Paulo P. Joazeiro, Juares Bianco, Manuela Kunz, Joanna F. Weber, and Stephen D. Waldman. Growth factor stimulation improves the structure and properties of scaffold-free engineered auricular cartilage constructs. *PLOS ONE*, 9(8), 2014.

[18] Tadanao Funakoshi, Tokifumi Majima, Norimasa Iwasaki, Shintaro Yamane, Tatsuya Masuko, Akio Minami, Kazuo Harada, Hiroshi Tamura, Seiichi Tokura, and Shin-Ichiro Nishimura. Novel chitosan-based hyaluronan hybrid polymer fibers as a scaffold in ligament tissue engineering. *Journal of Biomedical Materials Research Part A: An Official Journal of The Society for Biomaterials, The Japanese Society for Biomaterials, and The Australian Society for Biomaterials and the Korean Society for Biomaterials*, 74(3):338–346, 2005.

[19] Gemma Jones, Anthony Herbert, Helen Berry, Jennifer Helen Edwards, John Fisher, and Eileen Ingham. Decellularization and characterization of porcine superflexor tendon: a potential anterior cruciate ligament replacement. *Tissue Engineering Part A*, 23(3-4):124–134, 2017.

[20] Kalyani Nair, CV Muraleedharan, and GS Bhuvaneshwar. Developments in mechanical heart valve prosthesis. *Sadhana*, 28(3-4):575–587, 2003.

[21] Natalie Glaser, Veronica Jackson, Anders Franco-Cereceda, and Ulrik Sartipy. Survival after aortic valve replacement with bovine or porcine valve prostheses: a systematic review and meta-analysis. *The Thoracic and cardiovascular surgeon*, 67(04):282–290, 2019.

[22] Francesco Innocente, Delia Mandracchia, Erman Pektok, Benjamin Nottelet, Jean-Christophe Tille, Sarra de Valence, Giuseppe Faggian, Alessandro Mazzucco, Afksendiyos Kalangos, Robert Gurny, Michael Moeller, and Beat H. Walpoth. Paclitaxel-eluting biodegradable synthetic vascular prostheses: a step towards reduction of neointima formation? *Circulation*, 120:S37–45, Sep 2009.

[23] Chih-Hsun Lin, Kai Hsia, Hsu Ma, Hsinyu Lee, and Jen-Her Lu. In vivo performance of decellularized vascular grafts: a review article. *International journal of molecular sciences*, 19(7):2101, 2018.

[24] Sheila MacNeil. Biomaterials for tissue engineering of skin. *Materials today*, 11(5):26–35, 2008.

[25] Houman Savoji, Brent Godau, Mohsen Sheikh Hassani, and Mohsen Akbari. Skin tissue

substitutes and biomaterial risk assessment and testing. *Frontiers in bioengineering and biotechnology*, 6:86, 2018.

[26] Jyrki Vuola, Tom Böhling, Jaakko Kinnunen, Eero Hirvensalo, and Sirpa Asko-Seljavaara. Natural coral as bone-defect-filling material. *Journal of Biomedical Materials Research*, 51(1):117–122, 2000.

[27] Dimitrios Kouroupis, Thomas G. Baboolal, Elena Jones, and Peter V. Giannoudis. Native multipotential stromal cell colonization and graft expander potential of a bovine natural bone scaffold. *Journal of Orthopaedic Research*, 31(12):1950–1958, 2013.

[28] J. Kortsmit, N. J. B. Driessen, M. C. M. Rutten, and F. P. T. Baaijens. Real time, non-invasive assessment of leaflet deformation in heart valve tissue engineering. *Annals of Biomedical Engineering*, 37(3):532–541, 2009.

[29] Xiaoyun Xu, Woon-Chee Yee, Peter YK Hwang, Hanry Yu, Andrew CA Wan, Shujun Gao, Kum-Loong Boon, Hai-Quan Mao, Kam W Leong, and Shu Wang. Peripheral nerve regeneration with sustained release of poly (phosphoester) microencapsulated nerve growth factor within nerve guide conduits. *Biomaterials*, 24(13):2405–2412, 2003.

[30] P. H. Warnke, I. N. G. Springer, J. Wiltfang, Y. Acil, H. Eufinger, M. Wehmöller, P. A. J. Russo, H. Bolte, E. Sherry, E. Behrens, and H. Terheyden. Growth and transplantation of a custom vascularised bone graft in a man. *The Lancet*, 364(9436):766–770, 2004.

[31] Ranieri Cancedda, Paolo Giannoni, and Maddalena Mastrogiacomo. A tissue engineering approach to bone repair in large animal models and in clinical practice. *Biomaterials*, 28(29):4240–4250, 2007.

[32] Elias Volkmer, Inga Drosse, Sven Otto, Achim Stangelmayer, Michael Stengele, Bobby Cherian Kallukalam, Wolf Mutschler, and Matthias Schieker. Hypoxia in static and dynamic 3d culture systems for tissue engineering of bone. *Tissue Engineering Part A*, 14(8):1331–1340, 2008.

[33] Aaron D. Gitler, Paraminder Dhillon, and James Shorter. Neurodegenerative disease: models, mechanisms, and a new hope. *Disease Models and Mechanisms*, 10(5):499, 2017.

[34] Martha S. Windrem, Mikhail Osipovitch, Zhengshan Liu, Janna Bates, Devin Chandler-Militello, Lisa Zou, Jared Munir, Steven Schanz, Katherine McCoy, Robert H. Miller, Su Wang, Maiken Nedergaard, Robert L. Findling, Paul J. Tesar, and Steven A. Goldman. Human ipsc glial mouse chimeras reveal glial contributions to schizophrenia. *Cell Stem Cell*, 2017.

[35] Fred H. Gage. Mammalian neural stem cells. *Science*, 287(5457):1433–1438, 2000.

[36] J. E. Cheyne, L. Grant, C. Butler-Munro, J. W. Foote, B. Connor, and J. M. Montgomery. Synaptic integration of newly generated neurons in rat dissociated hippocampal cultures. *Molecular and Cellular Neuroscience*, 47(3):203–214, 2011.

[37] F. Féron, C. Perry, J. Cochrane, P. Licina, A. Nowitzke, S. Urquhart, T. Geraghty, and A. Mackay-Sim. Autologous olfactory ensheathing cell transplantation in human spinal cord injury. *Brain*, 128(12):2951, 2005.

[38] A. Mackay-Sim, F. Féron, J. Cochrane, L. Bassingthwaighte, C. Bayliss, W. Davies, P. Fronek, C. Gray, G. Kerr, P. Licina, A. Nowitzke, C. Perry, P. A. S. Silburn, S. Urquhart, and T. Geraghty. Autologous olfactory ensheathing cell transplantation in human paraplegia: a 3-year clinical trial. *Brain : a journal of neurology*, 131(18689435):2376–2386, September 2008.

[39] Pawel Tabakow, Wlodzimierz Jarmundowicz, Bogdan Czapiga, Wojciech Fortuna, Ryszard Miedzybrodzki, Marcin Czyz, Juliusz Huber, Dariusz Szarek, Stefan Okurowski, Pawel Szewczyk, Andrzej Gorski, and Geoffrey Raisman. Transplantation of autologous olfactory ensheathing cells in complete human spinal cord injury. *Cell Transplant*, 22(9):1591–1612, September 2013.

[40] Pallavi Madhusudanan, Gayathri Raju, and Sahadev Shankarappa. Hydrogel systems and their role in neural tissue engineering. *Journal of the Royal Society, Interface*, 17, Jan 2020.

[41] Jindrich Kopecek. Hydrogel biomaterials: a smart future? *Biomaterials*, 28(17697712):5185–5192, December 2007.

[42] O. WICHTERLE and D. L. Í. M. Hydrophilic gels for biological use. *Nature*, 185(4706):117–118, 1960.

[43] Herman F. Mark. *Encyclopedia of polymer science and technology, concise*. John Wiley and Sons, 2013.

[44] Johnson H. Y. Chung, Sina Naficy, Zhilian Yue, Robert Kapsa, Anita Quigley, Simon E. Moulton, and Gordon G. Wallace. Bio-ink properties and printability for extrusion printing living cells. *Biomaterials Science*, 1(7):763, 2013.

[45] Jeanie L. Drury and David J. Mooney. Hydrogels for tissue engineering: scaffold design variables and applications. *Biomaterials*, 24(24):4337–4351, 2003.

[46] Iris Mironi-Harpaz, Dennis Yingquan Wang, Subbu Venkatraman, and Dror Seliktar. Photopolymerization of cell-encapsulating hydrogels: Crosslinking efficiency versus cytotoxicity. *Acta Biomaterialia*, 8(5):1838–1848, 2012.

[47] Jenna M. Shapiro and Michelle L. Oyen. Hydrogel composite materials for tissue engineering scaffolds. *Journal of the Minerals Metals and Materials Society*, 65(4):505–516, 2013.

[48] P. Occhetta, R. Visone, L. Russo, L. Cipolla, M. Moretti, and M. Rasponi. Va-086 methacrylate gelatine photopolymerizable hydrogels: A parametric study for highly biocompatible 3d cell embedding. *Journal of Biomedical Materials Research Part A*, 103(6):2109–17, 2015.

[49] B. J. Klotz, D. Gawlitta, A. J. Rosenberg, J. Malda, and F. P. Melchels. Gelatin-methacryloyl hydrogels: Towards biofabrication-based tissue repair. *Trends in Biotechnology*, 34(5):394–407, 2016.

[50] Niamh Moriarty, Abhay Pandit, and Eilís Dowd. Encapsulation of primary dopaminergic neurons in a gdnf-loaded collagen hydrogel increases their survival, re-innervation and function after intra-striatal transplantation. *Scientific Reports*, 7(1):16033, 2017.

[51] Kun Qiao, Shaolin Guo, Yudong Zheng, Xuetao Xu, Haoye Meng, Jiang Peng, Ziyuan Fang, and Yajie Xie. Effects of graphene on the structure, properties, electro-response

behaviors of go/paa composite hydrogels and influence of electro-mechanical coupling on bmsc differentiation. *Materials Science and Engineering: C*, 93:853–863, 2018.

[52] Dongyoon Kim, Subeom Park, Insu Jo, Seong-Min Kim, Dong Hee Kang, Sung-Pyo Cho, Jong Bo Park, Byung Hee Hong, and Myung-Han Yoon. Multiscale modulation of nanocrystalline cellulose hydrogel via nanocarbon hybridization for 3d neuronal bilayer formation. *Small*, 13(26):1700331–n/a, 2017.

[53] X. F. Liu, A. L. Miller, S. Park, B. E. Waletzki, A. Terzic, M. J. Yaszemski, and L. C. Lu. Covalent crosslinking of graphene oxide and carbon nanotube into hydrogels enhances nerve cell responses. *Journal of Materials Chemistry B*, 4(43):6930–6941, 2016.

[54] N. Golafshan, M. Kharaziha, M. Fathi, B. L. Larson, G. Giatsidis, and N. Masoumi. Anisotropic architecture and electrical stimulation enhance neuron cell behaviour on a tough graphene embedded pva: alginate fibrous scaffold. *RSC Advances*, 8(12):6381–6389, 2018.

[55] Enas M. Ahmed. Hydrogel: Preparation, characterization, and applications: A review. *Journal of Advanced Research*, 6(2):105–121, 2015.

[56] Sytze J. Buwalda, Kristel W. M. Boere, Pieter J. Dijkstra, Jan Feijen, Tina Vermonden, and Wim E. Hennink. Hydrogels in a historical perspective: From simple networks to smart materials. *Journal of Controlled Release*, 190:254–273, 2014.

[57] Cees J. De Groot, Marja J. A. Van Luyn, Welmoed N. E. Van Dijk-Wolthuis, Jenny A. Cadée, Josée A. Plantinga, Willem Den Otter, and Wim E. Hennink. In vitro biocompatibility of biodegradable dextran-based hydrogels tested with human fibroblasts. *Biomaterials*, 22(11):1197–1203, 2001.

[58] Jason W. Nichol, Sandeep T. Koshy, Hojae Bae, Chang M. Hwang, Seda Yamanlar, and Ali Khademhosseini. Cell-laden microengineered gelatin methacrylate hydrogels. *Biomaterials*, 31(21):5536–5544, 2010.

[59] X. Hu, D. Li, F. Zhou, and C. Gao. Biological hydrogel synthesized from hyaluronic acid, gelatin and chondroitin sulfate by click chemistry. *Acta Biomater*, 7(4):1618–26, 2011.

[60] Khoon S. Lim, Marie H. Alves, Laura A. Poole-Warren, and Penny J. Martens. Covalent incorporation of non-chemically modified gelatin into degradable pva-tyramine hydrogels. *Biomaterials*, 34(29):7097–7105, 2013.

[61] H. Baniasadi, S. A. A. Ramazani, and S. Mashayekhan. Fabrication and characterization of conductive chitosan/gelatin-based scaffolds for nerve tissue engineering. *International Journal of Biological Macromolecules*, 74:360–366, 2015.

[62] John E. Moses and Adam D. Moorhouse. The growing applications of click chemistry. *Chemical Society Reviews*, 36(8):1249–1262, 2007.

[63] Sudhir Khetan and Jason Burdick. Cellular encapsulation in 3d hydrogels for tissue engineering. *Journal of Visualized Experiments : JoVE*, 32(32):1590, 2009.

[64] Payam Payamyar, Benjamin T. King, Hans Christian Öttinger, and A. Dieter Schlüter. Two-dimensional polymers: concepts and perspectives. *Chem. Commun.*, 52:18–34, 2016.

[65] Han Shih and Chien-Chi Lin. Cross-linking and degradation of step-growth hydrogels formed by thiol-ene photoclick chemistry. *Biomacromolecules*, 13(7):2003–2012, July 2012.

[66] M. P. Lutolf and J. A. Hubbell. Synthesis and physicochemical characterization of end-linked poly(ethylene glycol)-co-peptide hydrogels formed by michael-type addition. *Biomacromolecules*, 4(3):713–722, 2003.

[67] M. Mario Perera and Neil Ayres. Gelatin based dynamic hydrogels via thiol-norbornene reactions. *Polymer Chemistry*, 8(44):6741–6749, 2017.

[68] Chien-Chi Lin, Asad Raza, and Han Shih. Peg hydrogels formed by thiol-ene photo-click chemistry and their effect on the formation and recovery of insulin-secreting cell spheroids. *Biomaterials*, 32(36):9685–9695, 2011.

[69] Johnna S Temenoff, Heungsoo Shin, Daniel E Conway, Paul S Engel, and Antonios G Mikos. In vitro cytotoxicity of redox radical initiators for cross-linking of oligo (poly (ethylene glycol) fumarate) macromers. *Biomacromolecules*, 4(6):1605–1613, 2003.

[70] Chi Zhang and Allan J. Easteal. Study of poly(acrylamide-co-2-acrylamido-2-methylpropane sulfonic acid) hydrogels made using gamma radiation initiation. *Journal of Applied Polymer Science*, 89(5):1322–1330, August 2003.

[71] Zhongwei Guo, Shengli Mi, and Wei Sun. The multifaceted nature of catechol chemistry: bioinspired ph-initiated hyaluronic acid hydrogels with tunable cohesive and adhesive properties. *Journal of Materials Chemistry B*, 6(39):6234–6244, 2018.

[72] An I. Van Den Bulcke, Bogdan Bogdanov, Nadine De Rooze, Etienne H. Schacht, Maria Cornelissen, and Hugo Berghmans. Structural and rheological properties of methacrylamide modified gelatin hydrogels. *Biomacromolecules*, 1(1):31–38, 2000.

[73] Khoon S. Lim, Barbara J. Klotz, Gabriella C. J. Lindberg, Ferry P. W. Melchels, Gary J. Hooper, Jos Malda, Debby Gawlitta, and Tim B. F. Woodfield. Visible light cross-linking of gelatin hydrogels offers an enhanced cell microenvironment with improved light penetration depth. *Macromolecular Bioscience*, 19(6):1900098, June 2019.

[74] Guan Zhang, In Young Song, Kyo Han Ahn, Taiho Park, and Wonyong Choi. Free radical polymerization initiated and controlled by visible light photocatalysis at ambient temperature. *Macromolecules*, 44(19):7594–7599, 2011.

[75] Khoon S. Lim, Benjamin S. Schon, Naveen V. Mekhileri, Gabriella C. J. Brown, Catherine M. Chia, Sujay Prabakar, Gary J. Hooper, and Tim B. F. Woodfield. New visible-light photoinitiating system for improved print fidelity in gelatin-based bioinks. *ACS Biomaterials Science and Engineering*, 2(10):1752–1762, 2016.

[76] S. Bertlein, G. Brown, K. S. Lim, T. Jungst, T. Boeck, T. Blunk, J. Tessmar, G. J. Hooper, T. B. F. Woodfield, and J. Groll. Thiol-ene clickable gelatin: A platform bioink for multiple 3d biofabrication technologies. *Adv Mater*, 2017.

[77] K. Deshmukh, M. Basheer Ahamed, R. R. Deshmukh, S. K. Khadheer Pasha, P. R. Bhagat, and K. Chidambaram. Biopolymer composites with high dielectric performance: Interface engineering. In K.K. Sadasivuni, D. Ponnamma, J. Kim, J.-J. Cabibihan, and M.A. AlMaadeed, editors, *Biopolymer Composites in Electronics*, pages 27 – 128. Elsevier, 2017.

[78] Kan Yue, Grissel Trujillo-de Santiago, Mario Moisés Alvarez, Ali Tamayol, Nasim Annabi, and Ali Khademhosseini. Synthesis, properties, and biomedical applications of gelatin methacryloyl (gelma) hydrogels. *Biomaterials*, 73:254–271, 2015.

[79] K. S. Novoselov, A. K. Geim, S. V. Morozov, D. Jiang, Y. Zhang, S. V. Dubonos, I. V. Grigorieva, and A. A. Firsov. Electric field effect in atomically thin carbon films. *Science*, 306(5696):666, 2004.

[80] Snehal Mohite and Eswara Prasad. Graphene market by type (mono-layer and bi-layer graphene, few layer graphene, graphene oxide, and graphene nano platelets), and application (rfid, composites, sensors, research and development, energy storage, functional ink, and polymer additives): Global opportunity analysis and industry forecast 2020–2027. *MC : Advanced Materials*, 2020.

[81] B. C. Thompson, E. Murray, and G. G. Wallace. Graphite oxide to graphene. biomaterials to bionics. *Advanced Materials*, 27(46):7563–7582, 2015.

[82] Xiaoming Sun, Zhuang Liu, Kevin Welsher, Joshua Tucker Robinson, Andrew Goodwin, Sasa Zaric, and Hongjie Dai. Nano-graphene oxide for cellular imaging and drug delivery. *Nano Research*, 1(3):203–212, 2008.

[83] K. Y. Li, L. Z. Feng, J. W. Shen, Q. Zhang, Z. Liu, S. T. Lee, and J. Liu. Patterned substrates of nano-graphene oxide mediating highly localized and efficient gene delivery. *Acs Applied Materials and Interfaces*, 6(8):5900–5907, 2014.

[84] Cecilia Mattevi, Hokwon Kim, and Manish Chhowalla. A review of chemical vapour deposition of graphene on copper. *Journal of Materials Chemistry*, 21:3324–3334, 2011.

[85] Yanyan Xu, Huizhe Cao, Yanqin Xue, Biao Li, and Weihua Cai. Liquid-phase exfoliation of graphene: An overview on exfoliation media, techniques, and challenges. *Nanomaterials*, 8, November 2018.

[86] L. M. Malard, M. A. Pimenta, G. Dresselhaus, and M. S. Dresselhaus. Raman spectroscopy in graphene. *Physics Reports*, 473(5–6):51–87, 2009.

[87] Edward P. Randviir, Dale A. C. Brownson, and Craig E. Banks. A decade of graphene research: production, applications and outlook. *Materials Today*, 17(9):426–432, 2014.

[88] C. Choi, Y. Lee, K. W. Cho, J. H. Koo, and D. H. Kim. Wearable and implantable soft bioelectronics using two-dimensional materials. *Accounts of Chemical Research*, 52(1):73–81, 2019.

[89] William S. Hummers and Richard E. Offeman. Preparation of graphitic oxide. *Journal of the American Chemical Society*, 80(6):1339–1339, 1958.

[90] T. Chen, Zeng Baoqing, J. L. Liu, J. H. Dong, X. Q. Liu, Z. Wu, X. Z. Yang, and Z. M. Li. High throughput exfoliation of graphene oxide from expanded graphite with assistance of strong oxidant in modified hummers method. *Journal of Physics: Conference Series*, 188(1):012051, 2009.

[91] D. R. Dreyer, S. Park, C. W. Bielawski, and R. S. Ruoff. The chemistry of graphene oxide. *Chemical Society Reviews*, 39(1):228–240, 2010.

[92] D. R. Dreyer, A. D. Todd, and C. W. Bielawski. Harnessing the chemistry of graphene oxide. *Chemical Society Reviews*, 43(15):5288–5301, 2014.

[93] Anu Saini, Ashok Kumar, V Kumar, and S Chander. Synthesis of graphene oxide using modified hummers method and its reduction using hydrazine hydrate. *International Journal of Engineering: Trends in Technology*, 40:67–71, 2016.

[94] Inhwa Jung, Dmitriy A. Dikin, Richard D. Piner, and Rodney S. Ruoff. Tunable electrical conductivity of individual graphene oxide sheets reduced at low temperatures. *Nano Letters*, 8(12):4283–4287, December 2008.

[95] Sungjin Park, Jinho An, Jeffrey R. Potts, Aruna Velamakanni, Shanthi Murali, and Rodney S. Ruoff. Hydrazine-reduction of graphite- and graphene oxide. *Carbon*, 49(9):3019–3023, 2011.

[96] Yunlong Guo, Chong-an Di, Hongtao Liu, Jian Zheng, Lei Zhang, Gui Yu, and Yunqi Liu. General route toward patterning of graphene oxide by a combination of wettability modulation and spin-coating. *ACS nano*, 4(10):5749–5754, 2010.

[97] Shingjiang Jessie Lue, Yu-Li Pai, Chao-Ming Shih, Ming-Chung Wu, and Sun-Mou Lai. Novel bilayer well-aligned nafion/graphene oxide composite membranes prepared using spin coating method for direct liquid fuel cells. *Journal of Membrane Science*, 493:212–223, 2015.

[98] Emmanuel Kymakis, Kyriaki Savva, Minas M Stylianakis, Costas Fotakis, and Emmanuel Stratakis. Flexible organic photovoltaic cells with in situ nonthermal photoreduction of spin-coated graphene oxide electrodes. *Advanced Functional Materials*, 23(21):2742–2749, 2013.

[99] Yao Yao, Xiangdong Chen, Huihui Guo, Zuquan Wu, and Xiaoyu Li. Humidity sensing behaviors of graphene oxide-silicon bi-layer flexible structure. *Sensors and Actuators B: Chemical*, 161(1):1053–1058, 2012.

[100] Seul Ki Hong, Ji Eun Kim, Sang Ouk Kim, Sung-Yool Choi, and Byung Jin Cho. Flexible resistive switching memory device based on graphene oxide. *IEEE Electron device letters*, 31(9):1005–1007, 2010.

[101] Chenglong Chi, Xuerui Wang, Yongwu Peng, Yuhong Qian, Zhigang Hu, Jinqiao Dong, and Dan Zhao. Facile preparation of graphene oxide membranes for gas separation. *Chemistry of Materials*, 28(9):2921–2927, 2016.

[102] Sandy Peterhänsel, Hannu Laamanen, Joonas Lehtolahti, Markku Kuittinen, Wolfgang Osten, and Jani Tervo. Human color vision provides nanoscale accuracy in thin-film thickness characterization. *Optica*, 2(7):627–630, 2015.

[103] Noel Díez, Agata Śliwak, Stanisław Gryglewicz, Bartosz Grzyb, and Grażyna Gryglewicz. Enhanced reduction of graphene oxide by high-pressure hydrothermal treatment. *Rsc Advances*, 5(100):81831–81837, 2015.

[104] Perng Yang Puah, Pak Yan Moh, Ping Chin Lee, and Siew Eng How. Spin-coated graphene oxide as a biomaterial for whartons jelly derived mesenchymal stem cell growth: a preliminary study. *Materials Technology*, 33(13):835–843, 2018.

[105] Zhijuan Wang, Xiaozhu Zhou, Juan Zhang, Freddy Boey, and Hua Zhang. Direct electrochemical reduction of single-layer graphene oxide and subsequent functionalization with glucose oxidase. *The Journal of Physical Chemistry C*, 113(32):14071–14075, 2009.

[106] Velram Balaji Mohan, Reuben Brown, Krishnan Jayaraman, and Debes Bhattacharyya. Characterisation of reduced graphene oxide: Effects of reduction variables on electrical conductivity. *Materials Science and Engineering: B*, 193:49–60, 2015.

[107] Sungjin Park, Jinho An, Inhwa Jung, Richard D. Piner, Sung Jin An, Xuesong Li, Aruna Velamakanni, and Rodney S. Ruoff. Colloidal suspensions of highly reduced graphene oxide in a wide variety of organic solvents. *Nano Letters*, 9(4):1593–1597, April 2009.

[108] O. Akhavan, E. Ghaderi, E. Abouei, S. Hatamie, and E. Ghasemi. Accelerated differentiation of neural stem cells into neurons on ginseng-reduced graphene oxide sheets. *Carbon*, 66:395–406, 2014.

[109] Zhang Congcong, Chen Mingxi, Xu Xiaoyang, Zhang Li, Zhang Lei, Xia Fengling, Li Xichuan, Liu Yu, Hu Wenping, and Gao Jianping. Graphene oxide reduced and modified by environmentally friendly glycylglycine and its excellent catalytic performance. *Nanotechnology*, 25(13):135707, 2014.

[110] Sangiliyandi Gurunathan and Jin-Hoi Kim. Synthesis, toxicity, biocompatibility, and biomedical applications of graphene and graphene-related materials. *International journal of nanomedicine*, 11:1927, 2016.

[111] Ayrat M. Dimiev, Lawrence B. Alemany, and James M. Tour. Graphene oxide. origin of acidity, its instability in water, and a new dynamic structural model. *ACS Nano*, 7(1):576–588, 2013. PMID: 23215236.

[112] Ayrat M. Dimiev and Thomas A. Polson. Contesting the two-component structural model of graphene oxide and reexamining the chemistry of graphene oxide in basic media. *Carbon*, 93:544–554, 2015.

[113] Helen R. Thomas, Stephen P. Day, William E. Woodruff, Cristina Vallés, Robert J. Young, Ian A. Kinloch, Gavin W. Morley, John V. Hanna, Neil R. Wilson, and Jonathan P. Rourke.

Deoxygenation of graphene oxide: Reduction or cleaning? *Chemistry of Materials*, 25(18):3580–3588, 2013.

[114] Helen R. Thomas, Alexander J. Marsden, Marc Walker, Neil R. Wilson, and Jonathan P. Rourke. Sulfur-functionalized graphene oxide by epoxide ring-opening. *Angewandte Chemie International Edition*, 53(29):7613–7618, 2014.

[115] Jonathan P. Rourke and Neil R. Wilson. Letter to the editor: A defence of the two-component model of graphene oxide. *Carbon*, 96:339–341, 2016.

[116] Kenry, Wong Cheng Lee, Kian Ping Loh, and Chwee Teck Lim. When stem cells meet graphene: Opportunities and challenges in regenerative medicine. *Biomaterials*, 155:236–250, 2018.

[117] B. P. Chan and K. W. Leong. Scaffolding in tissue engineering: general approaches and tissue-specific considerations. *European Spine Journal*, 17(4):467–479, 2008.

[118] Y. Talukdar, J. T. Rashkow, G. Lalwani, S. Kanakia, and B. Sitharaman. The effects of graphene nanostructures on mesenchymal stem cells. *Biomaterials*, 35(18):4863–4877, 2014.

[119] M. L. Tang, Q. Song, N. Li, Z. Y. Jiang, R. Huang, and G. S. Cheng. Enhancement of electrical signaling in neural networks on graphene films. *Biomaterials*, 34(27):6402–6411, 2013.

[120] K. Joshi, B. Mazumder, P. Chattopadhyay, N. S. Bora, D. Goyary, and S. Karmakar. Graphene family of nanomaterials: Reviewing advanced applications in drug delivery and medicine. *Current Drug Delivery*, 16(3):195–214, 2019.

[121] A. Dominguez-Bajo, A. Gonzalez-Mayorga, C. R. Guerrero, F. J. Palomares, R. Garcia, E. Lopez-Dolado, and M. C. Serrano. Myelinated axons and functional blood vessels populate mechanically compliant rgo foams in chronic cervical hemisected rats. *Biomaterials*, 192:461–474, 2019.

[122] E. Lopez-Dolado, A. Gonzalez-Mayorga, M. C. Gutierrez, and M. C. Serrano. Immunomodulatory and angiogenic responses induced by graphene oxide scaffolds in chronic spinal hemisected rats. *Biomaterials*, 99:72–81, 2016.

[123] H. C. Tian, J. Q. Liu, D. X. Wei, X. Y. Kang, C. Zhang, J. C. Du, B. Yang, X. Chen, H. Y. Zhu, Y. N. NuLi, and C. S. Yang. Graphene oxide doped conducting polymer nanocomposite film for electrode-tissue interface. *Biomaterials*, 35(7):2120–2129, 2014.

[124] S. H. Ku, M. Lee, and C. B. Park. Carbon-based nanomaterials for tissue engineering. *Advanced Healthcare Materials*, 2(2):244–260, 2013.

[125] E. Bressan, L. Ferroni, C. Gardin, L. Sbricoli, L. Gobbato, F. S. Ludovichetti, I. Tocco, A. Carraro, A. Piattelli, and B. Zavan. Graphene based scaffolds effects on stem cells commitment. *Journal of Translational Medicine*, 12, 2014.

[126] G. R. Jin and K. Li. The electrically conductive scaffold as the skeleton of stem cell niche in regenerative medicine. *Materials Science and Engineering C-Materials for Biological Applications*, 45:671–681, 2014.

[127] Nelson Duran, Diego Stefani T. Martinez, Camila P. Silveira, Marcela Duran, Ana C. M. de Moraes, Mateus B. Simoes, Oswaldo L. Alves, and Wagner J. Favaro. Graphene oxide: A carrier for pharmaceuticals and a scaffold for cell interactions. *Current Topics in Medicinal Chemistry*, 15(4):309–327, 2015.

[128] Omid Akhavan. Graphene scaffolds in progressive nanotechnology/stem cell-based tissue engineering of the nervous system. *Journal of Materials Chemistry B*, 4(19):3169–3190, 2016.

[129] C. Gardin, A. Piattelli, and B. Zavan. Graphene in regenerative medcine: Focus on stem cells and neuronal differentiation. *Trends in Biotechnology*, 34(6):435–437, 2016.

[130] S. Kumar and K. Chatterjee. Comprehensive review on the use of graphene-based substrates for regenerative medicine and biomedical devices. *Acs Applied Materials and Interfaces*, 8(40):26431–26457, 2016.

[131] G. Lalwani, S. C. Patel, and B. Sitharaman. Two- and three-dimensional all-carbon nanomaterial assemblies for tissue engineering and regenerative medicine. *Annals of Biomedical Engineering*, 44(6):2020–2035, 2016.

[132] M. Duran, A. C. M. Luzo, J. G. de Souza, W. J. Favaro, P. Garcia, and N. Duran. Graphene oxide as scaffolds for stem cells: An overview. *Current Molecular Medicine*, 17(9):619–626, 2017.

[133] S. Syama and P. V. Mohanan. Comprehensive application of graphene: Emphasis on biomedical concern. *Nano-Micro Letters*, 11(1):31, 2019.

[134] M. C. Serrano, J. Patino, C. Garcia-Rama, M. L. Ferrer, J. L. G. Fierro, A. Tamayo, J. E. Collazos-Castro, F. del Monte, and M. C. Gutierrez. 3d free-standing porous scaffolds made of graphene oxide as substrates for neural cell growth. *Journal of Materials Chemistry B*, 2(34):5698–5706, 2014.

[135] S. Shah, P. T. Yin, T. M. Uehara, S. T. D. Chueng, L. T. Yang, and K. B. Lee. Guiding stem cell differentiation into oligodendrocytes using graphene-nanofiber hybrid scaffolds. *Advanced Materials*, 26(22):3673–3680, 2014.

[136] J. Liao, Y. Qu, B. Chu, X. Zhang, and Z. Qian. Biodegradable csma/peca/graphene porous hybrid scaffold for cartilage tissue engineering. *Scientific Reports*, 5:9879, 2015.

[137] J. Q. Song, H. C. Gao, G. L. Zhu, X. D. Cao, X. T. Shi, and Y. J. Wang. The preparation and characterization of polycaprolactone/graphene oxide biocomposite nanofiber scaffolds and their application for directing cell behaviors. *Carbon*, 95:1039–1050, 2015.

[138] P. Wilczek, R. Major, L. Lipinska, J. Lackner, and A. Mzyk. Thrombogenicity and biocompatibility studies of reduced graphene oxide modified acellular pulmonary valve tissue. *Materials Science and Engineering C-Materials for Biological Applications*, 53:310–321, 2015.

[139] Omid Akhavan, Elham Ghaderi, Soheil A. Shirazian, and Reza Rahighi. Rolled graphene oxide foams as three-dimensional scaffolds for growth of neural fibers using electrical stimulation of stem cells. *Carbon*, 97:71–77, 2016.

[140] W. B. Guo, S. Wang, X. Yu, J. C. Qiu, J. H. Li, W. Tang, Z. Li, X. N. Mou, H. Liu, and Z. L. Wang. Construction of a 3d rgo-collagen hybrid scaffold for enhancement of the neural differentiation of mesenchymal stem cells. *Nanoscale*, 8(4):1897–1904, 2016.

[141] Su Ryon Shin, Claudio Zihlmann, Mohsen Akbari, Pribpandao Assawes, Louis Cheung, Kaizhen Zhang, Vijayan Manoharan, Yu Shrike Zhang, Mehmet Yüksekkaya, Kai-tak Wan, Mehdi Nikkhah, Mehmet R. Dokmeci, Xiaowu Tang, and Ali Khademhosseini. Reduced graphene oxide-gelma hybrid hydrogels as scaffolds for cardiac tissue engineering. *Small*, 12(27):3677–3689, 2016.

[142] M. Vera-Sanchez, S. Aznar-Cervantes, E. Jover, D. Garcia-Bernal, R. E. Onate-Sanchez, D. Hernandez-Romero, J. M. Moraleda, M. Collado-Gonzalez, F. J. Rodriguez-Lozano, and J. L. Cenis. Silk-fibroin and graphene oxide composites promote human periodontal ligament stem cell spontaneous differentiation into osteo/cementoblast-like cells. *Stem Cells and Development*, 25(22):1742–1754, 2016.

[143] Kisuk Yang, Jaehong Lee, Jong Seung Lee, Dayeong Kim, Gyeong-Eon Chang, Jungmok Seo, Eunji Cheong, Taeyoon Lee, and Seung-Woo Cho. Graphene oxide hierarchical patterns for the derivation of electrophysiologically functional neuron-like cells from human neural stem cells. *ACS Applied Materials and Interfaces*, 8(28):17763–17774, 2016.

[144] K. H. Zhang, H. H. Zheng, S. Liang, and C. Y. Gao. Aligned plla nanofibrous scaffolds coated with graphene oxide for promoting neural cell growth. *Acta Biomaterialia*, 37:131–142, 2016.

[145] Gaurav Lalwani, Michael D'Agati, Anu Gopalan, Manisha Rao, Jessica Schneller, and Balaji Sitharaman. Three-dimensional macroporous graphene scaffolds for tissue engineering. *Journal of Biomedical Materials Research Part A*, 105(1):73–83, 2017.

[146] S. Sayyar, S. Gambhir, J. Chung, D. L. Officer, and G. G. Wallace. 3d printable conducting hydrogels containing chemically converted graphene. *Nanoscale*, 9(5):2038–2050, 2017.

[147] Y. S. More, G. Panella, G. Fioravanti, F. Perrozzi, M. Passacantando, F. Giansanti, M. Ardini, L. Ottaviano, A. Cimini, C. Peniche, and R. Ippoliti. Biocompatibility of composites based

on chitosan, apatite, and graphene oxide for tissue applications. *Journal of Biomedical Materials Research Part A*, 106(6):1585–1594, 2018.

[148] Y. Qian, J. L. Song, X. T. Zhao, W. Chen, Y. M. Ouyang, W. E. Yuan, and C. Y. Fan. 3d fabrication with integration molding of a graphene oxide/polycaprolactone nanoscaffold for neurite regeneration and angiogenesis. *Advanced Science*, 5(4):18, 2018.

[149] J. Wang, Y. Cheng, L. Chen, T. H. Zhu, K. Q. Ye, C. Jia, H. J. Wang, M. F. Zhu, C. Y. Fan, and X. M. Mo. In vitro and in vivo studies of electroactive reduced graphene oxide-modified nanofiber scaffolds for peripheral nerve regeneration. *Acta Biomaterialia*, 84:98–113, 2019.

[150] Amedea B. Seabra, Amauri J. Paula, Renata de Lima, Oswaldo L. Alves, and Nelson Durán. Nanotoxicity of graphene and graphene oxide. *Chemical Research in Toxicology*, 27(2):159–168, February 2014.

[151] Constantine P. Firme and Prabhakar R. Bandaru. Toxicity issues in the application of carbon nanotubes to biological systems. *Nanomedicine: Nanotechnology, Biology and Medicine*, 6(2):245–256, 2010.

[152] C. Fisher, A. E. Rider, Z. J. Han, S. Kumar, I. Levchenko, and K. Ostrikov. Applications and nanotoxicity of carbon nanotubes and graphene in biomedicine. *Journal of Nanomaterials*, 2012.

[153] Jifeng Yuan, Hongcai Gao, Jianjun Sui, Hongwei Duan, Wei N. Chen, and Chi B. Ching. Cytotoxicity Evaluation of Oxidized Single-Walled Carbon Nanotubes and Graphene Oxide on Human Hepatoma HepG2 cells: An iTRAQ-Coupled 2D LC-MS/MS Proteome Analysis. *Toxicological Sciences*, 126(1):149–161, December 2011.

[154] N. Li, X. M. Zhang, Q. Song, R. G. Su, Q. Zhang, T. Kong, L. W. Liu, G. Jin, M. L. Tang, and G. S. Cheng. The promotion of neurite sprouting and outgrowth of mouse hippocampal cells in culture by graphene substrates. *Biomaterials*, 32(35):9374–9382, 2011.

[155] G. M. D'Abaco, C. Mattei, B. K. Nasr, E. J. Hudson, A. J. Alshawaf, G. Chana, I. P. Everall, B. Nayagam, M. Dottori, and E. Skafidas. Graphene foam as a biocompatible scaffold for culturing human neurons. *Royal Society Open Science*, 5(3):11, 2018.

[156] N. Tasnim, V. Thakur, M. Chattopadhyay, and B. Joddar. The efficacy of graphene foams for culturing mesenchymal stem cells and their differentiation into dopaminergic neurons. *Stem Cells International*, page 12, 2018.

[157] E. Lopez-Dolado, A. Gonzalez-Mayorga, M. T. Portoles, M. J. Feito, M. L. Ferrer, F. Del Monte, M. C. Gutierrez, and M. C. Serrano. Subacute tissue response to 3d graphene oxide scaffolds implanted in the injured rat spinal cord. *Adv Healthc Mater*, 4(12):1861–8, 2015.

[158] Rongrong Guo, Shasha Zhang, Miao Xiao, Fuping Qian, Zuhong He, Dan Li, Xiaoli Zhang, Huawei Li, Xiaowei Yang, Ming Wang, Renjie Chai, and Mingliang Tang. Accelerating bioelectric functional development of neural stem cells by graphene coupling: Implications for neural interfacing with conductive materials. *Biomaterials*, 106:193–204, 2016.

[159] Ali H. Palejwala, Jared S. Fridley, Javier A. Mata, Errol L. G. Samuel, Thomas G. Luerssen, Laszlo Perlaky, Thomas A. Kent, James M. Tour, and Andrew Jea. Biocompatibility of reduced graphene oxide nanoscaffolds following acute spinal cord injury in rats. *Surgical Neurology International*, 7:75, 2016.

[160] Adam E. Jakus, Ethan B. Secor, Alexandra L. Rutz, Sumanas W. Jordan, Mark C. Hersam, and Ramille N. Shah. Three-dimensional printing of high-content graphene scaffolds for electronic and biomedical applications. *ACS Nano*, 9(4):4636–4648, 2015.

[161] Hanene Ali-Boucetta, Dimitrios Bitounis, Rahul Raveendran-Nair, Ania Servant, Jeroen Van den Bossche, and Kostas Kostarelos. Purified graphene oxide dispersions lack in vitro cytotoxicity and in vivo pathogenicity. *Advanced Healthcare Materials*, 2(3):433–441, 2012.

[162] Yingjie Li, Liangzhu Feng, Xiaoze Shi, Xiaojing Wang, Yinlong Yang, Kai Yang, Teng Liu, Guangbao Yang, and Zhuang Liu. Surface coating-dependent cytotoxicity and degradation of graphene derivatives: Towards the design of non-toxic, degradable nano-graphene. *Small*, 10(8):1544–1554, 2014.

[163] Emanuela Mari, Stefania Mardente, Emanuela Morgante, Marco Tafani, Emanuela Lococo,

Flavia Fico, Federica Valentini, and Alessandra Zicari. Graphene oxide nanoribbons induce autophagic vacuoles in neuroblastoma cell lines. *International Journal of Molecular Sciences*, 17(12), 2016.

[164] Chao Sun, Devin L Wakefield, Yimo Han, David A Muller, David A Holowka, Barbara A Baird, and William R Dichtel. Graphene oxide nanosheets stimulate ruffling and shedding of mammalian cell plasma membranes. *Chem*, 1(2):273–286, 2016.

[165] J. L. Yi, Z. Zhao, S. P. Li, Y. X. Yin, and X. Y. Wang. In vitro biological evaluation of graphene on neuronal cells. *Journal of Wuhan University of Technology-Materials Science Edition*, 31(4):925–930, 2016.

[166] J. C. Soares, T. C. B. Pereira, K. M. Costa, T. Maraschin, N. R. Basso, and M. R. Bogo. Developmental neurotoxic effects of graphene oxide exposure in zebrafish larvae (danio rerio). *Colloids and Surfaces B: Biointerfaces*, 157(Supplement C):335–346, 2017.

[167] Jingjing Guo, Xiaojun Yao, Lulu Ning, Qianqian Wang, and Huanxiang Liu. The adsorption mechanism and induced conformational changes of three typical proteins with different secondary structural features on graphene. *RSC Advances*, 4(20):9953–9962, 2014.

[168] Çağla Defteralı, Raquel Verdejo, Laura Peponi, Eduardo D. Martín, Ricardo Martínez-Murillo, Miguel Ángel López-Manchado, and Carlos Vicario-Abejón. Thermally reduced graphene is a permissive material for neurons and astrocytes and de novo neurogenesis in the adult olfactory bulb in vivo. *Biomaterials*, 82:84–93, 2016.

[169] A. Fabbro, D. Scaini, V. Leon, E. Vazquez, G. Cellot, G. Privitera, L. Lombardi, F. Torrisi, F. Tomarchio, F. Bonaccorso, S. Bosi, A. C. Ferrari, L. Ballerini, and M. Prato. Graphene-based interfaces do not alter target nerve cells. *Acs Nano*, 10(1):615–623, 2016.

[170] Y. J. Lee, W. Jang, H. Im, and J. S. Sung. Extremely low frequency electromagnetic fields enhance neuronal differentiation of human mesenchymal stem cells on graphene-based substrates. *Current Applied Physics*, 15:S95–S102, 2015.

[171] D. A. Balikov, B. Fang, Y. W. Chun, S. W. Crowder, D. Prasai, J. B. Lee, K. I. Bolotin, and H. J. Sung. Directing lineage specification of human mesenchymal stem cells by decou-

pling electrical stimulation and physical patterning on unmodified graphene. *Nanoscale*, 8(28):13730–13739, 2016.

[172] M. Bramini, G. Alberini, E. Colombo, M. Chiacchiaretta, M. L. DiFrancesco, J. F. Maya-Vetencourt, L. Maragliano, F. Benfenati, and F. Cesca. Interfacing graphene-based materials with neural cells. *Frontiers in Systems Neuroscience*, 12:22, 2018.

[173] Chunyi Zhi, Marta Skoda, Ilona Dudek, Anna Jarosz, and Dariusz Szukiewicz. Graphene: One material, many possibilities–application difficulties in biological systems. *Journal of Nanomaterials*, 2014:890246, 2014.

[174] Sakthivel Thangavel and Gunasekaran Venugopal. Understanding the adsorption property of graphene-oxide with different degrees of oxidation levels. *Powder Technology*, 257:141–148, 2014.

[175] Kasturi Muthoosamy, Renu Geetha Bai, Ibrahim Babangida Abubakar, Surya Mudavasseril Sudheer, Hong Ngee Lim, Hwei-San Loh, Nay Ming Huang, Chin Hua Chia, and Sivakumar Manickam. Exceedingly biocompatible and thin-layered reduced graphene oxide nanosheets using an eco-friendly mushroom extract strategy. *International journal of nanomedicine*, 10(25759577):1505–1519, February 2015.

[176] Wendi Zhang, Liang Yan, Meng Li, Ruisheng Zhao, Xiao Yang, Tianjiao Ji, Zhanjun Gu, Jun-Jie Yin, Xingfa Gao, and Guangjun Nie. Deciphering the underlying mechanisms of oxidation-state dependent cytotoxicity of graphene oxide on mammalian cells. *Toxicology Letters*, 237(2):61–71, 2015.

[177] Xue-Qin Wei, Li-Ying Hao, Xiao-Ru Shao, Quan Zhang, Xiao-Qin Jia, Zhi-Rong Zhang, Yun-Feng Lin, and Qiang Peng. Insight into the interaction of graphene oxide with serum proteins and the impact of the degree of reduction and concentration. *ACS Applied Materials and Interfaces*, 7(24):13367–13374, 2015.

[178] Ondřej Mrózek, Lucie Melounková, Darina Smržová, Aneta Machálková, Jaromír Vinklárek, Zuzana Němečková, Bára Komárková, and Petra Ecorchard. Salt-washed graphene oxide and its cytotoxicity. *Journal of Hazardous Materials*, 398:123114, 2020.

[179] André M. M. Sousa, Kyle A. Meyer, Gabriel Santpere, Forrest O. Gulden, and Nenad Sestan. Evolution of the human nervous system function, structure, and development. *Cell*, 170(28708995):226–247, July 2017.

[180] Rudolf Nieuwenhuys, Jan Voogd, and Christiaan Van Huijzen. *The human central nervous system: a synopsis and atlas*. Springer Science and Business Media, 2007.

[181] Silvia Velasco, Amanda J. Kedaigle, Sean K. Simmons, Allison Nash, Marina Rocha, Giorgia Quadrato, Bruna Paulsen, Lan Nguyen, Xian Adiconis, Aviv Regev, Joshua Z. Levin, and Paola Arlotta. Individual brain organoids reproducibly form cell diversity of the human cerebral cortex. *Nature*, 570(7762):523–527, 2019.

[182] J. A. W. van Dommelen, T. P. J. van der Sande, M. Hrapko, and G. W. M. Peters. Mechanical properties of brain tissue by indentation: Interregional variation. *Journal of the Mechanical Behavior of Biomedical Materials*, 3(2):158–166, 2010.

[183] S. Budday, G. Sommer, C. Birkl, C. Langkammer, J. Haybaeck, J. Kohnert, M. Bauer, F. Paulsen, P. Steinmann, E. Kuhl, and G. A. Holzapfel. Mechanical characterization of human brain tissue. *Acta Biomaterialia*, 48:319–340, 2017.

[184] Luke Souter and Jessica C. F. Kwok. Visualization of perineuronal nets in central nervous system tissue sections. *Methods in molecular biology (Clifton, N.J.)*, 2043:251–260, 2020.

[185] Lorraine W. Lau, Rowena Cua, Michael B. Keough, Sarah Haylock-Jacobs, and V. Wee Yong. Pathophysiology of the brain extracellular matrix: a new target for remyelination. *Nature Reviews Neuroscience*, 14(10):722–729, 2013.

[186] Michael K. McMillian, Linda Thai, J. S. Hong, James P. O'Callaghan, and Keith R. Pennypacker. Brain injury in a dish: a model for reactive gliosis. *Trends in Neurosciences*, 17(4):138–142, 1994.

[187] Alan I. Faden. Pharmacological treatment of central nervous system trauma. *Pharmacology and Toxicology*, 78(1):12–17, 1996.

[188] M. C. LaPlaca, C. M. Simon, G. R. Prado, D. K. Cullen, John T. Weber, and Andrew I. R. Maas. Cns injury biomechanics and experimental models. In *Progress in Brain Research*, volume 161, pages 13–26. Elsevier, 2007.

[189] Michael T. Fitch and Jerry Silver. Cns injury, glial scars, and inflammation: Inhibitory extracellular matrices and regeneration failure. *Experimental Neurology*, 209(2):294–301, 2008.

[190] LJ Noble and Jean R Wrathall. Distribution and time course of protein extravasation in the rat spinal cord after contusive injury. *Brain research*, 482(1):57–66, 1989.

[191] Dustin J. Donnelly and Phillip G. Popovich. Inflammation and its role in neuroprotection, axonal regeneration and functional recovery after spinal cord injury. *Experimental Neurology*, 209(2):378–388, 2008.

[192] Jorge Correale, María I. Gaitán, María C. Ysrraelit, and Marcela P. Fiol. Progressive multiple sclerosis: from pathogenic mechanisms to treatment. *Brain : a journal of neurology*, 140:527–546, 2017.

[193] JE Merrill, LJ Ignarro, MP Sherman, J Melinek, and TE Lane. Microglial cell cytotoxicity of oligodendrocytes is mediated through nitric oxide. *The Journal of Immunology*, 151(4):2132–2141, 1993.

[194] Olivera Nesic, Guo-Ying Xu, David McAdoo, Karin Westlund High, Claire Hulsebosch, and Regino Perez-Polo. Il-1 receptor antagonist prevents apoptosis and caspase-3 activation after spinal cord injury. *Journal of neurotrauma*, 18(9):947–956, 2001.

[195] Jerry Silver and Jared H. Miller. Regeneration beyond the glial scar. *Nature Reviews Neuroscience*, 5(2):146–156, 2004.

[196] Michael D Norenberg, Jon Smith, and Alex Marcillo. The pathology of human spinal cord injury: defining the problems, 2004.

[197] Michael V. Sofroniew. Molecular dissection of reactive astrogliosis and glial scar formation. *Trends in Neurosciences*, 32(12):638–647, 2009.

[198] F. White, J. A. Nicoll, and K. Horsburgh. Alterations in apoe and apoj in relation to degeneration and regeneration in a mouse model of entorhinal cortex lesion. *Experimental neurology*, 169:307–18, June 2001.

[199] Veronique E. Miron, Amanda Boyd, Jing-Wei Zhao, Tracy J. Yuen, Julia M. Ruckh, Jennifer L. Shadrach, Peter van Wijngaarden, Amy J. Wagers, Anna Williams, Robin J. M. Franklin, and Charles ffrench Constant. M2 microglia and macrophages drive oligodendrocyte differentiation during cns remyelination. *Nature Neuroscience*, 16(9):1211–1218, 2013.

[200] Ruben Orihuela, Christopher A. McPherson, and Gaylia Jean Harry. Microglial m1/m2 polarization and metabolic states. *British Journal of Pharmacology*, 173(4):649–665, February 2016.

[201] P. N. Koutsoudaki, F. Papastefanaki, A. Stamatakis, G. Kouroupi, E. Xingi, F. Stylianopoulou, and R. Matsas. Neural stem/progenitor cells differentiate into oligodendrocytes, reduce inflammation, and ameliorate learning deficits after transplantation in a mouse model of traumatic brain injury. *Glia*, 64(5):763–779, 2016.

[202] Z. Y. Jiang, Q. Song, M. L. Tang, L. Y. Yang, Y. L. Cheng, M. Zhang, D. S. Xu, and G. S. Cheng. Enhanced migration of neural stem cells by microglia grown on a three-dimensional graphene scaffold. *Acs Applied Materials and Interfaces*, 8(38):25069–25077, 2016.

[203] Christopher S. von Bartheld, Jami Bahney, and Suzana Herculano-Houzel. The search for true numbers of neurons and glial cells in the human brain: A review of 150 years of cell counting. *The Journal of comparative neurology*, 524(18):3865–3895, 2016.

[204] Joshua A Waxenbaum, Vamsi Reddy, and Bruno Bordoni. Anatomy, head and neck, cervical nerves. In *StatPearls [Internet]*. StatPearls Publishing, 2020.

[205] Sarah Melzer and Hannah Monyer. Diversity and function of corticopetal and corticofugal gabaergic projection neurons. *Nature Reviews Neuroscience*, 21(9):499–515, 2020.

[206] Tadeusz Wieloch and Karoly Nikolich. Mechanisms of neural plasticity following brain injury. *Current Opinion in Neurobiology*, 16(3):258–264, 2006.

[207] Gerd Kempermann, Hongjun Song, and Fred H. Gage. Neurogenesis in the adult hippocampus. *Cold Spring Harbor Perspectives in Biology*, 7(9), 2015.

[208] Giorgio Scivoletto, Federica Tamburella, Letizia Laurenza, Monica Torre, and Marco Molinari. Who is going to walk? a review of the factors influencing walking recovery after spinal cord injury. *Frontiers in Human Neuroscience*, 8:141, 2014.

[209] Maggie A. Khuu, Chelsea M. Pagan, Thara Nallamothu, Robert F. Hevner, Rebecca D. Hodge, Jan-Marino Ramirez, and Alfredo J. Garcia. Intermittent hypoxia disrupts adult neurogenesis and synaptic plasticity in the dentate gyrus. *The Journal of Neuroscience*, 39(7):1320, 2019.

[210] Guo-li Ming, John Henley, Marc Tessier-Lavigne, Hong-jun Song, and Mu-ming Poo. Electrical activity modulates growth cone guidance by diffusible factors. *Neuron*, 29(2):441–452, 2001.

[211] Kristjan R. Jessen. Glial cells. *The International Journal of Biochemistry and Cell Biology*, 36(10):1861–1867, 2004.

[212] Suzana Herculano-Houzel. The human brain in numbers: a linearly scaled-up primate brain. *Frontiers in Human Neuroscience*, 3:31, 2009.

[213] Michael V Sofroniew and Harry V Vinters. Astrocytes: biology and pathology. *Acta neuropathologica*, 119(1):7–35, 2010.

[214] Elizabeth M. Rhea and William A. Banks. Role of the blood-brain barrier in central nervous system insulin resistance. *Frontiers in neuroscience*, 13:521, 2019.

[215] Helmut Kettenmann, Uwe-Karsten Hanisch, Mami Noda, and Alexei Verkhratsky. Physiology of microglia. *Physiological Reviews*, 91(2):461–553, April 2011.

[216] Robert H. Miller. Oligodendrocyte origins. *Trends in Neurosciences*, 19(3):92–96, 1996.

[217] Jared M. Cregg, Marc A. DePaul, Angela R. Filous, Bradley T. Lang, Amanda Tran, and Jerry Silver. Functional regeneration beyond the glial scar. *Experimental Neurology*, 253:197–207, 2014.

[218] PAUL J Reier. Gliosis following cns injury: the anatomy of astrocytic scars and their influences on axonal elongation. *Astrocytes*, 3:263–324, 2012.

[219] Jerry Silver. The glial scar is more than just astrocytes. *Experimental Neurology*, 2016.

[220] Andrew M. Tan, Weibing Zhang, and Joel M. Levine. Ng2: a component of the glial scar that inhibits axon growth. *Journal of Anatomy*, 207(6):717–725, 2005.

[221] C. J. Van Den Berg and D. Garfinkel. A simulation study of brain compartments. Metabolism of glutamate and related substances in mouse brain. *Biochemical Journal*, 123(2):211–218, June 1971.

[222] U Sonnewald, N Westergaard, A Schousboe, JS Svendsen, G Unsgård, and SB Petersen. Direct demonstration by [13c] nmr spectroscopy that glutamine from astrocytes is a precursor for gaba synthesis in neurons. *Neurochemistry international*, 22(1):19–29, 1993.

[223] William Lee, Erik Malarkey, Reno Reyes, and Vladimir Parpura. Micropit: A new cell culturing approach for characterization of solitary astrocytes and small networks of these glial cells. *Frontiers in Neuroengineering*, 1:2, 2008.

[224] A. C. Charles, J. E. Merrill, E. R. Dirksen, and M. J. Sanderson. Intercellular signaling in glial cells: calcium waves and oscillations in response to mechanical stimulation and glutamate. *Neuron*, 6:983–92, June 1991.

[225] Raymond C. Koehler, Richard J. Roman, and David R. Harder. Astrocytes and the regulation of cerebral blood flow. *Trends in neurosciences*, 32:160–9, March 2009.

[226] Gerald Seifert, Giorgio Carmignoto, and Christian Steinhäuser. Astrocyte dysfunction in epilepsy. *Brain research reviews*, 63:212–21, May 2010.

[227] S. A. Liddelow, K. A. Guttenplan, L. E. Clarke, F. C. Bennett, C. J. Bohlen, L. Schirmer, M. L. Bennett, A. E. Munch, W. S. Chung, T. C. Peterson, D. K. Wilton, A. Frouin, B. A. Napier, N. Panicker, M. Kumar, M. S. Buckwalter, D. H. Rowitch, V. L. Dawson, T. M. Dawson, B. Stevens, and B. A. Barres. Neurotoxic reactive astrocytes are induced by activated microglia. *Nature*, 541(7638):481–487, 2017.

[228] Ting Li, Xuhui Chen, Chuanhan Zhang, Yue Zhang, and Wenlong Yao. An update on reactive astrocytes in chronic pain. *Journal of neuroinflammation*, 16(1):140, 2019.

[229] Laura Clarke, Shane Liddelow, Chandrani Chakraborty, Alexandra Munch, Myriam Heiman, and Ben Barres. Normal aging induces a1-like astrocyte reactivity. *Proceedings of the National Academy of Sciences*, 115:201800165, 2018.

[230] Seiji Okada, Masamitsu Hara, Kazu Kobayakawa, Yoshihiro Matsumoto, and Yasuharu Nakashima. Astrocyte reactivity and astrogliosis after spinal cord injury. *Neuroscience research*, 126:39–43, 2018.

[231] Mark A. Anderson, Timothy M. O'Shea, Joshua E. Burda, Yan Ao, Sabry L. Barlatey, Alexander M. Bernstein, Jae H. Kim, Nicholas D. James, Alexandra Rogers, Brian Kato, Alexander L. Wollenberg, Riki Kawaguchi, Giovanni Coppola, Chen Wang, Timothy J. Deming, Zhigang He, Gregoire Courtine, and Michael V. Sofroniew. Required growth facilitators propel axon regeneration across complete spinal cord injury. *Nature*, 2018.

[232] Sari S Hannila and Marie T Filbin. The role of cyclic amp signaling in promoting axonal regeneration after spinal cord injury. *Experimental neurology*, 209(2):321–332, 2008.

[233] Pia Rivetti di Val Cervo, Roman A. Romanov, Giada Spigolon, Débora Masini, Elisa Martín-Montañez, Enrique M. Toledo, Gioele La Manno, Michael Feyder, Christian Pifl, Yi-Han Ng, Sara Padrell Sánchez, Sten Linnarsson, Marius Wernig, Tibor Harkany, Gilberto Fisone, and Ernest Arenas. Induction of functional dopamine neurons from human astrocytes in vitro and mouse astrocytes in a parkinson's disease model. *Nature Biotechnology*, 2017.

[234] V Hugh Perry, James AR Nicoll, and Clive Holmes. Microglia in neurodegenerative disease. *Nature Reviews Neurology*, 6(4):193, 2010.

[235] Jong Seong Roh and Dong Hyun Sohn. Damage-associated molecular patterns in inflammatory diseases. *Immune network*, 18(30181915):e27–e27, August 2018.

[236] Carol A. Colton. Heterogeneity of microglial activation in the innate immune response in the brain. *Journal of Neuroimmune Pharmacology*, 4(4):399–418, 2009.

[237] Roslyn A. Taylor, Che-Feng Chang, Brittany A. Goods, Matthew D. Hammond, Brian Mac Grory, Youxi Ai, Arthur F. Steinschneider, Stephen C. Renfroe, Michael H. Askenase, Louise D. McCullough, Scott E. Kasner, Michael T. Mullen, David A. Hafler, J. Christopher Love, and Lauren H. Sansing. Tgf-1 modulates microglial phenotype and promotes recovery after intracerebral hemorrhage. *The Journal of clinical investigation*, 127:280–292, Jan 2017.

[238] Jenny S. Henkel, David R. Beers, Weihua Zhao, and Stanley H. Appel. Microglia in als: The good, the bad, and the resting. *Journal of Neuroimmune Pharmacology*, 4(4):389–398, 2009.

[239] Soraya Meghari, Yassina Bechah, Christian Capo, Hubert Lepidi, Didier Raoult, Peter J Murray, and Jean-Louis Mege. Persistent coxiella burnetii infection in mice overexpressing il-10: an efficient model for chronic q fever pathogenesis. *PLOS Pathog*, 4(2):e23, 2008.

[240] Alessandro Michelucci, Tony Heurtaux, Luc Grandbarbe, Eleonora Morga, and Paul Heuschling. Characterization of the microglial phenotype under specific pro-inflammatory and anti-inflammatory conditions: effects of oligomeric and fibrillar amyloid-β. *Journal of neuroimmunology*, 210(1-2):3–12, 2009.

[241] DY Vogel, EJ Vereyken, JE Glim, PD Heijnen, M Moeton, P van der Valk, S Amor, CE Teunissen, J van Horssen, and CD Dijkstra. Macrophages in inflammatory multiple sclerosis lesions have an intermediate activation status. j neuroinflamm 10: 35, 2013.

[242] Ben Emery. Regulation of oligodendrocyte differentiation and myelination. *Science*, 330(6005):779, November 2010.

[243] Monika Bradl and Hans Lassmann. Oligodendrocytes: biology and pathology. *Acta Neuropathologica*, 119(1):37–53, 2010.

[244] R. Smith. The basic protein of cns myelin: its structure and ligand binding. *Journal of neurochemistry*, 59:1589–608, November 1992.

[245] Ursula Fünfschilling, Lotti M. Supplie, Don Mahad, Susann Boretius, Aiman S. Saab, Julia Edgar, Bastian G. Brinkmann, Celia M. Kassmann, Iva D. Tzvetanova, Wiebke Möbius,

Francisca Diaz, Dies Meijer, Ueli Suter, Bernd Hamprecht, Michael W. Sereda, Carlos T. Moraes, Jens Frahm, Sandra Goebbels, and Klaus-Armin Nave. Glycolytic oligodendrocytes maintain myelin and long-term axonal integrity. *Nature*, 485(7399):517–521, 2012.

[246] Ana Amaral, Tore Meisingset, Mark Kotter, and Ursula Sonnewald. Metabolic aspects of neuron-oligodendrocyte-astrocyte interactions. *Frontiers in Endocrinology*, 4:54, 2013.

[247] AM Halliday and WI McDonald. Pathophysiology of demyelinating disease. *British medical bulletin*, 33(1):21–27, 1977.

[248] José Abad-Rodríguez and Natalia Díez-Revuelta. Axon glycoprotein routing in nerve polarity, function, and repair. *Trends in Biochemical Sciences*, 40(7):385–396, 2015.

[249] Yvonne Dombrowski, Thomas O'Hagan, Marie Dittmer, Rosana Penalva, Sonia R. Mayoral, Peter Bankhead, Samara Fleville, George Eleftheriadis, Chao Zhao, Michelle Naughton, Rachel Hassan, Jill Moffat, John Falconer, Amanda Boyd, Peter Hamilton, Ingrid V. Allen, Adrien Kissenpfennig, Paul N. Moynagh, Emma Evergren, Bernard Perbal, Anna C. Williams, Rebecca J. Ingram, Jonah R. Chan, Robin J. M. Franklin, and Denise C. Fitzgerald. Regulatory t cells promote myelin regeneration in the central nervous system. *Nature Neuroscience*, advance online publication, 2017.

[250] Emad Moeendarbary, Isabell P. Weber, Graham K. Sheridan, David E. Koser, Sara Soleman, Barbara Haenzi, Elizabeth J. Bradbury, James Fawcett, and Kristian Franze. The soft mechanical signature of glial scars in the central nervous system. *Nature communications*, 8:14787, Mar 2017.

[251] Richard D. Bartlett, Despoina Eleftheriadou, Rachael Evans, David Choi, and James B. Phillips. Mechanical properties of the spinal cord and brain: Comparison with clinical-grade biomaterials for tissue engineering and regenerative medicine. *Biomaterials*, 258:120303, Nov 2020.

[252] Johannes Weickenmeier, Rijk de Rooij, Silvia Budday, Timothy C. Ovaert, and Ellen Kuhl. The mechanical importance of myelination in the central nervous system. *Journal of the mechanical behavior of biomedical materials*, 76:119–124, Dec 2017.

[253] Duo Xu, Di Wu, Meng Qin, Lina R. Nih, Chaoyong Liu, Zheng Cao, Jie Ren, Xiangjun Chen, Zhanlong He, Wenhai Yu, Jiaoqiong Guan, Suqin Duan, Fang Liu, Xiangsheng Liu, Jesse Li, Dushawn Harley, Bin Xu, Lihua Hou, Irvin S. Y. Chen, Jing Wen, Wei Chen, Sina Pourtaheri, and Yunfeng Lu. Efficient delivery of nerve growth factors to the central nervous system for neural regeneration. *Advanced materials (Deerfield Beach, Fla.)*, 31:e1900727, Aug 2019.

[254] Anne Faust, Apoorva Kandakatla, Yolandi van der Merwe, Tanchen Ren, Luai Huleihel, George Hussey, Juan Diego Naranjo, Scott Johnson, Stephen Badylak, and Michael Steketee. Urinary bladder extracellular matrix hydrogels and matrix-bound vesicles differentially regulate central nervous system neuron viability and axon growth and branching. *Journal of biomaterials applications*, 31:1277–1295, Apr 2017.

[255] Xiaolei Yin, Benjamin E. Mead, Helia Safaee, Robert Langer, Jeffrey M. Karp, and Oren Levy. Engineering stem cell organoids. *Cell stem cell*, 18:25–38, Jan 2016.

[256] Bilal Cakir, Yangfei Xiang, Yoshiaki Tanaka, Mehmet H. Kural, Maxime Parent, Young-Jin Kang, Kayley Chapeton, Benjamin Patterson, Yifan Yuan, Chang-Shun He, Micha Sam B. Raredon, Jake Dengelegi, Kun-Yong Kim, Pingnan Sun, Mei Zhong, Sangho Lee, Prabir Patra, Fahmeed Hyder, Laura E. Niklason, Sang-Hun Lee, Young-Sup Yoon, and In-Hyun Park. Engineering of human brain organoids with a functional vascular-like system. *Nature methods*, 16:1169–1175, Nov 2019.

[257] Carla C. Winter, Kritika S. Katiyar, Nicole S. Hernandez, Yeri J. Song, Laura A. Struzyna, James P. Harris, and D. Kacy Cullen. Transplantable living scaffolds comprised of micro-tissue engineered aligned astrocyte networks to facilitate central nervous system regeneration. *Acta biomaterialia*, 38:44–58, Jul 2016.

[258] F. Veliev, A. Briancon-Marjollet, V. Bouchiat, and C. Delacour. Impact of crystalline quality on neuronal affinity of pristine graphene. *Biomaterials*, 86:33–41, 2016.

[259] Isao Ogino, Yuya Yokoyama, Shinichiro Iwamura, and Shin R. Mukai. Exfoliation of graphite oxide in water without sonication: Bridging length scales from nanosheets to macroscopic materials. *Chemistry of Materials*, 26(10):3334–3339, 2014.

[260] Jeong Soon Lee, Alexey Lipatov, Ligyeom Ha, Mikhail Shekhirev, Mohammad Nahid Andalib, Alexander Sinitskii, and Jung Yul Lim. Graphene substrate for inducing neurite outgrowth. *Biochemical and Biophysical Research Communications*, 460(2):267–273, 2015.

[261] Nishat Tasnim, Alok Kumar, and Binata Joddar. Attenuation of the in vitro neurotoxicity of 316l ss by graphene oxide surface coating. *Materials Science and Engineering: C*, 73:788–797, 2017.

[262] Xifeng Liu, A. Lee Miller, Sungjo Park, Brian E. Waletzki, Zifei Zhou, Andre Terzic, and Lichun Lu. Functionalized carbon nanotube and graphene oxide embedded electrically conductive hydrogel synergistically stimulates nerve cell differentiation. *ACS Applied Materials and Interfaces*, 9(17):14677–14690, 2017.

[263] Q. Song, Z. Y. Jiang, N. Li, P. Liu, L. W. Liu, M. L. Tang, and G. S. Cheng. Anti-inflammatory effects of three-dimensional graphene foams cultured with microglial cells. *Biomaterials*, 35(25):6930–6940, 2014.

[264] S. Das, M. K. Kumawat, S. Ranganathan, R. Kumar, J. Adamcik, P. Kadu, R. Padinhateeri, R. Srivastava, R. Mezzenga, and S. K. Maji. Cell alignment on graphene-amyloid composites. *Advanced Materials Interfaces*, 5(18):8, 2018.

[265] W. B. Guo, X. D. Zhang, X. Yu, S. Wang, J. C. Qiu, W. Tang, L. L. Li, H. Liu, and Z. L. Wang. Self-powered electrical stimulation for enhancing neural differentiation of mesenchymal stem cells on graphene-poly(3,4-ethylenedioxythiophene) hybrid microfibers. *Acs Nano*, 10(5):5086–5095, 2016.

[266] J. Kim, W. G. Bae, S. Park, Y. J. Kim, I. Jo, S. Park, N. L. Jeon, W. Kwak, S. Choi, J. Park, H. N. Kim, K. S. Choi, H. Seonwoo, Y. H. Choung, P. H. Choung, B. H. Hong, and J. H. Chung. Engineering structures and functions of mesenchymal stem cells by suspended large-area graphene nanopatterns. *2d Materials*, 3(3), 2016.

[267] G. Y. Chen, D. W. Pang, S. M. Hwang, H. Y. Tuan, and Y. C. Hu. A graphene-based platform for induced pluripotent stem cells culture and differentiation. *Biomaterials*, 33(2):418–27, 2012.

[268] Z. Q. Feng, K. Yan, C. M. Shi, X. R. Xu, T. Wang, R. T. Li, W. Dong, and J. Zheng. Neurogenic differentiation of adipose derived stem cells on graphene-based mat. *Materials Science and Engineering C-Materials for Biological Applications*, 90:685–692, 2018.

[269] Wong Cheng Lee, Candy Haley Y. X. Lim, Hui Shi, Lena A. L. Tang, Yu Wang, Chwee Teck Lim, and Kian Ping Loh. Origin of enhanced stem cell growth and differentiation on graphene and graphene oxide. *ACS Nano*, 5(9):7334–7341, 2011.

[270] Martina Chiacchiaretta, Mattia Bramini, Anna Rocchi, Andrea Armirotti, Emanuele Giordano, Ester Vázquez, Tiziano Bandiera, Stefano Ferroni, Fabrizia Cesca, and Fabio Benfenati. Graphene oxide upregulates the homeostatic functions of primary astrocytes and modulates astrocyte-to-neuron communication. *Nano letters*, 18:5827–5838, Sep 2018.

[271] Hiroyuki Itosaka, Satoshi Kuroda, Hideo Shichinohe, Hiroshi Yasuda, Shunsuke Yano, Shintaro Kamei, Ryoichi Kawamura, Kazutoshi Hida, and Yoshinobu Iwasaki. Fibrin matrix provides a suitable scaffold for bone marrow stromal cells transplanted into injured spinal cord: A novel material for cns tissue engineering. *Neuropathology*, 29(3):248–257, June 2009.

[272] Nicole J. Tester, Douglas J. Lorenz, Sarah P. Suter, Jeffrey J. Buehner, Daniel Falanga, Elizabeth Watson, Craig A. Velozo, Andrea L. Behrman, and D. Michele Basso. Responsiveness of the neuromuscular recovery scale during outpatient activity-dependent rehabilitation for spinal cord injury. *Neurorehabilitation and Neural Repair*, 30(6):528–538, 2016.

[273] D. Zbogar, J. J. Eng, W. C. Miller, A. V. Krassioukov, and M. C. Verrier. Movement repetitions in physical and occupational therapy during spinal cord injury rehabilitation. *Spinal Cord*, 2016.

[274] Ossila. Spin coating for organic electronics and nanotechnology, 2017.

[275] Johannes Schindelin, Ignacio Arganda-Carreras, Erwin Frise, Verena Kaynig, Mark Longair, Tobias Pietzsch, Stephan Preibisch, Curtis Rueden, Stephan Saalfeld, Benjamin Schmid, Jean-Yves Tinevez, Daniel James White, Volker Hartenstein, Kevin Eliceiri, Pavel Toman-

cak, and Albert Cardona. Fiji: an open-source platform for biological-image analysis. *Nature Methods*, 9(7):676–682, 2012.

[276] Brandon Van Leer, Ron Kelley, Arda Genc, and Aleksei Savenko. Xe+ fib milling and measurement of amorphous damage in diamond. *Microscopy and Microanalysis*, 22(S3):178–179, 2016.

[277] E. Meijering, M. Jacob, J.-C. F. Sarria, P. Steiner, H. Hirling, and M. Unser. Design and validation of a tool for neurite tracing and analysis in fluorescence microscopy images. *Cytometry. Part A*, 58:167–76, April 2004.

[278] Melanie L Hart, Jasmin C Lauer, Mischa Selig, Martha Hanak, Brandan Walters, and Bernd Rolauffs. Shaping the cell and the future: Recent advancements in biophysical aspects relevant to regenerative medicine. *Journal of Functional Morphology and Kinesiology*, 3(1):2, 2018.

[279] Hayssam Khalil, Tao Chen, Renée Riffon, Rutao Wang, and Zhao Wang. Synergy between polyethylenimine and different families of antibiotics against a resistant clinical isolate of pseudomonas aeruginosa. *Antimicrobial agents and chemotherapy*, 52(5):1635–1641, 2008.

[280] Marit Kjaervik, Karin Schwibbert, Paul Dietrich, Andreas Thissen, and Wolfgang E. S. Unger. Surface characterisation of escherichia coli under various conditions by near-ambient pressure xps. *Surface and Interface Analysis*, 50(11):996–1000, 2018.

[281] Anders J. Barlow, Robert T. Jones, Andrew J. McDonald, and Paul J. Pigram. Xpssurfa: An open collaborative xps data repository using the cmsshub platform. *Surface and Interface Analysis*, 50(5):527–540, 2018.

[282] Konstantin N. Kudin, Bulent Ozbas, Hannes C. Schniepp, Robert K. Prud'homme, Ilhan A. Aksay, and Roberto Car. Raman spectra of graphite oxide and functionalized graphene sheets. *Nano Letters*, 8(1):36–41, 2008.

[283] R. Al-Gaashani, A. Najjar, Y. Zakaria, S. Mansour, and M.A. Atieh. Xps and structural studies of high quality graphene oxide and reduced graphene oxide prepared by different chemical oxidation methods. *Ceramics International*, 45(11):14439–14448, 2019.

[284] Z. H. He, S. S. Zhang, Q. Song, W. Y. Li, D. Liu, H. W. Li, M. L. Tang, and R. J. Chai. The structural development of primary cultured hippocampal neurons on a graphene substrate. *Colloids and Surfaces B-Biointerfaces*, 146:442–451, 2016.

[285] LE Scriven. Physics and applications of dip coating and spin coating. *MRS Online Proceedings Library Archive*, 121, 1988.

[286] D. Graf, F. Molitor, K. Ensslin, C. Stampfer, A. Jungen, C. Hierold, and L. Wirtz. Spatially resolved raman spectroscopy of single- and few-layer graphene. *Nano Letters*, 7(2):238–242, 2007.

[287] Alice AK King, Benjamin R Davies, Nikan Noorbehesht, Peter Newman, Tamara L Church, Andrew T Harris, Joselito M Razal, and Andrew I Minett. A new raman metric for the characterisation of graphene oxide and its derivatives. *Scientific reports*, 6(1):1–6, 2016.

[288] H. W. Liu, W. C. Huang, C. S. Chiang, S. H. Hu, C. H. Liao, Y. Y. Chen, and S. Y. Chen. Arrayed rgosh/pmash microcapsule platform integrating surface topography, chemical cues, and electrical stimulation for three-dimensional neuron-like cell growth and neurite sprouting. *Advanced Functional Materials*, 24(24):3715–3724, 2014.

[289] Peng-Yuan Wang, Sandy Shen-Chi Hung, Helmut Thissen, Peter Kingshott, and Raymond Ching-Bong Wong. Binary colloidal crystals (bccs) as a feeder-free system to generate human induced pluripotent stem cells (hipscs). *Scientific reports*, 6(1):1–11, 2016.

[290] Edward G Hayman, Michael D Pierschbacher, Shintaro Suzuki, and Erkki Ruoslahti. Vitronectina major cell attachment-promoting protein in fetal bovine serum. *Experimental cell research*, 160(2):245–258, 1985.

[291] Sangiliyandi Gurunathan, Jae Woong Han, Vasuki Eppakayala, and Jin-Hoi Kim. Green synthesis of graphene and its cytotoxic effects in human breast cancer cells. *International Journal of Nanomedicine*, 8:1015–1027, 2013.

[292] Biwu Liu, Shehan Salgado, Vivek Maheshwari, and Juewen Liu. Dna adsorbed on graphene and graphene oxide: Fundamental interactions, desorption and applications. *Current Opinion in Colloid and Interface Science*, 26:41–49, 2016.

[293] Jane Kovalevich and Dianne Langford. *Considerations for the Use of SH-SY5Y Neuroblastoma Cells in Neurobiology*, pages 9–21. Humana Press, Totowa, NJ, 2013.

[294] Wang-Yang Wu, Yang-Yang Wu, Huan Huang, Can He, Wei-Zu Li, Hui-Li Wang, Han-Qing Chen, and Yan-Yan Yin. Biochanin a attenuates lps-induced pro-inflammatory responses and inhibits the activation of the mapk pathway in bv2 microglial cells. *International journal of molecular medicine*, 35:391–8, February 2015.

[295] P. Liesi, D. Dahl, and A. Vaheri. Laminin is produced by early rat astrocytes in primary culture. *The Journal of Cell Biology*, 96(3):920–924, 1983.

[296] Wenbing Hu, Cheng Peng, Min Lv, Xiaoming Li, Yujie Zhang, Nan Chen, Chunhai Fan, and Qing Huang. Protein corona-mediated mitigation of cytotoxicity of graphene oxide. *ACS Nano*, 5(5):3693–3700, May 2011.

[297] Garima Srivastava, Kritika Singh, Mahe Talat, Onkar Nath Srivastava, and Arvind M. Kayastha. Functionalized graphene sheets as immobilization matrix for fenugreek β-amylase: Enzyme kinetics and stability studies. *PLOS ONE*, 9(11):e113408, 2014.

[298] V. Bernal, A. Erto, L. Giraldo, and J. C. Moreno-Pirajan. Effect of solution ph on the adsorption of paracetamol on chemically modified activated carbons. *Molecules*, 22(7), 2017.

[299] Jie Zhu, Shuzhen Li, Yue Zhang, Guixia Ding, Chunhua Zhu, Songming Huang, Aihua Zhang, Zhanjun Jia, and Mei Li. Cox-2 contributes to lps-induced stat3 activation and il-6 production in microglial cells. *American journal of translational research*, 10(29636886):966–974, March 2018.

[300] Ai Ling Wang, Albert C. H. Yu, Lok Ting Lau, Chong Lee, Le Meng Wu, Xiu'An Zhu, and Mark O. M. Tso. Minocycline inhibits lps-induced retinal microglia activation. *Neurochemistry international*, 47:152–8, July 2005.

[301] K. Kobayashi, S. Imagama, T. Ohgomori, K. Hirano, K. Uchimura, K. Sakamoto, A. Hirakawa, H. Takeuchi, A. Suzumura, N. Ishiguro, and K. Kadomatsu. Minocycline selectively inhibits m1 polarization of microglia. *Cell Death and Disease*, 4(3):e525–e525, 2013.

[302] Kim S, Chen J, Cheng T, Gindulyte A, He J, He S, Li Q, Shoemaker BA, Thiessen PA, Yu B, Zaslavsky L, Zhang J, and Bolton EE. Compound summary for cid 54675783, minocycline. *Nucleic Acids Research*, 2020.

[303] Kim S, Chen J, Cheng T, Gindulyte A, He J, He S, Li Q, Shoemaker BA, Thiessen PA, Yu B, Zaslavsky L, Zhang J, and Bolton EE. Compound summary for cid 3672, ibuprofen. *Nucleic Acids Research*, 2020.

[304] Gamze Ersan, Onur G. Apul, Francois Perreault, and Tanju Karanfil. Adsorption of organic contaminants by graphene nanosheets: A review. *Water Research*, 126:385–398, 2017.

[305] Hailong Zhang, Kristen Bremmell, Sunil Kumar, and Roger St C. Smart. Vitronectin adsorption on surfaces visualized by tapping mode atomic force microscopy. *Journal of biomedical materials research. Part A*, 68:479–88, Mar 2004.

[306] W. G. Pitt, D. J. Fabrizius-Homan, D. F. Mosher, and S. L. Cooper. Vitronectin adsorption on polystyrene and oxidized polystyrene. *Journal of colloid and interface science*, 129(1):231–239, 1989.

[307] Priya Banerjee, Pinaki Das, Aisha Zaman, and Papita Das. Application of graphene oxide nanoplatelets for adsorption of ibuprofen from aqueous solutions: Evaluation of process kinetics and thermodynamics. *Process Safety and Environmental Protection*, 101:45 – 53, 2016. Air Pollution Control and Waste Management.

[308] N. M. Davies. Clinical pharmacokinetics of ibuprofen. the first 30 years. *Clinical pharmacokinetics*, 34:101–54, Feb 1998.

[309] Yuan Gao, Yan Li, Liang Zhang, Hui Huang, Junjie Hu, Syed Mazhar Shah, and Xingguang Su. Adsorption and removal of tetracycline antibiotics from aqueous solution by graphene oxide. *Journal of Colloid and Interface Science*, 368(1):540 – 546, 2012.

[310] Elizabeth Peruski Canovic, Bo Qing, Aleksandar S. Mijailovic, Anna Jagielska, Matthew J. Whitfield, Elyza Kelly, Daria Turner, Mustafa Sahin, and Krystyn J. Van Vliet. Characterizing multiscale mechanical properties of brain tissue using atomic force microscopy, impact indentation, and rheometry. *Journal of visualized experiments*, Sep 2016.

[311] Helen R. Thomas, Daniel J. Phillips, Neil R. Wilson, Matthew I. Gibson, and Jonathan P. Rourke. One-step grafting of polymers to graphene oxide. *Polymer chemistry*, 6(48):8270–8274, 2015.

[312] Iman Noshadi, Seonki Hong, Kelly E Sullivan, Ehsan Shirzaei Sani, Roberto Portillo-Lara, Ali Tamayol, Su Ryon Shin, Albert E Gao, Whitney L Stoppel, Lauren D Black III, et al. In vitro and in vivo analysis of visible light crosslinkable gelatin methacryloyl (gelma) hydrogels. *Biomaterials science*, 5(10):2093–2105, 2017.

[313] Richard F Wallin and EF Arscott. A practical guide to iso 10993-5: Cytotoxicity. *Medical Device and Diagnostic Industry*, 20:96–98, 1998.

[314] Gongming Wang, Fang Qian, Chad W Saltikov, Yongqin Jiao, and Yat Li. Microbial reduction of graphene oxide by shewanella. *Nano Research*, 4(6):563–570, 2011.

[315] K. Zhou, S. Motamed, G. A. Thouas, C. C. Bernard, D. Li, H. C. Parkington, H. A. Coleman, D. I. Finkelstein, and J. S. Forsythe. Graphene functionalized scaffolds reduce the inflammatory response and supports endogenous neuroblast migration when implanted in the adult brain. *PLOS ONE*, 11(3), 2016.

[316] Souvarish Sarkar, Emir Malovic, Deeksha Sarda, Vivek Lawana, Dharmin Rokad, Huajun Jin, Vellareddy Anantharam, Arthi Kanthasamy, and Anumantha G. Kanthasamy. Characterization and comparative analysis of a new mouse microglial cell model for studying neuroinflammatory mechanisms during neurotoxic insults. *Neurotoxicology*, 67:129–140, 2018.

[317] Krithika Delhiraja, Kowsalya Vellingiri, Danil W. Boukhvalov, and Ligy Philip. Development of highly water stable graphene oxide-based composites for the removal of pharmaceuticals and personal care products. *Industrial & Engineering Chemistry Research*, 58(8):2899–2913, 2019.

[318] Jiao Yang Lu, Qiu Yan Zhu, Xin Xing Zhang, Fu Rui Zhang, Wei Tao Huang, Xue Zhi Ding, Li Qiu Xia, Hong Qun Luo, and Nian Bing Li. Directly repurposing waste optical discs with

prefabricated nanogrooves as a platform for investigation of cell-substrate interactions and guiding neuronal growth. *Ecotoxicology and Environmental Safety*, 160:273–281, 2018.